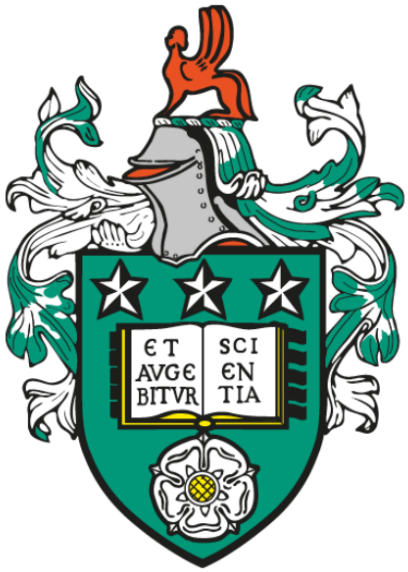
Instabilities in Rotating Two-layer Convection



Rhiannon Alexandra May Nicholls

University of Leeds

EPSRC Centre for Doctoral Training in Fluid Dynamics

Submitted in accordance with the requirements for the degree of
Doctor of Philosophy

June 2026

Intellectual Property Statement

I confirm that the work submitted is my own, except where work which has formed part of jointly authored publications has been included. My contribution and the other authors to this work has been explicitly indicated below. I confirm that appropriate credit has been given within the thesis where reference has been made to the work of others.

Chapter 3 contains material from the jointly authored publication:

Nicholls, R. A., Kersalé, E., Hughes, D. W., Davies, C. J. and Wilczyński, F. (2026). Rotating Rayleigh-Bénard convection with fixed-flux thermal boundary conditions, *J. Fluid Mech.* **1033**: A21. https://doi.org/10.1017/jfm.2026.11353

The co-authors provided ideas and guidance on this work and aided in writing the paper. All mathematical and scientific research contained in this work was undertaken by the candidate herself.

This copy has been supplied on the understanding that it is copyright material and that no quotation from the thesis may be published without proper acknowledgement.

© 2026 The University of Leeds and Rhiannon Alexandra May Nicholls.

The right of Rhiannon Alexandra May Nicholls to be identified as Author of this work has been asserted by Rhiannon Alexandra May Nicholls in accordance with the Copyright, Designs and Patents Act 1988.

Acknowledgements

First and foremost, I would like to express my sincere gratitude to my supervisors, Dr Evy Kersalé, Prof. David Hughes, Prof. Chris Davies, and Dr Fryderyk Wilczyński. Their unwavering support, insightful guidance, and extensive expertise have deepened my learning and understanding, underpinning my progress throughout the PhD. Their encouragement, enthusiasm, and mentorship have been instrumental in shaping the researcher I have become. Thank you for making this project so enjoyable and fulfilling; it has been a remarkable experience and a true privilege to work with you all.

I am grateful to the EPSRC Centre for Doctoral Training (CDT) in Fluid Dynamics for affording me the opportunity to conduct this research. I would also like to thank my CDT cohort, whose friendship and support have made this journey much more enjoyable. Special thanks to Tyler, Coker, Kasia, and Yatin for many helpful discussions, encouragement, and distractions along the way.

My heartfelt thanks to my family for their ongoing love and support. Thank you for always making me laugh, even through tough times. A huge thank you to my family-in-law for welcoming me so warmly and for giving me the same love and support as my own family. A special thanks goes to Buddy and Scruffy for keeping me company towards the end. Our walks were a much-needed distraction, and your presence brought a calm I truly needed.

My deepest appreciation goes to my mum, Mary. I am grateful that you encouraged me to leave home and pursue my interests elsewhere. In hindsight, it was the best decision you ever encouraged me to make, and I would not be where I am today without your unconditional love, unwavering support, belief and encouragement. I can never fully express how grateful I am for everything you do.

Most importantly, I want to thank my wife, Ash Howland-Hill. There is no way to properly acknowledge the part you have played. You have lived alongside this PhD as long as I have, sharing the excitement of breakthroughs, the frustration of setbacks, and everything in between. You have listened to me talk endlessly about convection, always making the effort to understand and help me think through whatever problem I was facing. You have celebrated every win with me and kept me going when things felt difficult. I am deeply grateful for your support and encouragement, and, most of all, for being there through it all. Thank you for being my constant throughout this journey. I now know that I can accomplish anything with you by my side, and I look forward to our next chapter together.

Abstract

Rotating Rayleigh—Bénard convection (RRBC) is the study of thermal convection in a horizontal fluid layer heated from below while the entire system rotates about the vertical axis, thereby combining buoyancy-driven and rotational effects. RRBC has been extensively studied to understand key aspects of fluid dynamics in many geophysical and astrophysical contexts.

Rotating convective systems, particularly in geophysical and astrophysical applications, exhibit strong depth-dependent variations in fluid properties. Simplified models that approximate the dominant dynamical processes, typically by treating depth-dependent properties as constant, are employed, rendering the problem computationally feasible while still capturing the essential physics. Consequently, the exploration and understanding of rotational effects in convective systems with depth-dependent properties remain limited, thereby motivating the systematic investigation presented in this study.

Two-layer convection is an extension of the classical RRBC framework, comprising two superposed, horizontally extended fluid layers that are heated from below. Each layer is characterised by distinct physical parameters, thereby enabling an explicit representation of depth-dependent variations in the fluid's properties. In this thesis, we aim to advance the theoretical understanding of rotating convection with depth-dependent variations in fluid properties by analysing the instabilities that arise in a simplified rotating two-layer configuration. We first examine the role of thermal boundary conditions in steady RRBC under rapid rotation and derive an asymptotic solution for fixed-flux boundaries. Our analysis demonstrates that, in the rapidly rotating limit, the influence of thermal boundary conditions becomes negligible. We then investigate instabilities in two related configurations. First, we consider a single-fluid-layer system overlain by a solid boundary slab of finite thickness and thermal conductivity, which serves as a reduced model for a two-fluid-layer system with a strong viscosity contrast. Subsequently, we extend the analysis to the fully coupled rotating two-layer configuration. In both configurations, we determine the onset conditions and conduct a comprehensive linear stability analysis to elucidate how the system's behaviour depends on the underlying fluid properties.

Contents

List of Figures xxii

List of Tables xxiii

1 Introduction 1

1.1 Motivation . . . 1

1.2 Thermal convection . . . 5

1.3 Thesis Structure . . . 10

2 Theoretical Framework of Rotating Rayleigh–Bénard Convection 13

2.1 Introduction . . . 13

2.2 Rotating frame of reference . . . 14

2.3 Governing equations . . . 15

2.3.1 The continuity equation . . . 15

2.3.2 The momentum equation . . . 15

2.3.3 The thermal energy equation . . . 16

2.3.4 The Boussinesq approximation . . . 17

2.4 The basic state . . . 19

2.5 The linear dimensionless perturbation equations . . . 19

2.6 Boundary conditions . . . 20

2.6.1 Mechanical boundary conditions . . . 21

2.6.2 Thermal boundary conditions . . . 21

2.7 Normal mode analysis . . . 22

2.8 Linear stability analysis . . . 24
2.8.1 Onset of non-rotating convection . . . 24
2.8.2 Onset of rotating convection . . . 26

3 Rotating Rayleigh–Bénard Convection with Fixed Flux Boundaries 31
3.1 Introduction . . . 31
3.2 Mathematical formation . . . 33
3.2.1 Governing equations . . . 33
3.2.2 Linear stability analysis . . . 35
3.3 Derivation of the 'departure system' . . . 36
3.4 Guidance from the numerical solutions . . . 39
3.5 Asymptotic determination of the departures . . . 41
3.5.1 Inner solutions . . . 42
3.5.2 Outer solutions . . . 44
3.5.3 Matching the inner and outer solutions . . . 45
3.5.4 Composite solutions . . . 46
3.6 Fixed-flux solutions . . . 49
3.7 Discussion . . . 53

4 Rotating Convection with a Boundary Slab of Finite Conductivity 55
4.1 Introduction . . . 55
4.2 Mathematical formulation . . . 57
4.2.1 Governing equations . . . 57
4.2.2 Linear stability analysis . . . 59
4.3 Onset of non-rotating convection . . . 59
4.4 Onset of rotating convection . . . 66
4.4.1 Steady modes of instability . . . 66
4.4.2 Oscillatory modes of instability . . . 74
4.5 Discussion . . . 78

5 Rotating Two-Layer Convection **81**

5.1 Introduction 81

5.2 Mathematical formulation 83

5.2.1 Governing equations 83

5.2.2 Linear stability analysis 87

5.2.3 Symmetry of the system 89

5.2.4 Limiting cases 89

5.3 Onset of non-rotating convection 91

5.3.1 The equal layer depth configuration 92

5.3.2 The non-equal layer depth configuration 97

5.4 Onset of rotating steady convection 104

5.4.1 Variation in the thermal diffusivity ratio 104

5.4.2 Variation in the viscosity ratio 111

5.5 Onset of rotating oscillatory convection 116

5.5.1 Variation in the thermal diffusivity ratio 117

5.5.2 Variation in the viscosity ratio 121

5.6 Discussion 133

6 Summary and Future Work **137**

6.1 Summary 137

6.2 Application to Jupiter 140

6.3 Future work 142

References **145**

List of Figures

1.1 (a) Polar projection of the south polar region from $-60°$ to $-90°$, built using four different images captured during the Cassini mission on 3 December 2008. (b) An equivalent projection of the north polar region from $60°$ to $90°$, captured during the Cassini mission on 14 June 2013. Taken from Read et al. (2022), who adapted from Antuñano et al. (2015). 3

1.2 Projected maps of the regions surrounding the (a) north and (b) south poles of Jupiter from data collected by NASA's Juno mission on 2 February 2017, during the 3rd science pass of NASA's Juno spacecraft. The latitude circle is $80°$ N or $80°$ S (planetocentric). Meridians are drawn every $15°$ of longitude. Taken from Adriani et al. (2018). 3

1.3 (a) Density ρ, Pressure P, and temperature T, and (b) coefficient of thermal expansion α, thermal diffusivity κ, and kinematic viscosity ν as a function of radius where $R_J = 6.9894 \times 10^7 \mathrm{m}$ is Jupiter's mean radius. Crosses are data points from French et al. (2012). 5

1.4 Schematic illustration of rotating Rayleigh–Bénard convection. A fluid layer is rotated about the vertical axis with a constant angular velocity, heated from below and cooled from above. The fluid movement, indicated by the arrows, rises when heated and descends when cooled, creating cellular flow patterns. 9

2.1 Schematic illustration of rotating Rayleigh–Bénard convection. 14

2.2 Marginal stability curves with $Ta = 10^4$. The red branch, equal in all panels, indicates the onset of steady convection with $Ra_s^c = 5377.12$ and $k_s^c = 5.698$. The blue branches represent the onset of oscillatory convection for (a) $Pr = 0.46$, (b) $Pr^t = 0.51186$, and (c) $Pr = 0.58$. 30

2.3 The transitional Prandtl number Pr^t as a function of the Taylor number Ta, as defined in (2.99). Steady convection is favoured for $Pr > Pr^t$, while oscillatory convection is preferred for $Pr < Pr^t$. The dashed lines indicate the critical values $Ta^c = 544.7$ and $Pr^c = 0.677$. 30

3.1 Eigenfunctions of (a) vertical velocity, (b) temperature and (c) vertical vorticity, for FT boundary conditions (dashed blue) and FF boundary conditions (solid red), with $Ta = 10^{10}$; the inset figures show a magnified view of the boundary layers within the boxed region near $z = 0$. The eigenfunctions are normalised so that $\max(w) = 1$. . 37

3.2 Numerically computed, asymptotically scaled critical (a) Rayleigh number and (b) wavenumber as functions of Taylor number for FT and FF conditions. The dashed line with open circles shows the values calculated from the explicit formula of Dowling (1988). (c) The relative difference, as a function of Ta, of the critical Rayleigh number (solid) and wavenumber (dashed) between solutions with FT and FF conditions. The relative difference for both critical values scale as $Ta^{-1/2}$. 37

3.3 Numerical solutions of (a) vertical velocity, (b) temperature, and (c) vertical vorticity of the difference between the FT and FF systems, with $Ta = 10^{10}$ and $\widetilde{k} = 1.3038$. . 40

3.4 Balance of terms close to the boundary $z = 0$ (top row) and within the bulk ($0.15 \lesssim z < 0.5$) (bottom row). The columns correspond to the temperature equation (3.25) (left), vorticity equation (3.26) (middle) and equation (3.27) (right), with $Ta = 10^{10}$ and $\widetilde{k} = 1.3038$. The legends given for (a), (b) and (c) also correspond to (d), (e) and (f), respectively. Solid lines indicate standard rotating Rayleigh–Bénard terms. The dashed line depicts the 'additional' term, given by the final term in equation (3.27), identifiable by its multiplication with $\sin \pi z$, to the standard rotating Rayleigh–Bénard terms. 40

3.5 Dashed black lines show the numerical results, while the red solid lines show the composite solutions of W, Θ and Z, as given by expressions (3.65)–(3.67), where $\widetilde{k}$ and $\widetilde{Ra}_t$ are determined numerically. Rows correspond to W, Θ, and Z, with $Ta = 10^{10}$ and $\widetilde{k} = 1.3038$. Columns correspond to the solutions close to the boundary $z = 0$ (left) and within the bulk ($0.15 \lesssim z < 0.5$) (right). 47

3.6 The maximum absolute error over the z-domain between numerical (subscript N) and asymptotic (subscript A) solutions of (a) W, (b) Θ, (c) Z, (d) $\mathcal{D}Z$, evaluated across a range of Taylor numbers. The asymptotic solutions of W, Θ, Z and $\mathcal{D}Z$ are given by expressions (3.65)–(3.68). The absolute error exhibits gradients of approximately -0.69 for W, -0.86 for Θ, -0.44 for Z, and -0.18 for $\mathcal{D}Z$. 48

3.7 Numerical (dashed black) and asymptotic (solid red) solutions of the (a) critical Rayleigh number and (b) critical wavenumber of the fixed flux system. Asymptotic solutions of the critical Rayleigh number and wavenumber are given by expressions (3.80) and (3.81), respectively. The absolute error between the numerical (subscript N) and asymptotic (subscript A) solutions of the (c) critical Rayleigh number and (d) critical wavenumber of the fixed flux system. The absolute error exhibits gradients of approximately -0.81 with respect to the Rayleigh number and -0.82 with respect to the wavenumber. 52

4.1 Schematic sketch of rotating Rayleigh–Bénard convection with a boundary slab of finite conductivity. 58

4.2 Variations of the critical (a) Rayleigh number Ra^c and (b) wavenumber k^c as functions of the thermal conductivity ratio K_r, with $Ta = 0$ and $\delta = 1$, for the system considered here (blue solid) and the one studied by Nield (1968) (red dashed), differing only in the mechanical condition imposed at the lower fluid boundary: no-slip in Nield (1968), and stress-free in our case. 61

4.3 Critical mode for $K_r = 10^3$ with $Ta = 0$ and $\delta = 1$, corresponding to $k^c = 2.68$ and $Ra^c = 1100.34$. The eigenfunctions are normalised such that $\max(w) = 1$. (a) Profiles of the eigenfunctions: vertical velocity w (blue) and temperature perturbation θ in the fluid and θ' in the solid (red); (b) temperature contours and velocity vector field in the x–z plane. 63

4.4 Same as figure 4.3 for $K_r = 10^{-3}$ with $Ta = 0$ and $\delta = 1$, corresponding to $k^c = 2.22$ and $Ra^c = 816.99$. 63

4.5 Variations of the critical (a) Rayleigh number Ra^c and (b) wavenumber k^c as functions of the layer depth ratio δ, with $Ta = 0$ and $K_r = 1$, for the system considered here (blue solid) and the one studied by Nield (1968) (red dashed), differing only in the mechanical condition imposed at the lower fluid boundary: no-slip in Nield (1968), and stress-free in our case. 64

4.6 Same as figure 4.3 for $\delta = 2$ with $Ta = 0$ and $K_r = 1$, corresponding to $k^c = 2.42$ and $Ra^c = 948.38$. 64

4.7 Colour map of the critical (a) Rayleigh number Ra^c and (b) wavenumber k^c as functions of the depth ratio δ and thermal conductivity ratio K_r, with $Ta = 0$. The colour scales represent the magnitudes of Ra^c and k^c, with warmer colours indicating higher values. 65

4.8 Variations of the critical (a) Rayleigh number Ra^c and (b) wavenumber k^c as functions of the thermal conductivity ratio K_r, for $Ta = 0$ (blue solid) and $Ta = 10^{14}$ (red dashed), with $\delta = 1$. 67

4.9 Variations of the critical (a) Rayleigh number Ra^c and (b) wavenumber k^c as functions of the thermal conductivity ratio K_r, for different Taylor numbers, with $\delta = 1$. Each quantity is normalised by its corresponding critical value for RRBC with fixed-temperature boundaries, where one boundary is stress-free and the other is no-slip, denoted by Ra^c_*, and k^c_*. The legend in (a) applies to (b). 67

4.10 Velocity profiles (top row) and temperature profiles (bottom row) of the critical modes for $Ta = 0$ (blue), and $Ta = 10^{14}$ (red), at $K_r = 10^{-3}$ (solid) and $K_r = 10^3$ (dashed), with $\delta = 1$. The solutions are normalised such that $\max(w) = 1$. The left column shows the profiles across the entire two-layer domain. The right column provides magnified views of the boundary layers near the solid-fluid interface at $z = 0$. The vertical range of w is restricted to $-4 \times 10^{-3} \leq z \leq -10^{-3}$ to highlight the shape of the boundary layer, while the vertical range of θ is restricted to $-0.01 \leq z \leq 0.01$. The corresponding critical wavenumbers and critical Rayleigh numbers are: (1) $Ta = 0$ and $K_r = 10^{-3}$: $k^c = 2.2$, $Ra^c = 817$; (2) $Ta = 0$ and $K_r = 10^3$: $k^c = 2.7$, $Ra^c = 1100.3$; (3) $Ta = 10^{14}$ and $K_r = 10^{-3}$: $k^c = 275.7$, $Ra^c = 1.8044 \times 10^{10}$; (4) $Ta = 10^{14}$ and $K_r = 10^3$: $k^c = 275.8$, $Ra^c = 1.8045 \times 10^{10}$. 69

4.11 Temperature contours and velocity vectors in the x–z plane of the critical mode for $K_r = 10^{-3}$, $Ta = 10^{14}$, and $\delta = 1$, with $k^c = 275.75$ and $Ra^c = 1.804 \times 10^{10}$. The eigenfunctions are normalised such that $\max(w) = 1$. Eigenfunction profiles are shown in figure 4.10. 70

4.12 Variations of the critical (a) Rayleigh number Ra^c and (b) wavenumber k^c as functions of the layer depth ratio δ, for $Ta = 0$ (blue) and $Ta = 10^{14}$ (red), with $K_r = 1$. . . . 71

4.13 Variations of the critical (a) Rayleigh number Ra^c and (b) wavenumber k^c as functions of the depth ratio δ, for different Taylor numbers, with $K_r = 1$. Each quantity is normalised by its corresponding critical value for RRBC with fixed-temperature boundaries, where one boundary is stress-free and the other is no-slip, denoted by Ra^c_*, and k^c_*. The legend in (a) applies to (b). 71

4.14 Velocity profiles (top row) and temperature profiles (bottom row) of the critical modes for $Ta = 0$ (blue), and 10^{14} (red), at $\delta = 10^{-4}$ (solid) and $\delta = 2$ (dashed), with $K_r = 1$. The solutions are normalised such that max $(w) = 1$. The left column shows the profiles across the entire two-layer domain. The right column provides magnified views of the boundary layers near the solid-fluid interface at $z = 0$. The vertical range of w is restricted to $-4 \times 10^{-3} \leq z \leq -10^{-3}$ to highlight the shape of the boundary layer, while the vertical range of θ is restricted to $-0.01 \leq z \leq 0.01$. The corresponding critical wavenumbers and critical Rayleigh numbers are: (1) $Ta = 0$ and $\delta = 10^{-4}$: $k^c = 2.7$, $Ra^c = 1100.6$; (2) $Ta = 0$ and $\delta = 2$: $k^c = 2.4$, $Ra^c = 948.4$; (3) $Ta = 10^{14}$ and $\delta = 10^{-4}$: $k^c = 275.8$, $Ra^c = 1.8045 \times 10^{10}$; (4) $Ta = 10^{14}$ and $\delta = 2$: $k^c = 275.8$, $Ra^c = 1.8044 \times 10^{10}$. 73

4.15 Colour map of the critical (a) Rayleigh number Ra^c and (b) wavenumber k^c as functions of the depth ratio δ and thermal conductivity ratio K_r, with $Ta = 10^{14}$. The colour scales represent the magnitudes of Ra^c and k^c, with warmer colours indicating higher values. The dashed black line shows the transition point at $Ta^{1/6} = 4.6 \times 10^{-3}$. 74

4.16 Asymptotically scaled critical (a) Rayleigh number $Ra^c/Ta^{2/3}$ and (b) wavenumber $k^c/Ta^{1/6}$ as functions of the Taylor number Ta for $K_r = 10^{-3}$ (blue) and $K_r = 10^3$ (red), with $\delta = 1$, at the onset of steady ($Pr = 1$) and oscillatory ($Pr = 0.01,\ 0.1,\ 0.4$) convection. 76

4.17 The transitional Prandtl number Pr^t as a function of Ta for RRBC with stress-free, fixed-temperature boundaries, defined by (2.99), and for RRBC-BS at $K_r = 10^{-3}$, $K_r = 1$, and $K_r = 10^3$ with $\delta = 1$, is determined numerically. Steady convection is favoured for $Pr > Pr^t$, while oscillatory convection is preferred for $Pr < Pr^t$. (a) The full range of Ta and Pr^t. The dashed lines indicate the critical values, $Ta^c = 544.7$ and $Pr^c = 0.677$, of the RRBC system. (b) An enlarged view of the region where the RRBC-BS system curves intersect. 77

4.18 Same as figure 4.3 for $K_r = 10^3$, $Ta = 10^4$ and $\delta = 1$. The top row corresponds to the steady instability with $Ra_s^c = 5142.20$ and $k_s^c = 5.36$, while the bottom row shows the oscillatory instability at $Pr^t = 0.3001$, where $Ra_o^c = 5142.20$, $k_o^c = 3.87$ and $\omega^c = 6.22$. 79

5.1 Schematic sketch of rotating two-layer convection. 84

5.2 Variation of the critical (a) Rayleigh numbers, Ra_1^c (solid) and Ra_2^c (dashed), and (b) wavenumber k^c as functions of the viscosity ratio ν_r, for the case where $\delta = \kappa_r = 1$. 93

5.3 Critical mode for $\nu_r = 10^4$ with $\delta = \kappa_r = 1$, corresponding to $k^c = 2.42$ and $Ra_1^c = 948.69$. The eigenfunctions are normalised such that $\max(w) = 1$. (a) Profiles of the eigenfunctions: vertical velocity w (blue) and temperature perturbation θ (red); (b) temperature contours and velocity vector field in the x–z plane. 93

5.4 Variation of the critical (a) Rayleigh numbers, Ra_1^c (solid) and Ra_2^c (dashed), and (b) wavenumber k^c as functions of the thermal diffusivity ratio κ_r, for the case where $\delta = \nu_r = 1$. 95

5.5 Same as figure 5.3 for $\kappa_r = 10^4$ with $\delta = \nu_r = 1$, corresponding to $k^c = 1.45$ and $Ra_1^c = 261.58$. 95

5.6 Variation of the critical (a) Rayleigh numbers, Ra_1^c (solid) and Ra_2^c (dashed), and (b) wavenumber k^c as functions of the viscosity ratio ν_r for different values of the thermal diffusivity ratio κ_r, for the case where $\delta = 1$. The dotted black line shows the critical values for single-layer convection with fixed-temperature boundaries (one no-slip, one stress-free) and a domain height of one: $Ra^c = 1100.65$ and $k^c = 2.68$. 96

5.7 Same as figure 5.3 for $\kappa_r = 100$ and $\nu_r = 10^8$ with $\delta = 1$, corresponding to $k^c = 2.68$ and $Ra_1^c = 1097.53$. 96

5.8 Same as figure 5.3 for $\kappa_r = 0.01$ and $\nu_r = 10^8$ with $\delta = 1$, corresponding to $k^c = 2.22$ and $Ra_1^c = 819.15$. 98

5.9 Same as figure 5.3 for $\kappa_r = 0.01$ and $\nu_r = 5 \times 10^4$ with $\delta = 1$, corresponding to $k^c = 1.26$ and $Ra_1^c = 688.80$. 98

5.10 Variation of the critical (a) Rayleigh numbers, Ra_1^c (solid) and Ra_2^c (dashed), and (b) wavenumber k^c as functions of the viscosity ratio ν_r for several values of the depth ratio δ, with $\kappa_r = 1$. The dotted black line shows the critical values for single-layer convection with fixed-temperature boundaries (one no-slip, one stress-free) and a domain height of one: $Ra^c = 1100.65$ and $k^c = 2.68$. 100

5.11 Marginal stability curve for $\nu_r = 2.217 \times 10^{-3}$ and $\delta = 0.5$, with $\kappa_r = 1$. The minima, $Ra_1^c = 32.7$, are at $k_l^c = 0.847$ and $k_h^c = 4.648$. 100

5.12 Same as figure 5.3 for $\nu_r = 2.217 \times 10^{-3}$ and $\delta = 0.5$ with $\kappa_r = 1$ corresponding to the minimum, $Ra_1^c = 32.7$, with $k_l^c = 0.847$ (top) and $k_h^c = 4.648$ (bottom) of the marginal stability curve in figure 5.11. 101

5.13 Variation of the critical (a) Rayleigh numbers, Ra_1^c (solid) and Ra_2^c (dashed), and (b) wavenumber k^c as functions of the thermal diffusivity ratio κ_r for different values of the depth ratio δ, with $\nu_r = 1$. The dotted black line shows the critical values for single-layer convection with stress-free fixed-temperature boundaries and a domain height of one: $Ra^c = 657.51$ and $k^c = 2.22$. 102

5.14 Same as figure 5.3 for $\kappa_r = 3.5 \times 10^{-3}$ and $\delta = 0.1$ with $\nu_r = 1$ corresponding to the minimum, $Ra_1^c = 26.8$, with $k_l^c = 2.2$ (top) and $k_h^c = 9.65$ (bottom) of the marginal stability curve with two equally preferred modes. 103

5.15 Variation of the scaled critical (a) Rayleigh numbers, Ra_1^c (solid) and Ra_2^c (dashed), and (b) wavenumber k^c as functions of the thermal diffusivity ratio κ_r, with $\delta = \nu_r = 1$, for different values of the Taylor number Ta_1. 105

5.16 Same as figure 5.3 for $\kappa_r = 10^4$ and $Ta_1 = 10^{14}$ with $\delta = \nu_r = 1$, corresponding to $k^c = 233.59$ and $Ra_1^c = 1.17 \times 10^{10}$. 105

5.17 Critical mode eigenfunctions of vertical velocity w (blue) and temperature perturbation θ (red) for $\delta = \nu_r = 1$. The top row corresponds to $Ta_1 = 10^{14}$ and the bottom row to $Ta_1 = 0$. Left column: $\kappa_r = 1$, with (a) $k^c = 223.12$, $Ra_1^c = 7.44 \times 10^9$, and (d) $k^c = 1.11$, $Ra_1^c = 41.09$. Middle column: $\kappa_r = 1.5$, with (b) $k^c = 225.80$, $Ra_1^c = 9.79 \times 10^9$, and (e) $k^c = 1.12$, $Ra_1^c = 60.18$. Right column: $\kappa_r = 3$, with (c) $k^c = 231.18$, $Ra_1^c = 1.12 \times 10^{10}$, and (f) $k^c = 1.15$, $Ra_1^c = 103.08$. 107

5.18 Variation of the scaled critical (a) Rayleigh number Ra_1^c, and (b) wavenumber k^c as functions of the Taylor number Ta_1, with $\delta = \nu_r = 1$, for $\kappa_r = 1$ (RRBC with domain height two) (blue) and $\kappa_r = 10^4$ (orange), and for rotating Rayleigh–Bénard convection bounded by stress-free fixed-temperature conditions with domain height one (magenta). 107

5.19 Variation of the critical (a) Rayleigh numbers, Ra_1^c (solid) and Ra_2^c (dashed), and (b) wavenumber k^c as functions of the thermal diffusivity ratio κ_r for different values of the depth ratio δ, with $\nu_r = 1$ and $Ta_1 = 10^{14}$. The dotted black line shows the critical values for single-layer convection with stress-free fixed-temperature boundaries and a domain height of one: $Ra^c = 1.87 \times 10^{10}$ and $k^c = 281.1$. 109

5.20 Same as figure 5.3 for $\kappa_r = 0.25$, $\delta = 0.1$, and $Ta_1 = 10^{14}$ with $\nu_r = 1$ corresponding to the minimum, $Ra_1^c = 1.44 \times 10^{10}$, with $k_l^c = 284.2$ (top) and $k_h^c = 446.1$ (bottom) of the marginal stability curve with two equally preferred modes. 110

5.21 Variation of the critical (a) Rayleigh number within each layer: Ra_1^c (solid) and Ra_2^c (dashed), and (b) wavenumber k^c as a function of the viscosity ratio ν_r, with $\delta = \kappa_r = 1$, for different Taylor numbers Ta_1. 112

5.22 Variation of the scaled critical (a) Rayleigh number Ra_1^c, and (b) wavenumber k^c as functions of the Taylor number Ta_1 of rotating two-layer convection with $\delta = \kappa_r = 1$, $\nu_r = 10^8$ (red circles) and $\nu_r = 10^{-8}$ (green crosses), rotating Rayleigh–Bénard convection bounded by a slab of fixed conductivity (solid blue), and rotating Rayleigh–Bénard convection bounded by stress-free fixed-temperature conditions with domain height one (dashed magenta). 112

5.23 Same as figure 5.3 for $\nu_r = 4327$ and $Ta_1 = 10^8$ with $\kappa_r = \delta = 1$ corresponding to the minimum, $Ra_1^c = 1.71 \times 10^6$, with $k_l^c = 2.1$ (top) and $k_h^c = 26.4$ (bottom) of the marginal stability curve with two equally preferred modes. 114

5.24 Variation of the (steady) scaled critical (a) Rayleigh number Ra_1^c, and (b) wavenumber k^c as functions of the Taylor number Ta_1, with $\delta = \kappa_r = 1$, for different values of the viscosity ratio $\nu_r \geq 1$. 115

5.25 Same as figure 5.3 for $\nu_r = 10^{-4}$ and $Ta_1 = 10^{14}$ with $\delta = \kappa_r = 1$, corresponding to $k^c = 281.09$ and $Ra_1^c = 1.87 \times 10^{10}$. 115

5.26 Asymptotically scaled critical (a) Rayleigh number $Ra_1^c Ta_1^{-2/3}$, (b) Rayleigh number in the range $Ra_1^c Ta_1^{-2/3} = 5$ to $Ra_1^c Ta_1^{-2/3} = 11$, and (c) wavenumber $k^c Ta_1^{-1/6}$ as functions of the Taylor number Ta_1 for $\kappa_r = 1$ (blue) and $\kappa_r = 10^3$ (orange), with $\nu_r = \delta = 1$, for the onset of steady ($Pr_1 = 1$) and oscillatory ($Pr_1 = 0.1,\ 0.4,\ 0.67$) convection. 118

5.27 Profiles of the (a) vertical velocity w and (b) temperature perturbation θ of the critical modes for $\kappa_r = 10^3$ and $Ta_1 = 10^{14}$ with $\delta = \nu_r = 1$ for steady ($Pr_1 = 1$) and oscillatory ($Pr_1 = 0.1,\ 0.4$) modes. The eigenfunctions are normalised such that $\max(w) = 1$. The corresponding critical wavenumbers and critical Rayleigh numbers are: (1) $Pr_1 = 1$: $k_s^c = 233.6$, $Ra_{1s}^c = 1.17 \times 10^{10}$; (2) $Pr_1 = 0.1$: $k_o^c = 100.1$, $Ra_{1o}^c = 1.24 \times 10^9$; (3) $Pr_1 = 0.4$: $k_o^c = 149.7$, $Ra_{1o}^c = 6.53 \times 10^9$. . . 118

5.28 The transitional Prandtl number Pr_1^t as a function of the Taylor number Ta_1 with $\delta = \nu_r = 1$, for different κ_r values. 120

5.29 The (a) asymptotically scaled critical wavenumber $k_o^c Ta_1^{-1/6}$, (b) transitional Prandtl numbers, Pr_1^t (solid) and Pr_2^t (dashed), and (c) asymptotically scaled critical frequency $\omega^c Ta_1^{-1/3}$ at the onset of oscillatory instabilities as functions of thermal diffusivity κ_r, with $\delta = \nu_r = 1$, for a range of Taylor numbers Ta_1. Panels (a) and (c) show results for the corresponding Pr_1^t values in (b). 121

5.30 Asymptotically scaled critical (a) Rayleigh number $Ra_1^c Ta_1^{-2/3}$, and (b) wavenumber $k^c Ta_1^{-1/6}$ as functions of the Taylor number Ta_1 for $\nu_r = 1$ (purple), $\nu_r = 10^2$ (blue), $\nu_r = 10^4$ (green), and $\nu_r = 10^8$ (yellow), with $\kappa_r = \delta = 1$, for the onset of steady ($Pr_1 = 1$) and oscillatory ($Pr_1 = 0.01,\ 0.1,\ 0.4$) convection. 122

5.31 Profiles of the vertical velocity w (left) and temperature perturbation θ (right) of the critical modes for $\nu_r = 10^8$ and $Ta_1 = 10^{14}$ with $\delta = \kappa_r = 1$ for steady ($Pr_1 = 1$) and oscillatory ($Pr_1 = 0.1,\ 0.4$, and $Pr_1^t = 0.62$) modes. The eigenfunctions are normalised such that $\max(w) = 1$. The top row shows the entire domain, while the bottom row shows the solutions near the interface. The corresponding critical wavenumbers and critical Rayleigh numbers are: (1) $Pr_1 = 1$: $k_s^c = 275.8$, $Ra_{1s}^c = 1.80 \times 10^{10}$; (2) $Pr_1 = 0.1$: $k_o^c = 129.8$, $Ra_{1o}^c = 1.93 \times 10^9$; (3) $Pr_1 = 0.4$: $k_o^c = 187.3$, $Ra_{1o}^c = 1.07 \times 10^{10}$; (4) $Pr_1^t = 0.62$: $k_o^c = 206$, $Ra_{1o}^c = 1.80 \times 10^{10}$. . 123

5.32 Variation of the (a) transitional Prandtl number Pr_1^t and (b) critical wavenumber k_s^c (solid) and k_o^c with $Pr_1 \equiv Pr_1^t$ (dashed) as functions of the Taylor number Ta_1, with $\delta = \kappa_r = 1$, for different viscosity ratios ν_r. 125

5.33 Variation of the (a) critical wavenumber k_s^c (solid) and k_o^c (dashed), (b) critical wavenumber for the interval $8 \leq \nu_r \leq 35$ with $Ta_1 = 10^5$, (c) transitional Prandtl number, Pr_1^t, and (d) critical frequency ω^c, for the onset of oscillatory instabilities as functions of the viscosity ratio ν_r, with $\delta = \kappa_r = 1$, for $Ta_1 = 10^3,\ 10^4,\ 10^5$. 126

5.34 Marginal stability curve with $Ta_1 = 10^3$ and $\nu_r = 47.3$. The red branch indicates the onset of steady convection. The blue branch represent the onset of oscillatory convection with $Pr_1^t = 0.162$. 128

5.35 Marginal stability curve with $Ta_1 = 10^4$ and (a) $\nu_r = 37.5$ with $Pr_1^t = 0.178$, and (b) $\nu_r = 54.5$ with $Pr_1^t = 0.292$. The red branch indicates the onset of steady convection. The blue branches represent the onset of oscillatory convection. 128

5.36 Same as figure 5.3 for $Ta_1 = 10^4$, $\nu_r = 37.5$ and $Pr_1^t = 0.178$ corresponding to the minimum, $Ra_1^c = 3894$ with $k_{o_1}^c = 2.15$ and $\omega_{o_1}^c = 0.35$ (top), $k_{s_1}^c = 2.29$ (middle) and $k_{o_2}^c = 3.70$ and $\omega_{o_2}^c = 3.12$ (bottom) of the marginal stability curve in figure 5.35(a). 129

5.37 Marginal stability curve with $Ta_1 = 10^5$ and (a) $\nu_r = 13.7$ with $Pr_1^t = 0.210$, and (b) $\nu_r = 14.15$ with $Pr_1^t = 0.204$. The red branch indicates the onset of steady convection. The blue branches represent the onset of oscillatory convection. 130

5.38 Same as figure 5.3 for $Ta_1 = 10^5$, $\nu_r = 14.15$ and $Pr_1^t = 0.204$ corresponding to the minimum, $Ra_1^c = 9064$, with $k_{o_2}^c = 3.66$ and $\omega_{o_2}^c = 0.42$ of the marginal stability curve in figure 5.37(b). 130

5.39 Marginal stability curve with $Ta_1 = 10^5$ and $\nu_r = 31.8$. The red branch indicates the onset of steady convection. The blue branches represent the onset of oscillatory convection with $Pr_1^t = 0.140$. 131

5.40 Same as figure 5.3 for $Ta_1 = 10^5$, $\nu_r = 31.8$ and $Pr_1^t = 0.140$ corresponding to the minimum, $Ra_1^c = 1.16 \times 10^4$, with $k_{s_1}^c = 2.86$ (top), $k_{o_1}^c = 3.59$ and $\omega_{o_1}^c = 2.76$ (middle) and $k_{o_2}^c = 5.72$ and $\omega_{o_2}^c = 10.43$ (bottom) of the marginal stability curve in figure 5.39. 132

List of Tables

5.1 Summary of the asymptotic scaling of the critical Rayleigh numbers and wavenumber at the onset of steady rapidly rotating two-layer convection. Results are given in the rapidly rotating limit ($Ta_1 \to \infty$), with all other parameters set to one. 134

6.1 Parameter values for the rotating two-layer configuration within the radial span $0.9R_J \lesssim r \lesssim R_J$ (where $R_J = 6.9894 \times 10^7$ m denotes Jupiter's mean radius). Tables 1 and 2 of French et al. (2012) provide values of each fluid property at specific radial locations within Jupiter. The outer region ($0.9R_J \lesssim r \lesssim R_J$) is divided into two layers, with the fluid properties averaged within each layer. The interface is placed at the largest and smallest radii within $0.9R_J < r < R_J$ reported in Tables 1 and 2 of French et al. (2012), corresponding to $z = 0.986R_J$ and $z = 0.94R_J$, and hence to $\delta = 0.1$ and $\delta = 1.8$. The resulting parameter ranges reflect the difference between configurations with a thin upper layer and those with a thick upper layer. . . 142

Chapter 1

Introduction

1.1 Motivation

Thermal convection is a fundamental process in fluid dynamics that arises when spatial temperature gradients within liquids, gases, or plasmas generate motion. It occurs when buoyancy forces, driven by temperature and density variations within the fluid, cause warmer, lighter regions to rise and cooler, denser regions to sink, creating a continuous overturning circulation. In general, the onset and nature of this motion are governed by the underlying thermodynamic gradients, though it often manifests as temperature-driven flow. The resulting motion provides an efficient mechanism for heat transport and fluid mixing.

Rotating convection is fundamental to many natural and industrial systems, with applications across geophysics, astrophysics, meteorology, oceanography, and engineering. It governs phenomena across a wide range of spatial and temporal scales, from large-scale atmospheric circulation (e.g., Mitchell et al., 2021), which sets climate regimes and weather patterns, to heat and mass transport in Earth's mantle (e.g., Aurnou et al., 2015) and stellar interiors (e.g., Miesch, 2005). Beyond its geophysical and astrophysical relevance, rotating convection is integral to numerous engineering applications, including thermal management in electronic components (e.g., Incropera, 1988), coolant flow and safety analysis in nuclear reactors (e.g., Sikorska et al., 2024), and heat and momentum transfer in chemical processing and renewable-energy systems (e.g., Zamora, 2023). Its ubiquity in both natural environments and engineered devices renders rotating convection simultaneously a subject of fundamental theoretical interest and a critical element in the design, optimisation, and interpretation of a variety of practical systems.

A large class of convective systems are characterised by strong depth-dependent variations in material properties. The significance of such variations was first recognised in the context of mantle convection, where material properties such as viscosity and thermal diffusivity change markedly with

depth (Richter and Johnson, 1974; Busse, 1981). Analogous configurations occur in stellar interiors, in which convectively unstable regions may be embedded between stably stratified layers (Hurlburt et al., 1986). Depth-dependent property variations also arise in industrial contexts, for instance, in the modelling of heat and particle transport in magnetically confined fusion plasmas (Wilczynski and Hughes, 2019), and in crystal growth processes (Prakash and Koster, 1994). A specific application of particular interest here concerns the emergence, stability, and morphology of large-scale polar vortices on gas giant planets, where rotating convection in a stratified fluid with depth-dependent variations in material properties is thought to play a central role.

Recent spacecraft missions to Jupiter and Saturn have yielded extensive new datasets, including high-resolution polar imagery that reveals intricate, complex, long-lived atmospheric structures. The Cassini mission (1997–2017) revealed that both of Saturn's poles are dominated by a central polar vortex encircled by multiple smaller vortices (Mitchell et al., 2021). This vortex system is embedded within, and bounded by, an eastward circumpolar jet stream (Read et al., 2022), as illustrated in figure 1.1. The northern circumpolar jet is particularly notable for its hexagonal shape, first identified in Voyager observations by Godfrey (1988). Juno observations (2011–present) have shown that Jupiter's north pole hosts a central cyclonic vortex surrounded by eight additional cyclones that together form a nearly regular octagonal circumpolar ring (Adriani et al., 2018; Mitchell et al., 2021). At the south pole, a central cyclonic vortex is encircled by five cyclones arranged in a pentagonal configuration, with relatively larger azimuthal separations (Adriani et al., 2018, 2020). These configurations are depicted in figure 1.2. Comprehensive observational and dynamical investigations of Saturn's polar atmosphere are presented in Porco et al. (2005); Vasavada et al. (2006); Antuñano et al. (2015); Mitchell et al. (2021), whereas corresponding studies of Jupiter's polar atmospheric dynamics are provided by Bolton et al. (2017); Adriani et al. (2018); Kaspi et al. (2018); Tabataba-Vakili et al. (2020).

Despite several decades of observations, the formation, vertical extent, and long-term stability of the polar vortices on Jupiter and Saturn remain poorly understood and are the subject of ongoing investigation and debate. Determining the vertical extent of these vortices remains particularly challenging; consequently, the specific atmospheric layers they occupy are still uncertain. Nonetheless, Juno's gravity measurements indicate that Jupiter's zonal winds penetrate to depths of approximately 3000 km below the visible cloud tops at low latitudes and 0–500 km at high latitudes (Kaspi et al., 2018; Guillot et al., 2020). Although the vertical structure in the polar region remains uncertain, a deep convective zone may also be present there. An analogous situation appears to hold for Saturn, where the longevity and inferred vertical coherence of the polar vortices suggest the presence of an energy source that is not restricted to a shallow weather layer (Mitchell et al., 2021; Read et al., 2022). A plausible explanatory framework suggests that deep-interior models can account for these vortices as products of rotating, turbulent convection driven by internal heat (e.g., Chan and Mayr, 2013; Yadav

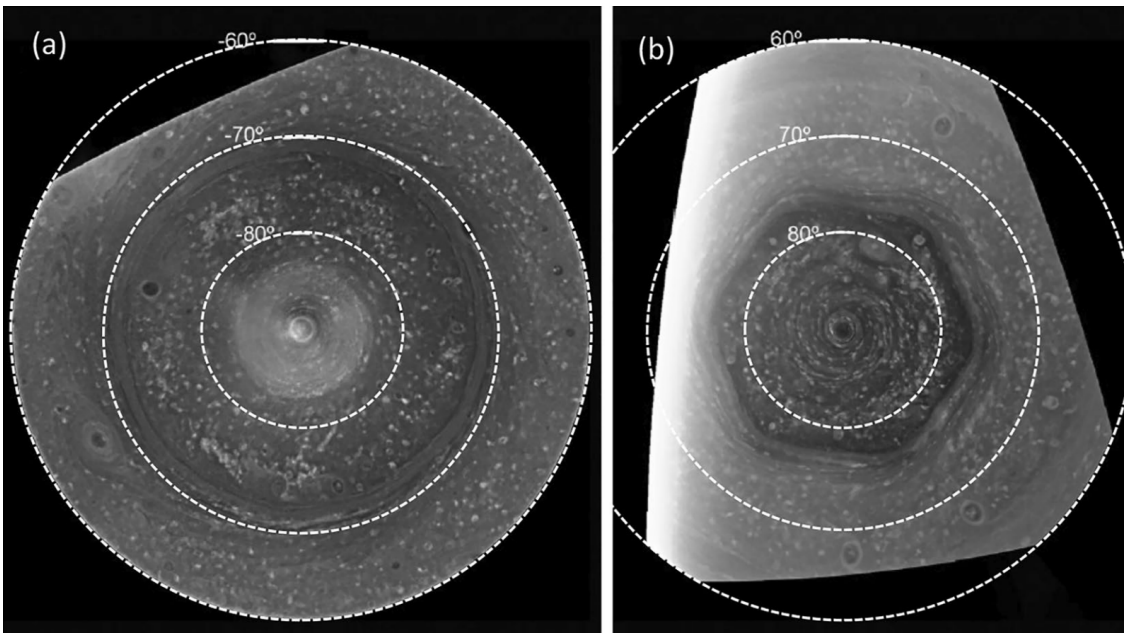
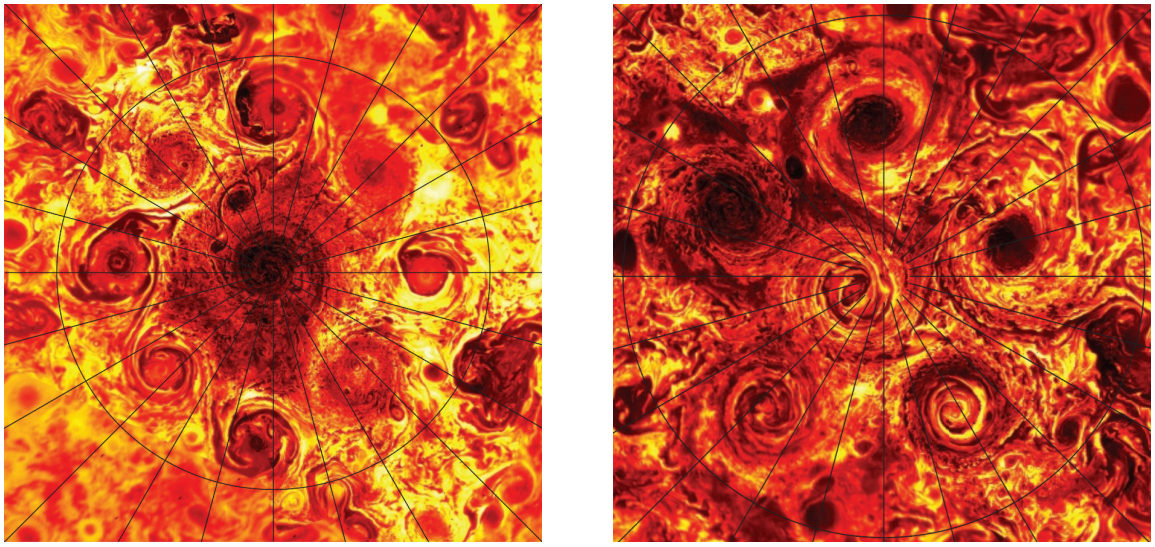


Figure 1.1: (a) Polar projection of the south polar region from $-60°$ to $-90°$, built using four different images captured during the Cassini mission on 3 December 2008. (b) An equivalent projection of the north polar region from $60°$ to $90°$, captured during the Cassini mission on 14 June 2013. Taken from Read et al. (2022), who adapted from Antuñano et al. (2015).



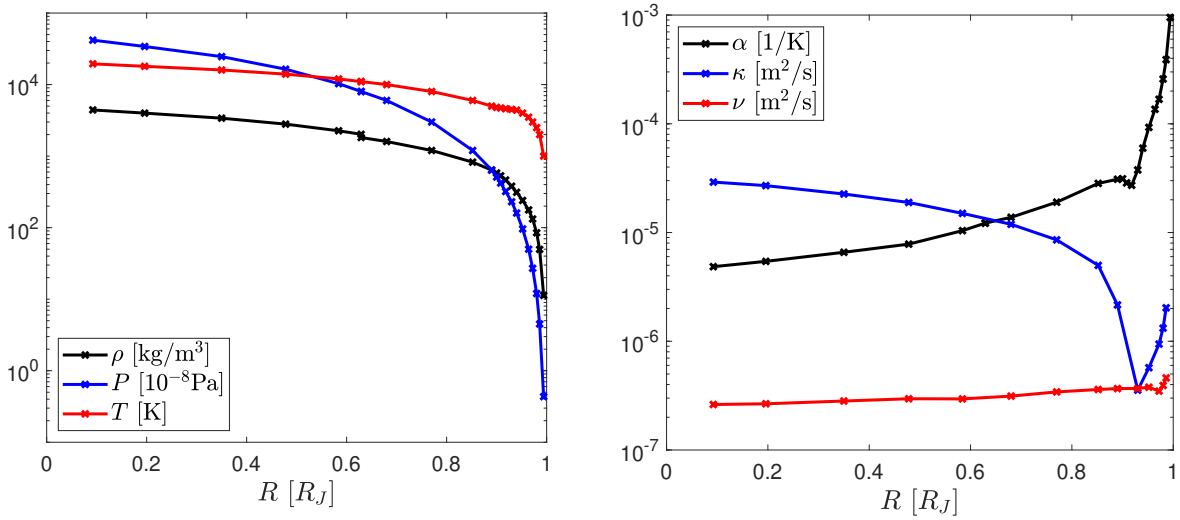
(a) (b)

Figure 1.2: Projected maps of the regions surrounding the (a) north and (b) south poles of Jupiter from data collected by NASA's Juno mission on 2 February 2017, during the 3rd science pass of NASA's Juno spacecraft. The latitude circle is $80°$ N or $80°$ S (planetocentric). Meridians are drawn every $15°$ of longitude. Taken from Adriani et al. (2018).

and Bloxham, 2020; Garcia et al., 2020; Cai et al., 2021). It is well established that rapidly rotating convection, both in 3D Cartesian geometries (e.g., Käpylä et al., 2011; Chan and Mayr, 2013; Guervilly et al., 2014; Favier et al., 2014; Rubio et al., 2014) and in spherical shells (e.g., Heimpel et al., 2016; Yadav et al., 2020; Lin and Jackson, 2021), can spontaneously generate large-scale, long-lived vortices or zonal jets. These motions, strongly constrained by rapid planetary rotation, organise into columnar structures aligned with the rotation axis that can concentrate vorticity preferentially at high latitudes (Aurnou et al., 2003). Using 3D simulations of turbulent convection in rapidly rotating spherical shells, Yadav et al. (2020) investigated vortex formation on Jupiter and Saturn driven by deep interior convection. Their results demonstrate that rotating turbulent convection naturally produces deep, axially aligned vortices. Complementary 3D simulations by Cai et al. (2021) of deep, rotating convection show that convectively driven vortices can form, persist, and remain closely packed at polar latitudes without merging. Their model successfully generates stable polygonal vortex configurations that closely resemble the pentagonal and hexagonal patterns observed at Jupiter's poles. Collectively, these results indicate that rapidly rotating, turbulent convection in the deep interiors of gas giants may play a central role in generating large-scale polar vortices.

Most of the models discussed above, however, rely on substantially simplifying assumptions about the planets' internal structures and material properties, primarily for numerical convenience. Planetary interiors constitute highly complex systems characterised by strongly coupled physical processes spanning many orders of magnitude in spatial and temporal scales. Direct numerical simulation of such systems with full physical fidelity remains beyond current computational capabilities. Consequently, researchers employ idealised configurations and reduced models that approximate the dominant dynamical processes, thereby rendering the problem computationally feasible while still capturing the essential physics. The reliability of any such simplified model, however, depends critically on the accuracy and physical justification of the approximations on which it is based.

French et al. (2012) employed *ab initio* simulations (first-principles calculations without empirical input) to determine detailed fluid properties along Jupiter's adiabat. Their results indicate that in the outer envelope, between $\sim 0.9R_J$ and R_J (where $R_J = 6.9894 \times 10^7$ m is Jupiter's mean radius), numerous quantities, including electrical conductivity and thermal diffusivity, exhibit significant radial variations. By contrast, in the deep interior, many properties vary only weakly with depth, as illustrated in figure 1.3 for a subset of these properties. Despite this, most studies that use rotating convection to model gas giant polar vortices do not incorporate a strong, realistic depth dependence in fluid properties such as viscosity, thermal diffusivity, and thermal expansion coefficient. Instead, they predominantly adopt idealised single-layer configurations with constant material properties. For instance, incompressible convection treatments based on the Boussinesq approximation assume constant density, except in the buoyancy term, and typically take material properties such as viscosity, thermal diffusivity and coefficient of thermal expansion to be uniform (e.g., Garcia et al., 2020; Lin



(a) (b)

Figure 1.3: (a) Density ρ, Pressure P, and temperature T, and (b) coefficient of thermal expansion α, thermal diffusivity κ, and kinematic viscosity ν as a function of radius where $R_J = 6.9894 \times 10^7$m is Jupiter's mean radius. Crosses are data points from French et al. (2012).

and Jackson, 2021). Similarly, anelastic formulations that incorporate a background density stratification frequently assume constant kinematic viscosity and thermal diffusivity (e.g., Gastine and Wicht, 2012; Yadav and Bloxham, 2020). In contrast, Yadav et al. (2020) adopted constant kinematic viscosity and thermal diffusivity but implemented a depth-dependent electrical conductivity, prescribed to vary with radius according to a hyperbolic tangent profile. More generally, many physical fluid systems are characterised by substantial spatial variations in their material properties, yet are commonly represented using simplified models with depth-independent coefficients.

In this thesis, we aim to advance the theoretical understanding of rotating systems exhibiting strong depth-dependent variations in material properties. To this end, we construct a simplified, rotating, two-layer convection model and conduct an extensive, systematic exploration of the associated parameter space in order to identify stability boundaries and characterise the resulting flow regimes. In this model, each layer possesses distinct physical properties, thereby introducing a controlled degree of variation in the material parameters across the domain.

1.2 Thermal convection

Rayleigh–Bénard convection (RBC) is the simplest model of thermal convection, yet it provides numerous opportunities to explore complex phenomena. It consists of a horizontal layer of fluid heated from below, which establishes a temperature gradient that can drive overturning motion once buoyancy

overcomes viscous and diffusive effects. RBC was first identified by Henri Bénard, who observed a regular cellular pattern in a thin layer of heated oil (Bénard, 1900, 1901). In his pioneering experiments (1900-1901), Bénard used spermaceti, a waxy substance, heated from below and cooled from above. As the temperature difference increased, he observed the spontaneous formation of regular hexagonal convection cells, with warm fluid rising at the centre and cooler fluid descending along the edges. These experiments provided the first visual evidence of convection-driven pattern formation, which later served as the experimental basis for Rayleigh's theoretical analysis of thermal instability.

In 1916, Lord Rayleigh (Rayleigh, 1916) provided the first theoretical explanation for the onset of convection observed in Bénard's experiments by applying a linear stability analysis to a horizontal fluid layer heated from below and cooled from above. He modelled the system using the equations of fluid motion and heat transfer, examining when the conduction state becomes unstable to small perturbations for a chosen horizontal wavenumber. His analysis showed that convection begins when the Rayleigh number Ra, a dimensionless parameter comparing buoyancy forces to the stabilising effects of viscosity and thermal diffusion, exceeds a critical threshold. This work not only explained the conditions for convection but also established a foundational framework for understanding fluid instabilities, forming the basis of what is known as Rayleigh–Bénard convection. The critical Rayleigh number, Ra^c, observed by Bénard differed significantly from Rayleigh's theoretical prediction, primarily due to a mismatch between experimental and analytical boundary conditions, which did not consider surface tension effects. This discrepancy motivated further refinements in linear stability theory, notably by Jeffreys (1926, 1928) and Pellew and Southwell (1940), who incorporated more realistic boundary conditions such as no-slip and stress-free velocity constraints to better capture the onset of convection in physical systems. Schmidt and Milverton (1935) performed further experiments that reproduced Bénard's results and provided empirical support for the refined theoretical framework developed by Jeffreys (1926, 1928). The development of linear theory was brought together by Chandrasekhar (1961), who considered various aspects of convection in a plane layer, including boundary conditions, rotation, and magnetic fields, and it has since become the standard reference for RBC.

While linear theory provides essential insight into the onset of convection by predicting conditions such as the critical Rayleigh number and the preferred convection patterns, it cannot account for the fully developed dynamics that occur beyond onset. When disturbances grow larger, their interactions become more important, so nonlinear terms are included to account for them. The inclusion of nonlinear terms in the governing equations enables the study of time-dependent behaviour and turbulent instabilities. Early weakly nonlinear analyses by Malkus (1954) and Malkus and Veronis (1958) investigated how finite-amplitude effects influence convection patterns. Their work demonstrated that the orientation, stability, and evolution of convection rolls are strongly influenced by the fluid's viscosity and thermal diffusivity, properties captured by the Prandtl number Pr, a dimensionless ratio of kinematic viscosity to thermal diffusivity (Prandtl, 1910). Low Pr fluids (like liquid metals) have high

thermal diffusivity relative to viscosity, while high Pr fluids (like oils) have high viscosity relative to thermal diffusivity. These studies laid the necessary groundwork for understanding how convection transitions from steady cellular patterns to complex, time-dependent flows and turbulence. The relationship between Ra, Pr and heat transport was formulated in detail by Kraichnan (1962), who developed a turbulent theory valid across arbitrary Pr and predicted a fully developed regime of convection in which boundary layers become turbulent, and heat transfer increases rapidly with thermal forcing. As the study of nonlinear RBC developed, researchers explored more complex systems that could no longer be solved analytically. This complexity led to the development of numerical models that use computational algorithms to approximate solutions to systems that are too complex to solve analytically or for which no closed-form solution exists. Veronis (1966) conducted one of the first numerical studies of nonlinear RBC in a 2D fluid layer. His work extended earlier linear theories by incorporating nonlinear effects, demonstrating how convection patterns evolve beyond onset and providing a foundational framework for later computational studies (e.g., Bodenschatz et al., 2000; Paul et al., 2002).

While the development of nonlinear theory and numerical models has greatly advanced our understanding of convection far beyond onset, important questions remain in the linear regime at the threshold of instability. Linear studies are crucial for accurately determining the critical conditions for the onset of convection, understanding the mechanisms of instability modes, and predicting initial pattern selection. This remains particularly relevant in rotating convection. The inclusion of rotation modifies the stability thresholds and introduces rich phenomena that are still being explored. The interplay of buoyancy and Coriolis terms introduces fundamentally new flow behaviours, pattern formations, and heat transport mechanisms. This additional complexity gives rise to phenomena absent in the non-rotating system, such as Taylor columns and Ekman boundary layers. An intriguing consequence of rotation is the potential for both steady and oscillatory instabilities.

The study of rotating convection began with foundational theoretical work by Proudman (1916), who first established that, in a rapidly rotating fluid, motions tend to be 2D along the axis of rotation, a result later formalised as the Taylor-Proudman theorem. Consequently, rapid rotation leads to columnar structures, often referred to as Taylor columns. These ideas were experimentally confirmed by Taylor (1923, 1936), who demonstrated the existence of Taylor columns and advanced understanding of hydrodynamic stability in rotating fluids. Chandrasekhar (1953) extended Rayleigh's convection theory to include rotation, deriving critical Rayleigh numbers and showing that rotation fundamentally alters convection onset conditions through the Coriolis term, which acts perpendicular to the direction of motion and the rotation axis, thereby constraining flow into columnar structures. In this framework, the Taylor number Ta was introduced as a dimensionless parameter that quantifies the relative importance of Coriolis forces to viscous forces in the system. Fultz et al. (1954) conducted pioneering experiments that revealed the first observations of oscillatory convection, demonstrating the onset of

time-dependent convection in a rotating system. This result was then placed within a broader theoretical and experimental framework for cellular convection in rotating fluids by Nakagawa and Frenzen (1955), and subsequently examined in greater quantitative detail, particularly for low Prandtl number mercury, by Fultz and Nakagawa (1955), who provided careful measurements of the critical conditions for overstability. Building on these developments, Busse (1978) extended the theoretical framework of RBC, including the effects of rotation, by performing weakly nonlinear analyses that showed how different convection patterns (e.g., rolls, squares, hexagons) emerge and stabilise at finite amplitude, thereby linking linear stability theory with experimentally observed flow structures. These theoretical and experimental advances set the stage for more systematic experiments on rotating convection, notably by Rossby (1969), who investigated the effects of rotation on RBC and demonstrated how increasing rotational influence suppresses large-scale motion and modifies heat transport. Together, these works provide the theoretical and experimental foundation for the modern study of rotating convection.

Geometry plays a central role in rotating convection, influencing the onset, structure and evolution of convective patterns (e.g., Busse, 1970, 1975). Factors such as aspect ratio, boundary curvature, and orientation relative to the rotation axis significantly alter the flow dynamics (Zhang, 1994), so it is crucial to select an appropriate configuration to model the system of interest. Many configurations have been developed in the study of rotating convection, e.g., a plane-layer (e.g., Boubnov and Golitsyn, 1990), a cylinder (e.g., Goldstein et al., 1993), and a spherical shell (e.g., Zhang and Gubbins, 1993). In the spherical shell domain, the rotational axis and the vertical axis are not aligned (except at the poles), as in the plane-layer and cylindrical domains (Busse, 1970; Gilman, 1977). While the spherical-shell geometry most closely represents planetary systems, it is impractical for many studies owing to numerical and experimental limitations. Therefore, simpler systems, such as plane-layer and cylindrical configurations, are used to represent regions of spherical-shell geometry, providing insight into spherical shells and thus planetary systems, while being much easier to analyse analytically and computationally. The use of plane-layer and cylindrical domains to model astrophysical and geophysical flows is often justified by their analogy to the polar regions of a planetary fluid layer, where the core heats the bottom of the configuration, with rotation and the vertical axis aligned (e.g., Cheng et al., 2015).

In this thesis, we shall utilise a plane-layer geometry, analogous to the polar regions of gas giant planets: the outer region of a planet can be modelled as a spherical shell, with the north-most section, neglecting curvature, representing the outer polar region. This leads to rotating Rayleigh–Bénard convection (RRBC). In its simplest form, RRBC consists of a horizontal fluid layer rotating about a vertical axis and heated from below. Figure 1.4 visualises a classic RRBC scenario. The fluid is bounded by a lower hot boundary and an upper cold boundary. As the temperature difference increases, organised cellular flow patterns develop, illustrated by the arrows. Each set of arrows

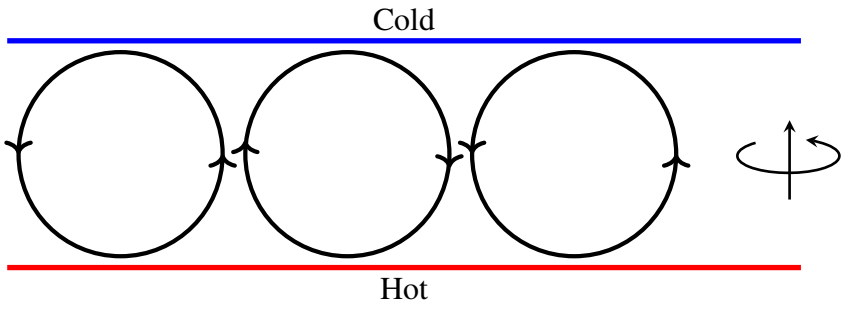


Figure 1.4: Schematic illustration of rotating Rayleigh–Bénard convection. A fluid layer is rotated about the vertical axis with a constant angular velocity, heated from below and cooled from above. The fluid movement, indicated by the arrows, rises when heated and descends when cooled, creating cellular flow patterns.

represents a convection roll, in which rising hot fluid is balanced by sinking cooler fluid, forming a repeating, structured flow. Rotation influences these flows by aligning the rolls along the rotation axis, suppressing large-scale vertical motion, and modifying the stability and size of the convection cells.

Most studies on rotating convection have assumed a simplified single-layer, constant-property model. However, in studies of large-scale polar vortices on Jupiter, for example, these investigations overlook the depth-dependent variations in material properties such as viscosity and thermal diffusivity, as shown in figure 1.3 using data from French et al. (2012). Figure 1.3 shows, for example, that the coefficients of thermal expansion and thermal diffusivity vary over three orders of magnitude across the radius of Jupiter, with the majority of the change occurring within the outer envelope.

To account for spatial variations in material properties, studies have adopted a two-layer convection model, in which each layer is characterised by distinct physical properties, thereby introducing variation in the fluid properties. In the non-rotating case, convection in multi-layer fluid systems has been extensively investigated owing to their intricate interfacial dynamics and their significance in a wide range of heat-transfer applications. Early work on two-layer convection was motivated by geophysical processes in the Earth's mantle (Richter and Johnson, 1974; Busse, 1981) and by astrophysical contexts such as stellar interiors, in which convectively unstable zones may be embedded between stably stratified layers (Hurlburt et al., 1986). Generalising the classical Rayleigh—Bénard convection configuration to multiple superposed layers gives rise to substantially richer dynamics, including interactions between adjacent convective regions, the onset of oscillatory modes of instability, and deformations of the interface separating the layers. Rasenat et al. (1989) examined the onset of thermal convection in a two-layer system composed of immiscible fluids and demonstrated that the initiation of steady convection in both layers can be driven by either thermal coupling or viscous coupling across the interface. Le Bars and Davaille (2002) combined marginal stability analysis with

laboratory experiments to study the stability of two-layer thermal convection in high Prandtl number fluids. They considered a configuration in which the two layers were miscible with a stably stratified density profile. The buoyancy number is the only parameter that matters at the interface. They found that, depending on the buoyancy number, the onset of convection may be stationary or oscillatory. The system's behaviour is highly sensitive to control parameters, such as the ratio of layer thicknesses and the material-property contrasts between the fluids, giving rise to qualitatively distinct instability modes. Consequently, many studies have focused on restricted regions of this parameter space in order to identify the conditions under which particular convective behaviour arises (e.g., Rasenat et al., 1989; Diwakar et al., 2014).

Despite the importance of rotating flows with depth-dependent variations in material properties, particularly in geophysical and astrophysical contexts, the specific problem of rotating two-layer convection with distinct physical properties in each layer has not been addressed. However, studies of penetrative convection often employ a rotating two-layer configuration (e.g., Narimousa, 1996). The problems are similar in that they create situations where dynamics in one layer induce dynamics in the other; however, the setups differ. The configuration we use in this thesis imposes a miscible interface with distinct material properties and governing equations in each layer (e.g., Le Bars and Davaille, 2002). Zhang and Schubert (1996) investigates penetrative convection and zonal flow on Jupiter; the governing equations are the rotating Boussinesq equations with a piecewise temperature gradient producing stable and unstable regions. They demonstrate that penetrative convection in a rapidly rotating fluid can generate zonal flows through Reynolds stresses, offering a mechanism for the formation of Jupiter's alternating jet streams. One of the earliest experimental contributions is that of Narimousa (1996), who investigated penetrative turbulent convection in a rotating two-layer fluid using a density interface. For a strong stratified interface (large density contrast between layers), convection remained confined to the upper layer, while weaker stratification allowed penetration into the lower layer. Rotation was found to suppress vertical motion and promote horizontal spreading of the mixed fluid along the interface.

Although there are multiple studies on penetrative convection between unstable and stable layers, the exploration of rotation and stratification in layered convection remains limited, leaving a significant gap in our understanding of rotating convection in systems with depth-dependent material properties and motivating the systematic analysis undertaken here.

1.3 Thesis Structure

This thesis endeavours to advance the theoretical understanding of rotating convection with depth-dependent variations in fluid properties by analysing the instabilities that develop in a rotating two-layer configuration, in which each layer is characterised by distinct physical parameters. The study

will employ a detailed linear stability analysis to determine how variations in fluid properties influence the nature and structure of the emergent solutions. Through this investigation, the work aims to provide deeper insight into the dynamics of rotating convection in stratified, multi-layer systems, with potential relevance not only to the formation and maintenance of large-scale vortices at the poles of gas giant planets, but also to a broader range of geophysical and astrophysical flows. For tractability, fluid compressibility and the potential influence of magnetic fields (e.g., Kirk and Stevenson, 1987) are neglected. The analysis is conducted within the framework of the Boussinesq approximation, which assumes incompressibility and disregards density variations except where they contribute to buoyancy forces.

We present a systematic analysis of plane-layer convection models of increasing complexity that are relevant to the rotating two-layer convection system. The outline of the thesis is as follows. In Chapter 2 we introduce the theoretical framework necessary to study rotating Rayleigh–Bénard convection. We introduce the momentum, continuity, and temperature equations under the Boussinesq approximation that govern the system, and derive the linear, dimensionless equations for perturbations about the basic state. We introduce various mechanical and thermal boundary conditions, and perform a linear stability analysis, distinguishing between steady and oscillatory modes of instability. In Chapter 3, we derive an asymptotic solution for the onset of steady, linear convection in a rapidly rotating system with stress-free, fixed-flux boundary conditions. In the rapidly rotating limit, the interior solution remains unaffected by the choice of thermal boundary conditions. Exploiting this property, we use an asymptotic approach to characterise the differences between the fixed-temperature and fixed-flux systems. This result provides insight into rotating two-layer convection, in which different asymptotic regimes converge to identical behaviour, displaying the same underlying dynamics. In Chapter 4, we study rotating Rayleigh–Bénard convection with a boundary slab of finite thermal conductivity, motivated by understanding the instabilities that arise in rotating two-layer convection in the limit of a large viscosity contrast, where the more viscous layer behaves effectively as a solid slab. In Chapter 5 we study the onset of instability in the full rotating two-layer convection model. In Chapter 6 we summarise and discuss possible avenues for further work.

Chapter 2

Theoretical Framework of Rotating Rayleigh–Bénard Convection

2.1 Introduction

This thesis aims to enhance our understanding of rotating convection with depth-dependent variations in fluid properties by investigating the instabilities that arise in a rotating two-layer system. Before introducing the rotating two-layer model, we first establish the theoretical framework for the canonical single-layer rotating Rayleigh–Bénard convection system, which provides the fundamental basis for the subsequent analysis of the full rotating two-layer configuration.

The focus in this thesis is on plane-layer, Boussinesq, linear, rotating convection. Figure 2.1 presents a schematic sketch of RRBC. A layer of incompressible fluid of infinite horizontal extent is bounded by two horizontal planes at $z = 0$ and $z = d$, where $d > 0$, and subject to heating from below. The lower boundary has temperature T_0, and the upper boundary has temperature $T_0 - \Delta T$, where $\Delta T > 0$ is the temperature difference across the system. The system rotates with uniform angular velocity $\boldsymbol{\Omega} = \Omega\hat{\boldsymbol{z}}$, where $\hat{\boldsymbol{z}}$ is the unit vector in the vertical direction on the Cartesian coordinate system. The acceleration due to gravity is $\boldsymbol{g} = -g\hat{\boldsymbol{z}}$. Localised heating causes fluid parcels to expand, thereby reducing their density. When a cool, dense layer overlies a warmer, lighter layer, the resulting configuration is top-heavy and may become dynamically unstable. Under these conditions, buoyancy redistributes the fluid, causing the warmer, less dense fluid to rise while the cooler, denser fluid sinks to take its place. This buoyancy-driven reorganisation is opposed by viscous stresses and thermal diffusion, which act to damp motion and smooth temperature gradients. If the imposed temperature difference across the layer exceeds a critical value, the destabilising buoyancy forces dominate over these stabilising mechanisms, leading to an overturning instability, conventionally referred to as thermal convection.

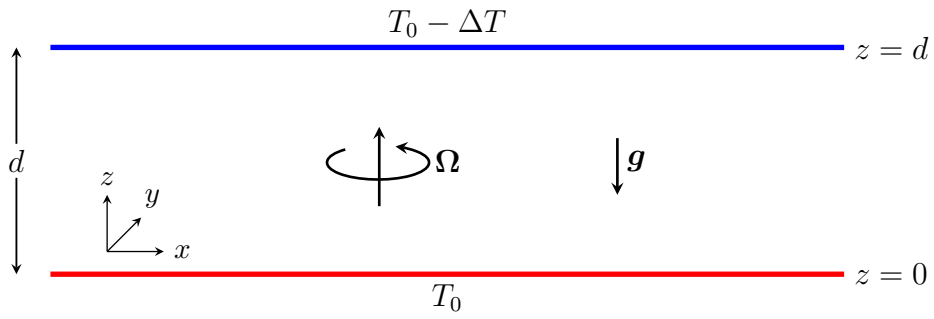


Figure 2.1: Schematic illustration of rotating Rayleigh–Bénard convection.

The governing equations of RRBC are well-established and detailed in, for example, Chandrasekhar (1961), Greenspan (1968), and Drazin and Reid (2004). This chapter draws mainly on Chandrasekhar (1961). We first introduce a rotating reference frame in §2.2, from which the Coriolis and centrifugal forces naturally emerge. The momentum, continuity, and temperature equations governing RRBC are derived in §2.3. The basic state is obtained in §2.4, and the linear, dimensionless perturbation equations are derived in §2.5. Standard thermal convection boundary conditions are discussed in §2.6. A normal mode analysis is presented in §2.7, followed by a linear stability analysis in §2.8.

2.2 Rotating frame of reference

An inertial frame of reference is one in which Newton's laws of motion hold in their standard form, without the introduction of fictitious forces. Although such frames are fundamental, it is often helpful to describe motion relative to a rotating frame of reference. When transforming the equations of motion to a rotating frame, the acceleration experienced by a fluid parcel differs from that in an inertial frame. Therefore, it is necessary to introduce further inertial forces — the Coriolis, centrifugal, and Euler forces — which are fundamental to the dynamics of rotating flows.

Consider a rotating frame with angular velocity $\boldsymbol{\Omega}\,(t)$ relative to an inertial frame. Acceleration in the inertial frame, $\boldsymbol{a}_I$, is given by

$$\boldsymbol{a}_I = \boldsymbol{a}_R + \underbrace{2\boldsymbol{\Omega} \times \boldsymbol{v}_R}_{\text{Coriolis}} - \underbrace{\frac{1}{2}\nabla|\boldsymbol{\Omega} \times \boldsymbol{r}|^2}_{\text{Centrifugal}} + \underbrace{\frac{\mathrm{d}\boldsymbol{\Omega}}{\mathrm{d}t} \times \boldsymbol{r}}_{\text{Euler}}, \tag{2.1}$$

where $\boldsymbol{v}_R$ and $\boldsymbol{a}_R$ are the velocity and acceleration in the rotating frame, and $\boldsymbol{r}\,(t)$ is the position vector. We restrict our attention to constant rotation, so the Euler term is zero.

2.3 Governing equations

2.3.1 The continuity equation

We begin by considering the continuity equation, which expresses mass conservation for the fluid. Consider an arbitrary fixed volume of fluid V with bounding surface S. The rate of change of mass inside the volume is given by the rate at which the fluid flows across the boundary,

$$\frac{\mathrm{d}}{\mathrm{d}t}\int_V \rho\, dV = -\int_S \rho\, \boldsymbol{u}\cdot\hat{\mathbf{n}}\, dS, \tag{2.2}$$

where ρ is the density, $\boldsymbol{u} = (u, v, w)$ is the velocity, and $\hat{\mathbf{n}}$ is the outward normal unit vector. Applying the divergence theorem, and since the volume is fixed, (2.2) becomes

$$\int_V \left(\frac{\partial \rho}{\partial t} + \nabla\cdot(\rho\boldsymbol{u})\right) dV = 0. \tag{2.3}$$

Since V is arbitrary, (2.3) must hold for all volumes V. Thus, the continuity equation is given by

$$\frac{\partial \rho}{\partial t} + \nabla\cdot(\rho\boldsymbol{u}) = 0. \tag{2.4}$$

2.3.2 The momentum equation

We next consider the momentum equation. By Newton's second law of motion, the rate of change of momentum in an arbitrary volume V is equal to the flow of momentum in V through a surface S and the sum of forces acting on V,

$$\frac{\mathrm{d}}{\mathrm{d}t}\int_V \rho\boldsymbol{u}\, dV = -\int_S \rho\boldsymbol{u}\,(\boldsymbol{u}\cdot\hat{\boldsymbol{n}})\, dS + \int_V \rho\boldsymbol{F}\, dV + \int_S \boldsymbol{\tau}\cdot\hat{\boldsymbol{n}}\, dS. \tag{2.5}$$

All body forces acting on the fluid are contained within $\boldsymbol{F}$. For a Newtonian viscous fluid, forces acting on the surface S are expressed in terms of the stress tensor $\boldsymbol{\tau}$, defined as

$$\boldsymbol{\tau} = -p\boldsymbol{I} + \mu\left(\nabla\boldsymbol{u} + (\nabla\boldsymbol{u})^T - \frac{2}{3}(\nabla\cdot\boldsymbol{u})\,\boldsymbol{I}\right), \tag{2.6}$$

where p is the pressure, $\boldsymbol{I}$ is the identity tensor, $\nabla\boldsymbol{u}$ is the velocity gradient tensor (with superscript T denoting its transpose), and μ is the dynamic viscosity, representing the fluid's internal 'stickiness' and its resistance to relative motion between adjacent layers. The stress tensor is fundamental, serving as the basis for deriving boundary conditions in §2.6 and continuity conditions at interfaces applied in Chapters 4 and 5. Applying the divergence theorem, making use of the continuity equation (2.4), and since the volume is arbitrary, (2.5) becomes

$$\rho\frac{\partial \boldsymbol{u}}{\partial t} + \rho\,(\boldsymbol{u}\cdot\nabla)\,\boldsymbol{u} = \rho\boldsymbol{F} + \nabla\cdot\boldsymbol{\tau}. \tag{2.7}$$

Within RRBC, the body forces acting on the fluid are gravitational and rotation-induced: $\boldsymbol{F} = \boldsymbol{F}_g + \boldsymbol{F}_r$. In a convective system, the gravitational force is

$$\rho \boldsymbol{F}_g = \rho \boldsymbol{g}. \tag{2.8}$$

In a rotating reference frame, two rotational forces arise: the centrifugal force and the Coriolis force, as expressed in (2.1). The total force associated with the rotation can be expressed as

$$\rho \boldsymbol{F}_r = -\rho \left(2\boldsymbol{\Omega} \times \boldsymbol{u} + \frac{1}{2} \nabla |\boldsymbol{\Omega} \times \boldsymbol{r}|^2 \right). \tag{2.9}$$

Substituting for the forces $\boldsymbol{F}_g$ and $\boldsymbol{F}_r$ from (2.8) and (2.9) into (2.7) yields the momentum equation:

$$\rho \frac{\partial \boldsymbol{u}}{\partial t} + \rho \left(\boldsymbol{u} \cdot \nabla \right) \boldsymbol{u} + 2\rho \boldsymbol{\Omega} \times \boldsymbol{u} = -\frac{1}{2} \rho \nabla |\boldsymbol{\Omega} \times \boldsymbol{r}|^2 - \rho g \hat{\boldsymbol{z}} + \nabla \cdot \boldsymbol{\tau}. \tag{2.10}$$

2.3.3 The thermal energy equation

Finally, an equation for temperature is necessary. The specific energy of the fluid, E, which is the sum of the kinetic energy and internal or thermal energy of the fluid, can be written as

$$E = \frac{1}{2} |\boldsymbol{u}|^2 + c_v T, \tag{2.11}$$

where T is the temperature and c_v is the specific heat at constant volume, representing the amount of heat required to raise the temperature of a unit mass of a substance by one degree while keeping its volume fixed. The rate of change of energy in a volume V of the fluid is equal to the rate at which this energy is advected or conducted (in the form of heat) into the volume through the surface S, and any work done by forces on the volume. This is given by

$$\begin{aligned} \frac{\partial}{\partial t} \int_V \left(\frac{1}{2} \rho |\boldsymbol{u}|^2 + \rho c_v T \right) dV = \int_S -\rho \left(\frac{1}{2} |\boldsymbol{u}|^2 + c_v T \right) \boldsymbol{u} \cdot \hat{\boldsymbol{n}} \, dS + \int_S K \nabla T \cdot \hat{\boldsymbol{n}} \, dS \\ + \int_S (\boldsymbol{u} \cdot \boldsymbol{\tau}) \cdot \hat{\boldsymbol{n}} \, dS + \int_V \rho \boldsymbol{F} \cdot \boldsymbol{u} \, dV, \end{aligned} \tag{2.12}$$

where K is the thermal conductivity, representing how easily a material allows heat to flow through it in response to a temperature difference. Making use of the divergence theorem, expanding the stress tensor $\boldsymbol{\tau}$, and since equation (2.12) must hold for all volumes V, it follows that

$$\begin{aligned} \frac{\partial}{\partial t} \left(\frac{1}{2} \rho |\boldsymbol{u}|^2 + \rho c_v T \right) + \nabla \cdot \left[\rho \left(\frac{1}{2} |\boldsymbol{u}|^2 + c_v T \right) \boldsymbol{u} \right] = \nabla \cdot (K \nabla T) - p \left(\nabla \cdot \boldsymbol{u} \right) - (\nabla p) \cdot \boldsymbol{u} \\ + \nabla \cdot (\boldsymbol{u} \cdot \boldsymbol{\varepsilon}) + \rho \boldsymbol{F} \cdot \boldsymbol{u}, \end{aligned} \tag{2.13}$$

where

$$\boldsymbol{\varepsilon} = \mu \left(\nabla \boldsymbol{u} + (\nabla \boldsymbol{u})^T - \frac{2}{3} \left(\nabla \cdot \boldsymbol{u} \right) \boldsymbol{I} \right), \tag{2.14}$$

is the viscous stress tensor. The evolution equation of the fluid's kinetic energy, obtained by taking the scalar product of (2.7) with $\boldsymbol{u}$, can be subtracted from (2.13), leaving the evolution of the fluid's internal energy

$$\frac{\partial}{\partial t}\left(\rho c_v T\right) + \nabla \cdot \left[\rho \left(c_v T\right) \boldsymbol{u}\right] = -p\left(\nabla \cdot \boldsymbol{u}\right) + \Phi + \nabla \cdot \left(K \nabla T\right), \tag{2.15}$$

where

$$\Phi = \boldsymbol{\varepsilon} : \nabla \boldsymbol{u} = \sum_{i,j} \varepsilon_{ij} \frac{\partial u_i}{\partial x_j} \tag{2.16}$$

is the rate of viscous dissipation per unit volume of fluid. Substituting for $\boldsymbol{\varepsilon}$ from (2.14) into (2.16) gives

$$\Phi = \frac{1}{2}\mu \sum_{i,j} \left(\frac{\partial u_i}{\partial x_j} + \frac{\partial u_j}{\partial x_i}\right)^2 - \frac{2}{3}\mu \left(\nabla \cdot \boldsymbol{u}\right)^2. \tag{2.17}$$

Hence, Φ is always positive, representing irreversible conversion of kinetic energy into heat.

Making use of the continuity equation (2.4), and assuming constant specific heat, the energy equation (2.15) simplifies to

$$\rho c_v \frac{\partial T}{\partial t} + \rho c_v \nabla \cdot \left(T \boldsymbol{u}\right) = -p\left(\nabla \cdot \boldsymbol{u}\right) + \Phi + \nabla \cdot \left(K \nabla T\right). \tag{2.18}$$

2.3.4 The Boussinesq approximation

The full set of equations for a compressible system is difficult to solve even in the linear regime. However, in systems where the vertical extent of the fluid layer is small compared with the pressure scale height, the system is well described by the Boussinesq approximation, thereby simplifying the equations. This approximation is based on two assumptions: (1) $d \ll H$, where d is the thickness of the layer and H is the scale height, and (2) variations of pressure, density, and temperature do not exceed their reference values. As a result, the Mach number $M = u/c = \mathcal{O}\left((d/H)^{1/2}\right) \ll 1$, where c is the speed of sound. Consequently, sound waves, which are not relevant to the problem of interest, are asymptotically filtered out. Furthermore, density can be treated as constant except in the buoyancy term, where these small variations drive motion (Spiegel and Veronis, 1960).

Under the Boussinesq approximation, density variations in the fluid arise mainly from temperature changes rather than pressure, meaning pressure perturbations have a negligible effect on the general thermodynamic relation $\rho = \rho\left(p, T\right)$. Expanding density in a Taylor series about the reference state (ρ_0, T_0) and retaining only the linear term in temperature yields the equation of state approximated as

$$\rho = \rho_0 \left(1 - \alpha \left(T - T_0\right)\right), \tag{2.19}$$

where

$$\alpha = -\frac{1}{\rho_0} \frac{\partial \rho}{\partial T}\Big|_{T_0} \tag{2.20}$$

is the coefficient of thermal expansion. Defined as the relative change in density with temperature at constant pressure, α plays a central role in the Boussinesq approximation by directly linking temperature variations to buoyancy forces that drive convection. In the Boussinesq approximation, α is typically treated as constant, evaluated at a reference temperature, although in reality it generally varies with temperature and pressure. This assumption simplifies the governing equations by allowing a linear relationship between density and temperature, which is valid when temperature variations are small compared to the reference state.

Since density is treated as constant everywhere except in the buoyancy term, where it drives convection, the continuity equation (2.4) reduces to the incompressibility condition:

$$\nabla \cdot \boldsymbol{u} = 0. \tag{2.21}$$

For an incompressible fluid with constant viscosity, the divergence of the stress tensor (2.6) is given by

$$\nabla \cdot \boldsymbol{\tau} = -\nabla p + \mu \nabla^2 \boldsymbol{u}. \tag{2.22}$$

Substituting for $\nabla \cdot \boldsymbol{\tau}$ from (2.22) and applying the Boussinesq approximation, (2.10) reduces to the momentum equation:

$$\frac{\partial \boldsymbol{u}}{\partial t} + (\boldsymbol{u} \cdot \nabla)\, \boldsymbol{u} + 2\boldsymbol{\Omega} \times \boldsymbol{u} = -\frac{1}{\rho_0} \nabla p^* - (1 - \alpha\,(T - T_0))\, g\hat{\boldsymbol{z}} + \nu \nabla^2 \boldsymbol{u}. \tag{2.23}$$

where $\nu = \mu/\rho_0$ is the kinematic viscosity, measuring the rate at which momentum diffuses through a fluid, combining the effects of the fluid's viscosity and density. The pressure term in (2.23) is a modified pressure which incorporates the centrifugal acceleration, given by

$$p^* = p + \frac{1}{2}\rho_0 |\boldsymbol{\Omega} \times \boldsymbol{r}|^2. \tag{2.24}$$

The contribution of viscous dissipation, Φ, as defined in (2.17), can be shown to be negligible relative to thermal conduction (e.g., Chandrasekhar, 1961). Consequently, under the Boussinesq approximation, the thermal energy equation (2.18), together with the incompressibility condition (2.21), reduces to the following temperature equation:

$$\frac{\partial T}{\partial t} + \boldsymbol{u} \cdot \nabla T = \kappa \nabla^2 T, \tag{2.25}$$

where $\kappa = K/\rho_0 c_v$ is the thermal diffusivity, taken as constant, measuring the rate at which temperature changes diffuse through a material.

Equations (2.21), (2.23), and (2.25) form the system of equations governing RRBC. Next, we obtain the basic state solutions and derive equations governing perturbations from the basic state.

2.4 The basic state

The basic state is a motionless, hydrostatic state in which the imposed heat flux is transported solely by thermal conduction. The lower boundary has a temperature T_0, and the upper boundary has a temperature $T_0 - \Delta T$, where $\Delta T > 0$. We denote the stationary steady basic state in pressure and temperature by $\bar{p}$ and $\bar{T}$. In the absence of motion, the temperature equation (2.25) reduces to

$$\nabla^2 \bar{T} = 0, \tag{2.26}$$

with solution

$$\bar{T} = T_0 - \beta z, \tag{2.27}$$

where $\beta = \Delta T/d$ is the adverse temperature gradient. The momentum equation (2.23) reduces to

$$\nabla \bar{p} = -\rho_0 \left(1 - \alpha \left(\bar{T} - T_0\right)\right) g\hat{\boldsymbol{z}}. \tag{2.28}$$

Substituting for $\bar{T}$ from (2.27), (2.28) can be integrated to give

$$\bar{p} = p_0 - \rho_0 g \left(z + \frac{\alpha\beta}{2} z^2\right), \tag{2.29}$$

where p_0 is the pressure at the lower boundary.

2.5 The linear dimensionless perturbation equations

It should be noted that the scope of this thesis is limited to the linear regime; consequently, the subsequent chapters will focus solely on the linear equations presented in this section.

Let the hydrostatic basic state described by $\bar{T}$ and $\bar{p}$ defined in (2.27) and (2.29) be slightly perturbed. We denote perturbations in velocity, pressure and temperature by $\boldsymbol{u} = (u, v, w)$, P and θ, respectively. The momentum and temperature equations governing the perturbations from the basic state are as follows:

$$\frac{\partial \boldsymbol{u}}{\partial t} + (\boldsymbol{u} \cdot \nabla)\, \boldsymbol{u} + 2\boldsymbol{\Omega} \times \boldsymbol{u} = -\frac{1}{\rho_0} \nabla P + \alpha g \theta \hat{\boldsymbol{z}} + \nu \nabla^2 \boldsymbol{u}, \tag{2.30}$$

$$\frac{\partial \theta}{\partial t} + \boldsymbol{u} \cdot \nabla \theta = \beta w + \kappa \nabla^2 \theta. \tag{2.31}$$

On adopting the scaling of length with d, time with d^2/κ, pressure with $\rho_0 \left(\kappa/d\right)^2$, velocity with κ/d and temperature with βd, the dimensionless equations governing linear perturbations from the basic state are

$$\frac{\partial \tilde{\boldsymbol{u}}}{\partial t} + PrTa^{1/2} \hat{\boldsymbol{z}} \times \tilde{\boldsymbol{u}} = -\nabla \tilde{P} + RaPr\tilde{\theta}\hat{\boldsymbol{z}} + Pr\nabla^2 \tilde{\boldsymbol{u}}, \tag{2.32}$$

$$\frac{\partial \tilde{\theta}}{\partial t} = \tilde{w} + \nabla^2 \tilde{\theta}, \tag{2.33}$$

where $\tilde{\boldsymbol{u}}$, $\tilde{P}$ and $\tilde{\theta}$ are the dimensionless forms of $\boldsymbol{u}$, P, and θ. The three dimensionless parameters of the system, the Rayleigh number, Prandtl number, and Taylor number, are defined by

$$Ra = \frac{\alpha g \beta d^4}{\nu \kappa}, \qquad Pr = \frac{\nu}{\kappa}, \qquad Ta = \frac{4\Omega^2 d^4}{\nu^2}. \tag{2.34}$$

The Rayleigh number represents the balance between buoyancy and diffusive effects and provides a dimensionless measure of the thermal driving. Buoyancy forces drive the hotter, lighter fluid to rise, promoting convection, while thermal diffusion and viscous effects counteract temperature gradients and suppress fluid motion, thereby inhibiting convection. The Prandtl number is an intrinsic property of the fluid, defined as the ratio of its kinematic viscosity to its thermal diffusivity and plays a key role in determining the buoyancy of moving fluid parcels. The Taylor number represents the ratio of Coriolis forces to viscous forces in the system, providing a dimensionless measure of the rotation rate.

In analysing equations (2.32) and (2.33), dropping the tildes, it is convenient to work with the temperature θ, vertical velocity w, and vertical vorticity

$$\zeta = \frac{\partial v}{\partial x} - \frac{\partial u}{\partial y}, \tag{2.35}$$

rather than the two components of the horizontal velocity, u and v. The pressure and the horizontal velocity components are eliminated by the standard procedure of applying the operators $\hat{\boldsymbol{z}} \cdot \boldsymbol{\nabla} \times$ and $\hat{\boldsymbol{z}} \cdot \boldsymbol{\nabla} \times \boldsymbol{\nabla} \times$ to equation (2.32), thus giving

$$\frac{\partial \zeta}{\partial t} - Pr\nabla^2 \zeta = PrTa^{1/2} \frac{\partial w}{\partial z}, \tag{2.36}$$

$$\frac{\partial}{\partial t}\nabla^2 w - Pr\nabla^4 w = -PrTa^{1/2} \frac{\partial \zeta}{\partial z} + RaPr\nabla_H^2 \theta, \tag{2.37}$$

where the horizontal Laplacian is defined by $\nabla_H^2 = \partial_x^2 + \partial_y^2$. The horizontal velocity components u and v can be recovered from w and ζ using the incompressibility condition (2.21) and the definition of the vorticity in (2.35).

Equations (2.33), (2.36), and (2.37) form the governing set of linear dimensionless perturbation equations. To obtain a solution for the system of equations, boundary conditions must be defined to restrict the fluid's behaviour at the edges of the domain. These conditions are outlined in the following section.

2.6 Boundary conditions

In RRBC, mechanical and thermal boundary conditions are applied to the velocity and the temperature, respectively. Mechanical and thermal boundary conditions are essential to applying simplified models to real-world scenarios (e.g., Sakuraba and Roberts, 2009; Long et al., 2020).

2.6.1 Mechanical boundary conditions

The most common mechanical boundary conditions are: impermeable and either stress-free or no-slip. The impermeable condition prevents fluid from penetrating the boundary, requiring that the normal component of the flow velocity be zero at the surface. For a horizontal boundary

$$w = 0, \tag{2.38}$$

for all x and y on the boundary.

The stress-free (or free) boundary condition removes tangential stresses at the bounding surfaces. For horizontal boundaries, this is equivalent to the components τ_{xz} and τ_{yz} of the stress tensor, defined in (2.6), vanishing everywhere on the boundary:

$$\tau_{xz} = \mu\left(\frac{\partial u}{\partial z} + \frac{\partial w}{\partial x}\right) = 0, \qquad \tau_{yz} = \mu\left(\frac{\partial v}{\partial z} + \frac{\partial w}{\partial y}\right) = 0. \tag{2.39}$$

Applying the impermeability condition (2.38), the stress-free condition (2.39) is simplified to

$$\frac{\partial u}{\partial z} = \frac{\partial v}{\partial z} = 0. \tag{2.40}$$

If the fluid is incompressible, then using (2.21), (2.40) becomes

$$\frac{\partial^2 w}{\partial z^2} = 0. \tag{2.41}$$

Furthermore, it follows from (2.40) that

$$\frac{\partial \zeta}{\partial z} = 0. \tag{2.42}$$

The no-slip (or rigid) boundary condition, on the other hand, requires that there is no fluid movement at the bounding surfaces, meaning

$$u = v = 0 \tag{2.43}$$

on horizontal boundaries. Since condition (2.43) must be met across all x and y coordinates, and if the fluid is incompressible, it follows from (2.21) that

$$\frac{\partial w}{\partial z} = 0. \tag{2.44}$$

Furthermore, it follows from (2.43) that

$$\zeta = 0. \tag{2.45}$$

2.6.2 Thermal boundary conditions

In studies of convection, the two most common thermal boundary conditions are: (1) 'perfectly conducting' or fixed-temperature (or isothermal), and (2) 'perfectly insulating' or fixed-flux. Thermal

boundary conditions relevant to geophysical and astrophysical contexts often lie between the extremes of fixed-flux and fixed-temperature.

If the temperature is fixed at the lower and upper boundary walls, at $z = 0$ and $z = 1$ respectively, then it must satisfy the boundary conditions

$$T\left(z=0\right)=T_0, \qquad T\left(z=1\right)=T_0-\Delta T, \tag{2.46}$$

and the temperature perturbation must exhibit no change, thus

$$\theta = 0 \qquad \text{on} \qquad z = 0, 1. \tag{2.47}$$

The fixed-flux boundary condition stipulates that the normal derivative of the temperature is fixed at the boundaries, that is

$$\frac{\partial T}{\partial z} = q, \qquad \text{on} \qquad z = 0,\ 1, \tag{2.48}$$

where q is a constant imposed heat flux. When $q = 0$, the system is a perfect insulator. In this case, the normal derivative of the temperature perturbation must vanish at the boundaries, thus

$$\frac{\partial \theta}{\partial z} = 0 \qquad \text{on} \qquad z = 0, 1. \tag{2.49}$$

In general, we assume impermeable, stress-free, and fixed-temperature boundaries, which enables explicit solutions where feasible. However, in Chapter 3, we specifically examine the influence of thermal boundary conditions in the rapidly rotating limit.

2.7 Normal mode analysis

Following the classical approach for formulating the linear theory of RRBC, we seek solutions to equations (2.33), (2.36), and (2.37) of the form

$$w = \hat{w}\left(z\right) f\left(x,y\right) e^{st}, \qquad \theta = \hat{\theta}\left(z\right) f\left(x,y\right) e^{st}, \qquad \zeta = \hat{\zeta}\left(z\right) f\left(x,y\right) e^{st}, \tag{2.50}$$

where $s = \sigma + i\omega$ is the complex growth rate, with $\sigma, \omega \in \mathbb{R}$, and $f\left(x,y\right)$ is a planform function. Substituting the ansatz (2.50) into (2.33) yields

$$\frac{s\hat{\theta} + \hat{w} - \hat{\theta}''}{\hat{\theta}} = \frac{\nabla_H^2 f}{f}. \tag{2.51}$$

The left-hand side of equation (2.51) depends solely on z, whereas the right-hand side depends on x and y. This means that both sides of (2.51) must be equal to a constant, taken as $-k^2$, where k is the horizontal wavenumber. Thus the planform function $f\left(x,y\right)$ satisfies

$$\nabla_H^2 f + k^2 f = 0. \tag{2.52}$$

This function describes the structure of the flow in horizontal planes, which can take the form of, e.g., rolls, rectangles, or hexagons.

Substituting the ansatz (2.50) into equations (2.33), (2.36), and (2.37), and dropping the hats, gives the following system:

$$\left(\mathcal{D}^2 - k^2 - s\right)\theta = -w, \tag{2.53}$$

$$\left(\mathcal{D}^2 - k^2 - \frac{s}{Pr}\right)\zeta = -Ta^{1/2}\mathcal{D}w, \tag{2.54}$$

$$\left(\mathcal{D}^2 - k^2\right)\left(\mathcal{D}^2 - k^2 - \frac{s}{Pr}\right)w = Ta^{1/2}\mathcal{D}\zeta + k^2 Ra\theta, \tag{2.55}$$

where $\mathcal{D} \equiv \mathrm{d}/\mathrm{d}z$. The governing equations (2.53)–(2.55) form an eighth-order system in space, necessitating eight boundary conditions. An explicit analytical solution can be obtained for the case in which both boundaries are impermeable, stress-free, and fixed-temperature, namely

$$w = \mathcal{D}^2 w = \mathcal{D}\zeta = \theta = 0 \qquad \text{on} \qquad z = 0, 1. \tag{2.56}$$

Conveniently, the system (2.53)–(2.55) can be reduced to a single eighth-order equation for w. Applying the operator $\left(\mathcal{D}^2 - k^2 - s\right)\left(\mathcal{D}^2 - k^2 - s/Pr\right)$ to equation (2.55) and making use of (2.53) and (2.54) to eliminate θ and ζ yields

$$\left(\mathcal{D}^2 - k^2 - s\right)\left[\left(\mathcal{D}^2 - k^2\right)\left(\mathcal{D}^2 - k^2 - \frac{s}{Pr}\right)^2 + Ta\mathcal{D}^2\right]w = \\ -k^2 Ra\left(\mathcal{D}^2 - k^2 - \frac{s}{Pr}\right)w. \tag{2.57}$$

By examining equation (2.55), the fixed-temperature condition can be replaced with

$$\left(\mathcal{D}^2 - k^2\right)\left(\mathcal{D}^2 - k^2 - \frac{s}{Pr}\right)w - Ta^{1/2}\mathcal{D}\zeta = 0 \qquad \text{on} \qquad z = 0, 1. \tag{2.58}$$

Under the impermeable and stress-free boundary conditions (2.56), condition (2.58) implies that $\mathcal{D}^4 w = 0$ on the boundaries. However, since (2.58) depends on ζ, equation (2.57) cannot be treated independently of (2.54). Therefore, it is necessary to consider both (2.54) and (2.57) together with the boundary conditions

$$w = \mathcal{D}^2 w = \mathcal{D}^4 w = \mathcal{D}\zeta = 0 \qquad \text{on} \qquad z = 0, 1. \tag{2.59}$$

In fact, by repeatedly differentiating (2.57), it can be shown that all even derivatives of w vanish at the boundaries. The general solution that satisfies such boundary conditions is a linear combination of sinusoidal functions

$$w(z) = A_n \sin(n\pi z), \tag{2.60}$$

where A_n is a constant (the set of A_n can be determined by boundary conditions) and $n \in \mathbb{N}$. The corresponding solutions for θ and ζ are

$$\theta = \frac{A_n}{n^2\pi^2 + k^2 + s} \sin(n\pi z), \tag{2.61}$$

$$\zeta = \frac{A_n n\pi Ta^{1/2}}{n^2\pi^2 + k^2 + s/Pr} \cos(n\pi z). \tag{2.62}$$

Substituting for w from (2.60) into (2.57) yields the dispersion relation

$$\left(n^2\pi^2 + k^2 + s\right)\left[\left(n^2\pi^2 + k^2\right)\left(n^2\pi^2 + k^2 + \frac{s}{Pr}\right)^2 + n^2\pi^2 Ta\right] = k^2 Ra\left(n^2\pi^2 + k^2 + \frac{s}{Pr}\right). \tag{2.63}$$

2.8 Linear stability analysis

2.8.1 Onset of non-rotating convection

2.8.1.1 The principle of the exchange of stabilities

In RRBC, the flow is stable at low Rayleigh numbers. However, once the Rayleigh number exceeds a critical value, a transition occurs, leading to an instability. In this section, we demonstrate that, in the absence of rotation, the principle of the exchange of stabilities is always valid, meaning that, at the onset of instability, the eigenvalue passes strictly through zero. Thus, at onset, the growth rate s is purely real (indicating $\omega = 0$), and the marginal states are characterised by $s = 0$ for all positive Ra.

Multiplying (2.53) by θ^*, the complex conjugate of θ, and integrating over z yields

$$\int_0^1 \theta^* \left(\mathcal{D}^2 - k^2 - s\right)\theta \,\mathrm{d}z = -\int_0^1 w\theta^* \,\mathrm{d}z. \tag{2.64}$$

Through integration by parts, we obtain

$$\int_0^1 \theta^* \mathcal{D}^2\theta \,\mathrm{d}z = -\int_0^1 |\mathcal{D}\theta|^2 \,\mathrm{d}z, \tag{2.65}$$

since the integrated term vanishes because θ vanishes on the boundaries. Thus, substituting (2.65) into (2.64) gives

$$\int_0^1 \left(|\mathcal{D}\theta|^2 + \left(k^2 + s\right)|\theta|^2\right) \mathrm{d}z = \int_0^1 w\theta^* \,\mathrm{d}z. \tag{2.66}$$

This can be written as

$$sI_0 + I_1 = \int_0^1 w\theta^* \,\mathrm{d}z, \tag{2.67}$$

where

$$I_0 = \int_0^1 |\theta|^2 \,\mathrm{d}z, \tag{2.68}$$

$$I_1 = \int_0^1 \left(|\mathcal{D}\theta|^2 + k^2|\theta|^2\right) \mathrm{d}z. \tag{2.69}$$

Similarly, multiplying (2.55) (with $Ta = 0$) by w^* and integrating over z gives

$$\int_0^1 w^* \left(\mathcal{D}^2 - k^2\right)\left(\mathcal{D}^2 - k^2 - \frac{s}{Pr}\right) w \,\mathrm{d}z = k^2 Ra \int_0^1 w^* \theta \,\mathrm{d}z. \tag{2.70}$$

By repeatedly applying integration by parts, we obtain

$$\int_0^1 w^* \left(|\mathcal{D}^2 w|^2 + \left(2k^2 + \frac{s}{Pr}\right)|\mathcal{D}w|^2 + k^2\left(k^2 + \frac{s}{Pr}\right)|w|^2\right) \mathrm{d}z = k^2 Ra \int_0^1 w^* \theta \,\mathrm{d}z. \tag{2.71}$$

The integrated part vanishes each time due to the boundary conditions $w = \mathcal{D}^2 w = 0$ on $z = 0,\, 1$. This can be written as

$$J_2 + \frac{s}{Pr} J_1 = k^2 Ra \int_0^1 w^* \theta \,\mathrm{d}z, \tag{2.72}$$

where

$$J_1 = \int_0^1 \left(|\mathcal{D}w|^2 + k^2 |w|^2\right) \mathrm{d}z, \tag{2.73}$$

$$J_2 = \int_0^1 \left(|\mathcal{D}^2 w|^2 + 2k^2 |\mathcal{D}w|^2 + k^4 |w|^2\right) \mathrm{d}z. \tag{2.74}$$

The integrals I_0, I_1, J_1, and J_2 are all positive. Subtracting the complex conjugate of (2.72) from the product of $k^2 Ra$ and (2.67) gives

$$k^2 Ra I_1 - J_2 + s k^2 Ra I_0 - \frac{s^*}{Pr} J_1 = 0. \tag{2.75}$$

The real and imaginary parts of (2.75) must vanish separately, giving

$$\sigma\left(k^2 Ra I_0 - \frac{1}{Pr} J_1\right) + k^2 Ra I_1 - J_2 = 0, \tag{2.76}$$

and

$$\omega\left(k^2 Ra I_0 + \frac{1}{Pr} J_1\right) = 0. \tag{2.77}$$

If $Ra < 0$, it follows from (2.76) that $\sigma < 0$, so all modes decay exponentially. Consequently, instability is possible only when $Ra > 0$. In this case, (2.77) implies that $\omega = 0$. Thus, $s = \sigma$ is real for positive Ra, confirming the principle of exchange of stabilities. This indicates that the transition from stability to instability must occur through a stationary (non-oscillatory) state. Therefore, to determine the marginal state, the exact threshold between stability and instability, we set $\sigma = 0$ in the governing equations, corresponding to the neutral state where disturbances neither grow nor decay. This argument was first given by Pellew and Southwell (1940).

For rotating convection, unlike the non-rotating case, the first instability may be oscillatory in nature. Thus, the classical principle of exchange of stabilities does not hold. The nature of the instability depends on the fluid's Prandtl number, Pr, and the rotation rate, Ta. In general, steady convection is preferred at high Pr and moderate Ta, whereas oscillatory convection is preferred at low Pr and high Ta (see figure 2.3).

2.8.1.2 Critical modes

By the principle of exchange of stabilities, the onset of instability occurs when the growth rate passes strictly through zero. Setting $s = 0$ and $Ta = 0$ in equation (2.63) gives the characteristic equation

$$Ra = \frac{\left(n^2\pi^2 + k^2\right)^3}{k^2}. \tag{2.78}$$

For a given wavenumber k, instabilities are marginally stable when the Rayleigh number equals the value specified by (2.78). Below this value, instabilities are stable, and above it, they are unstable. The Rayleigh number attains its minimum value when the wavenumber minimises (2.78). The critical Rayleigh number of the most readily destabilised mode ($n = 1$) is therefore determined by the condition

$$\frac{\mathrm{d}Ra}{\mathrm{d}k^2} = \frac{3k^2\left(\pi^2 + k^2\right)^2 - \left(\pi^2 + k^2\right)^3}{k^4} = 0. \tag{2.79}$$

Thus, the critical wavenumber and critical Rayleigh number corresponding to the onset of steady instability are

$$k^c = \frac{\pi}{\sqrt{2}} \approx 2.22, \qquad Ra^c = \frac{27}{4}\pi^4 \approx 657.51. \tag{2.80}$$

For $Ra < Ra^c$ the system is linearly stable, whereas for $Ra > Ra^c$ the system is linearly unstable and convective motion occurs.

Although Rayleigh–Bénard convection appears straightforward in its basic form, it serves as the foundation for modelling increasingly complex flows. Building on this, we next reintroduce rotation and present its important effects on Rayleigh–Bénard convection.

2.8.2 Onset of rotating convection

The Taylor–Proudman theorem, fundamental in geophysical and astrophysical fluid dynamics, states that in a rapidly rotating, inviscid, and incompressible fluid in steady motion velocity does not vary along the rotation axis: $(\boldsymbol{\Omega} \cdot \nabla)\,\boldsymbol{u} = 0$. If the rotation vector is aligned with z, this reduces to $\partial \boldsymbol{u}/\partial z = 0$, meaning $\boldsymbol{u}$ is independent of z. The theorem arises because the Coriolis force dominates inertia, constraining motion in the direction of rotation. Slowly moving fluid parcels therefore move in columnar structures, called Taylor columns, aligned with the rotation axis (e.g., Vallis, 2017).

For a rapidly rotating system to undergo convection, the Taylor—Proudman theorem must be violated. This occurs at small wavelengths (large wavenumbers), where viscous terms in the momentum equation become sufficiently large to disrupt the balance required by the Taylor-–Proudman constraint.

Rearranging (2.63), with $n = 1$, gives the following cubic dispersion relation for the growth rate s

$$s^3 + a_2 s^2 + a_1 s + a_0 = 0, \tag{2.81}$$

where

$$a_2 = \left(k^2 + \pi^2\right)(1 + 2Pr)\,, \tag{2.82}$$

$$a_1 = Pr\,(Pr + 2)\left(k^2 + \pi^2\right)^2 + \frac{\pi^2 Ta Pr^2 - k^2 Ra Pr}{k^2 + \pi^2}, \tag{2.83}$$

$$a_0 = Pr^2\left[\left(k^2 + \pi^2\right)^3 + \pi^2 Ta - k^2 Ra\right]. \tag{2.84}$$

Equation (2.81) can have either three real solutions or one real solution and a pair of complex conjugate solutions.

2.8.2.1 Steady modes of instability

Similarly to the non-rotating system, when convection manifests as a steady mode, the system's marginal state is characterised by $s = 0$. Setting $s = 0$ in (2.81) gives $a_0 = 0$. Equation (2.84) with a_0 set to zero yields the characteristic equation governing steady convection for the most readily destabilised mode as

$$Ra_s = \frac{1}{k_s^2}\left(\left(\pi^2 + k_s^2\right)^3 + \pi^2 Ta\right), \tag{2.85}$$

where the subscript s denotes a steady instability. When $Ta = 0$, the classical Rayleigh–Bénard characteristic equation, defined in (2.78), is recovered. When $Ta \neq 0$, the presence of rotation delays the onset of convection, shifting it to larger Rayleigh numbers. Thus, rotation has a stabilising influence.

The critical Rayleigh number Ra_s^c and the accompanying critical wavenumber k_s^c are determined by minimising Ra_s with respect to k_s, which is achieved when

$$2k_s^6 + 3\pi^2 k_s^4 = \pi^6 + \pi^2 Ta. \tag{2.86}$$

In the asymptotic limit of rapid rotation ($Ta \to \infty$), the critical values of k and Ra take the form

$$k_s^c \sim \left(\frac{\pi^2}{2} Ta\right)^{1/6} \approx 1.305\, Ta^{1/6}, \tag{2.87}$$

$$Ra_s^c \sim 3\left(\frac{\pi^2}{2} Ta\right)^{2/3} \approx 8.696\, Ta^{2/3}. \tag{2.88}$$

Thus, convection is inhibited as the rotation rate increases, while the critical mode's horizontal scale decreases. Consequently, in the limit of rapid rotation, convection takes the form of tall, thin columns aligned with the axis of rotation.

2.8.2.2 Oscillatory modes of instability

In this section, we investigate whether instabilities can arise as oscillations with increasing amplitude, a phenomenon sometimes known as overstability. In an overstable system, a displaced fluid parcel

undergoes oscillatory motion due to a restoring force and overshoots the equilibrium position due to inertia. If the net energy gained during each oscillation exceeds the energy dissipated, the oscillations grow in amplitude, resulting in overstability.

The perturbations of an oscillatory instability at onset are neutrally stable but time-periodic. Consequently, the growth rate is purely imaginary and may be written as $s = i\omega$, where $\omega \neq 0$ is the frequency. Setting $s = i\omega$ in (2.63) and taking the real and imaginary parts leads to expressions:

$$-\omega^2 (1+2Pr)\left(k_o^2+\pi^2\right) + Pr^2\left(k_o^2+\pi^2\right)^3 + \pi^2 TaPr^2 = k_o^2 Ra_o Pr^2, \tag{2.89}$$

$$-\omega^2\left(k_o^2+\pi^2\right) + \left(k_o^2+\pi^2\right)^3\left(2Pr+Pr^2\right) + \pi^2 TaPr^2 = k_o^2 Ra_o Pr, \tag{2.90}$$

where the subscript o denotes an oscillatory instability.

The marginal Rayleigh number is obtained by eliminating ω from (2.89) and (2.90), and is given by

$$Ra_o = \frac{2(1+Pr)}{k_o^2}\left(\left(k_o^2+\pi^2\right)^3 + \frac{Pr^2}{(1+Pr)^2}\pi^2 Ta\right). \tag{2.91}$$

The critical Rayleigh number Ra_o^c and corresponding critical wavenumber k_o^c are determined by minimising Ra_o with respect to k_o, which is achieved when

$$\left(k_o^2+\pi^2\right)^2(1+Pr)^2\left(2k_o^2-\pi^2\right) = \pi^2 Pr^2 Ta. \tag{2.92}$$

In the asymptotic limit of rapid rotation ($Ta \to \infty$) the critical values take the form

$$k_o^c \sim \left(\frac{Pr^2}{(1+Pr)^2}\frac{\pi^2}{2}Ta\right)^{1/6} = \left(\frac{Pr^2}{(1+Pr)^2}\right)^{1/6} k_s^c, \tag{2.93}$$

$$Ra_o^c \sim 6(1+Pr)\left(\frac{Pr^2}{(1+Pr)^2}\frac{\pi^2}{2}Ta\right)^{2/3} = 2(1+Pr)\left(\frac{Pr^2}{(1+Pr)^2}\right)^{2/3} Ra_s^c. \tag{2.94}$$

Since the Prandtl number is positive ($Pr > 0$), the factor $Pr^2/(1+Pr)^2$ is always less than one. Consequently, for fixed Ta, the critical wavenumber of the oscillatory mode is smaller than that of the steady mode, $k_o^c < k_s^c$, indicating that the oscillatory mode corresponds to a larger wavelength.

The frequency is determined by eliminating Ra_o from equations (2.89) and (2.90), giving

$$\omega^2 = \frac{Pr^2(1-Pr)}{(1+Pr)}\frac{\pi^2}{(k_o^2+\pi^2)}Ta - Pr^2\left(k_o^2+\pi^2\right)^2. \tag{2.95}$$

The critical frequency, in the asymptotic limit of rapid rotation, can be determined by substituting for k_o^c from (2.93) into (2.95) to give

$$\omega^c \sim \left(2-3Pr^2\right)^{1/2}\left(\frac{Pr^2}{(1+Pr)^2}\frac{\pi^2}{2}Ta\right)^{1/3}, \tag{2.96}$$

provided $Pr < \sqrt{2/3} \simeq 0.8164$.

Equation (2.95) shows that solutions corresponding to oscillatory instabilities can exist only if

$$Ta\frac{\pi^2}{(k_o^2+\pi^2)^3}\frac{(1-Pr)}{(1+Pr)}>1. \tag{2.97}$$

This result also follows from $Ra_o < Ra_s$, which shows that Ra_o is always less than Ra_s. From (2.97), it follows that for a fixed Ta, overstable solutions can exist only when $k_o < k_*$, where k_* is defined by

$$\left(k_*^2+\pi^2\right)^3=\pi^2 Ta\frac{(1-Pr)}{(1+Pr)}. \tag{2.98}$$

For fixed values of Pr and Ta, overstability cannot occur when $k > k_*$, and the instability can only set in as stationary convection. In contrast, when $k < k_*$, overstability becomes possible. This naturally raises the question of which form of instability is preferred for a given set of parameters.

The instability type at onset, steady or oscillatory, is set by the mode with the lower critical Rayleigh number. For a given Ta, a transitional Prandtl number, Pr^t, separates these regimes: steady modes are preferred for $Pr > Pr^t$, and oscillatory modes for $Pr < Pr^t$. For $Ta = 10^4$, figure 2.2 shows the steady marginal stability curve with $Ra_s^c = 5377.12$ and $k_s^c = 5.698$, and oscillatory branches with $Pr = 0.46$, $Pr = 0.51186$, and $Pr = 0.58$. At $Pr = 0.58$, steady modes are preferred, whereas at $Pr = 0.46$, oscillatory modes are favoured. At $Pr = 0.51186$, both the oscillatory and steady modes have the same critical Rayleigh number, indicating that both are equally preferred and marking a transition in the preferred mode of instability. Thus, at $Ta = 10^4$, $Pr^t = 0.51186$. An implicit expression for Pr^t, valid for arbitrary Taylor number, is given by Kloosterziel and Carnevale (2003) and Hughes et al. (2022) as

$$Ta=\frac{27\pi^4}{2}\frac{\left(1+Pr^t\right)^{1/2}\left[\sqrt{2}\left(1+Pr^t\right)^{1/2}-1\right]\left(1-Pr^t\right)^2\left(1+2Pr^t\right)^2}{\left[\left(1+Pr^t\right)^{1/2}-2\sqrt{2}\left(Pr^t\right)^2\right]^3}. \tag{2.99}$$

For $Ta < Ta^c = 27\pi^4\left(\sqrt{2}-1\right)/2 = 544.7$, steady convection is always preferred. The denominator of (2.99) vanishes when the Prandtl number is the positive root of $8Pr^4 = Pr + 1$, yielding $Pr^c = 0.67659$. For $Pr < Pr^c$, oscillatory modes are preferred when $Ta \gg 1$, whereas for $Pr > Pr^c$, instabilities will always initially manifest as stationary convection. Figure 2.3 illustrates Pr^t as a function of Ta.

Rotation introduces a restoring Coriolis force that allows the system to oscillate. For these oscillations to grow (overstability), rotation must be strong enough to dominate viscous damping (large Ta), and thermal diffusion must be fast enough relative to momentum diffusion to feed energy into the oscillations (small Pr). Therefore, overstability at onset requires large Ta and small Pr, as illustrated in figure 2.3. Otherwise, convection sets in as a steady instability.

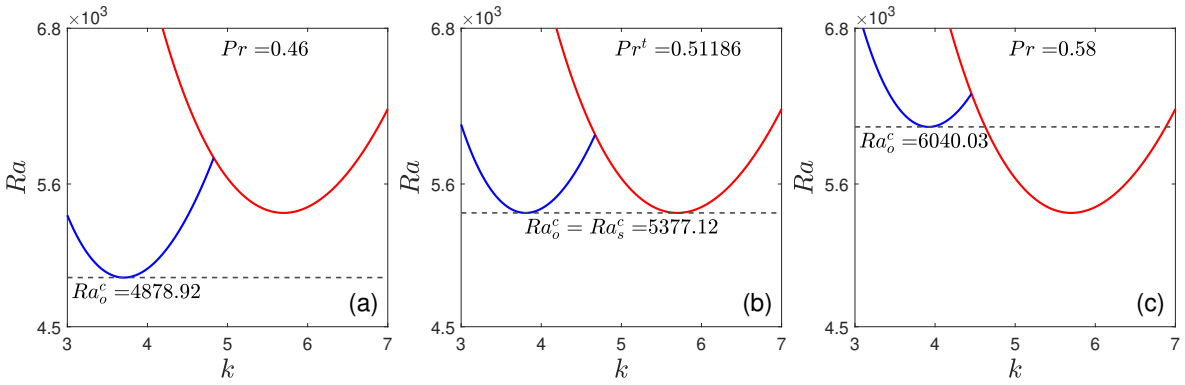


Figure 2.2: Marginal stability curves with $Ta = 10^4$. The red branch, equal in all panels, indicates the onset of steady convection with $Ra_s^c = 5377.12$ and $k_s^c = 5.698$. The blue branches represent the onset of oscillatory convection for (a) $Pr = 0.46$, (b) $Pr^t = 0.51186$, and (c) $Pr = 0.58$.

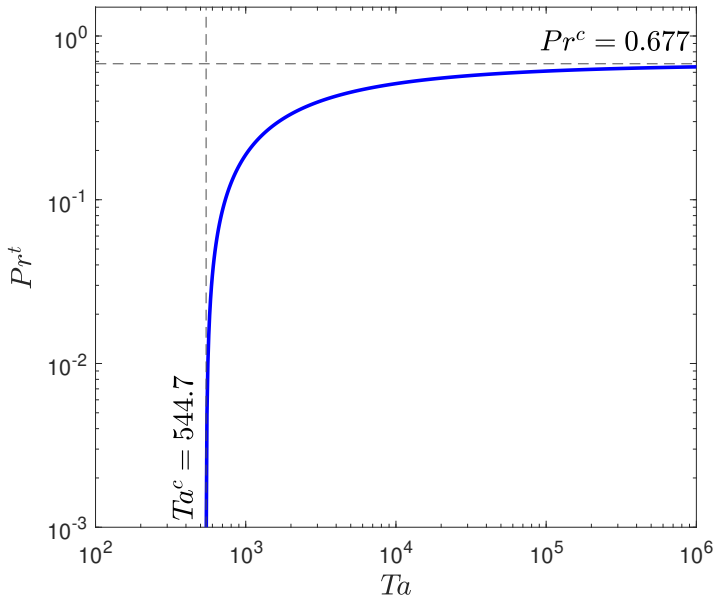


Figure 2.3: The transitional Prandtl number Pr^t as a function of the Taylor number Ta, as defined in (2.99). Steady convection is favoured for $Pr > Pr^t$, while oscillatory convection is preferred for $Pr < Pr^t$. The dashed lines indicate the critical values $Ta^c = 544.7$ and $Pr^c = 0.677$.

Chapter 3

Rotating Rayleigh–Bénard Convection with Fixed Flux Boundaries

3.1 Introduction

Mechanical and thermal boundary conditions are essential for applying simplified models to real-world scenarios (e.g., Sakuraba and Roberts, 2009; Long et al., 2020). In this chapter, we focus on the role of thermal boundary conditions. In studies of convection, two limiting cases are frequently examined: (1) fixed-temperature, where the temperature remains constant along the bounding surfaces; and (2) fixed-flux, where (for uniform thermal conductivity) the normal derivative of temperature is fixed at the boundaries. Thermal boundary conditions relevant to geophysical and astrophysical contexts often lie between these extremes, making an understanding of both limits crucial. In this chapter, we show that, in the rapidly rotating limit, the influence of thermal boundary conditions becomes negligible. This result provides insight into rotating two-layer convection, in which different asymptotic regimes converge to identical behaviour, displaying the same underlying dynamics.

For Boussinesq, linear, rotating Rayleigh–Bénard convection (RRBC) under rapid rotation, the case with impermeable, stress-free and fixed-temperature boundaries is notable as it can be solved analytically (e.g., Chandrasekhar, 1961). The case with fixed-flux boundaries is more complex, as the eigenfunctions are no longer simple trigonometric functions. However, since, under the constraint of rapid rotation, the balance between Coriolis, buoyancy and viscous terms leads to a very small preferred horizontal length scale, the solution in the bulk of the fluid is independent of the choice of boundary conditions. Thus, different boundary conditions can be explored through perturbative methods, enabling analytical progress beyond the impermeable, stress-free, and fixed-temperature case. Exploiting this property, we derive asymptotic solutions for the linear onset of steady RRBC under rapid rotation with impermeable, stress-free, fixed-flux boundary conditions.

In the absence of rotation, the most readily destabilised mode of linear Rayleigh–Bénard convection with impermeable, stress-free, fixed-temperature boundaries has a finite wavenumber (Chandrasekhar, 1961). In contrast, for fixed-flux boundary conditions, the wavenumber of the most readily destabilised mode is zero, imposing large aspect ratio cells at onset (Hurle et al., 1967). Chapman and Proctor (1980) considered the evolution of long but finite wavelength perturbations in the nonlinear regime, showing that steady solutions favour the growth of the longest possible wavelength in large domains. These wide cells continue to dominate at high Rayleigh number (Hewitt et al., 1980). Johnston and Doering (2009) showed using 2D numerical simulations that the heat transport of the fixed-temperature and fixed-flux systems converge at $Ra \approx 5 \times 10^6$ for a Prandtl number $Pr = 1$, and the flow becomes turbulent. In 3D simulations, the heat transport in both cases also becomes comparable, but at a higher Ra (Stevens et al., 2011).

The onset of linear RRBC with impermeable, stress-free and fixed-flux boundaries has been studied by Dowling (1988), who determined the rotational strength required for the critical wavenumber k^c to become non-zero. For $0 \leq Ta < 97.4$, the onset of convection is steady with $k^c = 0$. For $97.4 < Ta < 180.15$, either stationary convection with $k^c = 0$ or overstability with $k^c \neq 0$ occurs at onset, depending on Pr. For $Ta > 180.15$, the system can favour steady or oscillatory convection, both with $k^c > 0$. Takehiro et al. (2002) investigated both the weakly rotating and rapidly rotating linear systems with stress-free and fixed-flux boundary conditions at the onset of convection. Using a modal truncation approach, they demonstrated that, as $Ta \to \infty$, the critical Rayleigh number and wavenumber for both types of thermal boundary conditions converge.

In a related problem, Niiler and Bisshopp (1965) exploited the property of rapidly rotating convection being independent of the choice of boundary conditions in the bulk of the fluid by perturbing the stress-free, fixed-temperature solution to determine the role of no-slip boundary conditions. Niiler and Bisshopp (1965) focused on linear steady modes. Their work was extended by Heard and Veronis (1971), who considered both steady and oscillatory onset. The influence of the no-slip condition is manifested through the formation of Ekman boundary layers at the top and bottom surfaces. The Ekman layer has a thickness of $Ta^{-1/4}$ and adjusts the interior geostrophic flow to zero velocity at the bounding surfaces via Ekman suction. The Ekman layer also affects the temperature near the boundary. As a result, an additional diffusive boundary layer of thickness $Ta^{-1/6}$ is needed to satisfy the fixed-temperature condition, leading to a double boundary layer structure (Heard and Veronis, 1971). Instead of following the classical approach of solving inner and outer solutions separately before matching, Heard and Veronis (1971) constructed a uniformly valid composite expansion from the outset by incorporating multiple scales. This approach yields a system of equations that simultaneously involves both boundary layer and interior variables, making the solution valid across the entire domain. Similarly, satisfaction of the boundary conditions requires contributions from all relevant scales.

More recently, Calkins et al. (2015) pursued an asymptotic approach for small Rossby number (the ratio of inertial to Coriolis forces) to investigate the nonlinear regime for stress-free, fixed-flux RRBC under rapid rotation. From the outset, in a manner similar to that of Heard and Veronis (1971), they constructed a uniformly valid composite expansion by incorporating multiple scales, with the velocity, temperature, vorticity, and pressure decomposed into interior, middle, and Ekman layer components. The composite expansion relies on the premise that the interior flow resembles that of the fixed-temperature system. Calkins et al. (2015) derived the leading-order equations governing each of the interior, middle, and Ekman layer regions. Focusing on stress-free mechanical boundaries, they show that the influence of the boundary layers on the interior is asymptotically weak, and therefore that, to leading order, the solutions for fixed-temperature boundaries and fixed-flux boundaries are equivalent within the rapidly rotating limit.

In this chapter, we derive asymptotic solutions for the linear onset of steady, Boussinesq RRBC under rapid rotation ($Ta \gg 1$) with impermeable, stress-free, fixed-flux boundary conditions. Our approach centres on deriving the governing equations and corresponding solutions for the departures from the fixed-temperature system. Combining these departures with analytical solutions for the problem with fixed-temperature boundaries yields asymptotic solutions for the fixed-flux system.

The chapter begins with a brief overview of the linear stability analysis of the RRBC system, presented in §3.2. The governing equations for the differences between the solutions for the two different thermal boundary conditions are derived in §3.3. Before deriving solutions mathematically, the structure of the solutions is evaluated numerically in §3.4; the numerical results aid in determining the size of the small parameter used in the asymptotic expansions. An asymptotic expansion approach is conducted in §3.5. The solutions to the fixed-flux system are constructed in §3.6. Finally, concluding remarks are given in §3.7.

3.2 Mathematical formation

3.2.1 Governing equations

We consider the system described in Chapter 2, a layer of Boussinesq fluid of infinite horizontal extent confined between two horizontal planes located at $z = 0$ and $z = d$, heated from below. The system rotates with uniform angular velocity $\boldsymbol{\Omega} = \Omega\hat{\boldsymbol{z}}$, where $\hat{\boldsymbol{z}}$ is the unit vector in the vertical direction. The acceleration due to gravity is $\boldsymbol{g} = -g\hat{\boldsymbol{z}}$. The fluid has constant kinematic viscosity ν, coefficient of thermal expansion α and thermal diffusivity κ. The basic state is hydrostatic, and characterised by a linear temperature profile in z, with the lower boundary at temperature T_0, and the upper boundary at temperature $T_0 - \Delta T$. We denote perturbations from the basic state in velocity, pressure and temperature by $\boldsymbol{u} = (u, v, w)$, P and θ, respectively, and adopt the standard scaling of length with d,

time with d^2/κ, temperature with ΔT, velocity with κ/d, and pressure with $\rho_0 (\kappa/d)^2$, where ρ_0 is the (constant) reference value of the fluid density. The dimensionless equations governing the vertical velocity w, the vertical vorticity ζ, and the temperature θ from the basic state are given in (2.33), (2.36), and (2.37). The three dimensionless parameters of the system — the Rayleigh number, Prandtl number, and Taylor number — are defined respectively by

$$Ra = \frac{g\alpha \Delta T d^3}{\nu \kappa}, \qquad Pr = \frac{\nu}{\kappa}, \qquad Ta = \frac{4\Omega^2 d^4}{\nu^2}. \tag{3.1}$$

The Rayleigh number can equivalently be defined in terms of $\beta = \Delta T/d$, the basic state temperature gradient (e.g., Calkins et al., 2015).

Following the classical approach (see §2.7), we seek solutions to (2.33), (2.36), and (2.37) of the form

$$w = \hat{w}(z) f(x,y) e^{st}, \qquad \theta = \hat{\theta}(z) f(x,y) e^{st}, \qquad \zeta = \hat{\zeta}(z) f(x,y) e^{st}, \tag{3.2}$$

where $s = \sigma + i\omega$ is the complex growth rate, with $\sigma, \omega \in \mathbb{R}$, and $f(x,y)$ is a planform function satisfying $\nabla_H^2 f = -k^2 f$, where k is the horizontal wavenumber.

We shall restrict ourselves to a regime in which steady modes of instability are preferred. This is guaranteed for sufficiently large Pr; an implicit expression for the critical value of Pr above which steady modes are preferred, for arbitrary Taylor number, is given in (2.99). Furthermore, we consider marginally stable modes, which are characterised by having a growth rate $s = 0$. Substituting the ansatz (3.2) and $s = 0$ into equations (2.33), (2.36), and (2.37), and dropping the hats, gives the following system:

$$\left(\mathcal{D}^2 - k^2\right)\theta = -w, \tag{3.3}$$

$$\left(\mathcal{D}^2 - k^2\right)\zeta = -Ta^{1/2}\mathcal{D}w, \tag{3.4}$$

$$\left(\mathcal{D}^2 - k^2\right)^2 w = Ta^{1/2}\mathcal{D}\zeta + k^2 Ra\theta, \tag{3.5}$$

where $\mathcal{D} \equiv \mathrm{d}/\mathrm{d}z$. The onset of steady convection is independent of Pr.

We impose impermeable and stress-free mechanical boundary conditions, expressed as

$$w = \mathcal{D}^2 w = \mathcal{D}\zeta = 0 \quad \text{on} \quad z = 0, 1. \tag{3.6}$$

This chapter focuses on the two different thermal boundary conditions, namely fixed-temperature (FT) and fixed-flux (FF), defined respectively as

$$\theta = 0 \quad \text{on} \quad z = 0, 1, \tag{3.7}$$

and

$$\mathcal{D}\theta = 0 \quad \text{on} \quad z = 0, 1. \tag{3.8}$$

3.2.2 Linear stability analysis

Solutions to the FT system can be determined analytically (e.g., Chandrasekhar, 1961). Chapter 2 provides a comprehensive derivation. The most readily excited steady mode of instability is given by

$$w_t = \sin \pi z, \qquad \theta_t = \frac{1}{\pi^2 + k^2} \sin \pi z, \qquad \zeta_t = \frac{\pi Ta^{1/2}}{\pi^2 + k^2} \cos \pi z, \tag{3.9}$$

where the subscript t denotes solutions to the FT system. The Rayleigh number for marginal stability can be expressed as a function of the wavenumber and Taylor number as

$$Ra_t = \frac{\left(\pi^2 + k^2\right)^3}{k^2} + \frac{\pi^2 Ta}{k^2}. \tag{3.10}$$

The critical Rayleigh number Ra_t^c, defined as the threshold at which convection first sets in, and the associated critical wavenumber k_t^c of the most readily destabilised mode are determined by minimising Ra_t with respect to k. This procedure is 'exact', subject to the (numerical) solution of the cubic equation for the critical value of $(k_t^c)^2$:

$$2\left(k_t^c\right)^6 + 3\pi^2 \left(k_t^c\right)^4 - \left(\pi^6 + \pi^2 Ta\right) = 0. \tag{3.11}$$

In the asymptotic limit of very rapid rotation ($Ta \to \infty$), the critical values of Ra_t and k_t take the form

$$Ra_t^c \sim 3\left(\frac{1}{2}\pi^2 Ta\right)^{2/3}, \qquad k_t^c \sim \left(\frac{1}{2}\pi^2 Ta\right)^{1/6}. \tag{3.12}$$

Thus, convection is inhibited as the rotation rate increases, while the critical mode's horizontal scale decreases.

In contrast to the FT system, solutions to the FF system cannot be expressed in a straightforward analytical form. Nonetheless, equations (3.3)–(3.5) with boundary conditions (3.6) and (3.8) can be solved numerically. We use the MATLAB boundary value solver `BVP5C` to compute the eigenfunctions w_f, θ_f, and ζ_f, along with the corresponding marginal Rayleigh number Ra_f over a range of k, where the subscript f denotes solutions to the FF system. The `BVP5C` solver employs a fifth-order accurate finite-difference method that implements the 4-stage Lobatto IIIa formula (Shampine and Kierzenka, 2008). It uses a collocation approach, dividing the domain into subintervals and fitting a polynomial curve within each subinterval to satisfy the equations at four specific interior points (Lobatto points). The solver is particularly suited to this problem because it adaptively refines the mesh to ensure that all fine-scale structures are adequately resolved, requiring 400 mesh points for solutions with $Ta = 10^{14}$. Furthermore, its ability to accommodate a free parameter makes it well suited to eigenvalue problems. The marginal Rayleigh numbers are then minimised using the built-in function `fminbnd` to determine Ra_f^c and k_f^c. This function locates a function's minimum using a hybrid of golden-section search, which iteratively narrows the interval, and parabolic interpolation, which accelerates convergence by fitting a parabola through three points. This process is repeated across a range of Taylor numbers. The thesis applies the same numerical techniques consistently throughout.

Figure 3.1 shows w, θ and ζ for the FT and FF systems, with $Ta = 10^{10}$. The chosen Taylor number is sufficiently large to be in the rapidly rotating regime, while still allowing visualisation of most small-scale flow structures. At this global scale, the solutions are essentially identical in the bulk of the fluid, but they diverge noticeably near the top and bottom boundaries for θ and ζ. The influence of the boundary layers is small but clearly visible in the insets in figures 3.1(b, c) but not in 3.1(a). (The precise structure of the boundary layers will be made clearer in figure 3.3 in §3.4.) At this stage, the crucial point is that the similarity of the solutions in the bulk of the fluid suggests that analytical progress may be made by expressing the FF system as a small departure from the FT system.

Figure 3.2 presents the critical Rayleigh number and critical wavenumber versus Taylor number for the FT and FF systems. The critical values are scaled via the asymptotic relations (3.12), valid as $Ta \to \infty$. Accordingly, the scaled critical Rayleigh number and wavenumber are $Ra^c Ta^{-2/3}$ and $k^c Ta^{-1/6}$, respectively. Figure 3.2 also incorporates the analytical findings of Dowling (1988), who examined the opposite limit of the steady linear instability of a *weakly* rotating system. Figure 3.2 shows that the critical values of the FF system converge towards those of the FT system as $Ta \to \infty$. To illustrate the convergence of critical values more precisely, their respective relative differences, $|Ra_f^c/Ra_t^c - 1|$ and $|k_f^c/k_t^c - 1|$ are presented in figure 3.2(c). The relative difference for both critical values tends towards zero as the Taylor number increases, with a scaling of $Ta^{-1/2}$.

3.3 Derivation of the 'departure system'

We express solutions to the FF system as perturbations from the FT system as

$$w_f = w_t + W, \qquad \theta_f = \theta_t + \Theta, \qquad \zeta_f = \zeta_t + Z, \qquad Ra_f = Ra_t + \mathcal{R}, \tag{3.13}$$

where W, Θ, Z, and $\mathcal{R}$ represent the departures from the FT system. For a fixed Ta, we aim to find solutions for W, Θ, Z, and corresponding marginal values of $\mathcal{R}$ as a function of k.

We first consider equation (3.3), which, for both sets of thermal boundary conditions, takes the form

$$\left(\mathcal{D}^2 - k^2\right)\theta_{\{f,t\}} + w_{\{f,t\}} = 0. \tag{3.14}$$

On subtracting the FT variant of equation (3.14) from its FF counterpart, and using (3.13), we obtain

$$\left(\mathcal{D}^2 - k^2\right)\Theta + W = 0. \tag{3.15}$$

Repeating this process for equations (3.4) and (3.5) yields,

$$\left(\mathcal{D}^2 - k^2\right)Z + Ta^{1/2}\mathcal{D}W = 0, \tag{3.16}$$

$$\left(\mathcal{D}^2 - k^2\right)^2 W - Ta^{1/2}\mathcal{D}Z - k^2 Ra_f\Theta - k^2\left(Ra_f - Ra_t\right)\theta_t = 0. \tag{3.17}$$

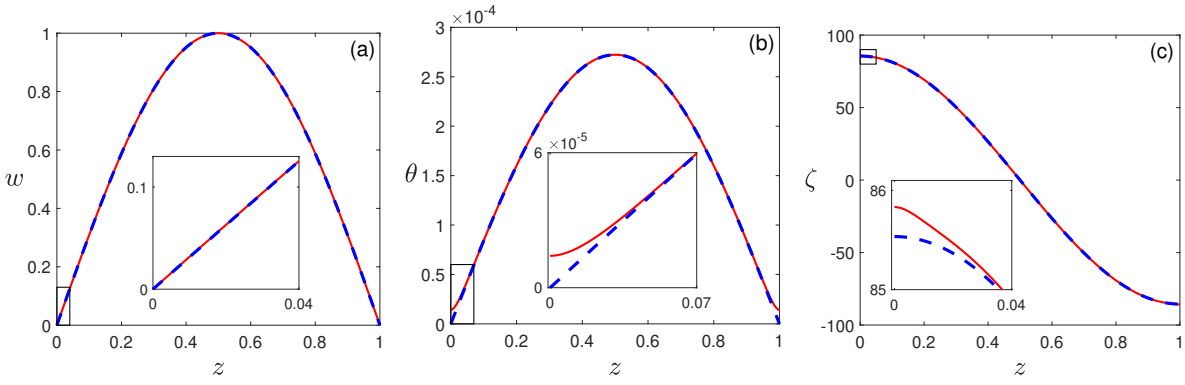


Figure 3.1: Eigenfunctions of (a) vertical velocity, (b) temperature and (c) vertical vorticity, for FT boundary conditions (dashed blue) and FF boundary conditions (solid red), with $Ta = 10^{10}$; the inset figures show a magnified view of the boundary layers within the boxed region near $z = 0$. The eigenfunctions are normalised so that $\max(w) = 1$.

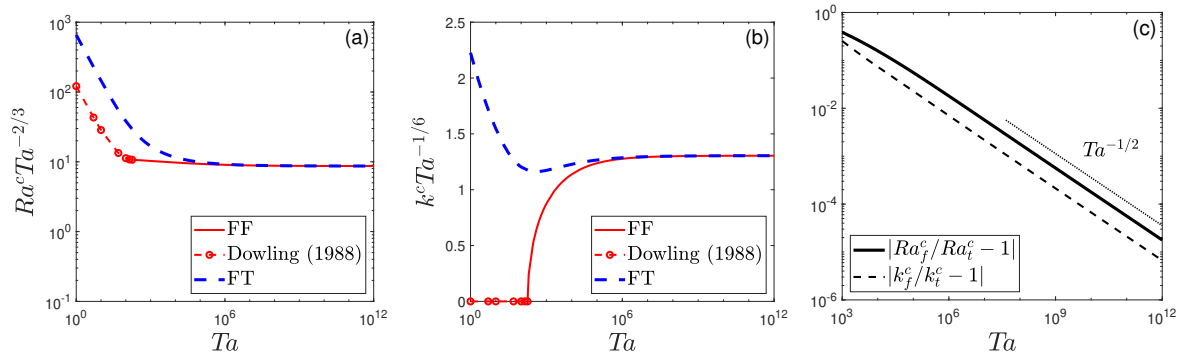


Figure 3.2: Numerically computed, asymptotically scaled critical (a) Rayleigh number and (b) wavenumber as functions of Taylor number for FT and FF conditions. The dashed lines with open circles show the values calculated from the explicit formula of Dowling (1988). (c) The relative difference, as a function of Ta, of the critical Rayleigh number (solid) and wavenumber (dashed) between solutions with FT and FF conditions. The relative difference for both critical values scale as $Ta^{-1/2}$.

In seeking solutions for Θ, Z and W, it is convenient to exploit the Boussinesq symmetry of the problem, which allows us to solve equations (3.15), (3.16) and (3.17) on the domain $z = [0, 1/2]$, with appropriate symmetry conditions imposed at $z = 1/2$. The complete solutions on the interval $z = [0, 1]$ are readily obtained from the symmetry relations

$$\Theta(z) = \Theta(1-z), \qquad W(z) = W(1-z), \qquad Z(z) = -Z(1-z), \tag{3.18}$$

for $z \in [1/2, 1]$, as confirmed by figure 3.1. The symmetry conditions (3.18), together with the normalisation condition of $w = 1$ at $z = 1/2$, provide the mid-point boundary conditions:

$$W = Z = \mathcal{D}W = \mathcal{D}\Theta = 0 \quad \text{at} \quad z = 1/2. \tag{3.19}$$

Impermeable and stress-free mechanical conditions on $z = 0$ for the FT and FF systems, given by (3.6), imply that the departure solutions must satisfy

$$W = \mathcal{D}^2 W = \mathcal{D}Z = 0 \quad \text{on} \quad z = 0. \tag{3.20}$$

The thermal boundary condition at $z = 0$ is given by

$$\mathcal{D}\Theta(0) = \mathcal{D}\theta_f(0) - \mathcal{D}\theta_t(0) = -\frac{\pi}{\pi^2 + k^2}, \tag{3.21}$$

where $\mathcal{D}\theta_f(0)$ is specified by the boundary condition in (3.8), and $\mathcal{D}\theta_t(0)$ is obtained from the solution of the FT system, as given in expression (3.9). At this stage, equations (3.15)–(3.17), with boundary conditions (3.19)–(3.21), are still exact. Henceforth, solving the governing equations will involve some degree of approximation.

Figure 3.2 shows that for large Taylor numbers, the critical values of Ra and k for the FT and FF problems agree at leading-order. It is therefore helpful to express the marginal values sufficiently close to critical for the FT and FF systems as: $Ra_{\{f,t\}} = Ta^{2/3}\widetilde{Ra}_{\{f,t\}}$ and $k = Ta^{1/6}\widetilde{k}$. Note that variables denoted with a tilde represent scaled quantities throughout.

Since, guided by the numerical solutions, the marginal Rayleigh number (sufficiently close to critical) for the two thermal conditions differ only at $\mathcal{O}\left(Ta^{-1/2}\right)$ (determined empirically, see figure 3.2), we may write

$$\widetilde{Ra}_f = \widetilde{Ra}_t + Ta^{-1/2}\widetilde{\mathcal{R}}. \tag{3.22}$$

Substituting (3.22) into (3.17) yields

$$\left(\mathcal{D}^2 - Ta^{1/3}\widetilde{k}^2\right)^2 W - Ta^{1/2}\mathcal{D}Z - Ta\widetilde{k}^2\left(\widetilde{Ra}_t + Ta^{-1/2}\widetilde{\mathcal{R}}\right)\Theta - Ta^{1/2}\widetilde{k}^2\widetilde{\mathcal{R}}\theta_t = 0. \tag{3.23}$$

At leading order, the FT solutions (3.9) become

$$w_t = \sin\pi z, \qquad \theta_t = \frac{1}{\widetilde{k}^2}Ta^{-1/3}\sin\pi z, \qquad \zeta_t = \frac{\pi}{\widetilde{k}^2}Ta^{1/6}\cos\pi z. \tag{3.24}$$

Substituting from (3.24) into equations (3.15), (3.16) and (3.23), and retaining only the dominant Θ term in (3.23), yields the governing equations for the departures from the FT system, expressed as

$$\left(\mathcal{D}^2 - Ta^{1/3}\widetilde{k}^2\right)\Theta + W = 0, \tag{3.25}$$

$$\left(\mathcal{D}^2 - Ta^{1/3}\widetilde{k}^2\right)Z + Ta^{1/2}\mathcal{D}W = 0, \tag{3.26}$$

$$\left(\mathcal{D}^2 - Ta^{1/3}\widetilde{k}^2\right)^2 W - Ta^{1/2}\mathcal{D}Z - Ta\widetilde{k}^2\widetilde{Ra}_t\Theta = Ta^{1/6}\widetilde{\mathcal{R}}\sin\pi z. \tag{3.27}$$

Note that in equation (3.27), $\widetilde{Ra}_t$ is known analytically as a function of the wavenumber $\widetilde{k}$, given in (3.10). It is also important to note that although the Taylor number dependence of Ra_t and k has been taken into account in (3.25)–(3.27) (in the scaled parameters $\widetilde{Ra}_t$ and $\widetilde{k}$), we have not, at this stage, determined the Taylor number scaling for Θ, W and Z.

It is worth striking a note of caution here about approximations made in which small terms are neglected, such as those in (3.24). The very essence of this chapter is to determine the small differences between the FT and FF systems. We must be careful to check later for consistency when, as in (3.24), our derivation proceeds by neglecting small terms of $\mathcal{O}\left(Ta^{-2/3}\right)$ in θ_t and $\mathcal{O}\left(Ta^{-1/6}\right)$ in ζ_t.

3.4 Guidance from the numerical solutions

Before tackling equations (3.25)–(3.27) via an asymptotic approach, which is the primary goal of this chapter and which we do in §3.5, we examine the numerical solutions for the two sets of boundary conditions, thereby allowing us to obtain valuable insights into the structure and form of the differences between the FT and FF systems. Solutions for the departures from the FT solutions are determined simply from the difference between the numerical FF solutions and the exact FT solutions.

Figure 3.3 presents the numerically calculated solutions for W, Θ and Z at $Ta = 10^{10}$, with the wavenumber equal to the critical wavenumber for the FF system: $\widetilde{k} = 1.3038$. On this scale, it is clear that three spatial scales are present in figure 3.3: a narrow boundary layer close to $z = 0$, seen in figure 3.3(a); an intermediate scale, seen in figure 3.3(b); and an interior scale (domain size), seen in figure 3.3(c). Figures 3.4(a-c) illustrate the balance of terms close to $z = 0$ for equations (3.25)–(3.27), with $Ta = 10^{10}$. Very close to the boundary ($0 \leq z \lesssim 0.02$), figure 3.4(c) shows a dominant balance in equation (3.27) between the viscous term $\mathcal{D}^4 W$, the Coriolis term $-Ta^{1/2}\mathcal{D}Z$, and the buoyancy term $-Ta\widetilde{k}^2\widetilde{Ra}_t\Theta$, with the buoyancy term varying only weakly with z, indicating the existence of an Ekman boundary layer (e.g. Greenspan, 1968). In this very narrow region, figure 3.4(b) shows a dominant balance in the vorticity equation (3.26) between $\mathcal{D}^2 Z$ and $Ta^{1/2}\mathcal{D}W$. At larger (yet still small) values of z ($0.02 \lesssim z \lesssim 0.15$), figure 3.4(a) shows a dominant balance in the temperature equation (3.25) between $\mathcal{D}^2\Theta$ and $-Ta^{1/3}\widetilde{k}^2\Theta$, thereby classifying it as a purely diffusive layer. In this region, figure 3.4(b) shows a dominant balance in the vorticity equation (3.26) between $\mathcal{D}^2 Z$ and

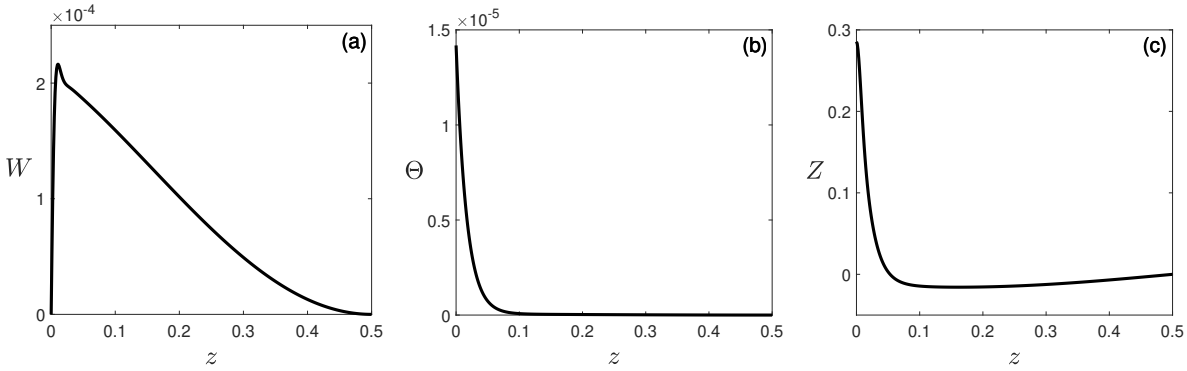


Figure 3.3: Numerical solutions of (a) vertical velocity, (b) temperature, and (c) vertical vorticity of the difference between the FT and FF systems, with $Ta = 10^{10}$ and $\widetilde{k} = 1.3038$.

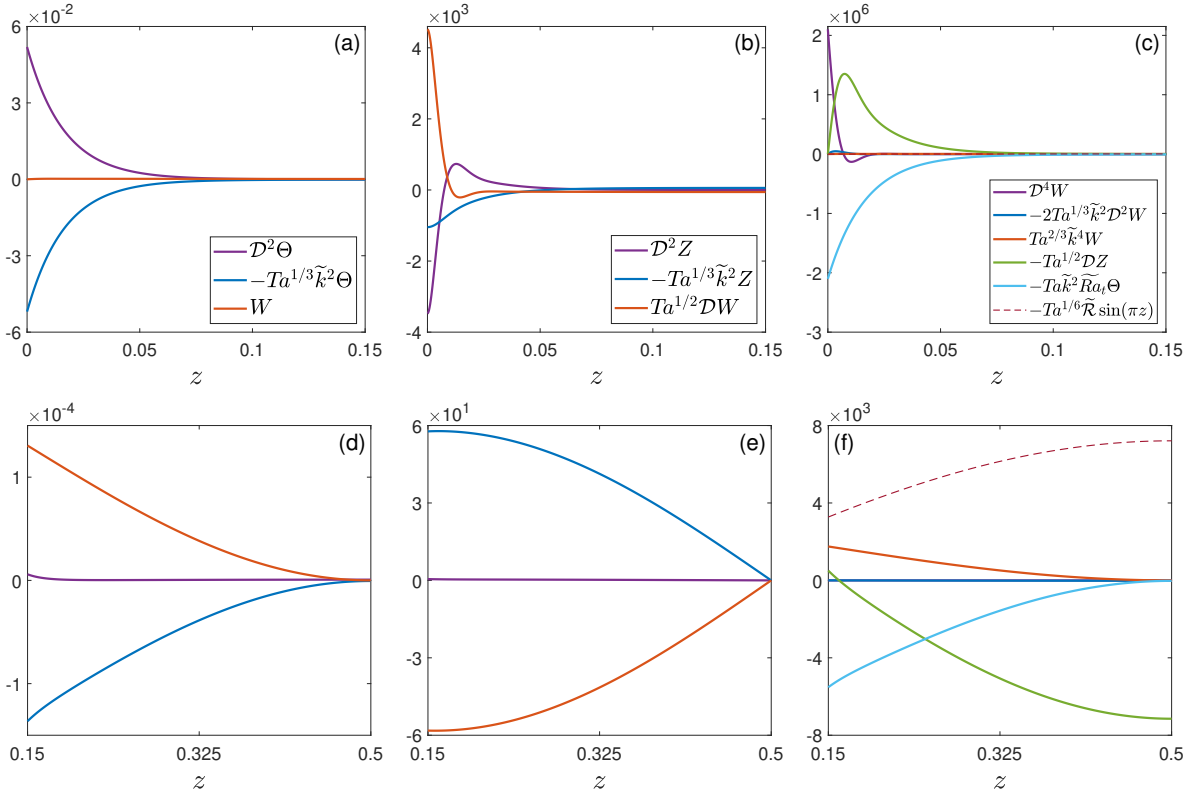


Figure 3.4: Balance of terms close to the boundary $z = 0$ (top row) and within the bulk ($0.15 \lesssim z < 0.5$) (bottom row). The columns correspond to the temperature equation (3.25) (left), vorticity equation (3.26) (middle) and equation (3.27) (right), with $Ta = 10^{10}$ and $\widetilde{k} = 1.3038$. The legends given for (a), (b) and (c) also correspond to (d), (e) and (f), respectively. Solid lines indicate standard rotating Rayleigh–Bénard terms. The dashed line depicts the 'additional' term, given by the final term in equation (3.27), identifiable by its multiplication with $\sin \pi z$, to the standard rotating Rayleigh–Bénard terms.

$-Ta^{1/3}\widetilde{k}^2 Z$, and figure 3.4(c) shows a dominant balance in equation (3.27) between the Coriolis term $-Ta^{1/2}\mathcal{D}Z$ and the buoyancy term $-Ta\widetilde{k}^2\widetilde{Ra}_t\Theta$. The balance of terms within the bulk of the domain ($0.15 \lesssim z \leq 0.5$) in equations (3.25)–(3.27) is depicted in figures 3.4(d-f). Departure solutions spread beyond the boundary layers into the bulk of the domain, albeit with a significantly smaller amplitude. It is instructive to compare the standard rotating Rayleigh–Bénard terms with the 'additional' term given by the right-hand side term in equation (3.27), identifiable by its $\sin \pi z$ dependence. In figure 3.4(c), this additional term, depicted by a dashed line, is insignificant. However, in the bulk of the fluid, it is of comparable magnitude to other terms, as shown by figure 3.4(f).

These numerical results suggest that there exist three distinct regions of importance: an Ekman boundary layer, a diffusive thermal boundary layer, and the bulk region outside the boundary layers. The thickness of the Ekman layer, δ_E, is established by equating the magnitudes of the dominant terms in equation (3.26) very close to the boundary at $z = 0$, namely $\mathcal{D}^2 Z$ and $Ta^{1/2}\mathcal{D}W$, and by making use of the fact that, also very close to the boundary, the $\mathcal{D}^4 W$ and $-Ta^{1/2}\mathcal{D}Z$ terms in equation (3.27) are of comparable magnitude. Letting $\mathcal{D} \sim 1/\delta_E$, the balance from each equation gives the scalings

$$\frac{Z}{\delta_E^2} \sim Ta^{1/2}\frac{W}{\delta_E} \qquad \text{and} \qquad \frac{W}{\delta_E^4} \sim Ta^{1/2}\frac{Z}{\delta_E}, \tag{3.28}$$

and hence we set

$$\delta_E = Ta^{-1/4}, \tag{3.29}$$

corresponding to the scaling of a classical Ekman layer (Greenspan, 1968).

The thickness of the thermal boundary layer, δ_T, is established by equating the sizes of the dominant terms in the temperature equation (3.25). Figure 3.4(a) indicates that the balance close to the boundary is between $\mathcal{D}^2\Theta$ and $-Ta^{1/3}\widetilde{k}^2\Theta$. Letting $\mathcal{D} \sim 1/\delta_T$, the dominant balance leads to

$$\frac{\Theta}{\delta_T^2} \sim Ta^{1/3}\Theta, \tag{3.30}$$

and hence we set

$$\delta_T = Ta^{-1/6}. \tag{3.31}$$

3.5 Asymptotic determination of the departures

In this section, we shall derive asymptotic solutions to the system of equations (3.25)–(3.27), with boundary conditions (3.19)–(3.21). We begin by determining the *inner solutions* within the two boundary layers: the Ekman and thermal. We then determine the *outer solutions*, which are valid in the bulk of the domain. Finally, we match the inner and outer solutions. It is helpful to introduce

$$\varepsilon = \frac{\delta_E}{\delta_T} = Ta^{-1/12} \tag{3.32}$$

as the small parameter in the asymptotic analysis, since it allows both boundary layer scales to be captured in terms of integer powers of ε.

3.5.1 Inner solutions

To describe the boundary layer structure close to $z = 0$, which involves both an Ekman layer and a thermal layer, we introduce the stretched coordinates $\mathcal{S}$ and $\mathcal{Z}$, defined by

$$z = \delta_E \mathcal{S} = \varepsilon^3 \mathcal{S} \qquad \text{and} \qquad z = \delta_T \mathcal{Z} = \varepsilon^2 \mathcal{Z}. \tag{3.33}$$

In the temperature equation (3.25), the relevant boundary layer length scale is $\delta_T = \varepsilon^2$. In terms of the stretched coordinate $\mathcal{Z}$, (3.25) becomes

$$\frac{\mathrm{d}^2\Theta}{\mathrm{d}\mathcal{Z}^2} - \widetilde{k}^2\Theta + \varepsilon^4 W = 0. \tag{3.34}$$

Since we do not yet know the magnitudes of Θ and W, we cannot at this stage pin down the definitive dominant balance in (3.34). We proceed by neglecting the third term $\left(\mathcal{O}\left(\varepsilon^4 W\right)\right)$, but we must check the resulting solutions for self-consistency. Under these assumptions, (3.34) is approximated by

$$\frac{\mathrm{d}^2\Theta}{\mathrm{d}\mathcal{Z}^2} - \widetilde{k}^2\Theta = 0, \tag{3.35}$$

with a general solution

$$\Theta = A\exp\left(-\widetilde{k}\mathcal{Z}\right) + B\exp\left(\widetilde{k}\mathcal{Z}\right), \tag{3.36}$$

where A and B are constants. On moving out of the boundary layer ($\mathcal{Z} \to \infty$), the inner solution must remain finite: thus, $B = 0$. For large Taylor numbers, the boundary condition (3.21) on Θ at $z = 0$ can be asymptotically expanded in powers of $\widetilde{k}^{-2}$ and is, to leading-order, given by

$$\frac{\mathrm{d}\Theta}{\mathrm{d}\mathcal{Z}}(0) = -\varepsilon^6 \frac{\pi}{\widetilde{k}^2}. \tag{3.37}$$

Ensuring that Θ, given by (3.36) (with $B = 0$), satisfies the condition (3.37), yields $A = \varepsilon^6\pi/\widetilde{k}^3$. Hence, the leading-order inner solution for Θ across the entire thermal boundary layer is given by

$$\Theta_{in} = \varepsilon^6 \frac{\pi}{\widetilde{k}^3}\exp\left(-\widetilde{k}\mathcal{Z}\right). \tag{3.38}$$

We next determine the velocity within the boundary layer region. The relevant length scale is now the thickness of the Ekman layer, $\delta_E = \varepsilon^3$, and so we work in terms of the stretched coordinate $\mathcal{S}$. Equations (3.26) and (3.27) become

$$\left(\frac{\mathrm{d}^2}{\mathrm{d}\mathcal{S}^2} - \varepsilon^2\widetilde{k}^2\right) Z + \varepsilon^{-3}\frac{\mathrm{d}W}{\mathrm{d}\mathcal{S}} = 0, \tag{3.39}$$

$$\left(\frac{\mathrm{d}^2}{\mathrm{d}\mathcal{S}^2} - \varepsilon^2\widetilde{k}^2\right)^2 W - \varepsilon^3\frac{\mathrm{d}Z}{\mathrm{d}\mathcal{S}} = \widetilde{k}^2\widetilde{Ra}_t\Theta + \varepsilon^{10}\widetilde{\mathcal{R}}\sin\left(\pi\varepsilon^3\mathcal{S}\right). \tag{3.40}$$

By differentiating equation (3.39) with respect to $\mathcal{S}$ and applying the operator $\left(\mathrm{d}^2/\mathrm{d}\mathcal{S}^2 - \varepsilon^2\widetilde{k}^2\right)$ to (3.40), the vorticity can be eliminated between these two equations to give the following sixth-order equation for W:

$$\left(\frac{\mathrm{d}^2}{\mathrm{d}\mathcal{S}^2} - \varepsilon^2\widetilde{k}^2\right)^3 W + \frac{\mathrm{d}^2 W}{\mathrm{d}\mathcal{S}^2} = \widetilde{k}^2\widetilde{Ra}_t\left(\frac{\mathrm{d}^2}{\mathrm{d}\mathcal{S}^2} - \varepsilon^2\widetilde{k}^2\right)\Theta + \varepsilon^{10}\widetilde{\mathcal{R}}\left(\frac{\mathrm{d}^2}{\mathrm{d}\mathcal{S}^2} - \varepsilon^2\widetilde{k}^2\right)\sin\left(\pi\varepsilon^3\mathcal{S}\right). \tag{3.41}$$

On substituting the inner solution of Θ from (3.38), with $\mathcal{Z}$ replaced by $\varepsilon\mathcal{S}$, the first term on the right-hand side of (3.41) becomes zero, thereby removing any dependence on the inner solution for the temperature. Equation (3.41) then becomes

$$\frac{\mathrm{d}^6 W}{\mathrm{d}\mathcal{S}^6} - 3\varepsilon^2\widetilde{k}^2\frac{\mathrm{d}^4 W}{\mathrm{d}\mathcal{S}^4} + 3\varepsilon^4\widetilde{k}^4\frac{\mathrm{d}^2 W}{\mathrm{d}\mathcal{S}^2} - \varepsilon^6\widetilde{k}^6 W + \frac{\mathrm{d}^2 W}{\mathrm{d}\mathcal{S}^2} = -\varepsilon^{12}\widetilde{\mathcal{R}}\left(\pi^2\varepsilon^4 + \widetilde{k}^2\right)\sin\left(\pi\varepsilon^3\mathcal{S}\right). \tag{3.42}$$

Proceeding under the assumption that $W > \mathcal{O}\left(\varepsilon^{12}\right)$(which will be confirmed later), the leading order terms of (3.42) give

$$\frac{\mathrm{d}^6 W}{\mathrm{d}\mathcal{S}^6} + \frac{\mathrm{d}^2 W}{\mathrm{d}\mathcal{S}^2} = 0. \tag{3.43}$$

Assuming a solution of the form $W \propto \exp\left(\lambda\mathcal{S}\right)$, we obtain the characteristic equation

$$\lambda^2\left(\lambda^4 + 1\right) = 0. \tag{3.44}$$

The solution must remain bounded as it exits the boundary layer, i.e., as $\mathcal{S} \to \infty$. Therefore, any solutions for λ with positive real parts are discarded. This results in three relevant roots:

$$\lambda = 0, \quad \frac{1}{\sqrt{2}}\left(-1 + i\right), \quad \text{and} \quad \frac{1}{\sqrt{2}}\left(-1 - i\right). \tag{3.45}$$

Hence, the general solution of W that remains bounded as $\mathcal{S} \to \infty$ is given by

$$W = A + \exp\left(\frac{-\mathcal{S}}{\sqrt{2}}\right)\left[B\cos\left(\frac{\mathcal{S}}{\sqrt{2}}\right) + C\sin\left(\frac{\mathcal{S}}{\sqrt{2}}\right)\right], \tag{3.46}$$

where A, B, and C are constants. Application of the conditions (3.20)(a,b), namely $W = \mathcal{D}^2 W = 0$ on $\mathcal{S} = 0$, gives $A + B = 0$ and $C = 0$. Thus,

$$W = A\left[1 - \exp\left(\frac{-\mathcal{S}}{\sqrt{2}}\right)\cos\left(\frac{\mathcal{S}}{\sqrt{2}}\right)\right]. \tag{3.47}$$

The inner solution for Z is obtained by substituting for $\mathrm{d}W/\mathrm{d}\mathcal{S}$ from (3.47) into (3.39), resulting in

$$\left(\frac{\mathrm{d}^2}{\mathrm{d}\mathcal{S}^2} - \varepsilon^2\widetilde{k}^2\right) Z = -\varepsilon^{-3}\frac{A}{\sqrt{2}}\exp\left(\frac{-\mathcal{S}}{\sqrt{2}}\right)\left[\cos\left(\frac{\mathcal{S}}{\sqrt{2}}\right) + \sin\left(\frac{\mathcal{S}}{\sqrt{2}}\right)\right], \tag{3.48}$$

where all terms in (3.48) are needed to solve for Z. The inner solution that remains bounded on leaving the boundary layer ($\mathcal{S} \to \infty$) and that satisfies the condition $\mathcal{D}Z = 0$ on $\mathcal{S} = 0$ is therefore

$$Z = \varepsilon^{-4}\frac{A}{\widetilde{k}}\exp\left(-\varepsilon\widetilde{k}\mathcal{S}\right) + \varepsilon^{-3}\frac{A}{\sqrt{2}}\exp\left(\frac{-\mathcal{S}}{\sqrt{2}}\right)\left[\sin\left(\frac{\mathcal{S}}{\sqrt{2}}\right) - \cos\left(\frac{\mathcal{S}}{\sqrt{2}}\right)\right]. \tag{3.49}$$

Finally, the constant A appearing in the expressions for W and Z in (3.47) and (3.49) is obtained by inserting the inner solutions from (3.38), (3.47), and (3.49) into (3.40), yielding

$$A = \varepsilon^6 \frac{\pi \widetilde{Ra}}{\widetilde{k}}. \tag{3.50}$$

Consequently, the inner solutions for W and Z take the form:

$$W_{in} = \varepsilon^6 \frac{\pi \widetilde{Ra}}{\widetilde{k}} \left[1 - \exp\left(\frac{-\mathcal{S}}{\sqrt{2}}\right) \cos\left(\frac{\mathcal{S}}{\sqrt{2}}\right)\right], \tag{3.51}$$

$$Z_{in} = \varepsilon^2 \frac{\pi \widetilde{Ra}}{\widetilde{k}^2} \exp\left(-\varepsilon \widetilde{k} \mathcal{S}\right) + \varepsilon^3 \frac{\pi \widetilde{Ra}}{\sqrt{2}\widetilde{k}} \exp\left(\frac{-\mathcal{S}}{\sqrt{2}}\right) \left[\sin\left(\frac{\mathcal{S}}{\sqrt{2}}\right) - \cos\left(\frac{\mathcal{S}}{\sqrt{2}}\right)\right]. \tag{3.52}$$

Note that, although the second term in expression (3.52) is asymptotically smaller than the first, their derivatives are of the same magnitude — and hence the inclusion of both terms is essential to satisfy the boundary condition $\mathcal{D}Z = 0$ on $\mathcal{S} = 0$.

Having determined the leading-order inner solutions for Θ, W, and Z, it can be shown that the assumptions made en route are indeed self-consistent. From expression (3.51) we know that $W = \mathcal{O}\left(\varepsilon^6\right)$. Therefore, the $\varepsilon^4 W$ term in (3.34) is $\mathcal{O}\left(\varepsilon^{10}\right)$, whereas the other terms in the equation are $\mathcal{O}\left(\varepsilon^6\right)$. Hence, neglecting the $\varepsilon^4 W$ term in (3.34) is justified. Furthermore, in equation (3.42), we assumed that the magnitude of W is greater than $\mathcal{O}\left(\varepsilon^{12}\right)$, which is also a valid assumption. It is important to note that the inner solutions are already fully determined, with no free parameters.

3.5.2 Outer solutions

We now turn to the evaluation of the outer solutions, which are valid in the bulk of the domain and satisfy the mid-point (symmetry) conditions (3.19). Since length scales in the bulk are $\mathcal{O}\left(1\right)$, the terms involving $\mathcal{D}^2$ are negligible compared with $Ta^{1/3}\widetilde{k}^2$ in equations (3.25)–(3.27). This is confirmed by figures 3.4(d–f). Therefore, the dominant terms of (3.25)–(3.27) within the outer regions satisfy, respectively,

$$\Theta = \varepsilon^4 \widetilde{k}^{-2} W, \tag{3.53}$$

$$Z = \varepsilon^{-2} \widetilde{k}^{-2} \mathcal{D}W, \tag{3.54}$$

$$\varepsilon^4 \widetilde{k}^4 W - \varepsilon^6 \mathcal{D}Z - \widetilde{k}^2 \widetilde{Ra}_t \Theta = \varepsilon^{10} \widetilde{\mathcal{R}} \sin \pi z. \tag{3.55}$$

Since the derivative terms $\mathcal{D}^4$ and $\mathcal{D}^2$ have been neglected in the simplification from (3.25)–(3.27) to (3.53)–(3.55), there is freedom to impose only two boundary conditions. By imposing the mid-point conditions on W and $\mathcal{D}W$ — i.e., $W = \mathcal{D}W = 0$ at $z = 1/2$ — the ansatzes for Θ and Z, (3.53) and (3.54), are (critically) self-consistent in that their mid-point conditions are also satisfied — i.e., $\mathcal{D}\Theta = Z = 0$ at $z = 1/2$.

On substituting for Θ from (3.53) and for Z from (3.54), equation (3.55) becomes

$$\mathcal{D}^2 W + \widetilde{k}^2 \left(\widetilde{Ra}_t - \widetilde{k}^4 \right) W = -\varepsilon^6 \widetilde{k}^2 \widetilde{\mathcal{R}} \sin \pi z. \tag{3.56}$$

The term $\widetilde{k}^2 \left(\widetilde{Ra}_t - \widetilde{k}^4 \right)$ in (3.56) can be evaluated asymptotically via the relation (3.10) linking $\widetilde{Ra}_t$ and $\widetilde{k}$. When rewritten in terms of the scaled variables, (3.10) becomes

$$\widetilde{Ra}_t = \frac{\left(\widetilde{k}^2 + \varepsilon^4 \pi^2 \right)^3}{\widetilde{k}^2} + \frac{\pi^2}{\widetilde{k}^2}. \tag{3.57}$$

To leading order, (3.57) reduces to

$$\widetilde{k}^2 \left(\widetilde{Ra}_t - \widetilde{k}^4 \right) = \pi^2. \tag{3.58}$$

On substituting for $\widetilde{k}^2 \left(\widetilde{Ra}_t - \widetilde{k}^4 \right)$ from (3.58), equation (3.56) becomes

$$\mathcal{D}^2 W + \pi^2 W = -\varepsilon^6 \widetilde{k}^2 \widetilde{\mathcal{R}} \sin \pi z. \tag{3.59}$$

The solution of (3.59) satisfying the mid-point conditions $W\left(1/2\right) = \mathcal{D}W\left(1/2\right) = 0$ is thus given by

$$W_{out} = \varepsilon^6 \frac{\widetilde{k}^2}{4\pi} \widetilde{\mathcal{R}} \left(2z - 1 \right) \cos \pi z. \tag{3.60}$$

The outer solutions for Θ and Z are then obtained by substituting (3.60) into (3.53) and (3.54), respectively, yielding

$$\Theta_{out} = \varepsilon^{10} \frac{1}{4\pi} \widetilde{\mathcal{R}} \left(2z - 1 \right) \cos \pi z, \tag{3.61}$$

$$Z_{out} = \varepsilon^4 \frac{1}{4\pi} \widetilde{\mathcal{R}} \left[2 \cos \pi z + \pi \left(1 - 2z \right) \sin \pi z \right]. \tag{3.62}$$

Note that the (scaled) departure of the Rayleigh number, $\widetilde{\mathcal{R}}$, has not yet been determined.

3.5.3 Matching the inner and outer solutions

To complete the solution, and hence determine $\widetilde{\mathcal{R}}$, we match the inner and outer solutions at the edge of the relevant boundary layer. We employ Prandtl's matching technique, which stipulates that the inner limit of the outer solution must match the outer limit of the inner solution (e.g., Van Dyke, 1964). For W, this requirement can be expressed as

$$\lim_{z \to 0} W_{out} = \lim_{\mathcal{S} \to \infty} W_{in}. \tag{3.63}$$

Applying the matching condition (3.63) to the inner and outer solutions given by (3.51) and (3.60) determines $\widetilde{\mathcal{R}}$ as a function of $\widetilde{k}$ from the $\mathcal{O}\left(\varepsilon^6\right)$ terms as

$$\widetilde{\mathcal{R}} = -\frac{4\pi^2 \widetilde{Ra}_t}{\widetilde{k}^3}. \tag{3.64}$$

From (3.38), $\Theta_{in} = \mathcal{O}\left(\varepsilon^6\right)$, whereas from (3.61), $\Theta_{out} = \mathcal{O}\left(\varepsilon^{10}\right)$. Since $\Theta_{in} \to 0$ as $\mathcal{Z} \to \infty$, matching at the largest order $\left(\mathcal{O}\left(\varepsilon^6\right)\right)$ is immediately satisfied. Matching of the leading order vorticity is achieved similarly, since $Z_{in} = \mathcal{O}\left(\varepsilon^2\right)$ with $Z_{in} \to 0$ as $\mathcal{Z} \to \infty$ (from (3.52)), and $Z_{out} = \mathcal{O}\left(\varepsilon^4\right)$ (from (3.62)).

3.5.4 Composite solutions

Combining the inner solutions (3.38), (3.51), and (3.52) with the outer solutions (3.60)–(3.62) and substituting for $\widetilde{\mathcal{R}}$ from (3.64) yields the following composite solutions, valid across the entire domain:

$$W = \varepsilon^6 \frac{\pi \widetilde{Ra}_t}{\widetilde{k}} \left[(1-2z)\cos\pi z - \exp\left(\frac{-\varepsilon^{-3}z}{\sqrt{2}}\right)\cos\left(\frac{\varepsilon^{-3}z}{\sqrt{2}}\right)\right], \tag{3.65}$$

$$\Theta = \varepsilon^6 \frac{\pi}{\widetilde{k}^3}\left[\exp\left(-\varepsilon^{-2}\widetilde{k}z\right) + \varepsilon^4 \widetilde{Ra}_t\,(1-2z)\cos\pi z\right], \tag{3.66}$$

$$Z = \varepsilon^2 \frac{\pi \widetilde{Ra}_t}{\widetilde{k}^2}\left[\exp\left(-\varepsilon^{-2}\widetilde{k}z\right) + \varepsilon\frac{\widetilde{k}}{\sqrt{2}}\exp\left(\frac{-\varepsilon^{-3}z}{\sqrt{2}}\right)\left(\sin\left(\frac{\varepsilon^{-3}z}{\sqrt{2}}\right) - \cos\left(\frac{\varepsilon^{-3}z}{\sqrt{2}}\right)\right) + \varepsilon^2 \frac{1}{\widetilde{k}}\left(\pi\,(2z-1)\sin\pi z - 2\cos\pi z\right)\right]. \tag{3.67}$$

It should be noted that (3.66) and (3.67) contain only the leading order inner and outer solutions. For the temperature, for example, we have retained the $O\left(\varepsilon^{10}\right)$ outer solution (the leading-order term), but have neglected the sub-dominant $O\left(\varepsilon^{10}\right)$ correction to the inner solution.

Figure 3.5 compares the asymptotic expressions (3.65)–(3.67) with the numerically determined results for W, Θ and Z, close to the boundary $z = 0$ and within the bulk ($0.15 \lesssim z < 0.5$), with $Ta = 10^{10}$ and $\widetilde{k} = 1.3038$, demonstrating the strong agreement between the composite solutions and the numerical results. This agreement is further validated in figure 3.6, which presents the maximum absolute error over the z-domain between the numerical (subscript N) and asymptotic (subscript A) solutions for W, Θ and Z, and $\mathcal{D}Z$ (as we shall see below, to determine the order of the next term in the expansion of Z, we examine its derivative), evaluated across a range of Taylor numbers. Furthermore, from figure 3.6, we can deduce that the absolute errors in W, Θ and Z scale as $Ta^{-0.69} \approx \varepsilon^8$, $Ta^{-0.86} \approx \varepsilon^{10}$, and $Ta^{-0.44} \approx \varepsilon^5$, suggesting that the next terms in their respective expansions are $\mathcal{O}\left(\varepsilon^8\right)$, $\mathcal{O}\left(\varepsilon^{10}\right)$, and $\mathcal{O}\left(\varepsilon^5\right)$. We note that numerical solutions remain reliable up to $Ta \approx 10^{11}$. At higher Ta, resolving small differences between the FT and FF systems becomes increasingly challenging. For example, when $Ta = 10^{10}$, the small parameter is $\varepsilon = 0.15$, giving $\varepsilon^{10} = 4.6 \times 10^{-9}$. Consequently, when computing FT and FF eigenfunctions, the accuracy of the numerical solutions must exceed ten significant figures.

The leading-order terms in both the inner and outer expansions of W are found to be $\mathcal{O}\left(\varepsilon^6\right)$. Based on figure 3.6(a), the next term scales as $\mathcal{O}\left(\varepsilon^8\right)$, though further analysis is required to verify this. The leading-order term in the outer solution of Θ is $\mathcal{O}\left(\varepsilon^{10}\right)$, while the inner counterpart is of $\mathcal{O}\left(\varepsilon^6\right)$. In the matching process, the inner solution is matched to zero at leading-order, so the corresponding outer solution is not required. Consequently, the next order correction in the inner solution must match the leading-order outer solution — an expectation that aligns with the numerical results.

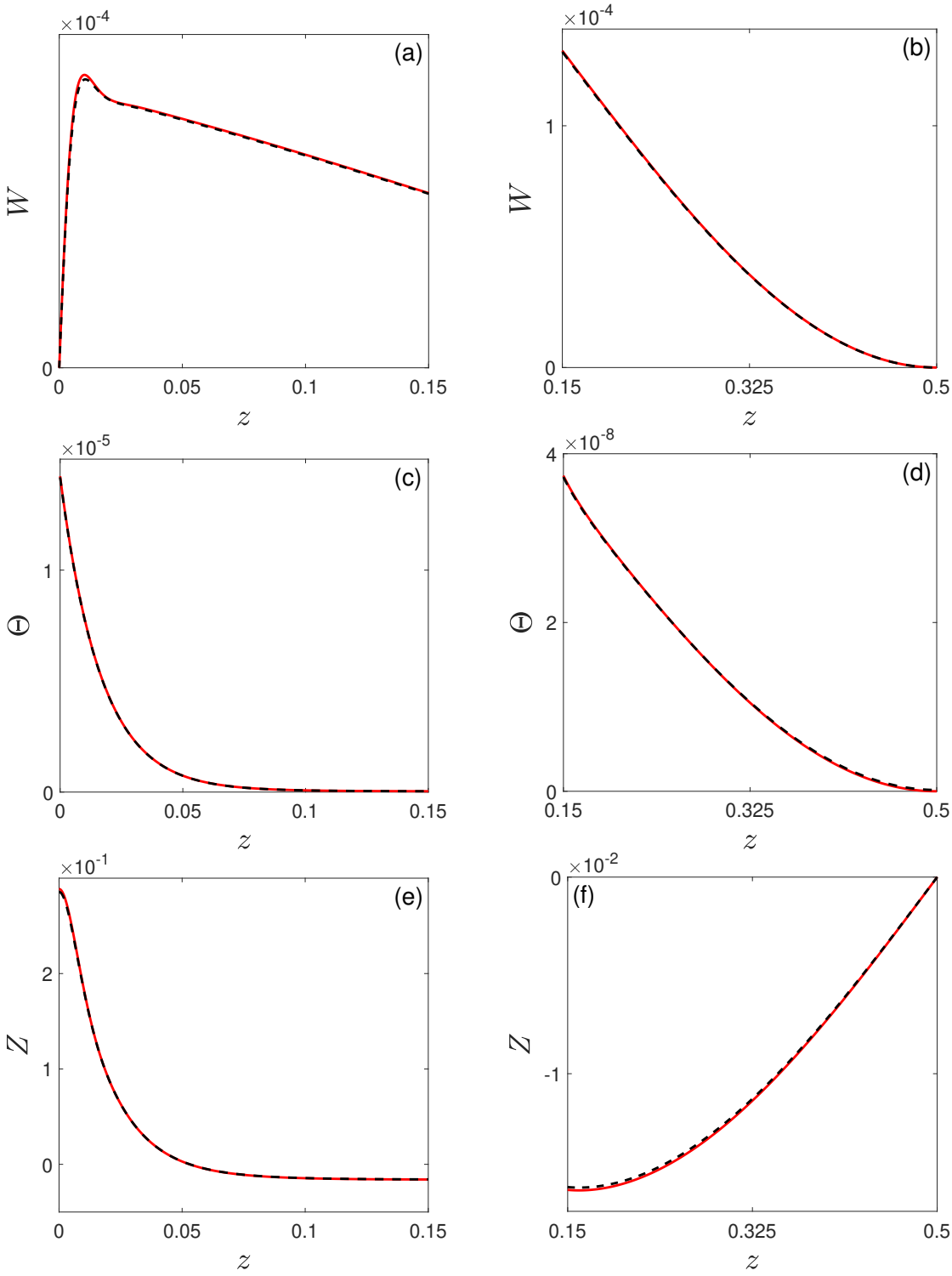


Figure 3.5: Dashed black lines show the numerical results, while the red solid lines show the composite solutions of W, Θ and Z, as given by expressions (3.65)–(3.67), where $\widetilde{k}$ and $\widetilde{Ra}_t$ are determined numerically. Rows correspond to W, Θ, and Z, with $Ta = 10^{10}$ and $\widetilde{k} = 1.3038$. Columns correspond to the solutions close to the boundary $z = 0$ (left) and within the bulk ($0.15 \lesssim z < 0.5$) (right).

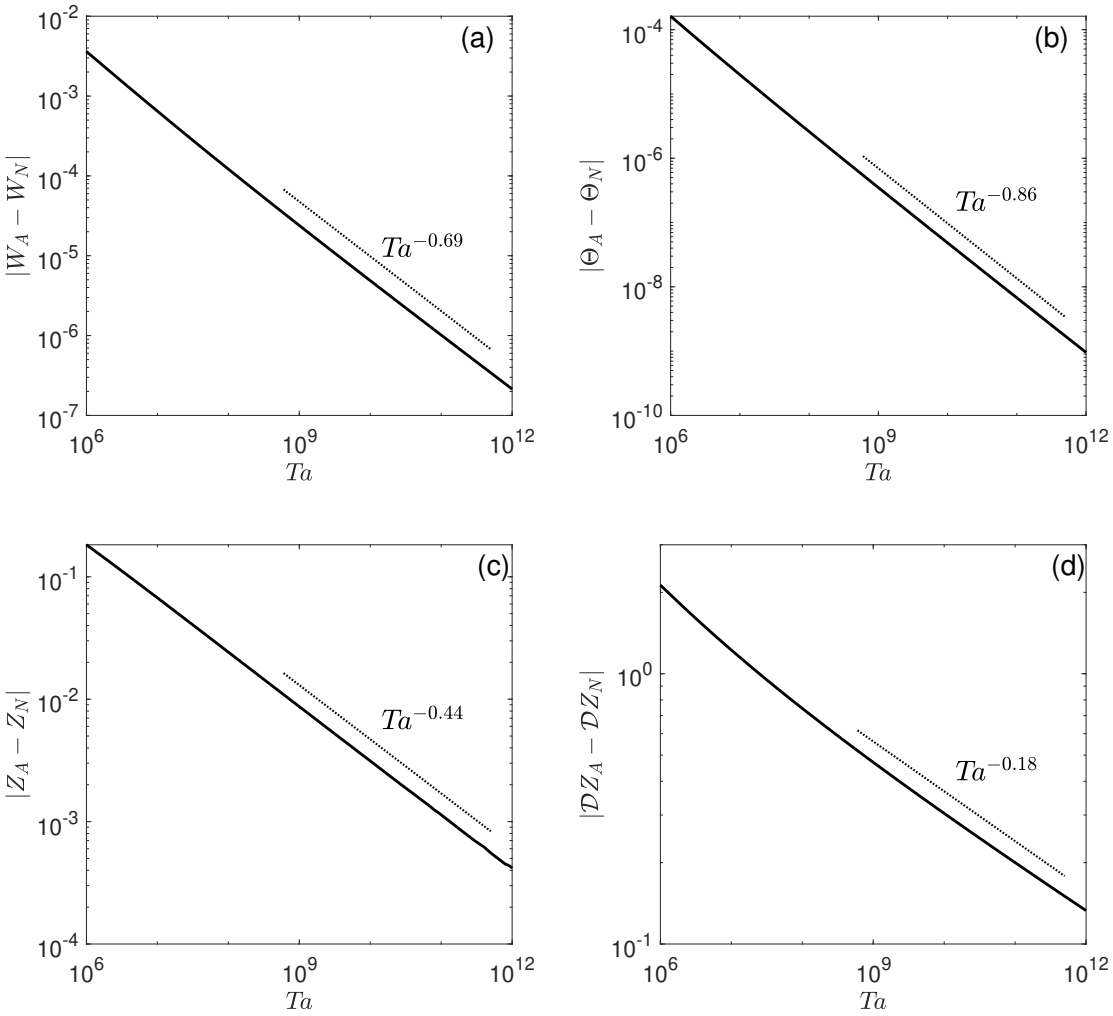


Figure 3.6: The maximum absolute error over the z-domain between numerical (subscript N) and asymptotic (subscript A) solutions of (a) W, (b) Θ, (c) Z, (d) $\mathcal{D}Z$, evaluated across a range of Taylor numbers. The asymptotic solutions of W, Θ, Z and $\mathcal{D}Z$ are given by expressions (3.65)–(3.68). The absolute error exhibits gradients of approximately -0.69 for W, -0.86 for Θ, -0.44 for Z, and -0.18 for $\mathcal{D}Z$.

The error related to Z is more challenging to interpret. Based on figure 3.6(c), the absolute error in Z scales as $Ta^{-0.44} \approx \varepsilon^5$, suggesting that the next term in the expansion is $\mathcal{O}\left(\varepsilon^5\right)$. To determine why the error appears at this order, we examine the derivative of Z, given by

$$\mathcal{D}Z = \frac{\pi \widetilde{Ra}_t}{\widetilde{k}} \left[-\exp\left(-\varepsilon^{-2}\widetilde{k}z\right) + \exp\left(\frac{-\varepsilon^{-3}z}{\sqrt{2}}\right) \cos\left(\frac{\varepsilon^{-3}z}{\sqrt{2}}\right) + \varepsilon^4 \frac{\pi}{\widetilde{k}^2} \left(\pi\left(2z-1\right)\cos\pi z + 4\sin\pi z\right) \right]. \quad (3.68)$$

The first two terms of (3.68) originate from the inner solution of Z, while the remaining terms arise from the outer solution. The inner solutions of Z and $\mathcal{D}Z$ exhibit different scalings: $\mathcal{O}\left(\varepsilon^2\right)$ and $\mathcal{O}\left(1\right)$. In contrast, their outer solutions scale identically as $\mathcal{O}\left(\varepsilon^4\right)$. Based on figure 3.6(d), the absolute error in $\mathcal{D}Z$ scales as $Ta^{-0.18} \approx \varepsilon^2$, suggesting that the next term in its expansion is $\mathcal{O}\left(\varepsilon^2\right)$. A possible explanation for this scaling is the presence of a term in Z_{in} of the form $f\left(z\right)\varepsilon^5 \exp\left(-\varepsilon^{-3}z\right)$, where f is a function of z. This would yield a corresponding term in $\mathcal{D}Z$ of the form $\left(f' - f\right)\varepsilon^2 \exp\left(-\varepsilon^{-3}z\right)$, with $f' - f = 0$ at $z = 0$, ensuring the boundary conditions are satisfied. It should be noted that the error arising from $\mathcal{D}Z_{out}\left(0\right) = \mathcal{O}\left(\varepsilon^4\right) \neq 0$ is not significant at this order of correction.

3.6 Fixed-flux solutions

The final step is to construct the solutions for the FF system using the relations given in (3.13). By taking the FT solutions from (3.9), the solutions for the departures from expressions (3.65)–(3.67), and substituting for $\widetilde{Ra}_t$ using equation (3.57), we obtain the FF solutions for the velocity, temperature, and vorticity as

$$w_f = w_t + \varepsilon^6 \left(\pi\widetilde{k}^3 + \frac{\pi^3}{\widetilde{k}^3}\right) \left[\left(1-2z\right)\cos\pi z - \exp\left(\frac{-\varepsilon^{-3}z}{\sqrt{2}}\right)\cos\left(\frac{\varepsilon^{-3}z}{\sqrt{2}}\right)\right], \quad (3.69)$$

$$\theta_f = \theta_t + \varepsilon^6 \frac{\pi}{\widetilde{k}^3} \exp\left(-\varepsilon^{-2}\widetilde{k}z\right) + \varepsilon^{10}\left(\pi\widetilde{k} + \frac{\pi^3}{\widetilde{k}^5}\right)\left(1-2z\right)\cos\pi z, \quad (3.70)$$

$$\zeta_f = \zeta_t + \varepsilon^2 \left(\pi\widetilde{k}^2 + \frac{\pi^3}{\widetilde{k}^4}\right) \exp\left(-\varepsilon^{-2}\widetilde{k}z\right) + \varepsilon^3 \frac{\pi}{\sqrt{2}} \left(\widetilde{k}^3 + \frac{\pi^2}{\widetilde{k}^3}\right) \exp\left(\frac{-\varepsilon^{-3}z}{\sqrt{2}}\right) \left[\sin\left(\frac{\varepsilon^{-3}z}{\sqrt{2}}\right) - \cos\left(\frac{\varepsilon^{-3}z}{\sqrt{2}}\right)\right] + \varepsilon^4 \left(\pi\widetilde{k} + \frac{\pi^3}{\widetilde{k}^5}\right)\left[\pi(2z-1)\sin\pi z - 2\cos\pi z\right], \quad (3.71)$$

where, from (3.9), and using $Ta = \varepsilon^{-12}$,

$$w_t = \sin\pi z, \qquad \theta_t = \frac{1}{\pi^2 + k^2}\sin\pi z, \qquad \zeta_t = \varepsilon^{-6}\frac{\pi}{\pi^2 + k^2}\cos\pi z. \quad (3.72)$$

To obtain an asymptotic ordering, we must also expand θ_t and ζ_t, giving

$$w_f = \sin\pi z + \varepsilon^6\left(\pi\widetilde{k}^3 + \frac{\pi^3}{\widetilde{k}^3}\right)\left[(1-2z)\cos\pi z - \exp\left(\frac{-\varepsilon^{-3}z}{\sqrt{2}}\right)\cos\left(\frac{\varepsilon^{-3}z}{\sqrt{2}}\right)\right] + \mathcal{O}\left(\varepsilon^8\right), \quad (3.73)$$

$$\theta_f = \varepsilon^4\frac{1}{\widetilde{k}^2}\sin\pi z + \varepsilon^6\frac{\pi}{\widetilde{k}^3}\exp\left(-\varepsilon^{-2}\widetilde{k}z\right) - \varepsilon^8\frac{\pi^2}{\widetilde{k}^4}\sin\pi z + \varepsilon^{10}\left(\pi\widetilde{k} + \frac{\pi^3}{\widetilde{k}^5}\right)(1-2z)\cos\pi z + \mathcal{O}\left(\varepsilon^{10}\right), \quad (3.74)$$

$$\zeta_f = \varepsilon^{-2}\frac{\pi}{\widetilde{k}^2}\cos\pi z + \varepsilon^2\left[\left(\pi\widetilde{k}^2 + \frac{\pi^3}{\widetilde{k}^4}\right)\exp\left(-\varepsilon^{-2}\widetilde{k}z\right) - \frac{\pi^3}{\widetilde{k}^4}\cos\pi z\right] + \varepsilon^3\frac{\pi}{\sqrt{2}}\left(\widetilde{k}^3 + \frac{\pi^2}{\widetilde{k}^3}\right)\exp\left(\frac{-\varepsilon^{-3}z}{\sqrt{2}}\right)\left[\sin\left(\frac{\varepsilon^{-3}z}{\sqrt{2}}\right) - \cos\left(\frac{\varepsilon^{-3}z}{\sqrt{2}}\right)\right] + \varepsilon^4\left(\pi\widetilde{k} + \frac{\pi^3}{\widetilde{k}^5}\right)\left[\pi\left(2z-1\right)\sin\pi z - 2\cos\pi z\right] + \mathcal{O}\left(\varepsilon^5\right), \quad (3.75)$$

where we have also included estimates of the error terms. The magnitudes of the error terms for w_f and ζ_f are as suggested by the numerical results in figure 3.6; we have not carried out the formal asymptotic analysis to these higher orders. By contrast, in (3.74), the error in θ_f is (strictly) $\mathcal{O}\left(\varepsilon^{10}\right)$, since, although we have retained the (dominant) $\mathcal{O}\left(\varepsilon^{10}\right)$ outer solution, we have neglected the (sub-dominant) $\mathcal{O}\left(\varepsilon^{10}\right)$ correction to the inner solution, which would be necessary for satisfaction of the boundary condition (3.8) at $\mathcal{O}\left(\varepsilon^{10}\right)$.

The marginal Rayleigh number of the FF system is given by $\widetilde{Ra}_f = \widetilde{Ra}_t + \varepsilon^6\widetilde{\mathcal{R}}$. Substituting for $\widetilde{Ra}_t$ using (3.57) and for $\widetilde{\mathcal{R}}$ using (3.64) gives the following expression for $\widetilde{Ra}_f$ as a function of the wavenumber $\widetilde{k}$:

$$\widetilde{Ra}_f = \left(\frac{\left(\widetilde{k}^2 + \varepsilon^4\pi^2\right)^3}{\widetilde{k}^2} + \frac{\pi^2}{\widetilde{k}^2}\right)\left(1 - \varepsilon^6\frac{4\pi^2}{\widetilde{k}^3}\right). \quad (3.76)$$

The critical Rayleigh number $\widetilde{Ra}_f^c$ is determined by minimising equation (3.76) with respect to $\widetilde{k}$, which leads to the following equation for $\widetilde{k}_f^c$:

$$2\left(\widetilde{k}_f^c\right)^9 + 3\pi^2\varepsilon^4\left(\widetilde{k}_f^c\right)^7 - 2\pi^2\varepsilon^6\left(\widetilde{k}_f^c\right)^6 + 6\pi^4\varepsilon^{10}\left(\widetilde{k}_f^c\right)^4 - \pi^2\left(1+\pi^4\varepsilon^{12}\right)\left(\widetilde{k}_f^c\right)^3 + 18\pi^6\varepsilon^{14}\left(\widetilde{k}_f^c\right)^2 + 10\pi^4\varepsilon^6\left(1+\pi^4\varepsilon^{12}\right) = 0. \quad (3.77)$$

Since ε occurs only in powers of ε^2, the critical wavenumber may be expressed as

$$\widetilde{k}_f^c = \widetilde{k}_0 + \widetilde{k}_2\varepsilon^2 + \widetilde{k}_4\varepsilon^4 + \widetilde{k}_6\varepsilon^6 + \widetilde{k}_8\varepsilon^8 + \mathcal{O}\left(\varepsilon^{10}\right). \quad (3.78)$$

Substituting the expansion (3.78) into (3.77) and equating terms at each order of ε gives:

$$\mathcal{O}(1): \quad 2\widetilde{k}_0^6 - \pi^2 = 0, \tag{3.79a}$$

$$\mathcal{O}(\varepsilon^2): \quad 18\widetilde{k}_0^8\widetilde{k}_2 - 3\pi^2\widetilde{k}_0\widetilde{k}_2 = 0, \tag{3.79b}$$

$$\mathcal{O}(\varepsilon^4): \quad 6\widetilde{k}_0^6\widetilde{k}_4 - \pi^2\widetilde{k}_4 + \pi^2\widetilde{k}_0^5 = 0, \tag{3.79c}$$

$$\mathcal{O}(\varepsilon^6): \quad 18\widetilde{k}_0^8\widetilde{k}_6 - 3\pi^2\widetilde{k}_0^2\widetilde{k}_6 - 2\pi^2\widetilde{k}_0^6 + 10\pi^4 = 0, \tag{3.79d}$$

$$\mathcal{O}(\varepsilon^8): \quad 6\widetilde{k}_0^7\widetilde{k}_8 - \pi^2\widetilde{k}_0\widetilde{k}_8 + 24\widetilde{k}_0^6\widetilde{k}_4^2 + 7\pi^2\widetilde{k}_0^6\widetilde{k}_4 - \pi^2\widetilde{k}_4^2 = 0. \tag{3.79e}$$

Manipulation of (3.79a)–(3.79e) yields the following expression for the FF critical wavenumber:

$$\widetilde{k}_f^c = \left(\frac{\pi^2}{2}\right)^{1/6} - \frac{1}{2}\left(\frac{\pi^2}{2}\right)^{5/6}\varepsilon^4 - 3\left(\frac{\pi^2}{2}\right)^{2/3}\varepsilon^6 + \frac{3}{8}\left(\frac{\pi^2}{2}\right)^{3/2}\varepsilon^8. \tag{3.80}$$

Substituting for $\widetilde{k}_f^c$ using (3.80) into (3.76) then gives the following expression for the FF critical Rayleigh number:

$$\widetilde{Ra}_f^c = 3\left(\frac{\pi^2}{2}\right)^{2/3} + 6\left(\frac{\pi^2}{2}\right)^{4/3}\varepsilon^4 - 24\left(\frac{\pi^2}{2}\right)^{7/6}\varepsilon^6 + 9\left(\frac{\pi^2}{2}\right)^{2}\varepsilon^8. \tag{3.81}$$

To distinguish which terms in the expansions of $\widetilde{k}_f^c$ and $\widetilde{Ra}_f^c$ originate from the FT system and which are a result of the departures from the FT system to the FF system, we compare equation (3.77) with (3.11). From this, we see that the terms $2\left(\widetilde{k}_f^c\right)^9$, $3\pi^2\varepsilon^4\left(\widetilde{k}_f^c\right)^7$ and $-\pi^2\left(1+\pi^4\varepsilon^{12}\right)\left(\widetilde{k}_f^c\right)^3$ in (3.77) originate from the FT system, while the remaining terms arise from the FF system. Therefore, the terms in both $\widetilde{k}_f^c$ and $\widetilde{Ra}_f^c$ of $\mathcal{O}(1)$, $\mathcal{O}(\varepsilon^4)$, and $\mathcal{O}(\varepsilon^8)$ stem from the FT system, whose expansion progresses in powers of ε^4. In contrast, the terms of $\mathcal{O}(\varepsilon^6)$ represent a combination of contributions from both the FT and FF systems. In (3.79d), the first and second terms originate from the FT system, while the third and fourth terms result from the FF system. An explicit expansion of equation (3.77), using (3.78), reveals that the next order corrections in the expansions of $\widetilde{k}_f^c$ and $\widetilde{Ra}_f^c$ are $\mathcal{O}(\varepsilon^{10})$, with contributions arising from both systems.

Figures 3.7(a,b) demonstrate the strong agreement between the asymptotic expressions (3.81) and (3.80) and the numerically determined values of the critical Rayleigh number $\widetilde{Ra}_f^c$ and critical wavenumber $\widetilde{k}_f^c$ of the FF system, respectively. Figures 3.7(c,d) illustrate the absolute error between the numerical and asymptotic critical values. As noted earlier, numerical validation is possible only up to $Ta \approx 10^{11}$; beyond this, resolving small-scale structures becomes challenging, as shown in figure 3.7(d). The absolute errors for $\widetilde{Ra}_f^c$ and $\widetilde{k}_f^c$ scale as $Ta^{-0.81} \approx \varepsilon^{10}$ and $Ta^{-0.82} \approx \varepsilon^{10}$, respectively, indicating that, as expected, the next term in their expansions is $\mathcal{O}(\varepsilon^{10})$.

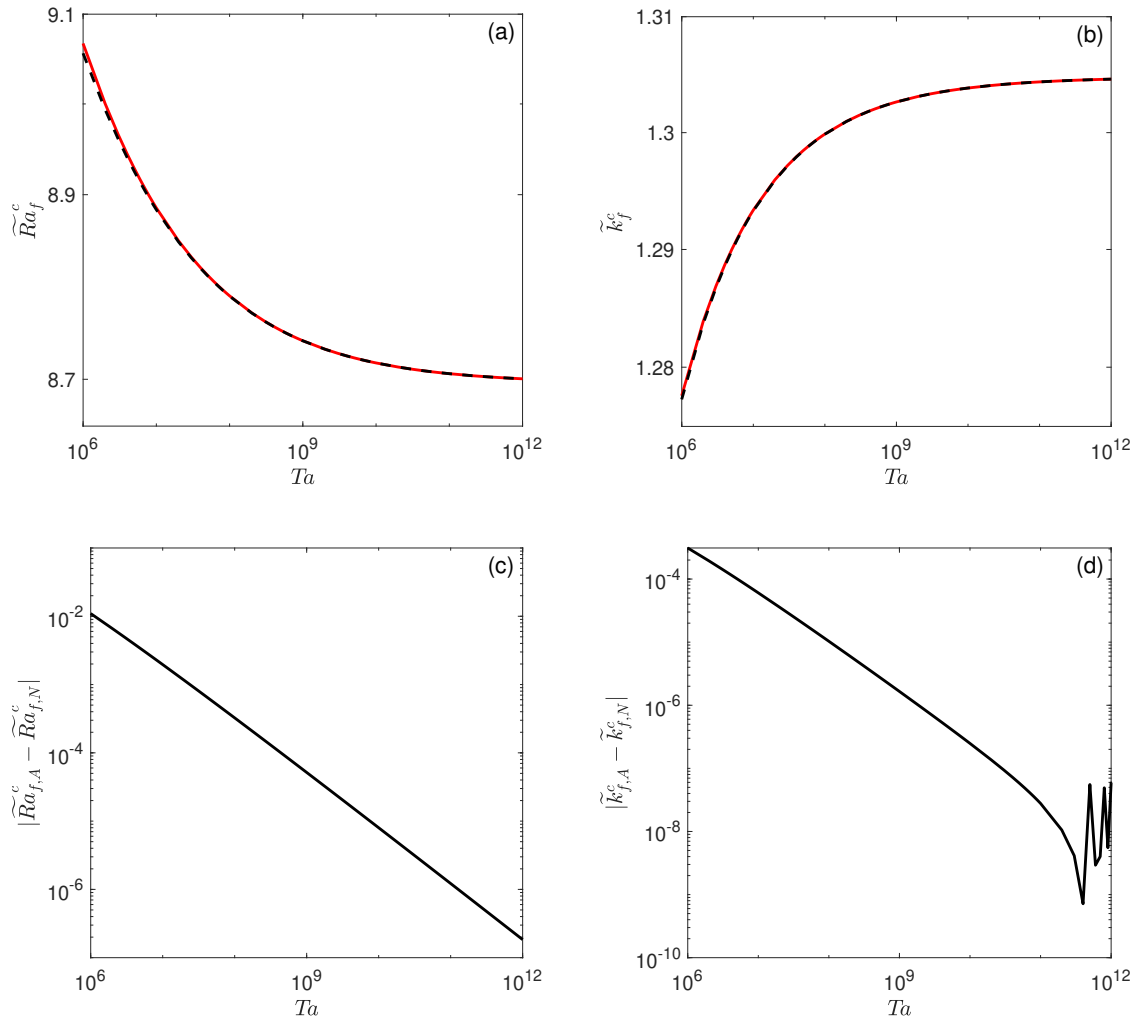


Figure 3.7: Numerical (dashed black) and asymptotic (solid red) solutions of the (a) critical Rayleigh number and (b) critical wavenumber of the fixed flux system. Asymptotic solutions of the critical Rayleigh number and wavenumber are given by expressions (3.80) and (3.81), respectively. The absolute error between the numerical (subscript N) and asymptotic (subscript A) solutions of the (c) critical Rayleigh number and (d) critical wavenumber of the fixed flux system. The absolute error exhibits gradients of approximately -0.81 with respect to the Rayleigh number and -0.82 with respect to the wavenumber.

3.7 Discussion

We have demonstrated that for linear, rapidly rotating Rayleigh–Bénard convection with impermeable, stress-free boundaries, the FF system can be approximated by combining the FT system with a small departure from the FT system. This formulation hinges on the observation that, to leading order, the interior solutions of the FF and FT systems are equivalent. At the boundaries of the FF system, an Ekman layer of thickness $Ta^{-1/4}$ develops, which, in turn, modifies the temperature profile near the bounding surfaces. To accommodate the FF boundary condition, an additional thermal boundary layer of thickness $Ta^{-1/6}$ is required. Rather than directly solving for the full FF system, we have determined asymptotic solutions for the departures from the FT system. These departures over the domain $z \in [0, 1/2]$ are governed by equations (3.25)–(3.27) (with boundary conditions given by (3.19)–(3.21)), with solutions given by (3.65)–(3.67), while the difference in the marginal Rayleigh number for a given wavenumber $\widetilde{k}$ is provided by (3.64). Finally, these asymptotic departure solutions are combined with the FT system to obtain solutions for the FF system; the final asymptotic solutions are given by expressions (3.73)–(3.75), with the corresponding critical values for the wavenumber and Rayleigh number provided in (3.80) and (3.81). The terms in (3.80) and (3.81) of $\mathcal{O}(1)$, $\mathcal{O}\left(Ta^{-1/3}\right)$, and $\mathcal{O}\left(Ta^{-2/3}\right)$ originate from the FT system, whose expansion progresses in powers of $Ta^{-1/3}$. In contrast, the $\mathcal{O}\left(Ta^{-1/2}\right)$ terms contain mixed contributions from both the FT and FF systems. The next terms in the expansions of $\widetilde{k}_f^c$ and $\widetilde{Ra}_f^c$ will appear at $\mathcal{O}\left(Ta^{-5/6}\right)$, and will also involve contributions from both systems. This is consistent with the numerical predictions. Further analysis would be required to explicitly determine the higher-order terms in the expansions of $\widetilde{Ra}_f^c$ and $\widetilde{k}_f^c$.

The asymptotic solutions are compared with numerical results obtained using MATLAB's boundary value solver `BVP5C`. While capturing finer-scale structures at large Taylor numbers is numerically challenging, solutions can still be computed at sufficiently high Taylor numbers to conclusively verify the accuracy of the asymptotic theory. It is important to note that difficulties in verifying the asymptotic solution at high Ta do not lie in the asymptotic solution itself, but rather in obtaining accurate numerical solutions to the extremely small differences between the FT and FF systems. This highlights the value of the asymptotic approach: it provides reliable insights without recourse to numerical methods, which can be inaccurate or even fail in rapidly rotating regimes.

An important progression of the work in this chapter is to investigate how the different thermal boundary conditions influence the onset of oscillatory instabilities in the rapidly rotating regime, which occur for sufficiently small Prandtl number. The approach would be similar to that pursued here, although with the added complications of dealing with complex eigenfunctions and of also determining the departure in frequency.

In the next chapter, we examine rotating Rayleigh–Bénard convection with a boundary slab of finite thermal conductivity. It is observed that, within certain parameter ranges, the system can be mod-

elled by RRBC with either FT or FF boundaries, depending on the limiting regime. For sufficiently high Taylor numbers, the limiting regimes exhibit identical behaviour because, as demonstrated in this chapter, the influence of the boundary conditions becomes negligible in the rapidly rotating limit.

Chapter 4

Rotating Convection with a Boundary Slab of Finite Conductivity

4.1 Introduction

Wilczynski and Hughes (2019), in their study of non-rotating two-layer convection, demonstrated that in the limit of a large viscosity contrast, the more viscous layer behaves effectively as a solid slab. Consequently, the dynamics of a two-layer system in this regime can be modelled by Rayleigh–Bénard convection with a boundary slab of finite conductivity. We will see in Chapter 5 that this analogy remains valid in the presence of rotation. Motivated by this analogy, we consider the rotating counterpart of the boundary slab system in this chapter. Rotating Rayleigh–Bénard convection with a boundary slab of finite conductivity (RRBC-BS) is modelled as a horizontally infinite layer of Boussinesq fluid rotating about the vertical, bounded above by a solid layer, a plane below, and subject to heating from below. Understanding the instabilities that develop in RRBC-BS will help us better understand rotating two-layer convection in the limit of a large viscosity contrast.

Nield (1968) (N68 hereafter) investigated the onset of non-rotating, stationary, linear Rayleigh–Bénard convection in a fluid layer bounded by a solid slab of finite conductivity. Nield's model comprised a horizontally infinite Boussinesq fluid layer of depth d and thermal conductivity K, bounded above by a solid layer of finite conductivity K' and thickness d', and heated from below. In this configuration, the fluid layer obeys the standard steady, linear momentum and temperature equations, while the solid layer is governed by Laplace's equation. The no-slip condition is applied at the fluid-layer boundaries, i.e., at the bottom plate and at the fluid-solid interface. The thermal boundary conditions consist of fixed-temperature at the bottom of the fluid and the top of the solid, and of continuity of temperature and heat flux at the fluid-solid interface.

N68 determined the critical Rayleigh number Ra^c and the corresponding wavenumber k^c as functions of the depth ratio d'/d and the thermal conductivity ratio K'/K. Consequently, there are four key limiting cases to consider: $K'/K \to 0$ or $K'/K \to \infty$, and $d'/d \to 0$ or $d'/d \to \infty$. We first consider the limits of the thermal conductivity ratio, which hold for all values of d'/d. As $K'/K \to \infty$, the critical Rayleigh number and critical wavenumber approach

$$Ra^c = 1707.8, \qquad k^c = 3.117. \tag{4.1}$$

These values correspond to the onset of convection in a layer bounded by rigid isothermal plates (e.g., Chandrasekhar, 1961). When K' is infinite, the boundary condition at the top of the solid instantaneously propagates through the solid to the fluid's upper surface. As $K'/K \to 0$, the critical Rayleigh number and critical wavenumber converge to

$$Ra^c = 1295.8 \qquad k^c = 2.553. \tag{4.2}$$

These values correspond to the onset of convection in a layer with one rigid, isothermal boundary and one rigid, fixed-flux boundary. In this scenario, as $K'/K \to 0$, the continuity of heat-flux condition at the fluid-solid interface transitions to a condition of zero heat-flux, rendering the solid layer a perfect insulator.

Now, let us consider the limits of the depth ratio. When $d'/d \to 0$, the critical Rayleigh number and critical wavenumber converge to the values given by (4.1), matching the results in the limit $K'/K \to \infty$. As d' approaches zero, the boundary condition at the top of the solid can promptly be transmitted through the thin solid layer to the upper surface of the fluid. In this asymptotic limit, Ra^c and k^c are independent of K'/K and are therefore given by (4.1) for all K'/K. In the limit $d'/d \to \infty$, both Ra^c and k^c decrease towards asymptotic values. However, unlike the other three limits, these asymptotic values depend on K'/K, as will be shown in §4.3.

In this chapter, we examine a model similar to that studied by N68, but with two key differences: the inclusion of rotation and a stress-free condition at the lower fluid boundary, rather than the rigid condition used by Nield. Specifically, we consider the RRBC-BS system with a stress-free condition at the lower fluid boundary and a no-slip condition at the fluid-solid interface. The thermal boundary conditions consist of fixed-temperature at the bottom of the fluid and the top of the solid, and continuity of temperature and heat flux at the fluid-solid interface. Imposing these boundary conditions enables direct comparison with the rotating two-layer system in Chapter 5.

A linear stability analysis of the RRBC-BS system is presented in §4.2. This yields a solution for the temperature perturbation within the solid and a well-defined set of governing equations for the variables in the fluid layer. The onset of instabilities in the non-rotating configuration is examined and compared with the results of N68 in §4.3. The onset of instabilities in a rotating system is explored in §4.4. Owing to the inclusion of rotational effects, oscillatory instabilities can emerge at onset. Finally, concluding remarks are given in §4.5.

4.2 Mathematical formulation

4.2.1 Governing equations

We consider an infinite horizontal layer of Boussinesq fluid of depth d, bounded below by a plane and above by a solid layer of thickness d' and finite conductivity K'. The solid layer is characterised by $K' = \rho_0 c_v \kappa'$, where κ' is the thermal diffusivity (primes denote variables in the solid layer). We assume the reference density ρ_0 and specific heat capacity at constant volume c_v are identical in both layers. The system is heated from below. The system rotates with angular velocity $\boldsymbol{\Omega} = \Omega\hat{\boldsymbol{z}}$, where $\hat{\boldsymbol{z}}$ is the unit vector in the vertical direction. The acceleration due to gravity is $\boldsymbol{g} = -g\hat{\boldsymbol{z}}$. Each layer has distinct properties. The fluid layer is characterised by the thermal expansion coefficient α, kinematic viscosity ν, thermal conductivity K, and thermal diffusivity κ. The interface is fixed at $z = 0$. The fluid occupies the region $-d < z < 0$ and the solid occupies the region $0 < z < d' = \delta d$, where δ represents the depth ratio. The planes $z = -d$ and $z = d'$ are held at uniform temperatures T_b and T_u, respectively, with $T_b > T_u$. A sketch of the configuration is shown in figure 4.1.

The basic state is hydrostatic and characterised by a piecewise linear temperature profile in z:

$$T' = T_u - \beta' \left(z - d'\right), \qquad 0 \le z \le d', \tag{4.3}$$

$$T = T_b - \beta \left(z + d\right), \qquad -d \le z < 0, \tag{4.4}$$

where β and β' are the adverse temperature gradients in the fluid and the solid (see §2.4 for a detailed derivation of the basic state solutions). Continuity of temperature and heat-flux at the fluid-solid interface requires that

$$\beta = \frac{K'\left(T_b - T_u\right)}{Kd' + K'd}, \qquad \beta' = \frac{K\left(T_b - T_u\right)}{Kd' + K'd}. \tag{4.5}$$

Thus, the overall temperature difference is divided between the two layers, with the drop across each determined by the thermal conductivities and depths of both layers.

Under the Boussinesq approximation, the fluid layer is governed by the incompressibility condition (2.21), the momentum equation (2.23), and the temperature equation (2.25), which together form the system governing rotating Rayleigh–Bénard convection (RRBC) (see Chapter 2). A small perturbation to the basic hydrostatic state yields the perturbation equations (2.30) and (2.31). The perturbation equations are expressed in dimensionless form by scaling variables with the thermal and mechanical properties of the lower fluid layer: scaling length with d, time with d^2/κ, pressure with $\rho_0 \left(\kappa/d\right)^2$, velocity with κ/d and temperature with βd. Furthermore, since it is convenient to express the system in terms of the vertical velocities w, vertical vorticities ζ and temperatures θ, the pressure and horizontal velocity components are eliminated by the standard procedure of applying the operators $\hat{\boldsymbol{z}} \cdot \nabla\times$ and $\hat{\boldsymbol{z}} \cdot \nabla \times \nabla\times$. The dimensionless equations governing linear perturbations from the

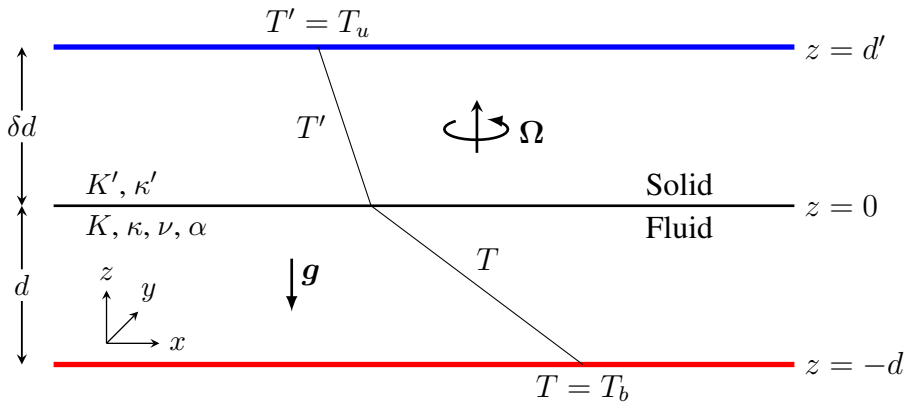


Figure 4.1: Schematic sketch of rotating Rayleigh–Bénard convection with a boundary slab of finite conductivity.

basic state in $-1 \leq z \leq 0$ may then be written as

$$\frac{\partial \theta}{\partial t} = w + \nabla^2 \theta, \tag{4.6}$$

$$\frac{\partial \zeta}{\partial t} - Pr\nabla^2 \zeta = PrTa^{1/2}\frac{\partial w}{\partial z}, \tag{4.7}$$

$$\frac{\partial}{\partial t}\nabla^2 w - Pr\nabla^4 w = -PrTa^{1/2}\frac{\partial \zeta}{\partial z} + RaPr\nabla_H^2 \theta, \tag{4.8}$$

where the horizontal Laplacian is defined by $\nabla_H^2 = \partial_x^2 + \partial_y^2$. The dimensionless parameters of the system, the Rayleigh number, Prandtl number and Taylor number, are defined as

$$Ra = \frac{g\alpha\beta d^4}{\nu\kappa}, \qquad Pr = \frac{\nu}{\kappa}, \qquad Ta = \frac{4\Omega^2 d^4}{\nu^2}. \tag{4.9}$$

In the solid layer, $0 \leq z \leq \delta$, fluid motion is absent, and heat transfer is described entirely by the dimensionless temperature equation:

$$\frac{\partial \theta'}{\partial t} = \frac{\kappa'}{\kappa}\nabla^2 \theta'. \tag{4.10}$$

The lower fluid boundary is assumed to be stress-free, and the upper fluid boundary is assumed to be no-slip. The thermal boundary conditions consist of fixed-temperature at the bottom of the fluid and the top of the solid, and continuity of temperature and heat flux at the fluid-solid interface. Thus,

$$w = \frac{\partial^2 w}{\partial z^2} = \frac{\partial \zeta}{\partial z} = \theta = 0 \qquad \text{at} \qquad z = -1, \tag{4.11}$$

$$w = \frac{\partial w}{\partial z} = \zeta = 0, \quad \theta = \theta', \quad K\frac{\partial \theta}{\partial z} = K'\frac{\partial \theta'}{\partial z} \qquad \text{at} \qquad z = 0, \tag{4.12}$$

$$\theta' = 0 \qquad \text{at} \qquad z = \delta. \tag{4.13}$$

4.2.2 Linear stability analysis

We seek solutions to (4.6)–(4.8) and (4.10) of the form

$$w = \hat{w}(z) f(x,y) e^{st}, \qquad \theta = \hat{\theta}(z) f(x,y) e^{st},$$
$$\zeta = \hat{\zeta}(z) f(x,y) e^{st}, \qquad \theta' = \hat{\theta}'(z) f(x,y) e^{st}, \tag{4.14}$$

where $s = \sigma + i\omega$ is the complex growth rate, with $\sigma, \omega \in \mathbb{R}$, and $f(x,y)$ is a planform function satisfying $\nabla_H^2 f = -k^2 f$, where k is the horizontal wavenumber. Substituting the ansatz (4.14) into (4.6)–(4.8) and (4.10), and dropping the hats gives the following system in $-1 \le z \le 0$,

$$\left(\mathcal{D}^2 - k^2 - s\right)\theta = -w, \tag{4.15}$$

$$\left(\mathcal{D}^2 - k^2 - \frac{s}{Pr}\right)\zeta = -Ta^{1/2}\mathcal{D}w, \tag{4.16}$$

$$\left(\mathcal{D}^2 - k^2\right)\left(\mathcal{D}^2 - k^2 - \frac{s}{Pr}\right)w = Ta^{1/2}\mathcal{D}\zeta + k^2 Ra\theta, \tag{4.17}$$

while in $0 \le z \le \delta$,

$$\left(\mathcal{D}^2 - k^2 - \frac{s}{K_r}\right)\theta' = 0, \tag{4.18}$$

where $\mathcal{D} \equiv \mathrm{d}/\mathrm{d}z$ and

$$K_r = \frac{K'}{K}, \tag{4.19}$$

is the thermal conductivity ratio. As ρ_0 and c_v are assumed identical within each layer, $K'/K = \kappa'/\kappa$. The boundary and interface conditions (4.11)–(4.13) may be written as

$$w = \mathcal{D}^2 w = \mathcal{D}\zeta = \theta = 0 \qquad \text{at} \qquad z = -1, \tag{4.20}$$

$$w = \mathcal{D}w = \zeta = 0, \quad \theta = \theta', \quad \mathcal{D}\theta = K_r \mathcal{D}\theta' \qquad \text{at} \qquad z = 0, \tag{4.21}$$

$$\theta' = 0 \qquad \text{at} \qquad z = \delta. \tag{4.22}$$

4.3 Onset of non-rotating convection

In the absence of rotation, the principle of exchange of stabilities (see §2.8.1.1) implies that instabilities occur when the growth rate passes strictly through zero. Thus, setting $Ta = 0$ and $s = 0$, (4.15)–(4.18) reduce to

$$\left(\mathcal{D}^2 - k^2\right)\theta = -w, \tag{4.23}$$

$$\left(\mathcal{D}^2 - k^2\right)^2 w = k^2 Ra\theta \tag{4.24}$$

in $-1 \le z \le 0$, and

$$\left(\mathcal{D}^2 - k^2\right)\theta' = 0 \tag{4.25}$$

in $0 \leq z \leq \delta$. Equations (4.23)–(4.25) are identical to those studied by N68. However, Nield imposes a no-slip condition at the fluid's lower boundary rather than a stress-free condition, as we do here.

Equation (4.25) with boundary condition (4.22) has the solution

$$\theta' = C \sinh\left(k\left(\delta - z\right)\right), \tag{4.26}$$

where C is a constant. A simplified interface condition is obtained on substituting for θ' from (4.26) into (4.21), yielding

$$\mathcal{D}\theta = L\theta \qquad \text{at} \qquad z = 0, \tag{4.27}$$

where,

$$L = -K_r k \coth\left(\delta k\right) \tag{4.28}$$

is the heat transfer parameter. This reduces the problem to the set of equations (4.23) and (4.24) subject to boundary conditions

$$w = \mathcal{D}^2 w = \theta = 0 \qquad \text{at} \qquad z = -1, \tag{4.29}$$

$$w = \mathcal{D}w = 0, \quad \mathcal{D}\theta = L\theta \qquad \text{at} \qquad z = 0. \tag{4.30}$$

The thermal interface condition (4.30) depends on the heat transfer parameter (4.28), which depends on K_r, δ, and k. Therefore, we analyse how the critical modes depend on K_r and δ.

Equations (4.23) and (4.24), subject to boundary conditions (4.29) and (4.30), are solved numerically using MATLAB's boundary value solver `BVP5C`, yielding the eigenfunctions w and θ and critical values Ra^c and k^c, as described in §3.2. The analytical solution for θ' is given in (4.26). The constant C is determined by applying the interface condition $\theta = \theta'$ at $z = 0$, yielding $C = \theta\left(0\right) \operatorname{csch}\left(\delta k\right)$ for given k and δ. Therefore, the temperature within the solid ($0 \leq z \leq \delta$) is given by

$$\theta' = \theta\left(0\right) \operatorname{csch}\left(\delta k\right) \sinh\left(k\left(\delta - z\right)\right), \tag{4.31}$$

where $\theta\left(0\right)$ is computed numerically through the MATLAB routine `BVP5C`.

We begin by considering the case of equal layer depths, i.e., $\delta = 1$, and examine how variations in the thermal conductivity ratio K_r affect the system. Figure 4.2 shows how the critical Rayleigh number Ra^c and wavenumber k^c vary with K_r for the system considered here and the one studied by N68, which differs only in the mechanical condition imposed at the lower fluid boundary: no-slip in N68 and stress-free in our case. The dependence of Ra^c and k^c on K_r is qualitatively similar. In both systems, Ra^c and k^c exhibit the same monotonic behaviour with K_r. However, the system studied by N68 yields higher critical values (given explicitly in (4.1) and (4.2) for the asymptotic limits of K_r) due to the presence of a no-slip condition on the lower fluid boundary. The critical Rayleigh number depends on how strongly the boundaries damp motion through viscosity. No-slip conditions

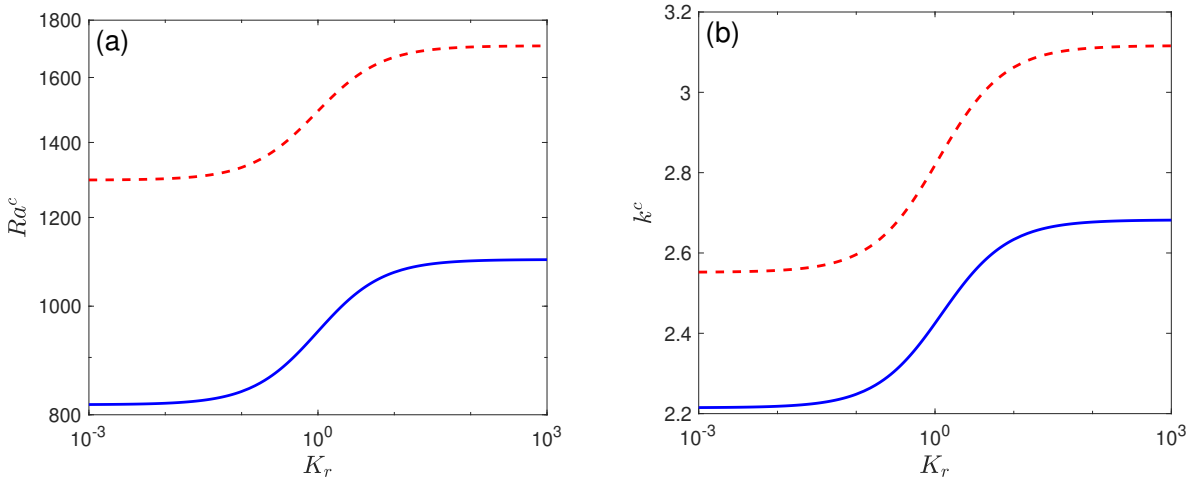


Figure 4.2: Variations of the critical (a) Rayleigh number Ra^c and (b) wavenumber k^c as functions of the thermal conductivity ratio K_r, with $Ta = 0$ and $\delta = 1$, for the system considered here (blue solid) and the one studied by Nield (1968) (red dashed), differing only in the mechanical condition imposed at the lower fluid boundary: no-slip in Nield (1968), and stress-free in our case.

force the velocity to zero at the boundaries, creating steeper gradients and strong viscous dissipation. As a result, convection sets in at a higher critical Rayleigh number. In contrast, stress-free conditions eliminate shear stresses at the boundaries, reducing viscous damping and lowering the onset threshold. A mixed case lies in between the two (Kuo and Chen, 2009). Thus, the more restrictive the velocity boundary conditions, the greater the viscous resistance to motion, and the higher the Rayleigh number needed to overcome it (Drazin and Reid, 2004).

Consider the system with stress-free conditions at the lower fluid boundary. When $K_r = 1$, convection cells span the fluid domain, while temperature perturbations extend into both the fluid and solid layers. As K_r varies, convection cells continue to fill the fluid layer, whereas temperature perturbations enter the solid layer only for certain values of K_r. As K_r increases from one, there is a sharp increase in Ra^c and k^c, indicating a shift in the preferred horizontal length scale towards smaller cells. As $K_r \to \infty$, the critical Rayleigh number and wavenumber increase to the asymptotic values:

$$Ra^c = 1100.34, \qquad k^c = 2.68. \tag{4.32}$$

These values correspond to the onset of convection in a layer bounded by fixed-temperature conditions, with one stress-free and one no-slip boundary (e.g., Chandrasekhar, 1961). When K' is infinite, the conditions at the top of the solid are transmitted immediately through the solid to the fluid-solid interface. Convection cells and temperature perturbations are confined to the fluid layer, as shown in figure 4.3. In contrast, as $K_r \to 0$, the critical Rayleigh number and wavenumber decrease, indicating a shift in the preferred horizontal length scale towards larger cells, approaching the asymptotic values:

$$Ra^c = 816.99, \qquad k^c = 2.22. \tag{4.33}$$

These values correspond to the onset of convection between a stress-free, fixed-temperature boundary and a no-slip, fixed-flux boundary. As $K_r \to 0$, the interface becomes perfectly insulating. Convection cells fill the fluid layer, while temperature perturbations extend into the solid, as shown in figure 4.4.

We will now consider the case of equal thermal conductivities, i.e., $K_r = 1$, and examine the effect of the depth ratio δ. Figure 4.5 shows how the critical Rayleigh number Ra^c and wavenumber k^c vary with δ for the system considered here and the one studied by N68. In a similar manner to the previous case, when K_r is varied with fixed $\delta = 1$, the dependence of Ra^c and k^c on δ is qualitatively similar. Furthermore, Ra^c and k^c exhibit the same monotonic behaviour with δ in both systems. The system studied by N68 yields higher critical values, which is similarly caused by the no-slip condition on the lower boundary.

Consider the system under stress-free conditions at the lower fluid boundary. As δ decreases from one, Ra^c and k^c increase sharply, indicating a shift in the preferred horizontal length scale towards smaller cells. As $\delta \to 0$, Ra^c and k^c gradually approach the asymptotic values given in (4.32), analogous to the results in the limit $K_r \to \infty$ with $\delta = 1$. This outcome is logically consistent. As the depth of the solid layer approaches zero, the boundary condition at the top of the solid is rapidly transmitted through the thin solid layer to the fluid's upper surface. The system therefore behaves as a single-layer convection system. Notably, from figure 4.5, Ra^c and k^c enter the $\delta \to 0$ regime at $\delta \approx 10^{-2}$. At this value, the heat transfer parameter L, defined in (4.28), is sufficiently large that the interface condition $\mathcal{D}\theta = L\theta$ behaves as a fixed-temperature condition.

As δ increases from one, the critical Rayleigh number and wavenumber decrease, indicating a shift in the preferred horizontal length scale towards larger cells, approaching the asymptotic values:

$$Ra^c = 948.379, \qquad k^c = 2.417. \tag{4.34}$$

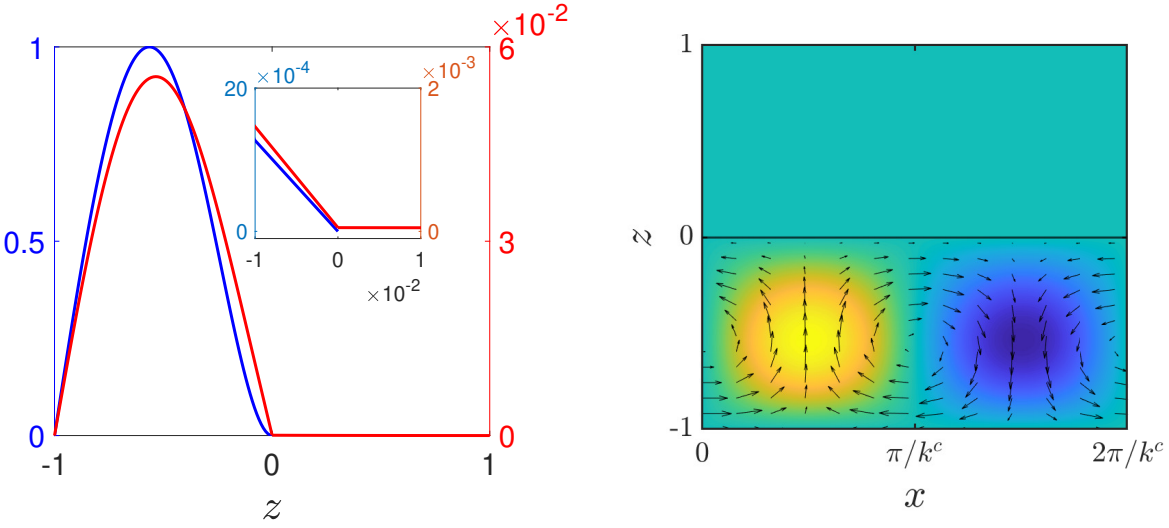
For sufficiently large δ, $\coth(\delta k) \to 1$. Thus, the heat transfer parameter in (4.28) reduces to $L = -K_r k$. Consequently, the asymptotic values in (4.34) correspond to the onset of convection in a layer bounded by one stress-free, fixed-temperature boundary and one no-slip boundary with a thermal Robin condition: $\mathcal{D}\theta = -k\theta$ (with $K_r = 1$). In fact, because $\coth(\delta k)$ rapidly approaches one when $\delta k > 1$, the system reaches the large depth ratio regime by $\delta \approx 2$. In this regime, convection cells span the fluid layer, while temperature perturbations extend across both the fluid and solid layers, as shown in figure 4.6 for $\delta = 2$. The temperature in the solid, given in (4.31), can be expressed as

$$\theta' = \theta(0)\left(\cosh(kz) - \coth(k\delta)\sinh(kz)\right). \tag{4.35}$$

Since $\coth(k\delta)$ rapidly approaches one, even for moderate values of δ, (4.35) reduces, for $\delta \gtrsim 2$, to

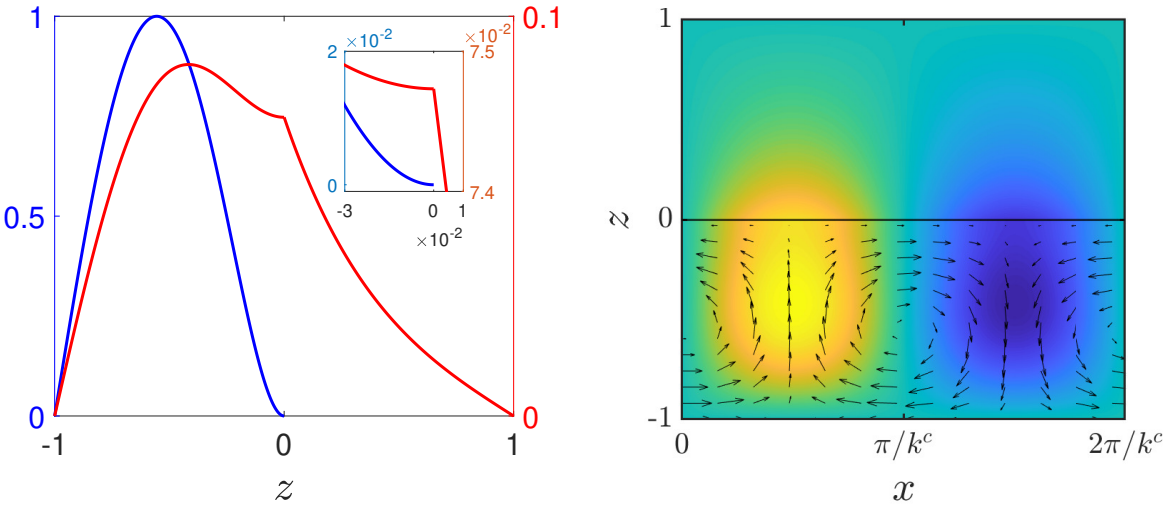
$$\theta' = \theta(0)\exp(-kz), \tag{4.36}$$

eliminating any dependence on δ. With k given in (4.34), the resulting profile is identical across $0 \le z \le 2$ for all $\delta > 2$. Thus, figure 4.6 represents the critical modes for all $\delta > 2$ with $K_r = 1$.



(a) (b)

Figure 4.3: Critical mode for $K_r = 10^3$ with $Ta = 0$ and $\delta = 1$, corresponding to $k^c = 2.68$ and $Ra^c = 1100.34$. The eigenfunctions are normalised such that $\max(w) = 1$. (a) Profiles of the eigenfunctions: vertical velocity w (blue) and temperature perturbation θ in the fluid and θ' in the solid (red); (b) temperature contours and velocity vector field in the x–z plane.



(a) (b)

Figure 4.4: Same as figure 4.3 for $K_r = 10^{-3}$ with $Ta = 0$ and $\delta = 1$, corresponding to $k^c = 2.22$ and $Ra^c = 816.99$.

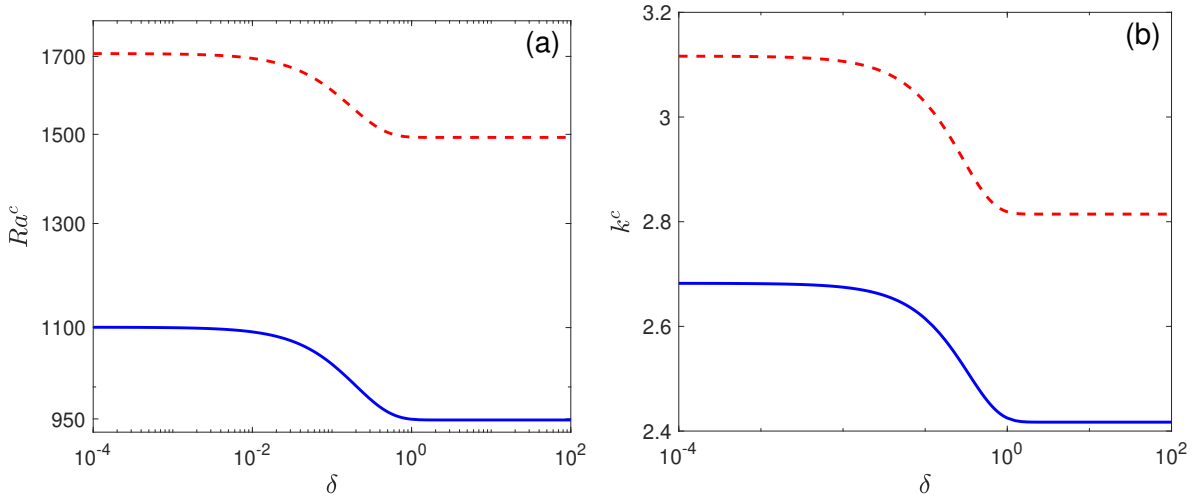
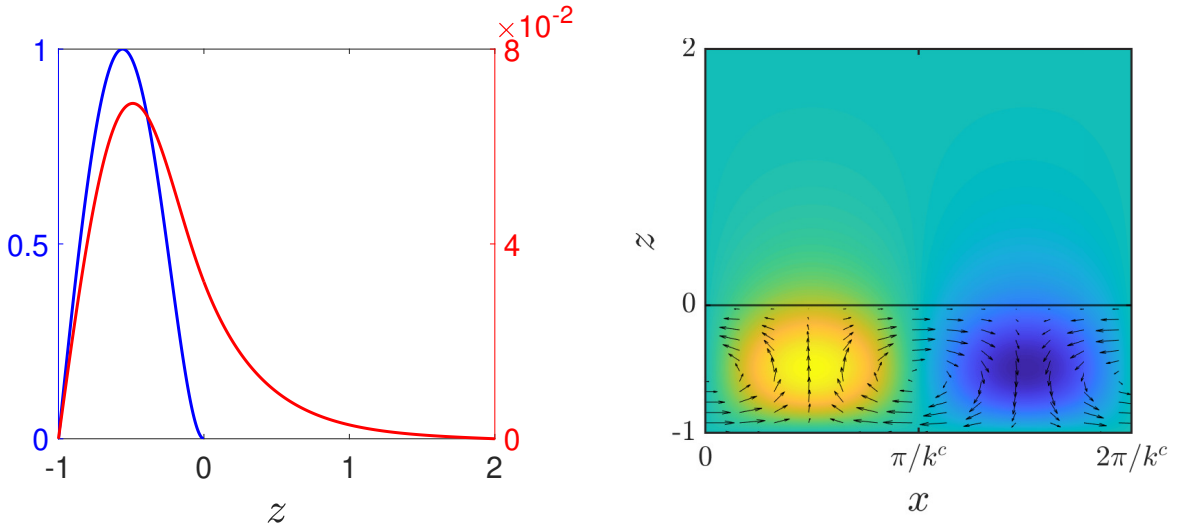
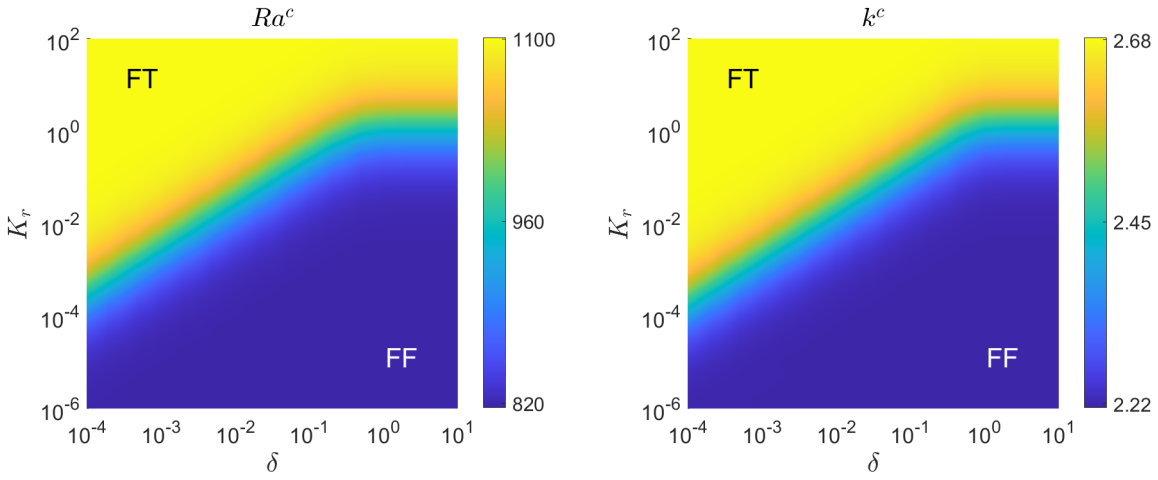


Figure 4.5: Variations of the critical (a) Rayleigh number Ra^c and (b) wavenumber k^c as functions of the layer depth ratio δ, with $Ta = 0$ and $K_r = 1$, for the system considered here (blue solid) and the one studied by Nield (1968) (red dashed), differing only in the mechanical condition imposed at the lower fluid boundary: no-slip in Nield (1968), and stress-free in our case.



(a) (b)

Figure 4.6: Same as figure 4.3 for $\delta = 2$ with $Ta = 0$ and $K_r = 1$, corresponding to $k^c = 2.42$ and $Ra^c = 948.38$.



(a) (b)

Figure 4.7: Colour map of the critical (a) Rayleigh number Ra^c and (b) wavenumber k^c as functions of the depth ratio δ and thermal conductivity ratio K_r, with $Ta = 0$. The colour scales represent the magnitudes of Ra^c and k^c, with warmer colours indicating higher values.

Figure 4.7 shows how the critical Rayleigh number Ra^c and critical wavenumber k^c vary with the depth ratio δ and thermal conductivity ratio K_r. The dependence of Ra^c and k^c on K_r and δ is qualitatively similar. The asymptotic behaviour of K_r identified when $\delta = 1$ persists for all δ. In particular, as $K_r \to 0$ ($K_r \to \infty$), the critical Rayleigh number and associated critical wavenumber approach the critical values observed for RRBC bounded by one stress-free, fixed-temperature plate and one no-slip, fixed-flux (fixed-temperature) plate, for all δ. In contrast, the asymptotic behaviour of δ depends on K_r. For $K_r < \mathcal{O}\left(10^{-4}\right)$, the thermal interface condition behaves as a fixed-flux condition across the range of δ considered here: $10^{-4} \leq \delta \leq 10$. For $K_r > \mathcal{O}(1)$, it behaves as a fixed-temperature condition over the same range of δ. Between these limits, for $\mathcal{O}\left(10^{-4}\right) < K_r < \mathcal{O}(1)$, a transition occurs between the two boundary regimes. For $\delta > \mathcal{O}(1)$ the transition remains fixed at $K_r \sim \mathcal{O}(1)$. Consider the heat transfer parameter L given in (4.28). Since $\coth(\delta k)$ rapidly approaches one for $\delta k > 1$, and $k \equiv k^c \sim \mathcal{O}(1)$, L becomes independent of δ for values only modestly above one, reducing to $L = -K_r k$. Consequently, L, and thus the thermal interface condition, depend solely on K_r for $\delta > \mathcal{O}(1)$. In the opposite limit, as δ decreases from $\delta \sim \mathcal{O}(1)$ to $\delta = 10^{-4}$, the transition between the two boundary regimes smoothly shifts to lower values of K_r, from $K_r \sim \mathcal{O}(1)$ to $K_r \sim \mathcal{O}\left(10^{-4}\right)$. This occurs because, when δ is small, a smaller K_r suffices for L to be large enough that the thermal interface condition effectively behaves as a fixed-temperature condition. Consequently, the transition between the two asymptotic limits takes place at a lower K_r when δ is small.

4.4 Onset of rotating convection

4.4.1 Steady modes of instability

We now return to the problem governed by equations (4.15)–(4.18) and boundary conditions (4.20)–(4.22). When convection manifests as a steady mode, the system's marginal state is characterised by $s = 0$. Substituting $s = 0$ into (4.15)–(4.17), which govern the fluid motion in the lower layer, yields

$$\left(\mathcal{D}^2 - k^2\right)\theta = -w, \tag{4.37}$$

$$\left(\mathcal{D}^2 - k^2\right)\zeta = -Ta^{1/2}\mathcal{D}w, \tag{4.38}$$

$$\left(\mathcal{D}^2 - k^2\right)^2 w = Ta^{1/2}\mathcal{D}\zeta + k^2 Ra\theta. \tag{4.39}$$

As in the non-rotating system discussed in §4.3, θ' satisfies equation (4.25), with the solution given in (4.31). The thermal interface conditions (4.21) simplify to (4.27). This reduces the problem to the set of equations (4.37)–(4.39) subject to the boundary conditions

$$w = \mathcal{D}w = \zeta = 0, \quad \mathcal{D}\theta = L\theta \qquad \text{at} \qquad z = 0, \tag{4.40}$$

$$w = \mathcal{D}^2 w = \mathcal{D}\zeta = \theta = 0 \qquad \text{at} \qquad z = -1, \tag{4.41}$$

where L is the heat transfer parameter defined in (4.28).

As in the non-rotating system, the behaviour of the thermal interface condition (4.40) is determined by L, which depends on K_r, δ, and k. Having previously investigated how critical modes vary with K_r and δ in the absence of rotation (see §4.3), our objective now is to examine how the critical modes vary with the Taylor number.

We begin with equal layer depths and examine the effects of varying the thermal conductivity ratio K_r and the Taylor number Ta. Figure 4.8 shows how the critical Rayleigh number Ra^c and the corresponding critical wavenumber k^c vary with K_r for $Ta = 0$ and $Ta = 10^{14}$ with $\delta = 1$. An initial observation is that Ra^c and k^c exhibit the same monotonic behaviour for both Taylor numbers. This trend persists across rotational strengths from $Ta = 0$ to $Ta = 10^{14}$. For all values of Ta, as K_r approaches either zero or infinity, Ra^c and k^c converge to distinct asymptotic values. The asymptotic behaviour of K_r identified in the non-rotating system (§4.3) persists when rotation is introduced. In particular, as $K_r \to 0$ ($K_r \to \infty$), the critical Rayleigh number and associated critical wavenumber approach the critical values observed for RRBC bounded by one stress-free, fixed-temperature plate and one no-slip, fixed-flux (fixed-temperature) plate.

Figure 4.9 shows the critical Rayleigh number Ra^c and the corresponding critical wavenumber k^c as functions of the thermal conductivity ratio K_r for different Taylor numbers, with $\delta = 1$. Each quantity is normalised by its corresponding critical value for RRBC with fixed-temperature boundaries, where one boundary is stress-free and the other is no-slip, denoted by Ra^c_* and k^c_*. For a fixed

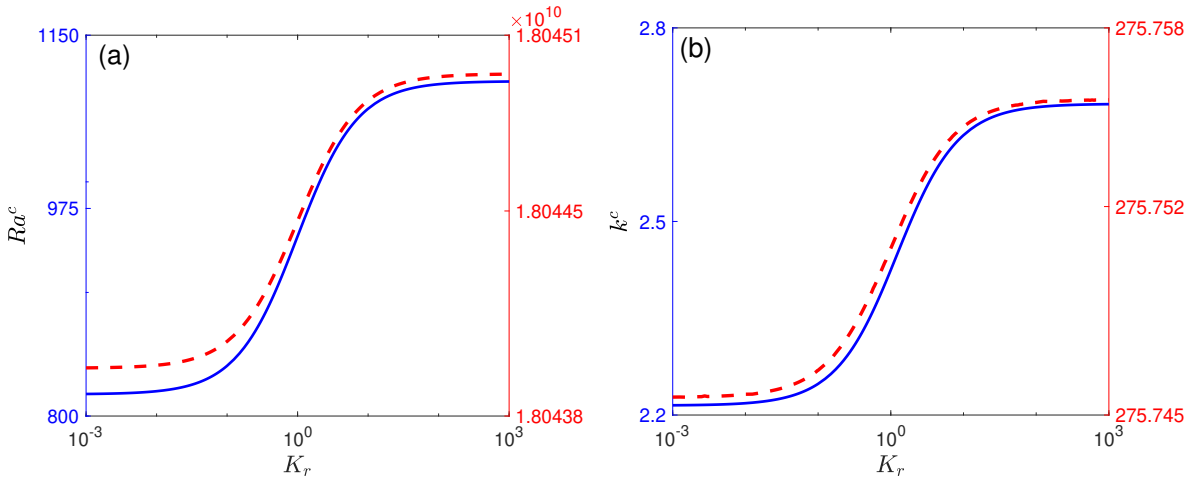


Figure 4.8: Variations of the critical (a) Rayleigh number Ra^c and (b) wavenumber k^c as functions of the thermal conductivity ratio K_r, for $Ta = 0$ (blue solid) and $Ta = 10^{14}$ (red dashed), with $\delta = 1$.

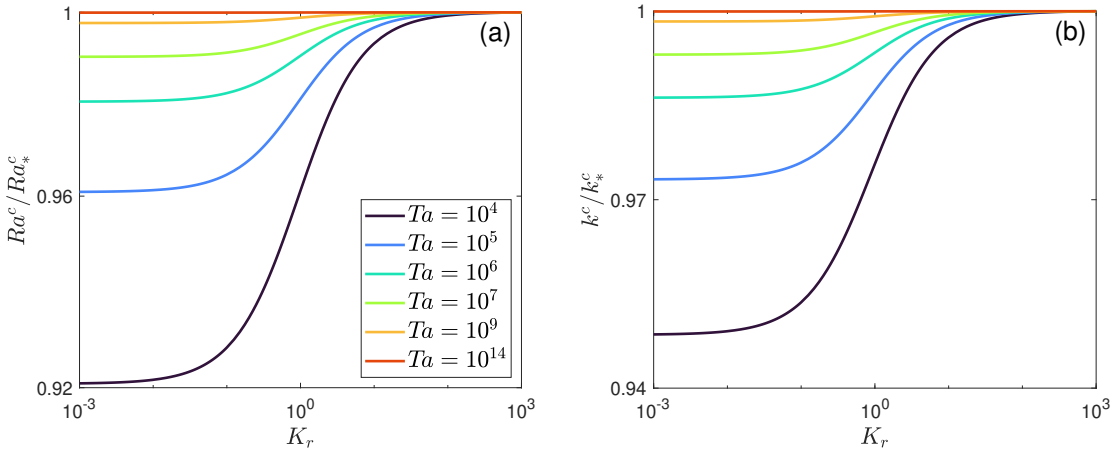


Figure 4.9: Variations of the critical (a) Rayleigh number Ra^c and (b) wavenumber k^c as functions of the thermal conductivity ratio K_r, for different Taylor numbers, with $\delta = 1$. Each quantity is normalised by its corresponding critical value for RRBC with fixed-temperature boundaries, where one boundary is stress-free and the other is no-slip, denoted by Ra^c_*, and k^c_*. The legend in (a) applies to (b).

Ta, as $K_r \to \infty$, the ratios Ra^c/Ra_*^c and k^c/k_*^c tend to one. This is expected, since $Ra^c \to Ra_*^c$ and $k^c \to k_*^c$ as $K_r \to \infty$. In contrast, as $K_r \to 0$, the ratios Ra^c/Ra_*^c and k^c/k_*^c tend to an asymptotic value that increases towards one with increasing Ta. This behaviour is expected, as discussed in Chapter 3, because the influence of the thermal boundary condition diminishes at sufficiently high Taylor numbers, where the dynamics are dominated by the bulk rather than the boundary conditions.

Figure 4.10 presents the velocity and temperature profiles of the critical mode for $Ta = 0$ and $Ta = 10^{14}$ at $K_r = 10^{-3}$ and $K_r = 10^3$, with $\delta = 1$. Figure 4.10(d) shows that, at the limits of K_r for both $Ta = 0$ and $Ta = 10^{14}$, the expected boundary conditions are recovered. In particular, the thermal condition at the fluid-solid interface behaves as fixed-flux in the limit $K_r \to 0$ and as fixed-temperature in the limit $K_r \to \infty$. Figure 4.10(a) indicates that, qualitatively, the velocity profiles at $K_r = 10^{-3}$ and $K_r = 10^3$ are similar for both $Ta = 0$ and $Ta = 10^{14}$. The maximum absolute difference between these profiles over the z-domain occurs near the fluid-solid interface. This difference decreases with increasing Ta and scales approximately as $Ta^{-1/3}$ (determined empirically), indicating that the velocity profiles converge at higher rotation rates.

At sufficiently large Taylor numbers, an Ekman boundary layer forms near the fluid-solid interface, scaling as $Ta^{-1/4}$, as shown in figure 4.10(b) for $Ta = 10^{14}$. This boundary layer arises from a balance between the viscous and Coriolis terms, allowing the no-slip condition to be satisfied while adjusting the interior flow to match the rotational constraints (Greenspan, 1968). Furthermore, when the boundary conditions are identical at both boundaries, w is symmetric about the midpoint of the domain, with $\max(w)$ occurring at $z = -0.5$. In the present case, however, the boundary conditions are asymmetric. For $Ta = 0$ and $K_r = 10^3$, $\max(w)$ occurs at $z = -0.56$. At large Taylor numbers, the position of the maximum shifts closer to the centre of the domain, e.g., when $Ta = 10^{14}$, $\max(w)$ occurs at $z = -0.48$. As discussed in Chapter 3, the influence of the boundary conditions becomes minimal in the rapidly rotating limit. Thus, as Ta increases, the asymmetric thermal boundary conditions have less influence on the bulk of the solutions, leading to a more symmetric velocity profile. This is confirmed by the red dashed line in figure 4.10(a) not being visible.

Figure 4.10(c) shows that, qualitatively, the temperature profiles at $K_r = 10^{-3}$ and $K_r = 10^3$ are similar for $Ta = 10^{14}$ but differ significantly for $Ta = 0$. The maximum absolute difference between these profiles over the z-domain occurs at the fluid-solid interface. This difference decreases with increasing Ta and scales approximately as $Ta^{-2/5}$ (determined empirically), indicating that the temperature profiles converge at higher rotation rates. At $Ta = 0$, the temperature perturbation with $K_r = 10^3$ is confined to the solid layer (figure 4.3), whereas for $K_r = 10^{-3}$ it spans both the fluid and solid layers (figure 4.4). With increasing Ta, the temperature perturbation with $K_r = 10^{-3}$ progressively retreats from the solid until it is restricted to the fluid layer. Recall that θ' is given by (4.35). As $k^c \sim Ta^{1/6}$, $\coth(k)$ rapidly approaches one for sufficiently large Ta, and θ' reduces to (4.36). Consequently, as Ta increases, θ' takes an exponential form with a large exponent, becoming

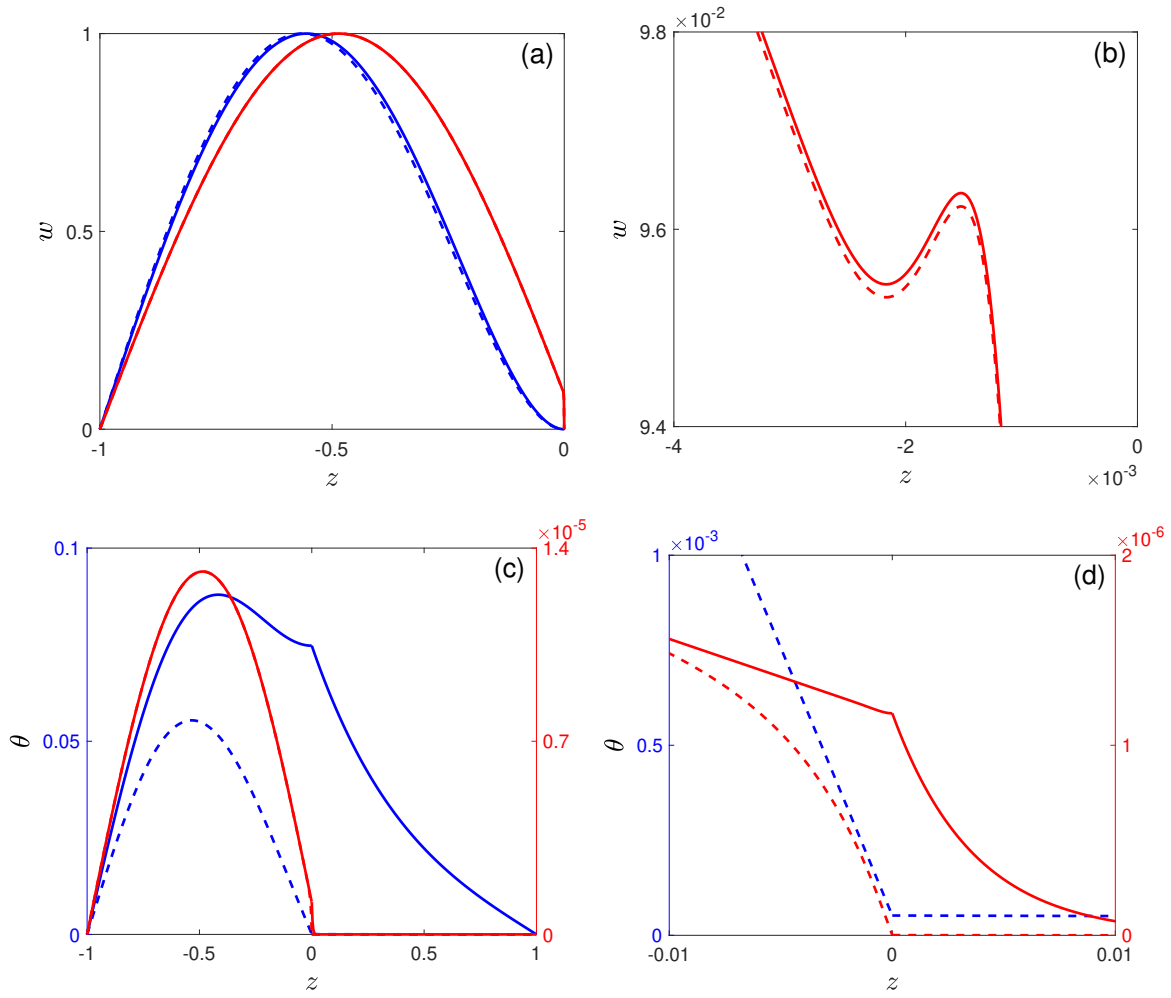


Figure 4.10: Velocity profiles (top row) and temperature profiles (bottom row) of the critical modes for $Ta = 0$ (blue), and $Ta = 10^{14}$ (red), at $K_r = 10^{-3}$ (solid) and $K_r = 10^{3}$ (dashed), with $\delta = 1$. The solutions are normalised such that max $(w) = 1$. The left column shows the profiles across the entire two-layer domain. The right column provides magnified views of the boundary layers near the solid-fluid interface at $z = 0$. The vertical range of w is restricted to $-4 \times 10^{-3} \leq z \leq -10^{-3}$ to highlight the shape of the boundary layer, while the vertical range of θ is restricted to $-0.01 \leq z \leq 0.01$. The corresponding critical wavenumbers and critical Rayleigh numbers are: (1) $Ta = 0$ and $K_r = 10^{-3}$: $k^c = 2.2$, $Ra^c = 817$; (2) $Ta = 0$ and $K_r = 10^{3}$: $k^c = 2.7$, $Ra^c = 1100.3$; (3) $Ta = 10^{14}$ and $K_r = 10^{-3}$: $k^c = 275.7$, $Ra^c = 1.8044 \times 10^{10}$; (4) $Ta = 10^{14}$ and $K_r = 10^{3}$: $k^c = 275.8$, $Ra^c = 1.8045 \times 10^{10}$.

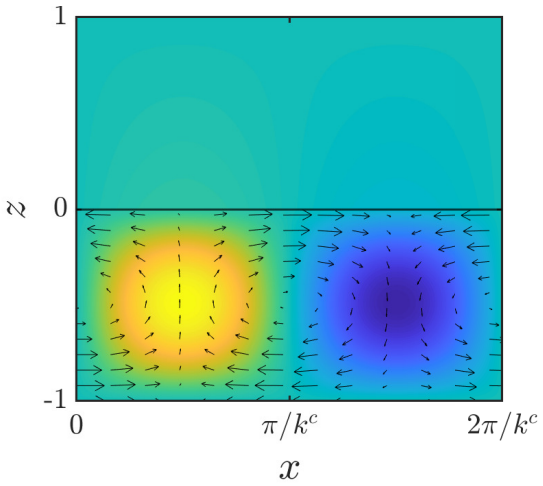


Figure 4.11: Temperature contours and velocity vectors in the x–z plane of the critical mode for $K_r = 10^{-3}$, $Ta = 10^{14}$, and $\delta = 1$, with $k^c = 275.75$ and $Ra^c = 1.804 \times 10^{10}$. The eigenfunctions are normalised such that $\max(w) = 1$. Eigenfunction profiles are shown in figure 4.10.

increasingly concentrated near the fluid-solid boundary, thereby restricting temperature perturbations to the fluid layer. The behaviour of the critical mode in the x–z plane is shown in figure 4.11 for $K_r = 10^{-3}$ and $Ta = 10^{14}$. The convective cells are small, with a wavelength of $2\pi/k^c = 0.023$, compared with the non-rotating system, which has a wavelength of $2\pi/k^c = 2.83$ (see figure 4.4). At large Ta and for all K_r, the temperature perturbation is confined to the fluid layer, so figure 4.11 represents the critical mode at $Ta = 10^{14}$ for all K_r. We will next see that figure 4.11 also represents the critical mode for all values of δ at $Ta = 10^{14}$.

We now consider the case of equal thermal conductivity and examine the effects of varying the depth ratio δ and the Taylor number Ta. Figure 4.12 shows how the critical Rayleigh number Ra^c and critical wavenumber k^c vary with δ for $Ta = 0$ and $Ta = 10^{14}$. As observed when K_r varies with fixed δ (figure 4.8), the behaviour of Ra^c and k^c remains monotonic for both Taylor numbers. This trend holds across the range of rotational strengths from $Ta = 0$ to $Ta = 10^{14}$. For all values of Ta, as δ approaches either zero or infinity, the critical mode behaves similarly to that identified in the non-rotating system (§4.3). In particular, as $\delta \to 0$ ($\delta \to \infty$), Ra^c and k^c approach the critical values observed for RRBC bounded by one stress-free, fixed-temperature plate and one no-slip, fixed-temperature (thermal Robin condition: $\mathcal{D}\theta = -K_r k\theta$) plate.

Figure 4.13 shows the normalised critical Rayleigh number Ra^c/Ra^c_* and wavenumber k^c/k^c_* as functions of the depth ratio δ for different Taylor numbers, with $K_r = 1$. As in the limiting cases of K_r (see figure 4.9), for fixed Ta, as $\delta \to 0$, the ratios Ra^c/Ra^c_* and k^c/k^c_* tend to one, as expected. As $\delta \to \infty$, both Ra^c/Ra^c_* and k^c/k^c_* tend to an asymptotic value that increases towards one with increasing Ta. However, unlike K_r, the transition between the two asymptotic limits shifts

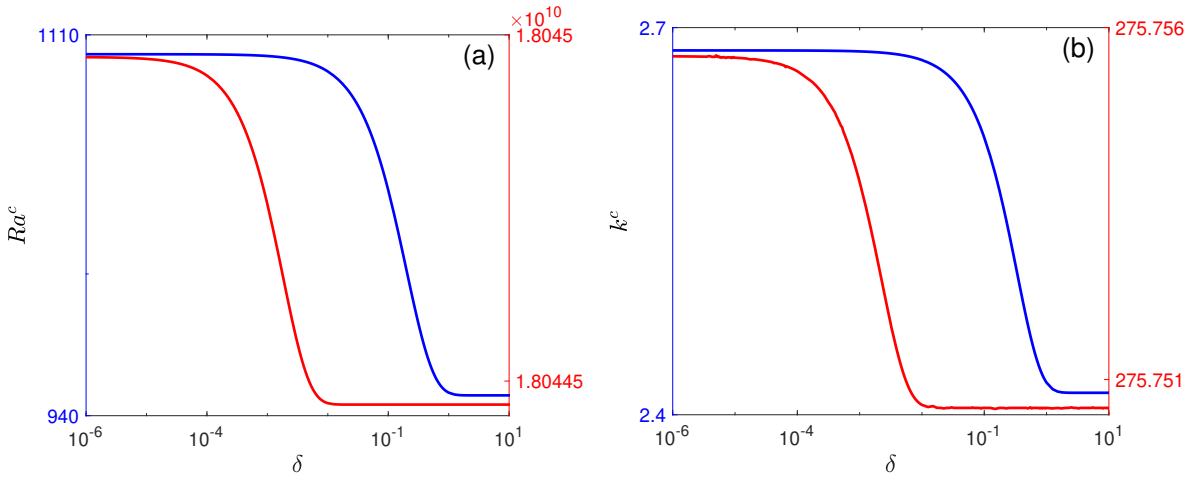


Figure 4.12: Variations of the critical (a) Rayleigh number Ra^c and (b) wavenumber k^c as functions of the layer depth ratio δ, for $Ta = 0$ (blue) and $Ta = 10^{14}$ (red), with $K_r = 1$.

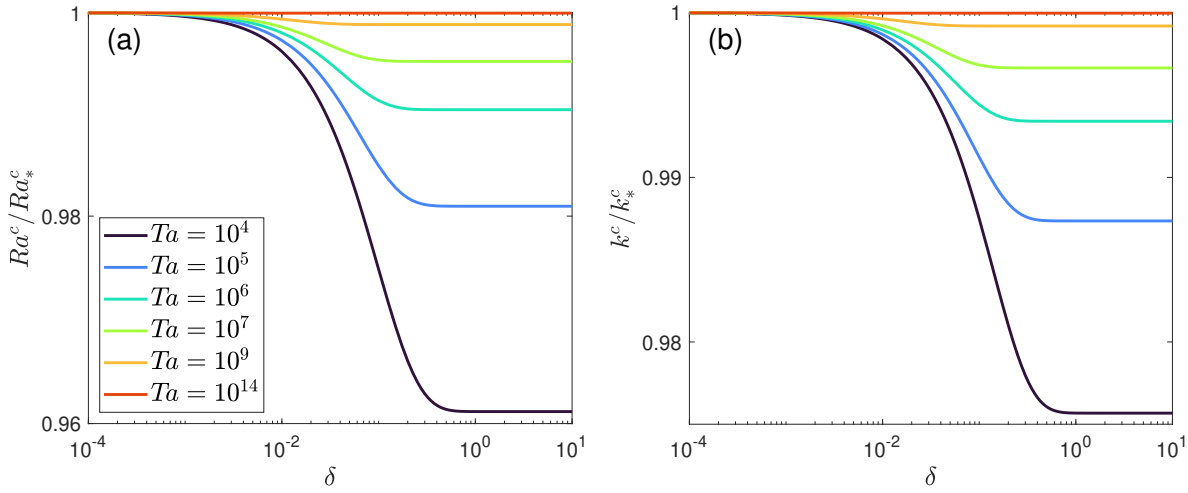


Figure 4.13: Variations of the critical (a) Rayleigh number Ra^c and (b) wavenumber k^c as functions of the depth ratio δ, for different Taylor numbers, with $K_r = 1$. Each quantity is normalised by its corresponding critical value for RRBC with fixed-temperature boundaries, where one boundary is stress-free and the other is no-slip, denoted by Ra^c_*, and k^c_*. The legend in (a) applies to (b).

to lower values of δ as Ta increases. Recall that in the non-rotating system, $\delta = 2$ is sufficiently large to be classified within the $\delta \to \infty$ regime. When rotation is introduced, δ can be several orders of magnitude smaller and still be classified within the $\delta \to \infty$ regime. This is clearly observed in figure 4.12 for $Ta = 10^{14}$, where critical modes with $\delta = 10^{-2}$ lie within the $\delta \to \infty$ regime. This occurs because $k^c \sim Ta^{1/6}$. So $\coth(\delta k)$ tends to one at progressively smaller values of δ as Ta increases. Consequently, the thermal interface condition (4.40) reduces to $\mathcal{D}\theta = -K_r k\theta$ at smaller δ as Ta increases. The value of δ at which the critical mode enters the $\delta \to \infty$ asymptotic regime scales with $Ta^{-1/6}$. Thus, the system is within the $\delta \to \infty$ asymptotic regime when $\delta \gtrsim \mathcal{O}\left(Ta^{-1/6}\right)$.

Figure 4.14 shows the velocity and temperature profiles of the critical mode for $Ta = 0$ and $Ta = 10^{14}$ at $\delta = 10^{-4}$ and $\delta = 2$, with $K_r = 1$. The features of the critical modes are analogous to those in the scenario where K_r varies with fixed $\delta = 1$ (figure 4.10). The maximum absolute difference between the velocity profiles over the z-domain, evaluated at the limits of δ, occurs within the Ekman boundary layer and scales as $Ta^{-1/3}$ (determined empirically), whereas the maximum temperature profile difference arises at the fluid-solid interface and scales as $Ta^{-2/5}$. This indicates that the velocity and temperature profiles converge at higher rotation rates. As observed when K_r varies with fixed δ, for a sufficiently large Ta, the convection and temperature perturbation cells are confined to the fluid layer regardless of the size of δ. Consequently, figure 4.11 not only represents the critical mode for all values of K_r with $\delta = 1$, but also for all values of δ with $K_r = 1$.

Figure 4.15 shows how the critical Rayleigh number Ra^c and critical wavenumber k^c vary with the depth ratio δ and thermal conductivity ratio K_r, with $Ta = 10^{14}$. These plots exhibit behaviour similar to that of the non-rotating system in figure 4.7. The asymptotic behaviour of K_r identified when $\delta = 1$ persists for all δ. In particular, as $K_r \to 0$ ($K_r \to \infty$), Ra^c and k^c approach the critical values observed for RRBC bounded by one stress-free, fixed-temperature plate and one no-slip, fixed-flux (fixed-temperature) plate, for all δ. In contrast, the asymptotic behaviour of δ depends on K_r. For $K_r < \mathcal{O}\left(10^{-2}\right)$, the thermal interface condition behaves as a fixed-flux condition for all δ considered ($10^{-4} \leq \delta \leq 10$), while for $K_r > \mathcal{O}(1)$, it behaves as a fixed-temperature condition. In the intermediate range $\mathcal{O}\left(10^{-2}\right) < K_r < \mathcal{O}(1)$, the system transitions between the two boundary regimes. For $\delta > \mathcal{O}\left(10^{-2}\right)$, the transition remains fixed at $K_r \sim \mathcal{O}(1)$. By contrast, as δ decreases from $\delta \sim \mathcal{O}\left(10^{-2}\right)$ to $\delta = 10^{-4}$, the transition smoothly shifts to lower values of K_r, from $K_r \sim \mathcal{O}(1)$ to $K_r \sim \mathcal{O}\left(10^{-2}\right)$. This transition arises for the same reasons discussed for the non-rotating system in §4.3. However, the value of δ at which the transition becomes fixed at $K_r \sim \mathcal{O}(1)$ decreases with increasing Ta. This occurs because $k^c \sim Ta^{1/6}$. Consequently, $\coth(\delta k)$ rapidly approaches one at progressively smaller values of δ as Ta increases. Therefore, the thermal interface condition (4.40) reduces to $\mathcal{D}\theta = -K_r k\theta$ at increasingly smaller values of δ as Ta increases, scaling as $Ta^{-1/6}$. Thus, the transition between the two boundary regimes becomes fixed at $K_r = \mathcal{O}(1)$ when $\delta \gtrsim \mathcal{O}\left(Ta^{-1/6}\right)$. Notably, both Ra^c and k^c show only small variations, as expected for larger Ta.

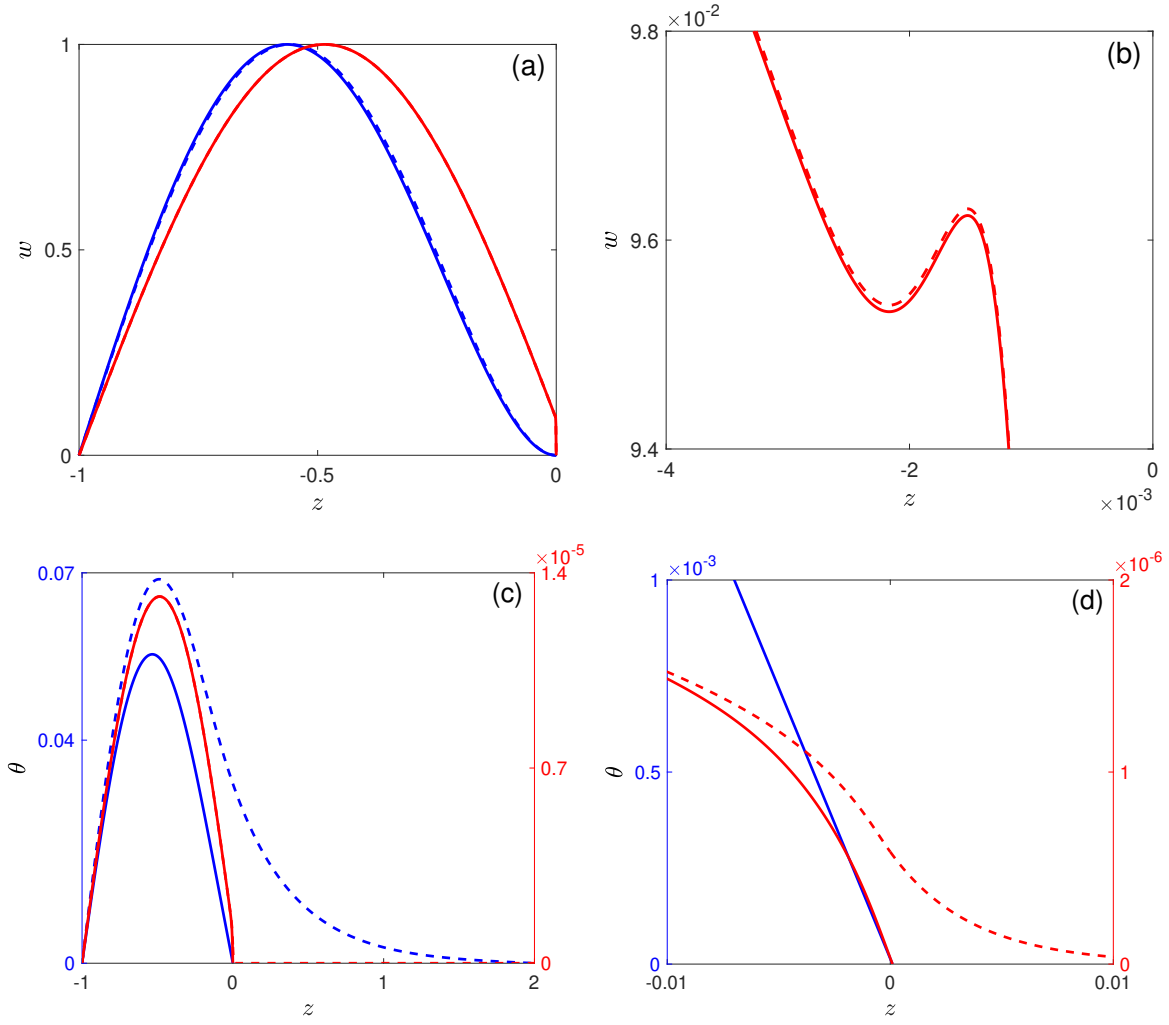
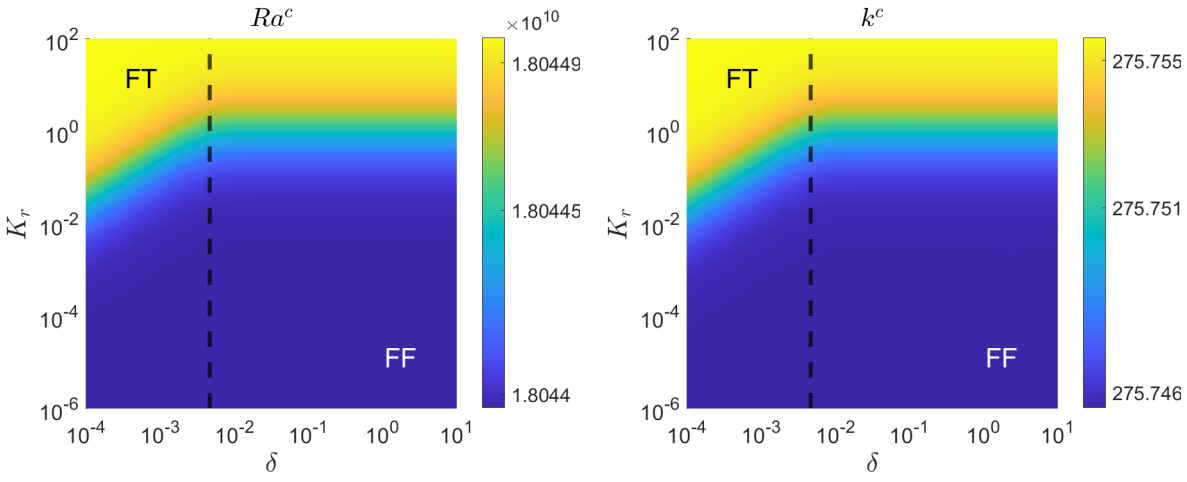


Figure 4.14: Velocity profiles (top row) and temperature profiles (bottom row) of the critical modes for $Ta = 0$ (blue), and 10^{14} (red), at $\delta = 10^{-4}$ (solid) and $\delta = 2$ (dashed), with $K_r = 1$. The solutions are normalised such that max $(w) = 1$. The left column shows the profiles across the entire two-layer domain. The right column provides magnified views of the boundary layers near the solid-fluid interface at $z = 0$. The vertical range of w is restricted to $-4 \times 10^{-3} \leq z \leq -10^{-3}$ to highlight the shape of the boundary layer, while the vertical range of θ is restricted to $-0.01 \leq z \leq 0.01$. The corresponding critical wavenumbers and critical Rayleigh numbers are: (1) $Ta = 0$ and $\delta = 10^{-4}$: $k^c = 2.7$, $Ra^c = 1100.6$; (2) $Ta = 0$ and $\delta = 2$: $k^c = 2.4$, $Ra^c = 948.4$; (3) $Ta = 10^{14}$ and $\delta = 10^{-4}$: $k^c = 275.8$, $Ra^c = 1.8045 \times 10^{10}$; (4) $Ta = 10^{14}$ and $\delta = 2$: $k^c = 275.8$, $Ra^c = 1.8044 \times 10^{10}$.



(a) (b)

Figure 4.15: Colour map of the critical (a) Rayleigh number Ra^c and (b) wavenumber k^c as functions of the depth ratio δ and thermal conductivity ratio K_r, with $Ta = 10^{14}$. The colour scales represent the magnitudes of Ra^c and k^c, with warmer colours indicating higher values. The dashed black line shows the transition point at $Ta^{1/6} = 4.6 \times 10^{-3}$.

4.4.2 Oscillatory modes of instability

We return to the system (4.15)–(4.18) with boundary conditions (4.20)–(4.22), and now consider the case in which convection manifests as an oscillatory instability. The marginal state of the system is characterised by a complex growth rate with a non-zero imaginary part. Accordingly, we set $s = i\omega$, where $\omega \in \mathbb{R}$ is the oscillation frequency.

Following the same approach as for the steady system (§4.4.1), the solution to equation (4.18) with boundary condition (4.22) is

$$\theta' = C \sinh\left((\lambda + i\mu)(\delta - z)\right), \tag{4.42}$$

where C is a constant and

$$\lambda = \frac{1}{2^{1/2}} \left[\left(k^4 + \left(\frac{\omega}{K_r} \right)^2 \right)^{1/2} + k^2 \right]^{1/2}, \qquad \mu = \frac{1}{2^{1/2}} \left[\left(k^4 + \left(\frac{\omega}{K_r} \right)^2 \right)^{1/2} - k^2 \right]^{1/2}. \tag{4.43}$$

A simplified interface condition is obtained on substituting for θ' from (4.42) into (4.21), giving

$$\mathcal{D}\theta = L\theta \qquad \text{at} \qquad z = 0 \tag{4.44}$$

where,

$$L = -K_r (\lambda + i\mu) \coth\left((\lambda + i\mu)\delta\right) \tag{4.45}$$

is the heat transfer parameter. This simplifies the problem to the set of equations (4.15)–(4.17) subject to boundary conditions

$$w = \mathcal{D}w = \zeta = 0, \quad \mathcal{D}\theta = L\theta \qquad \text{at} \qquad z = 0, \tag{4.46}$$

$$w = \mathcal{D}^2 w = \mathcal{D}\zeta = \theta = 0 \qquad \text{at} \qquad z = -1. \tag{4.47}$$

The thermal interface condition (4.46) is determined by the heat transfer parameter (4.45). However, in this case, L is complex, depending on K_r, δ, k, and ω; notably, it now varies with frequency. Setting $\omega = 0$ reduces (4.45) to (4.28), yielding the form of L for the steady system. Our objective now is to examine how oscillatory modes vary with the parameters K_r, δ, Ta, and Pr.

Equations (4.15)–(4.17), subject to boundary conditions (4.46) and (4.47), are solved using MATLAB's boundary value solver `BVP5C`. The same code can also handle complex-valued solutions. In the steady system, there is a single free parameter, Ra, whereas in the oscillatory system, two parameters, Ra and ω, must be determined. This is addressed by decomposing the solutions and boundary conditions into real and imaginary components, providing enough boundary conditions to determine both free parameters. An analytical expression for θ' is given in (4.42). The constant C is determined by enforcing the interface condition $\theta = \theta'$ at $z = 0$, yielding $C = \theta\,(0)\ \mathrm{csch}\left((\lambda + i\mu)\,\delta k\right)$ for given k, ω, and δ. Therefore, the temperature within the solid ($0 \leq z \leq \delta$) is calculated as

$$\theta' = \theta\,(0)\,\mathrm{csch}\left((\lambda + i\mu)\,\delta k\right)\sinh\left((\lambda + i\mu)\,(\delta - z)\right), \tag{4.48}$$

where $\theta\,(0)$ is computed numerically through the MATLAB routine `BVP5C`.

We begin with equal layer depths and examine how varying the thermal conductivity ratio K_r and Taylor number Ta affects the system at a fixed Prandtl number. Although a similar analysis could vary δ with $K_r = 1$, the results in §4.4.1 indicate that the limiting cases of δ closely resemble those obtained by varying K_r with $\delta = 1$. The same holds for oscillatory instabilities. Therefore, in this section we focus on variations in K_r with $\delta = 1$. Figure 4.16 shows the critical Rayleigh number Ra^c and wavenumber k^c as functions of Ta, evaluated at the asymptotic limits $K_r = 10^{-3}$ and $K_r = 10^3$, for the onset of steady modes (preferred or not with $Pr = 1$), and for oscillatory modes ($Pr = 0.01,\ 0.1,\ 0.4$) only when oscillatory convection is favoured at the given Ta. The critical values are scaled using the asymptotic relations for RRBC with stress-free fixed-temperature boundaries in the limit of rapid rotation, as shown in expressions (2.87) and (2.88). Accordingly, the scaled critical Rayleigh number and wavenumber are $Ra^c Ta^{-2/3}$ and $k^c Ta^{-1/6}$. In the steady system, solutions of RRBC bounded by one stress-free fixed-temperature plate and one no-slip plate with either fixed-temperature ($K_r \to \infty$) or fixed-flux ($K_r \to 0$) conditions become comparable as $Ta \to \infty$ (see §4.4.1). Similarly, the thermal interface condition for the onset of oscillatory instabilities behaves as a fixed-flux (fixed-temperature) condition as $K_r \to 0$ ($K_r \to \infty$). Furthermore, figure 4.16 shows that, for a fixed Prandtl number, Ra^c and k^c at the limits of K_r converge as $Ta \to \infty$.

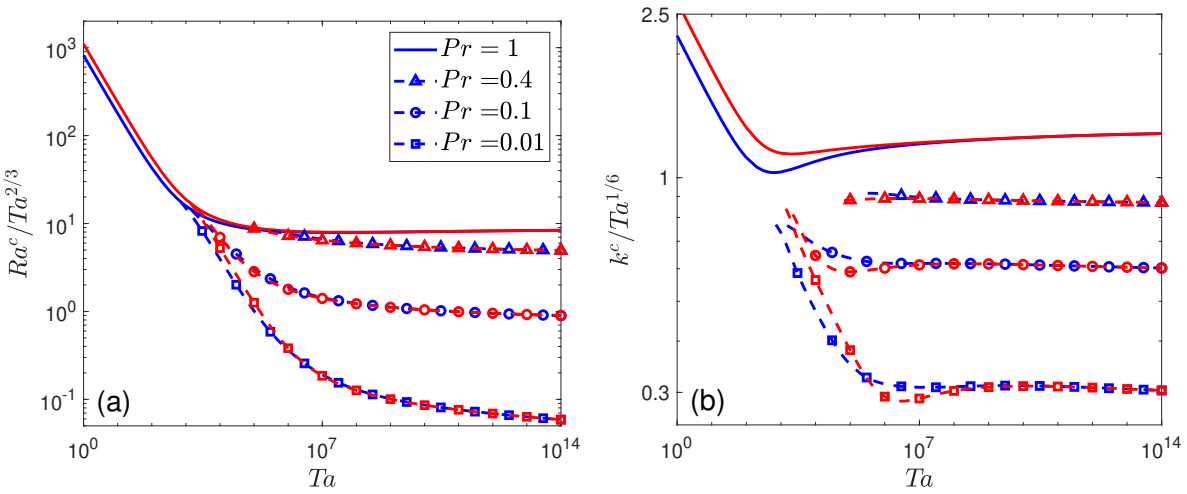


Figure 4.16: Asymptotically scaled critical (a) Rayleigh number $Ra^c/Ta^{2/3}$ and (b) wavenumber $k^c/Ta^{1/6}$ as functions of the Taylor number Ta for $K_r = 10^{-3}$ (blue) and $K_r = 10^3$ (red), with $\delta = 1$, at the onset of steady ($Pr = 1$) and oscillatory ($Pr = 0.01,\ 0.1,\ 0.4$) convection.

The type of instability that emerges at onset, either steady or oscillatory, depends on which mode yields the lowest critical Rayleigh number. For a given Ta, a transitional Prandtl number, Pr^t, marks the threshold below which oscillatory modes are preferred. Specifically, steady modes are preferred for $Pr > Pr^t$, while oscillatory modes are favoured for $Pr < Pr^t$. In figure 4.16(a), for a fixed Ta, the value of Pr at which the oscillatory and steady branches of Ra^c intersect corresponds to the transitional Prandtl number. In the RRBC system, the relationship between Ta and Pr^t can be expressed explicitly, as given by Kloosterziel and Carnevale (2003) and Hughes et al. (2022) (see equation (2.99)). Although this relationship cannot be expressed explicitly for the RRBC-BS system, Pr^t can be determined numerically. For a fixed Ta, a numerical iterative method is employed to determine the value of Pr at which the critical Rayleigh numbers of the steady and oscillatory branches are equal.

Figure 4.17 shows the transitional Prandtl number, Pr^t, as a function of the Taylor number, Ta, for RRBC with stress-free, fixed-temperature boundaries, and for the RRBC-BS system at $K_r = 10^{-3}$, $K_r = 1$, and $K_r = 10^3$, with $\delta = 1$. For $K_r = 10^3$, the thermal interface condition of the RRBC-BS system behaves like a fixed-temperature condition. In this regime, the only difference between the two systems is the mechanical condition at one boundary: stress-free in RRBC versus no-slip in RRBC-BS. Conversely, for $K_r = 10^{-3}$, the thermal interface condition in the RRBC-BS system behaves like a fixed-flux condition. In this case, both the mechanical and thermal conditions at one boundary differ between the two systems: stress-free, fixed-temperature in RRBC versus no-slip, fixed-flux in RRBC-BS. On this basis, one might expect that the RRBC-BS results for $K_r = 10^3$ would more closely resemble those of the RRBC system than those for $K_r = 10^{-3}$. This expectation is not readily apparent in figure 4.17. For $Ta \lesssim 3900$, the values of Pr^t for $K_r = 10^{-3}$ are in

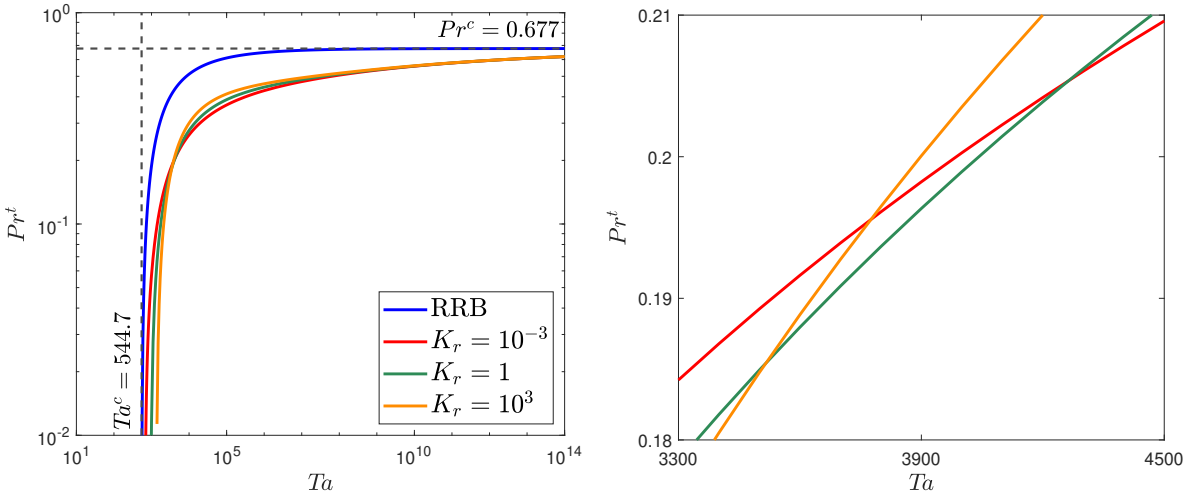


Figure 4.17: The transitional Prandtl number Pr^t as a function of Ta for RRBC with stress-free, fixed-temperature boundaries, defined by (2.99), and for RRBC-BS at $K_r = 10^{-3}$, $K_r = 1$, and $K_r = 10^3$ with $\delta = 1$, is determined numerically. Steady convection is favoured for $Pr > Pr^t$, while oscillatory convection is preferred for $Pr < Pr^t$. (a) The full range of Ta and Pr^t. The dashed lines indicate the critical values, $Ta^c = 544.7$ and $Pr^c = 0.677$, of the RRBC system. (b) An enlarged view of the region where the RRBC-BS system curves intersect.

fact closer to those of the RRBC system than the corresponding values for $K_r = 10^3$. Moreover, as Ta decreases from 3900, the value of Pr^t for $K_r = 10^{-3}$ approaches those of the RRBC system. However, there is no compelling evidence that the curves tend asymptotically to the same critical value, $Ta^c = 544.7$. Further analysis is required to characterise the asymptotic behaviour of the RRBC-BS system as $Pr \to 0$. The functional dependence of Pr^t on Ta is more intricate than the corresponding relation for the RRBC system given by (2.99). Consequently, a simple curve-fitting function does not adequately represent the asymptotic behaviour for extrapolation.

The solutions of the RRBC-BS system with different K_r values intersect near $Ta = 3900$. Although figure 4.17(a) suggests that all three curves intersect at a single point, this is not the case. Each curve crosses at a slightly different Taylor number close to $Ta = 3900$; this is shown clearly in figure 4.17(b). For Taylor numbers above the intersection value, Pr^t for $K_r = 10^3$ lies closer to that of the RRBC system than the corresponding value for $K_r = 10^{-3}$, as predicted. As Ta increases further, the transitional Prandtl number of the RRBC system asymptotes towards $Pr^c = 0.677$ as $Ta \to \infty$. Heard and Veronis (1971) demonstrated that, at sufficiently large Taylor numbers, the influence of the mechanical boundary condition becomes negligible for the onset of steady and oscillatory modes of instability. Similarly, we demonstrated in Chapter 3 that, for steady instabilities, the critical modes become independent of the thermal boundary condition in the rapidly rotating regime. Therefore, al-

though this is not entirely apparent from figure 4.17, it is expected that the solutions of the RRBC-BS system for all values of K_r will tend towards $Pr^c = 0.677$.

Figure 4.18 shows the velocity and temperature profiles of the steady and oscillatory critical modes for $K_r = 10^3$, $\delta = 1$, and $Ta = 10^4$ with $Pr \equiv Pr^t = 0.300055$. In this case, the most significant difference between the two modes is the wavelength. The steady mode has a shorter wavelength, $2\pi/k_s^c = 1.17$, compared with the oscillatory mode, which has a wavelength of $2\pi/k_o^c = 1.62$. A sharper contrast between the steady and oscillatory modes at the transitional Prandtl number is evident in Chapter 5, which considers the effects of two interacting fluids.

4.5 Discussion

This chapter has examined the linear stability of rotating convection with a boundary slab of finite conductivity to gain insight into the onset of rotating two-layer convection with a large viscosity contrast. We studied the onset of convection as a function of the thermal conductivity contrast, layer depth ratio, rotational strength, and Prandtl number. In the asymptotic limits of these parameters, the problem can be modelled by a simpler system. For both steady and oscillatory instabilities, as $K_r \to 0$, the thermal interface condition behaves as a fixed-flux condition, while as $K_r \to \infty$ or $\delta \to 0$, it behaves as a fixed-temperature condition. In these three limits, the system behaves as single-layer rotating Rayleigh–Bénard convection with one stress-free, fixed-temperature boundary and one no-slip boundary with either a fixed-flux or fixed-temperature condition. In the limit $\delta \to \infty$, the thermal interface condition behaves as the Robin condition: $\mathcal{D}\theta = -K_r k\theta$, and the system again reduces to single-layer rotating Rayleigh–Bénard convection with this thermal Robin condition.

As $Ta \to \infty$, the critical values for the onset of steady and oscillatory convection in the four limits $K_r \to 0$, $K_r \to \infty$, $\delta \to 0$ and $\delta \to \infty$ converge. Therefore, the critical values for single-layer rotating Rayleigh–Bénard convection with one stress-free, fixed-temperature boundary and one no-slip boundary with either a fixed-flux or fixed-temperature condition converge as $Ta \to \infty$. Heard and Veronis (1971) showed that, at sufficiently large Taylor numbers, the influence of the mechanical boundary condition becomes negligible for the onset of both steady and oscillatory instabilities. Similarly, in Chapter 3, we demonstrated that the influence of the thermal boundary condition becomes negligible in this regime for steady instabilities. The results presented in this chapter suggest that, as $Ta \to \infty$, the impact of the various mechanical and thermal boundaries becomes negligible for both steady and oscillatory modes.

We observed oscillatory behaviour across varying Ta with $Pr \equiv Pr^t$ at different K_r values, marking the transition between steady and oscillatory mode preference. Steady modes are favoured when $Pr > Pr^t$, while oscillatory modes are preferred when $Pr < Pr^t$. In rotating Rayleigh Bénard

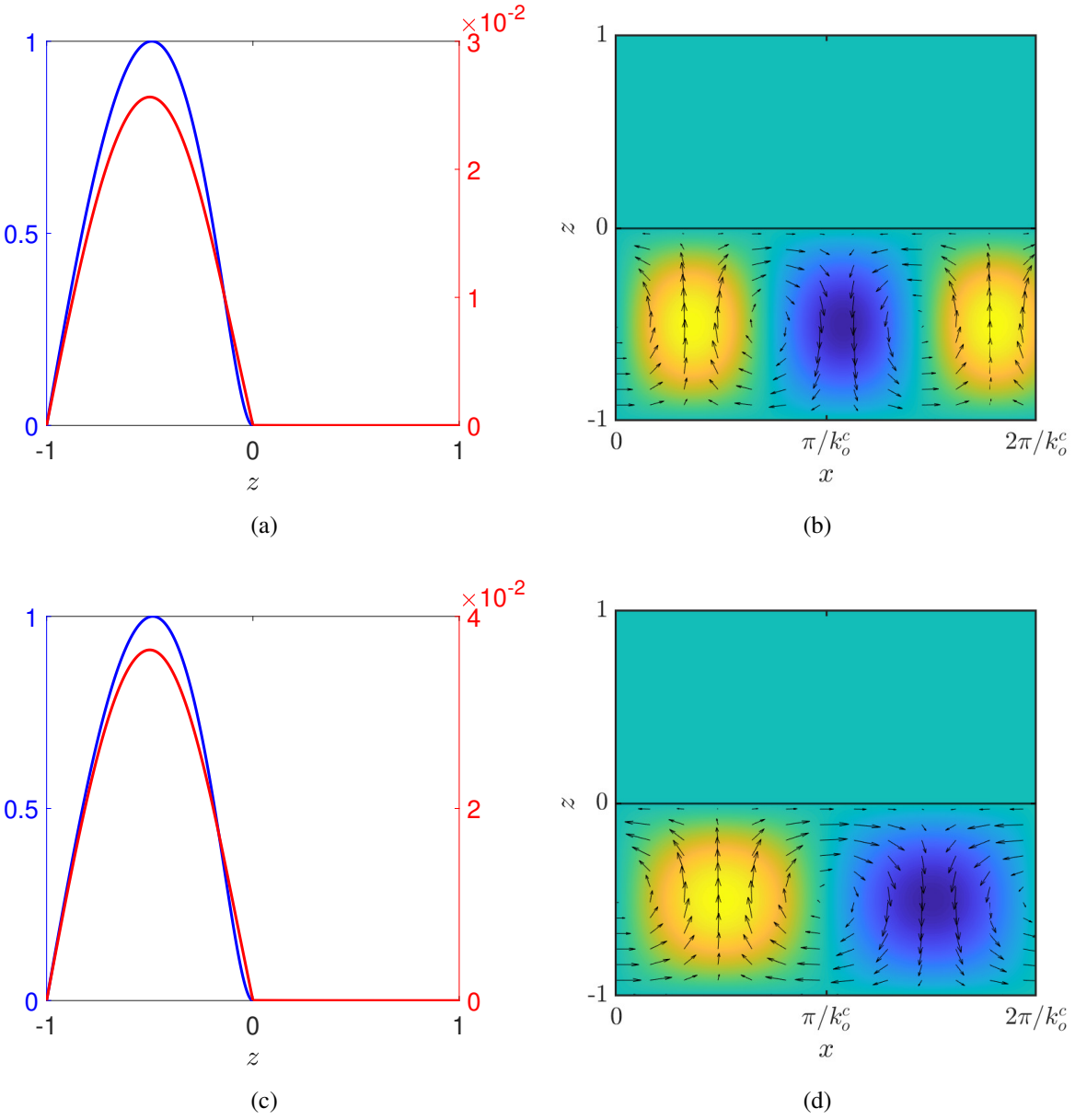


Figure 4.18: Same as figure 4.3 for $K_r = 10^3$, $Ta = 10^4$ and $\delta = 1$. The top row corresponds to the steady instability with $Ra_s^c = 5142.20$ and $k_s^c = 5.36$, while the bottom row shows the oscillatory instability at $Pr^t = 0.3001$, where $Ra_o^c = 5142.20$, $k_o^c = 3.87$ and $\omega^c = 6.22$.

convection, the transitional Prandtl number approaches $Pr^c = 0.67659$ as $Ta \to \infty$ and the Taylor number approaches $Ta^c = 544.7$ as $Pr \to 0$. Although further analysis is needed to determine the asymptotic behaviour of the RRBC-BS system, prior work by Heard and Veronis (1971) and results from Chapter 3 suggest that, at sufficiently large Ta, the influence of both mechanical and thermal boundary conditions becomes negligible. Thus, despite not being clearly visible in figure 4.17, the transitional Prandtl number of the RRBC-BS system for all K_r and δ is expected to tend towards $Pr^c = 0.677$ as $Ta \to \infty$.

This thesis aims to deepen our understanding of rotating convection with depth-dependent variations in fluid properties by investigating the instabilities that arise in a simplified rotating two-layer system. In this chapter, we have examined the linear stability of rotating convection with a boundary slab of finite conductivity, providing insight into the onset of rotating two-layer convection with a strong viscosity contrast. This work represents an essential step towards the broader goal and lays the groundwork for analytical exploration of more complex models. In the next chapter, we begin our investigation of the full rotating two-layer convection system and directly compare its results with those presented here.

Chapter 5

Rotating Two-Layer Convection

5.1 Introduction

A broad class of rotating convective systems exhibit pronounced depth-dependent variations in material properties. For instance, French et al. (2012) demonstrated that key material properties, including viscosity, the coefficient of thermal expansion, and thermal diffusivity, vary substantially along Jupiter's adiabat (see Chapter 1). Nonetheless, models of rotating convection that seek to reproduce the large-scale polar vortices observed on Jupiter and Saturn generally neglect depth-dependent effects, and instead assume constant viscosity and thermal diffusivity throughout the convecting layer (e.g., Gastine and Wicht, 2012; Yadav and Bloxham, 2020). To address this limitation and improve the theoretical description of rotating convection with depth-dependent fluid properties, we extend the single-layer rotating Rayleigh–Bénard convection (RRBC) framework developed in Chapter 2 to a two-layer configuration. In this model, each layer is characterised by its own set of physical parameters, enabling an explicit representation of depth-dependent variations in fluid properties.

Rotating two-layer convection comprises two superposed, horizontally extended fluid layers that are heated from below. The layers may possess different thicknesses and are characterised by distinct thermal and mechanical properties, including density, viscosity, and thermal diffusivity. The entire system rotates about a vertical axis aligned with the direction of gravitational acceleration. A thin interface separates the layers and couples their dynamics through mechanical and thermal continuity conditions. This interface may remain flat or undergo deformation.

Compared with its single-layer counterpart, the rotating two-layer system exhibits a substantially richer and more intricate dynamical behaviour. Rotating convection in a single Boussinesq fluid layer, as discussed in Chapter 2, is completely described by three dimensionless parameters: the Rayleigh number, Prandtl number, and Taylor number. By contrast, rotating two-layer convection can depend on up to 14 nondimensional parameters. In particular, the layer depth ratio, rotational strength, and

various material property ratios between layers can alter the onset conditions and preferred mode of convection, leading to a broad spectrum of distinct convective regimes. In this chapter, we employ linear stability theory to examine how variations in the Taylor number, Prandtl number, viscosity ratio, thermal diffusivity ratio, and layer depth ratio affect the critical conditions for the onset of convection and the associated spatial structure of the convective modes in the rotating two-layer system.

In the absence of rotation, convection in multi-layer fluid systems has been extensively investigated, primarily due to its relevance in geophysical and astrophysical fluid dynamics. Early work on two-layer convection was motivated by its proposed relevance to processes in the Earth's mantle (Richter and Johnson, 1974; Busse, 1981). Richter and Johnson (1974) investigated layers of equal depth and viscosity but different densities, representing compositional stratification in the mantle. Busse (1981) extended this framework to layers of unequal thickness and examined the coupling between convection in the upper and lower mantle. Analogous configurations arise in stellar interiors, where convectively unstable regions may be embedded between stably stratified layers (Hurlburt et al., 1986). Layered convective systems also occur in technological contexts, such as in the analysis of heat transport in magnetically confined fusion plasmas (Wilczynski and Hughes, 2019). Beyond these applications, convection in superposed fluid layers has attracted sustained attention owing to the complexity and richness of the underlying dynamics. Extending the classical Rayleigh–Bénard convection framework to configurations with multiple layers introduces a variety of additional phenomena, including interlayer coupling and competition between instabilities, the emergence of oscillatory modes at onset, and deformation of the interfaces separating the layers. This enhanced dynamical complexity reflects the increased dimensionality of the associated parameter space. Consequently, many investigations have focused on restricted subsets of this parameter space in order to identify the regimes in which particular forms of convective behaviour occur (e.g., Rasenat et al., 1989; Diwakar et al., 2014).

Although rotating stratified flows play a central role in geophysical and astrophysical fluid dynamics, rotating two-layer convection has been investigated far less than simpler configurations. The combined effects of rotation and stratification in layered convective systems remain poorly characterised, leaving a substantial gap in our understanding of rotating convection in systems with depth-dependent material properties and thereby motivating the systematic analysis undertaken here.

In this chapter, we expand single-layer rotating Rayleigh–Bénard convection introduced in Chapter 2 to a two-layer configuration that incorporates depth-dependent variations in fluid properties. Owing to the large number of potentially relevant parameters, it is of theoretical interest to understand how these parameters influence the onset of instability and whether distinct regimes of behaviour arise. We begin by formulating the linear problem and introducing a new mathematical model in §5.2. The onset of instability is then examined in the non-rotating configuration, which is identical to that studied by Wilczynski and Hughes (2019), in §5.3, followed by the rotating system at the onset of steady instabilities in §5.4, and oscillatory instabilities in §5.5. Finally, §5.6 presents concluding remarks.

5.2 Mathematical formulation

5.2.1 Governing equations

We consider two infinite, horizontal, miscible layers of Boussinesq fluid, one above the other, separated by a thin, flat interface, and heated from below. For simplicity, we will focus on the case where both fluids have the same density ρ, thereby reducing the number of parameters. Each fluid layer is defined by distinct thermal and mechanical properties. Specifically, the layers have thermal diffusivities κ_i, kinematic viscosities ν_i, and coefficients of thermal expansion α_i, where $i = 1$ corresponds to the lower layer and $i = 2$ to the upper layer. The fluids may have different depths: the lower layer has depth d_1, and the upper layer has depth $d_2 = \delta d_1$, where δ is the depth ratio. The interface is fixed at $z = 0$. Hence, the lower layer occupies $-d_1 < z < 0$ and the upper layer occupies $0 < z < d_2$. The planes $z = -d_1$ and $z = d_2$ are held at uniform temperatures T_b and T_u, with $T_b > T_u$. The acceleration due to gravity is $\boldsymbol{g} = -g\hat{\boldsymbol{z}}$, and the system rotates about the vertical z-axis with angular velocity $\boldsymbol{\Omega} = \Omega\hat{\boldsymbol{z}}$. A sketch of the configuration is shown in figure 5.1.

The basic state is hydrostatic, and the imposed temperature difference produces a linear conductive temperature profile in each layer, similar to that in the problem bounded by a solid slab (as shown in equations (4.3) and (4.4)), which is described by

$$T_2 = T_u - \beta_2 \left(z - d_2\right), \qquad 0 \le z \le d_2, \tag{5.1}$$

$$T_1 = T_b - \beta_1 \left(z + d_1\right), \qquad -d_1 \le z < 0, \tag{5.2}$$

where β_i are the adverse temperature gradients within each layer. Continuity of temperature and heat-flux, where the specific heat is constant, at the interface requires that

$$\beta_1 = \frac{\kappa_2 \left(T_b - T_u\right)}{\kappa_1 d_2 + \kappa_2 d_1}, \qquad \beta_2 = \frac{\kappa_1 \left(T_b - T_u\right)}{\kappa_1 d_2 + \kappa_2 d_1}. \tag{5.3}$$

Thus, the overall temperature difference is split into temperature drops across each layer, with the drop in each layer depending on the thermal diffusivities and depths of the two layers. We note that

$$\frac{\beta_2}{\beta_1} = \frac{\kappa_1}{\kappa_2}. \tag{5.4}$$

The ratio of the thermal diffusivities fixes the ratio of thermal gradients.

The governing equations of the rotating two-layer system can be derived by analysing each layer separately. After nondimensionalising the entire system, certain dimensionless parameters emerge that couple the two sets of equations, thereby linking the layers. When each layer is analysed independently, the governing equations, under the Boussinesq approximation, for the perturbations in velocity $\boldsymbol{u}_i = (u_i, v_i, w_i)$, pressure P_i, and temperature θ_i from the basic (hydrostatic) state are equivalent to those of the single-layer rotating Rayleigh–Bénard system (see §2.5). The linear equations governing

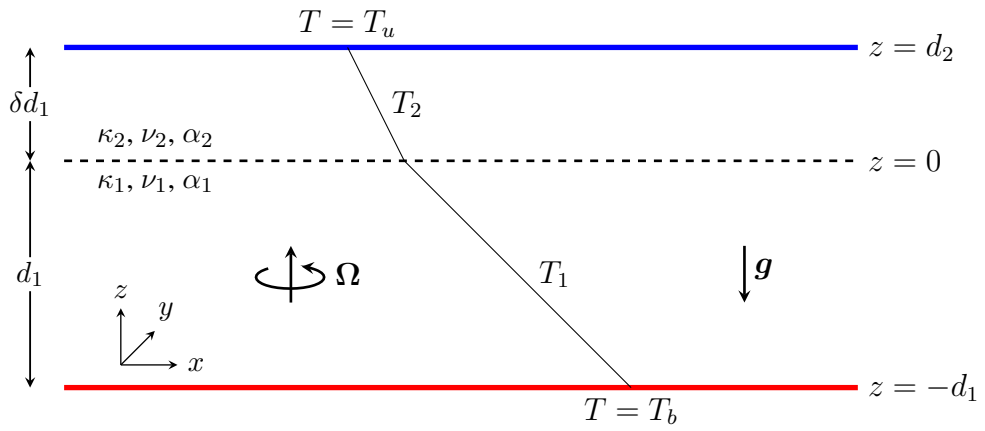


Figure 5.1: Schematic sketch of rotating two-layer convection.

the perturbations from the basic state can thus be expressed as

$$\frac{\partial \boldsymbol{u}_i}{\partial t} + 2\boldsymbol{\Omega} \times \boldsymbol{u}_i = -\frac{1}{\rho_0}\nabla P_i + \alpha_i \theta_i g \hat{\boldsymbol{z}} + \nu_i \nabla^2 \boldsymbol{u}_i, \tag{5.5}$$

$$\nabla \cdot \boldsymbol{u}_i = 0, \tag{5.6}$$

$$\frac{\partial \theta_i}{\partial t} = \beta_i w_i + \kappa_i \nabla^2 \theta_i. \tag{5.7}$$

The governing equations (5.5)–(5.7) are expressed in dimensionless form by scaling variables with the thermal and mechanical properties of the lower layer: scaling length with d_1, time with d_1^2/κ_1, pressure with $\rho_0 (\kappa_1/d_1)^2$, velocity with κ_1/d_1 and temperature with $\beta_1 d_1$. Furthermore, since it is convenient to express the system in terms of the vertical velocities w_i, vertical vorticities ζ_i and temperatures θ_i, the pressure and horizontal velocity components are eliminated by the standard procedure of applying the operators $\hat{\boldsymbol{z}} \cdot \nabla\times$ and $\hat{\boldsymbol{z}} \cdot \nabla \times \nabla\times$ to equation (5.5). The dimensionless equations governing linear perturbations from the basic state may then be written as

$$\frac{\partial \theta_1}{\partial t} + \nabla^2 \theta_1 = w_1, \tag{5.8}$$

$$\frac{\partial \zeta_1}{\partial t} - Pr_1 \nabla^2 \zeta_1 = Pr_1 Ta_1^{1/2} \frac{\partial w_1}{\partial z}, \tag{5.9}$$

$$\frac{\partial}{\partial t}\nabla^2 w_1 - Pr_1 \nabla^4 w_1 = -Pr_1 Ta_1^{1/2} \frac{\partial \zeta_1}{\partial z} + Ra_1 Pr_1 \nabla_H^2 \theta_1, \tag{5.10}$$

$$\frac{\partial \theta_2}{\partial t} + \kappa_r \nabla^2 \theta_2 = \beta_r w_2, \tag{5.11}$$

$$\frac{\partial \zeta_2}{\partial t} - \nu_r Pr_1 \nabla^2 \zeta_2 = Pr_1 Ta_1^{1/2} \frac{\partial w_2}{\partial z}, \tag{5.12}$$

$$\frac{\partial}{\partial t}\nabla^2 w_2 - \nu_r Pr_1 \nabla^4 w_2 = -Pr_1 Ta_1^{1/2} \frac{\partial \zeta_2}{\partial z} + Ra_1 Pr_1 \alpha_r \nabla_H^2 \theta_2. \tag{5.13}$$

where the horizontal Laplacian is defined by $\nabla_H^2 = \partial_x^2 + \partial_y^2$. The seven dimensionless parameters of the system -— the Rayleigh number, Prandtl number, Taylor number, and the ratios of the coefficients

of thermal expansion, viscosity, temperature gradient, and thermal diffusivity between the two layers -— are defined respectively by

$$Ra_1 = \frac{g\alpha_1\beta_1 d_1^4}{\nu_1\kappa_1}, \qquad Pr_1 = \frac{\nu_1}{\kappa_1}, \qquad Ta_1 = \frac{4\Omega^2 d_1^4}{\nu_1^2}, \tag{5.14}$$

$$\alpha_r = \frac{\alpha_2}{\alpha_1}, \qquad \nu_r = \frac{\nu_2}{\nu_1}, \qquad \beta_r = \frac{\beta_2}{\beta_1}, \qquad \kappa_r = \frac{\kappa_2}{\kappa_1}. \tag{5.15}$$

The 'ratio' parameters defined in (5.15) are essential for coupling the two layers, thereby enabling equations (5.8)–(5.13) to be solved simultaneously. Additionally, it follows from (5.4) that

$$\beta_r = \kappa_r^{-1}, \tag{5.16}$$

which reduces the number of parameters we need to consider. We shall see that one of the difficulties in understanding the results with varying κ_r is that β_r also varies.

In dimensionless units, the lower layer occupies $-1 \leq z < 0$, and the upper layer occupies $0 < z \leq \delta$. The outer boundaries are assumed to be impermeable, stress-free, and fixed-temperature, thus

$$w_1 = \frac{\partial^2 w_1}{\partial z^2} = \frac{\partial \zeta_1}{\partial z} = \theta_1 = 0 \qquad \text{on} \qquad z = -1, \tag{5.17}$$

$$w_2 = \frac{\partial^2 w_2}{\partial z^2} = \frac{\partial \zeta_2}{\partial z} = \theta_2 = 0 \qquad \text{on} \qquad z = \delta. \tag{5.18}$$

At the interface between the two layers ($z = 0$), we assume a number of continuity conditions. As the fluid velocities $\boldsymbol{u}_i = (u_i, v_i, w_i)$ are continuous across the interface, $\partial u_i/\partial x$ and $\partial v_i/\partial y$ must also be continuous across the interface. Thus, continuity of velocity and incompressibility give

$$w_1 = w_2, \qquad \frac{\partial w_1}{\partial z} = \frac{\partial w_2}{\partial z}. \tag{5.19}$$

Furthermore, $\partial u_i/\partial y$ and $\partial v_i/\partial x$ must also be continuous across the interface. Therefore, the vertical component of vorticity, $\zeta_i = \partial v_i/\partial x - \partial u_i/\partial y$, must be continuous across the interface. Continuity of vorticity results in

$$\zeta_1 = \zeta_2. \tag{5.20}$$

Continuity of temperature and heat-flux gives

$$\theta_1 = \theta_2, \qquad \frac{\partial \theta_1}{\partial z} = \kappa_r \frac{\partial \theta_2}{\partial z}. \tag{5.21}$$

Three continuity conditions — the continuity of tangential stress, normal stress, and the vertical vorticity gradient — follow from the stress tensor defined in equation (2.6). In dimensionless form, the stress tensor can be expressed as

$$\boldsymbol{\tau}_i = -P_i \boldsymbol{I} + \nu_r Pr_1 \left(\nabla \boldsymbol{u}_i + (\nabla \boldsymbol{u}_i)^T\right), \tag{5.22}$$

for each fluid layer. We start by analysing the continuity of tangential stress. The tangential components of the stress tensor, τ_{xz} and τ_{yz}, must be continuous across the interface. Equating the expressions for τ_{xz} in the upper and lower layers yields

$$\frac{\partial u_1}{\partial z} + \frac{\partial w_1}{\partial x} = \nu_r \left(\frac{\partial u_2}{\partial z} + \frac{\partial w_2}{\partial x} \right). \tag{5.23}$$

Differentiating (5.23) with respect to x and substituting for $\partial u_i/\partial x$ from the incompressibility condition (5.6) yields

$$\nu_r \frac{\partial^2 v_2}{\partial y \partial z} - \frac{\partial^2 v_1}{\partial y \partial z} + \frac{\partial^2 w_1}{\partial x^2} - \frac{\partial^2 w_1}{\partial z^2} = \nu_r \left(\frac{\partial^2 w_2}{\partial x^2} - \frac{\partial^2 w_2}{\partial z^2} \right). \tag{5.24}$$

Equating the expressions for τ_{yz} in the upper and lower layers gives

$$\frac{\partial v_1}{\partial z} + \frac{\partial w_1}{\partial y} = \nu_r \left(\frac{\partial v_2}{\partial z} + \frac{\partial w_2}{\partial y} \right). \tag{5.25}$$

Differentiating (5.25) with respect to y yields

$$\nu_r \frac{\partial^2 v_2}{\partial y \partial z} - \frac{\partial^2 v_1}{\partial y \partial z} = \frac{\partial^2 w_1}{\partial y^2} - \nu_r \frac{\partial^2 w_2}{\partial y^2}. \tag{5.26}$$

Substituting for the first two terms of (5.26) into (5.24) yields the continuity condition for the tangential stress as

$$\frac{\partial^2 w_1}{\partial x^2} + \frac{\partial^2 w_1}{\partial y^2} - \frac{\partial^2 w_1}{\partial z^2} = \nu_r \left(\frac{\partial^2 w_2}{\partial x^2} + \frac{\partial^2 w_2}{\partial y^2} - \frac{\partial^2 w_2}{\partial z^2} \right). \tag{5.27}$$

The normal component of the stress tensor, τ_{zz}, must also be continuous across the interface. Equating the expressions for τ_{zz} in the upper and lower layers yields

$$-P_1 + 2Pr_1 \frac{\partial w_1}{\partial z} = -P_2 + 2\nu_r Pr_1 \frac{\partial w_2}{\partial z}. \tag{5.28}$$

The pressure terms in (5.28) are eliminated using the dimensionless form of the momentum equation (5.5). Consider layer 1: differentiating the x-component of (5.5) with respect to x and the y-component with respect to y, and summing the results, gives

$$-\nabla_H^2 P_1 = -\frac{\partial^2 w_1}{\partial t \partial z} - Ta_1^{1/2} Pr_1 \zeta_1 + Pr_1 \nabla^2 \frac{\partial w_1}{\partial z}. \tag{5.29}$$

Similarly, for layer two,

$$-\nabla_H^2 P_2 = -\frac{\partial^2 w_2}{\partial t \partial z} - Ta_1^{1/2} Pr_1 \zeta_2 + \nu_r Pr_1 \nabla^2 \frac{\partial w_2}{\partial z}. \tag{5.30}$$

Applying the operator ∇_H^2 to equation (5.28), substituting for $\nabla_H^2 P_1$ and $\nabla_H^2 P_2$ from (5.29) and (5.30), and using (5.20) yields the continuity of normal stress as

$$\frac{\partial^2 w_1}{\partial t \partial z} - Pr_1 \frac{\partial}{\partial z} \left(\nabla^2 + 2\nabla_H^2 \right) w_1 = \frac{\partial^2 w_2}{\partial t \partial z} - \nu_r Pr_1 \frac{\partial}{\partial z} \left(\nabla^2 + 2\nabla_H^2 \right) w_2. \tag{5.31}$$

Finally, we derive the condition for the continuity of the vertical vorticity gradient. Differentiating (5.23) with respect to y and (5.25) with respect to x, gives

$$\frac{\partial^2 u_1}{\partial z \partial y} - \nu_r \frac{\partial^2 u_2}{\partial z \partial y} + \frac{\partial^2 w_1}{\partial x \partial y} = \nu_r \frac{\partial^2 w_2}{\partial x \partial y}, \tag{5.32}$$

and

$$\frac{\partial^2 v_1}{\partial z \partial x} - \nu_r \frac{\partial^2 v_2}{\partial z \partial x} + \frac{\partial^2 w_1}{\partial x \partial y} = \nu_r \frac{\partial^2 w_2}{\partial x \partial y}. \tag{5.33}$$

Subtracting (5.32) from (5.33) yields the continuity of the vertical vorticity gradient as

$$\frac{\partial \zeta_1}{\partial z} = \nu_r \frac{\partial \zeta_2}{\partial z}. \tag{5.34}$$

5.2.2 Linear stability analysis

We seek normal mode solutions of the form

$$w_i = \hat{w}_i(z) f_i(x,y) e^{st}, \qquad \theta_i = \hat{\theta}_i(z) f_i(x,y) e^{st}, \qquad \zeta_i = \hat{\zeta}_i(z) f_i(x,y) e^{st}, \tag{5.35}$$

where $s = \sigma + i\omega$ is the complex growth rate, with $\sigma, \omega \in \mathbb{R}$, and where the planform functions $f_i(x,y)$ satisfy $\nabla_H^2 f_i = -k^2 f_i$, where k is the horizontal wavenumber. Substituting the ansatz (5.35) into equations (5.8)–(5.13), and dropping the hats, gives the following system:

$$\left(\mathcal{D}^2 - k^2 - s\right)\theta_1 = -w_1, \tag{5.36}$$

$$\left(\mathcal{D}^2 - k^2 - \frac{s}{Pr_1}\right)\zeta_1 = -Ta_1^{1/2}\mathcal{D}w_1, \tag{5.37}$$

$$\left(\mathcal{D}^2 - k^2 - \frac{s}{Pr_1}\right)\left(\mathcal{D}^2 - k^2\right)w_1 = Ta_1^{1/2}\mathcal{D}\zeta_1 + k^2 Ra_1\theta_1, \tag{5.38}$$

$$\left(\mathcal{D}^2 - k^2 - \frac{s}{\kappa_r}\right)\theta_2 = -\frac{1}{\kappa_r^2}w_2, \tag{5.39}$$

$$\left(\mathcal{D}^2 - k^2 - \frac{s}{\nu_r Pr_1}\right)\zeta_2 = -\frac{1}{\nu_r}Ta_1^{1/2}\mathcal{D}w_2, \tag{5.40}$$

$$\left(\mathcal{D}^2 - k^2 - \frac{s}{\nu_r Pr_1}\right)\left(\mathcal{D}^2 - k^2\right)w_2 = \frac{1}{\nu_r}Ta_1^{1/2}\mathcal{D}\zeta_2 + \frac{\alpha_r}{\nu_r}k^2 Ra_1\theta_2, \tag{5.41}$$

where $\mathcal{D} \equiv \mathrm{d}/\mathrm{d}z$. The boundary and interface conditions (5.17)–(5.21), (5.27), (5.31), and (5.34) may be written as

$$w_1 = \mathcal{D}^2 w_1 = \mathcal{D}\zeta_1 = \theta_1 = 0 \qquad \text{on} \qquad z = -1, \tag{5.42}$$

$$w_2 = \mathcal{D}^2 w_2 = \mathcal{D}\zeta_2 = \theta_2 = 0 \qquad \text{on} \qquad z = \delta, \tag{5.43}$$

$$w_1 = w_2, \qquad \mathcal{D}w_1 = \mathcal{D}w_2,$$

$$\zeta_1 = \zeta_2, \qquad \mathcal{D}\zeta_1 = \nu_r \mathcal{D}\zeta_2,$$

$$\theta_1 = \theta_2, \qquad \mathcal{D}\theta_1 = \kappa_r \mathcal{D}\theta_2,$$
$$\left(\mathcal{D}^2 + k^2\right) w_1 = \nu_r \left(\mathcal{D}^2 + k^2\right) w_2,$$
$$s\mathcal{D}w_1 - Pr_1 \left(\mathcal{D}^3 - 3k^2\mathcal{D}\right) w_1 = s\mathcal{D}w_2 - \nu_r Pr_1 \left(\mathcal{D}^3 - 3k^2\mathcal{D}\right) w_2, \qquad \text{on} \qquad z = 0. \tag{5.44}$$

To understand the onset of convection in a two-layer system, it is important to consider the contribution of each layer. Therefore, it is useful to define effective Rayleigh, Taylor, and Prandtl numbers for the upper layer, as follows

$$Ra_2 = \frac{g\alpha_2\beta_2 d_2^4}{\nu_2\kappa_2} = \frac{\alpha_r\delta^4}{\nu_r\kappa_r^2} Ra_1, \tag{5.45}$$

$$Ta_2 = \frac{4\Omega^2 d_2^4}{\nu_2^2} = \frac{\delta^4}{\nu_r^2} Ta_1, \tag{5.46}$$

$$Pr_2 = \frac{\nu_2}{\kappa_2} = \frac{\nu_r}{\kappa_r} Pr_1. \tag{5.47}$$

The ratio Ra_1/Ra_2 quantifies the relative contributions of the two layers to the onset of buoyancy-driven instability. When this ratio deviates substantially from unity, the instability is predominantly localised in one of the layers, while the other behaves essentially as a passive region (Rasenat et al., 1989). Fluid motions in the latter layer are weak and arise primarily from mechanical forcing at the interface. This type of asymmetry occurs when ν_r, κ_r, α_r, or δ are either very small or very large. It is important to emphasise, however, that it is not instructive to consider the effective Rayleigh numbers individually. For instance, recall from (5.3) that the basic state temperature gradient can be written as

$$\beta_1 = \frac{T_b - T_u}{d_1\left(1 + \kappa_r^{-1}\delta\right)}, \qquad \beta_2 = \frac{T_b - T_u}{d_1\left(\delta + \kappa_r\right)}, \tag{5.48}$$

and consider the case where $\delta = \nu_r = \alpha_r = 1$ and a significant thermal diffusivity contrast is present. From (5.48), it follows that as $\kappa_r \to 0$, $\beta_1 \to 0$ and $\beta_2 \to \left(T_b - T_u\right)/\delta d_1$. Consequently, the temperature drop is entirely confined to the upper layer, whereas the lower layer experiences no buoyancy, resulting in $Ra_1 \to 0$. This indicates that the lower layer is passive and does not trigger convection. Conversely, as $\kappa_r \to \infty$, $\beta_1 \to \left(T_b - T_u\right)/d_1$ and $\beta_2 \to 0$, so the lower layer becomes the sole driver of convection, with the upper layer remaining passive.

The ratio Ta_1/Ta_2 reflects the relative rotational strength between the two layers. When this ratio deviates significantly from unity, occurring when ν_r or δ is either very small or very large, it indicates that the instability is predominantly localised in one of the layers, while the other behaves essentially as a passive region. As discussed in Chapter 2, the presence of rotation delays the onset of convection. Therefore, rotation generally has a stabilising effect. If the effective rotational strength is weaker in one layer than in the other, that layer will become unstable at lower local Rayleigh numbers, causing convection to occur, while the stronger rotational strength in the other inhibits the onset of convection. The influence of differing rotational strengths between the layers is explored in §5.4, where it is shown that the critical mode favours convection in the layer with lower effective rotational strength.

5.2.3 Symmetry of the system

In this section, we discuss the symmetry of the configuration. If the governing equations (5.5)–(5.7) are instead scaled using the thermal and mechanical properties of the upper layer instead of the lower layer — scaling length with δd_1, time with $(\delta d_1)^2/\kappa_2$, pressure with $\rho_0 (\kappa_2/\delta d_1)^2$, velocity with $\kappa_2/(\delta d_1)$ and temperature with $\beta_2 \delta d_1$ — then, upon applying the operators $\hat{\boldsymbol{z}} \cdot \nabla\times$ and $\hat{\boldsymbol{z}} \cdot \nabla \times \nabla\times$, the governing equations take the form

$$\frac{\partial \theta_1}{\partial t} = \beta_r^{-1} w_1 + \kappa_r^{-1} \nabla^2 \theta_1, \tag{5.49}$$

$$\frac{\partial \zeta_1}{\partial t} - \nu_r^{-1} Pr_2 \nabla^2 \zeta_1 = Pr_2 Ta_2^{1/2} \frac{\partial w_1}{\partial z}, \tag{5.50}$$

$$\frac{\partial}{\partial t}\nabla^2 w_1 - \nu_r^{-1} Pr_2 \nabla^4 w_1 = -Pr_2 Ta_2^{1/2} \frac{\partial \zeta_1}{\partial z} + \alpha_r^{-1} Ra_2 Pr_2 \nabla_H^2 \theta_1, \tag{5.51}$$

$$\frac{\partial \theta_2}{\partial t} = w_2 + \nabla^2 \theta_2, \tag{5.52}$$

$$\frac{\partial \zeta_2}{\partial t} - Pr_2 \nabla^2 \zeta_2 = Pr_2 Ta_2^{1/2} \frac{\partial w_2}{\partial z}, \tag{5.53}$$

$$\frac{\partial}{\partial t}\nabla^2 w_2 - Pr_2 \nabla^4 w_2 = -Pr_2 Ta_2^{1/2} \frac{\partial \zeta_2}{\partial z} + Ra_2 Pr_2 \nabla_H^2 \theta_2. \tag{5.54}$$

In this case, the lower layer occupies $-\delta^{-1} < z < 0$ and the upper layer occupies $0 < z < 1$.

Comparing equations (5.49)–(5.54) and (5.8)–(5.13), we observe that the equations are identical on interchanging

$$(Ta_1, Ra_1, Pr_1, k, \omega, \delta, \nu_r, \kappa_r, \beta_r, \alpha_r)$$

and

$$\left(Ta_2, Ra_2, Pr_2, \frac{k}{\delta}, \frac{\omega\kappa_r}{\delta^2}, \frac{1}{\delta}, \frac{1}{\nu_r}, \frac{1}{\kappa_r}, \frac{1}{\beta_r}, \frac{1}{\alpha_r}\right),$$

where the change in the wavenumber k to k/δ and frequency ω to $\omega\kappa_r/\delta^2$ arises from the length and time scaling. These symmetries reduce the size of the parameter space to cover; for instance, it suffices to consider the case $\delta \leq 1$, as the case with $\delta > 1$ can be recovered through symmetry arguments. Furthermore, by fixing the coefficient of thermal expansion ratio to $\alpha_r = 1$, the problem simplifies to determining the critical solutions as functions of the parameters Ta_1, Pr_1, ν_r, κ_r, and $\delta \leq 1$.

5.2.4 Limiting cases

When the fluid properties of each layer are equal, meaning $\nu_r = \kappa_r = 1$, the problem simplifies to that of classical (single-layer) rotating Rayleigh–Bénard convection, discussed in Chapter 2, with the onset of steady instabilities in the non-rotating system occurring at

$$k^c = \frac{1}{\sqrt{2}}\left(\frac{\pi}{1+\delta}\right), \qquad Ra_1^c = \frac{27}{4}\left(\frac{\pi}{1+\delta}\right)^4. \tag{5.55}$$

In the rapidly rotating limit, the critical wavenumber and Rayleigh number for steady instabilities scale as

$$k^c \sim \left(\frac{1}{2}\left(\frac{\pi}{1+\delta}\right)^2 Ta_1\right)^{1/6}, \qquad Ra_1^c \sim 3\left(\frac{1}{2}\left(\frac{\pi}{1+\delta}\right)^2 Ta_1\right)^{2/3}, \tag{5.56}$$

while oscillatory instabilities in this limit occur, when $Pr_1 < 0.677$, at

$$k^c \sim \left(\frac{Pr_1^2}{(1+Pr_1)^2}\frac{\pi^2}{2(1+\delta)^2}Ta_1\right)^{1/6}, \tag{5.57}$$

$$Ra_1^c \sim 6(1+Pr_1)\left(\frac{Pr_1^2}{(1+Pr_1)^2}\frac{\pi^2}{2(1+\delta)^2}Ta_1\right)^{2/3}, \tag{5.58}$$

$$\omega^c \sim \left(2-3Pr_1^2\right)^{1/2}\left(\frac{Pr_1^2}{(1+Pr_1)^2}\frac{\pi^2}{2(1+\delta)^2}Ta_1\right)^{1/3}. \tag{5.59}$$

For a fixed Taylor number and Prandtl number, variations in the fluid properties of the two layers give rise to four distinct limiting behaviours of the system:

1. when one layer is infinitely more thermally diffusive than the other ($\kappa_r \to \infty$ or $\kappa_r \to 0$);
2. when one layer is infinitely more viscous than the other ($\nu_r \to \infty$ or $\nu_r \to 0$);
3. when one layer is simultaneously infinitely more viscous and thermally diffusive than the other ($\kappa_r, \nu_r \to \infty$ or $\kappa_r, \nu_r \to 0$);
4. when one layer is infinitely more viscous while the other is infinitely more thermally diffusive ($\kappa_r \to 0$ and $\nu_r \to \infty$ or $\kappa_r \to \infty$ and $\nu_r \to 0$).

The limiting behaviour of ν_r in cases 2, 3, and 4, can be understood by comparing them with the results in Chapter 4, which examines the onset of linear rotating convection in a fluid layer of depth d with thermal conductivity K, bounded below by a plate and above by a solid slab of depth d' with finite conductivity K' (see figure 4.1). In this configuration, the fluid layer obeys equations (5.8)–(5.10), while the solid layer obeys $\nabla^2\theta' = 0$, where θ' is the temperature perturbation in the solid. A stress-free condition is imposed at the lower boundary of the fluid layer, and a no-slip condition at the fluid-solid interface. Fixed-temperature boundary conditions are imposed at the bottom of the fluid and the top of the solid. At the fluid-solid interface, temperature and heat flux are continuous.

In Chapter 4, we determined the critical Rayleigh number and wavenumber as functions of the depth ratio $\delta = d'/d$ and the thermal conductivity ratio $K_r = K'/K$ (analogous to κ_r in the two-fluid-layer problem). Two key limiting cases are: $K_r \to 0$ and $K_r \to \infty$. For all values of Ta, as $K_r \to 0$ (or $K_r \to \infty$), the thermal interface condition acts as a fixed-flux (or fixed-temperature) condition. Therefore, in these limits, the critical mode approaches that observed for single-layer RRBC bounded by a lower stress-free, fixed-temperature plate and an upper no-slip, fixed-flux (fixed-temperature) plate.

The limiting behaviour of κ_r (case 1) could be understood and simplified by considering an analogous problem to the one discussed in Chapter 4. Although this was not investigated here, one possible approach would be to examine the onset of convection in a fluid layer bounded below by a plate and above by an ideally thermally insulating layer. Temperature perturbations are strictly confined to the lower layer, whereas fluid motions may extend across both layers and are completely driven by the mechanical forcing at the interface.

In addition to the four limiting cases associated with ν_r and κ_r, we are also interested in the limit $Ta_1 \to \infty$, i.e., the rapidly rotating regime. In conjunction with limiting cases 2, 3, and 4, the rapidly rotating regime can be understood by comparison with the limiting behaviour of the system discussed in Chapter 4. In fact, in the three limiting cases, the critical mode approaches that observed for single-layer RRBC with stress-free, fixed-temperature boundaries as $Ta_1 \to \infty$. As shown in Chapter 3, thermal boundary conditions have little influence in the rapidly rotating regime, with Heard and Veronis (1971) finding an analogous result for mechanical boundary conditions.

5.3 Onset of non-rotating convection

In the absence of rotation, the problem outlined in this section is identical to that studied by Wilczynski and Hughes (2019) and Wilczynski (2019); the material in this section is particularly influenced by their work. We reproduce their results to verify that our code yields correct solutions, focusing on the main features of the non-rotating system pertinent to the rotating case. We emphasise that the results corresponding to figures 5.13 and 5.14 are original.

The non-rotating system is a special case of the system studied by Le Bars and Davaille (2002), in which the fluid layers are assumed to differ in depth, viscosity, and density, introducing an additional parameter called the buoyancy number B, which is a ratio of two density differences — one thermal and one chemical. The two problems are equivalent when $B = 0$. The nature of the solutions at onset, whether steady or oscillatory, depends on the value of B. In the absence of density stratification, that is, when $B = 0$, the frequency at the onset of instability approaches zero, signalling the formation of a steady mode. Therefore, in the absence of rotation, we focus on stationary convection, where $s = 0$. As a result, the Prandtl number does not influence the analysis.

When $s = 0$ and $Ta_1 = 0$, equations (5.36)–(5.41) reduce to

$$\left(\mathcal{D}^2 - k^2\right)\theta_1 = -w_1, \tag{5.60}$$

$$\left(\mathcal{D}^2 - k^2\right)^2 w_1 = k^2 Ra_1 \theta_1, \tag{5.61}$$

$$\left(\mathcal{D}^2 - k^2\right)\theta_2 = -\frac{1}{\kappa_r^2} w_2, \tag{5.62}$$

$$\left(\mathcal{D}^2 - k^2\right)^2 w_2 = \frac{1}{\nu_r} k^2 Ra_1 \theta_2, \tag{5.63}$$

and the boundary and interface conditions (5.42)–(5.44) simplify to

$$w_1 = \mathcal{D}^2 w_1 = \theta_1 = 0 \qquad \text{on} \qquad z = -1, \tag{5.64}$$

$$w_2 = \mathcal{D}^2 w_2 = \theta_2 = 0 \qquad \text{on} \qquad z = \delta, \tag{5.65}$$

$$\begin{gathered} w_1 = w_2, \qquad \mathcal{D}w_1 = \mathcal{D}w_2, \\ \theta_1 = \theta_2, \qquad \mathcal{D}\theta_1 = \kappa_r \mathcal{D}\theta_2, \\ \left(\mathcal{D}^2 + k^2\right) w_1 = \nu_r \left(\mathcal{D}^2 + k^2\right) w_2, \\ \left(\mathcal{D}^3 - 3k^2\mathcal{D}\right) w_1 = \nu_r \left(\mathcal{D}^3 - 3k^2\mathcal{D}\right) w_2, \qquad \text{on} \qquad z = 0. \end{gathered} \tag{5.66}$$

Equations (5.60)–(5.63), subject to boundary and interface conditions (5.64)–(5.66), are solved numerically using MATLAB's boundary value solver `BVP5C`, which yields the eigenfunctions w, θ, and ζ, along with the corresponding critical values Ra^c and k^c, as described in §3.2. The `BVP5C` solver provides an option to include a free parameter, making it suitable for solving eigenvalue problems, and also allows the domain to be divided into multiple regions. The domain is treated as a single interval, with interface points included in the mesh, enabling piecewise equations and interface conditions to be resolved accurately.

5.3.1 The equal layer depth configuration

We begin by examining the case where the two layers have equal thermal diffusivity, $\kappa_r = 1$, and equal depth, $\delta = 1$, and explore how variations in the viscous ratio, ν_r, affect the system. Figure 5.2 shows how the critical Rayleigh numbers, Ra_1^c, Ra_2^c, and the critical wavenumber, k^c, change with ν_r. Owing to the system's symmetry (see §5.2.3), when $\delta = 1$, the curves of Ra_1^c and Ra_2^c are reflectionally symmetric about $\nu_r = 1$ on a log scale. Similarly, k^c is symmetric about $\nu_r = 1$. Therefore, we focus on $\nu_r \geq 1$ without loss of generality. A key feature in figure 5.2 is the non-monotonic behaviour of k^c. When $\nu_r = 1$, the system corresponds to single-layer convection, where convection cells extend across the entire domain, and Ra_1^c and k^c are given by (5.55). Introducing a viscosity contrast between the layers initially decreases k^c, indicating a preference for larger convection cells. This change is accompanied by an increase in Ra_1^c and a decrease in Ra_2^c. When $\nu_r > 1$, $Ra_2^c < Ra_1^c$, indicating that the convection driving is comparatively weaker in the upper layer. Consequently, the lower layer becomes the primary source of the instability. As ν_r further increases, k^c rises sharply. At this stage, convection cells move away from the higher-viscosity upper layer, and the flow concentrates in the lower-viscosity layer. This behaviour is illustrated in figure 5.3, where the eigenfunctions are normalised such that $\max(w) = 1$; this convention is used consistently throughout the entire chapter.

As $\nu_r \to \infty$, the interface between the layers acts as a no-slip boundary, and the viscous upper layer behaves like a solid slab, with fluid motion becoming concentrated in the less viscous lower

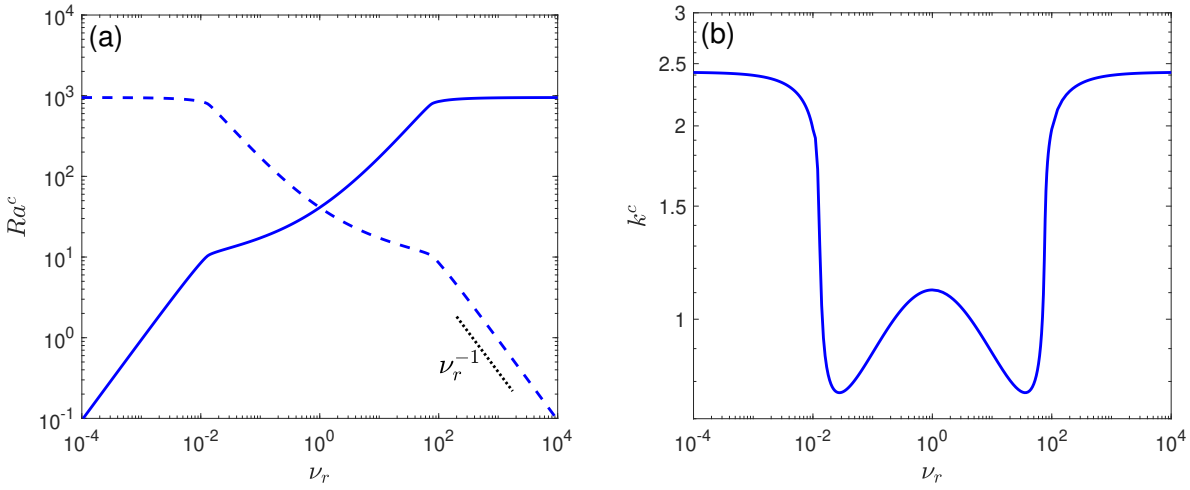
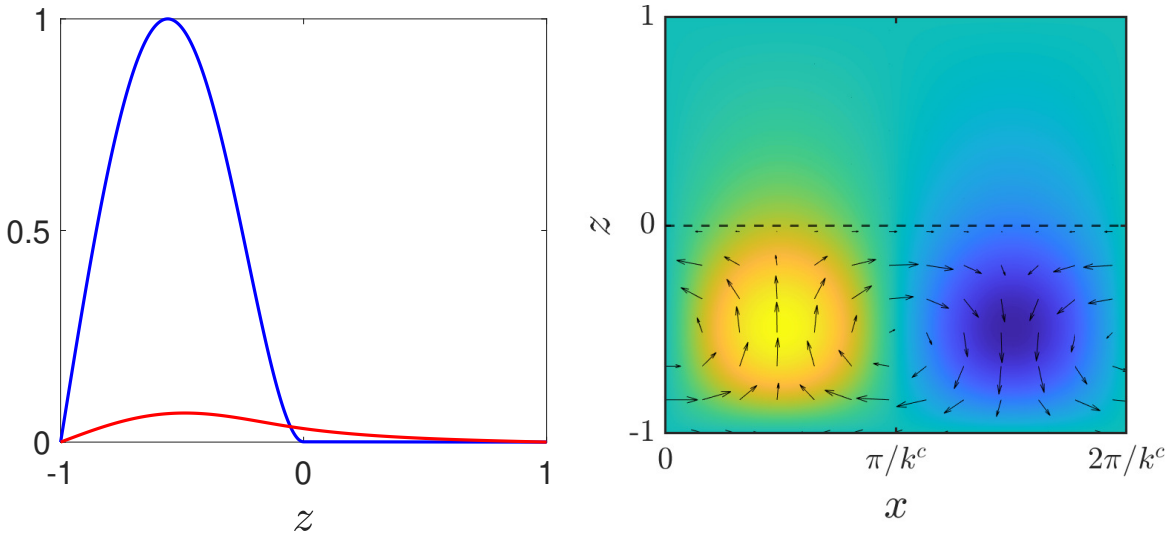


Figure 5.2: Variation of the critical (a) Rayleigh numbers, Ra_1^c (solid) and Ra_2^c (dashed), and (b) wavenumber k^c as functions of the viscosity ratio ν_r, for the case where $\delta = \kappa_r = 1$.



(a) (b)

Figure 5.3: Critical mode for $\nu_r = 10^4$ with $\delta = \kappa_r = 1$, corresponding to $k^c = 2.42$ and $Ra_1^c = 948.69$. The eigenfunctions are normalised such that $\max(w) = 1$. (a) Profiles of the eigenfunctions: vertical velocity w (blue) and temperature perturbation θ (red); (b) temperature contours and velocity vector field in the x–z plane.

layer. In this scenario, Ra_1^c and k^c converge to asymptotic values, while Ra_2^c decreases indefinitely with ν_r^{-1} (from (5.45)). The asymptotic values of Ra_1^c and k^c correspond to the onset of convection in a fluid layer bounded below by a plate and above by a solid slab of finite thermal conductivity and thickness, with the velocity at this boundary satisfying the no-slip condition. As a result, in the $\nu_r \to \infty$ limit, the problem reduces to the one studied in Chapter 4. Fluid motion in the upper layer ceases, and the dynamics are driven solely by the diffusion of the temperature perturbation (governed by $\left(\mathcal{D}^2 - k^2\right)\theta_2 = 0$).

We now examine the case of two layers with equal viscosity and depth, $\nu_r = \delta = 1$, while varying the thermal diffusivity ratio, κ_r (and consequently the temperature gradient ratio $\beta_r = \kappa_r^{-1}$). Figure 5.4 shows how the critical Rayleigh numbers, Ra_1^c and Ra_2^c, and critical wavenumber, k^c, change with κ_r. As with the case where ν_r varies, the curves of Ra_1^c, Ra_2^c, and k^c are symmetric about $\kappa_r = 1$ on a log scale, allowing us to focus on $\kappa_r \geq 1$. As $\kappa_r \to \infty$, Ra_1^c and k^c approach asymptotic values, while Ra_2^c decreases indefinitely with κ_r^{-2} (from (5.45)). The fixed-temperature condition propagates rapidly through the thermally diffusive upper layer, localising the temperature perturbation within the lower layer, as shown in figure 5.5. Fluid motion persists across the entire domain, with motion in the upper layer governed solely by $\left(\mathcal{D}^2 - k^2\right)^2 w_2 = 0$, and is completely driven by the mechanical forcing at the interface. In this limit, the problem could be understood and simplified by considering an analogous system to the one discussed in Chapter 4. Although this was not investigated here, one possible approach would be to examine the onset of convection in a fluid layer bounded below by a plate and above by an ideally thermally insulating layer.

Figure 5.6 shows how Ra_1^c, Ra_2^c, and k^c vary with respect to ν_r across different values of κ_r. The symmetry about $\nu_r = 1$ persists (with $\kappa_r \to \kappa_r^{-1}$); thus, we focus on $\nu_r \geq 1$. The non-monotonic behaviour of k^c as ν_r varies, as observed at $\kappa_r = 1$, occurs for all values of κ_r considered. When $\kappa_r > 1$, increasing ν_r from one initially causes a decrease in k^c until reaching a minimum. As ν_r is further increased, k^c exhibits a sharp rise approaching an asymptotic limit. Higher values of κ_r reduce the initial decrease in k^c, with the minimum of k^c and the subsequent sharp rise occurring at smaller ν_r. In the limit $\nu_r \to \infty$, the system can be modelled by the one in Chapter 4. As $\nu_r \to \infty$, the limiting values of Ra_1^c and k^c increase with κ_r, while Ra_2^c decreases indefinitely with ν_r^{-1}. This behaviour aligns with the findings of Chapter 4, which shows that both k^c and Ra_1^c rise with a higher solid-to-fluid thermal conductivity ratio. With ν_r held infinite, letting $\kappa_r \to \infty$ makes the viscous upper layer infinitely conducting. The interface between the layers acts as a no-slip fixed-temperature boundary. In this limit, the convection cells and temperature perturbations are confined to the layer with lower viscosity and thermal diffusivity, as shown in figure 5.7 (analogous to figure 4.3). The asymptotic values of Ra_1^c and k^c consequently align with those found in single-layer convection with a domain height of one bounded by fixed-temperature conditions, with a stress-free lower boundary

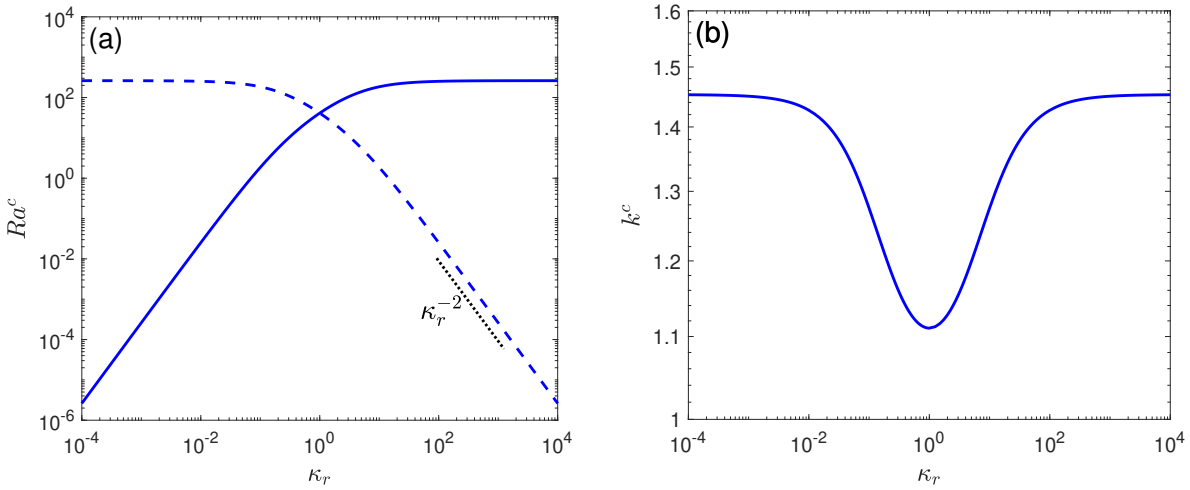
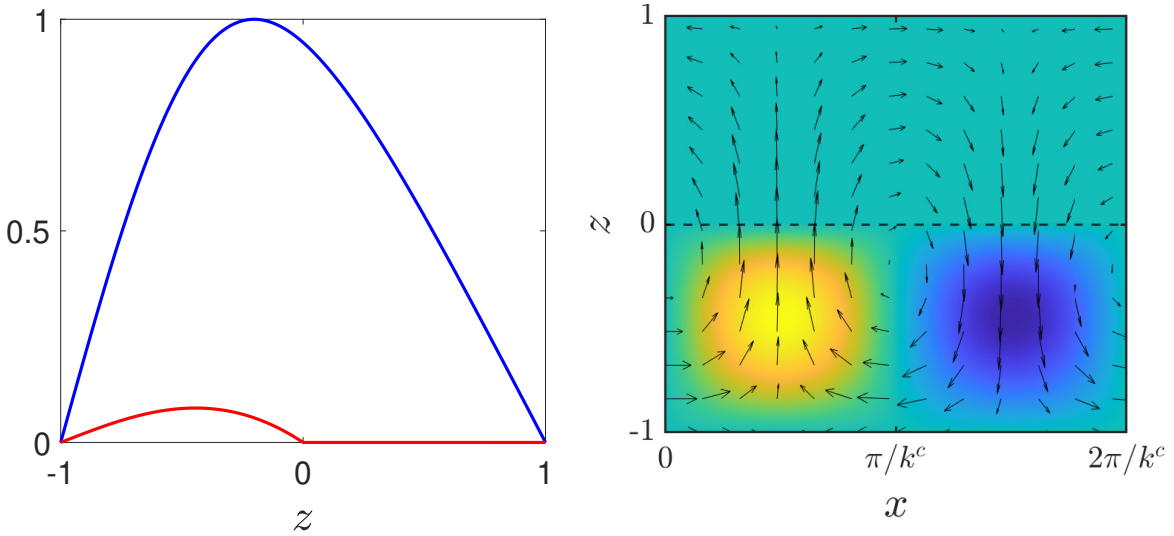


Figure 5.4: Variation of the critical (a) Rayleigh numbers, Ra_1^c (solid) and Ra_2^c (dashed), and (b) wavenumber k^c as functions of the thermal diffusivity ratio κ_r, for the case where $\delta = \nu_r = 1$.



(a) (b)

Figure 5.5: Same as figure 5.3 for $\kappa_r = 10^4$ with $\delta = \nu_r = 1$, corresponding to $k^c = 1.45$ and $Ra_1^c = 261.58$.

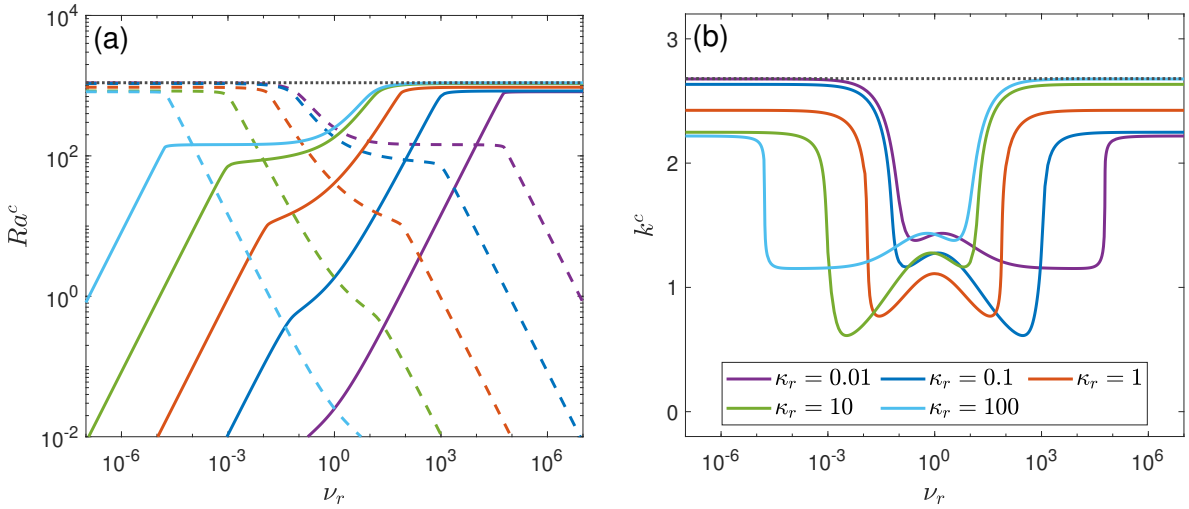


Figure 5.6: Variation of the critical (a) Rayleigh numbers, Ra_1^c (solid) and Ra_2^c (dashed), and (b) wavenumber k^c as functions of the viscosity ratio ν_r for different values of the thermal diffusivity ratio κ_r, for the case where $\delta = 1$. The dotted black line shows the critical values for single-layer convection with fixed-temperature boundaries (one no-slip, one stress-free) and a domain height of one: $Ra^c = 1100.65$ and $k^c = 2.68$.

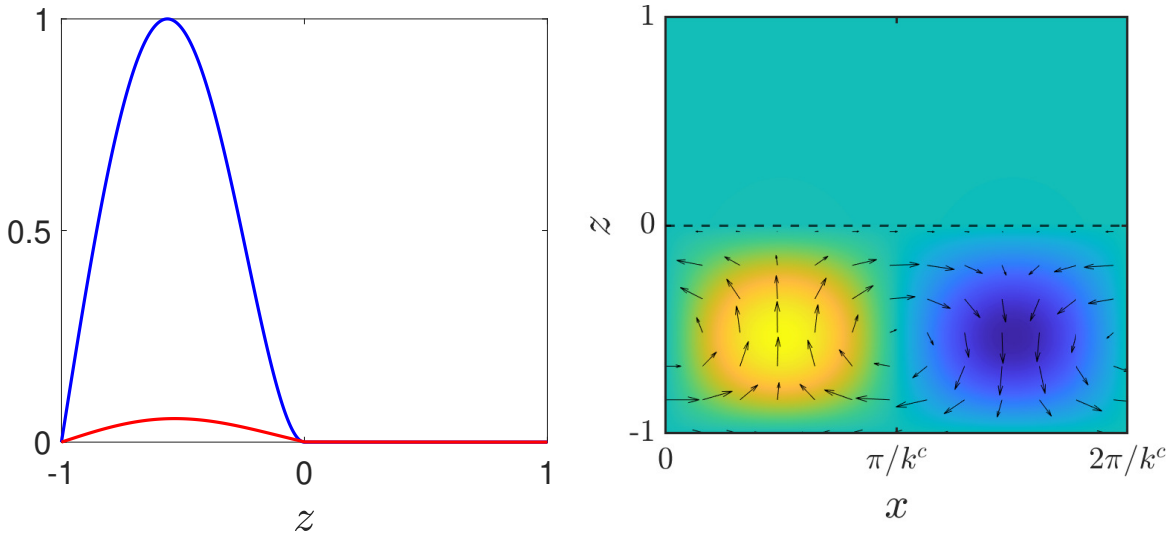


Figure 5.7: Same as figure 5.3 for $\kappa_r = 100$ and $\nu_r = 10^8$ with $\delta = 1$, corresponding to $k^c = 2.68$ and $Ra_1^c = 1097.53$.

and a no-slip upper boundary (calculated numerically):

$$Ra^c = 1100.65, \qquad k^c = 2.68. \tag{5.67}$$

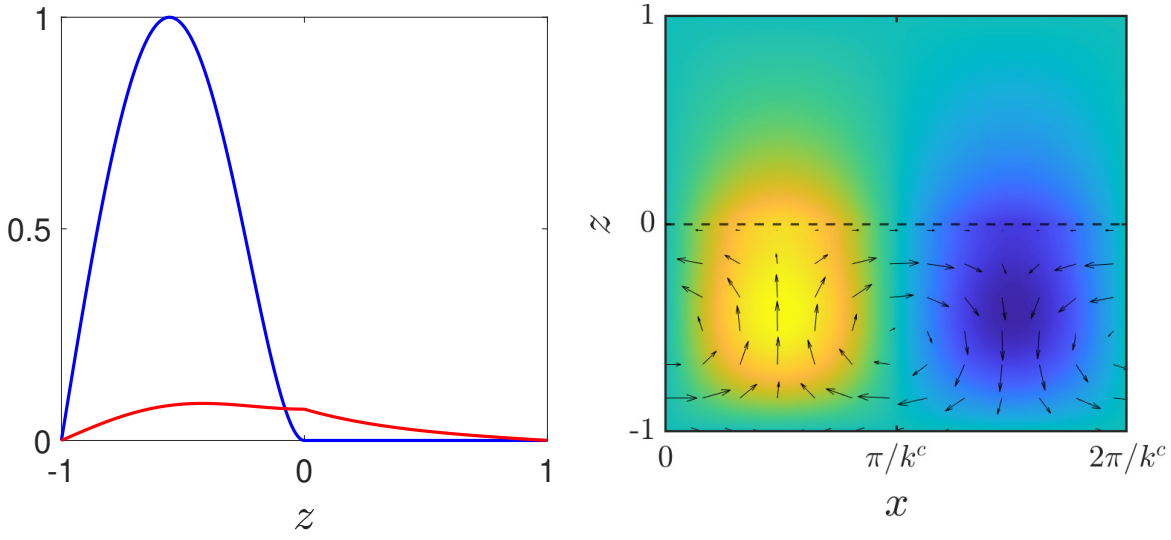
When $\kappa_r < 1$, as ν_r increases from one, k^c exhibits a small increase followed by a decrease until reaching a minimum and a sharp rise toward the asymptotic limit. Smaller values of κ_r reduce the decrease in k^c, with the minimum of k^c and the subsequent sharp rise occurring at larger ν_r. When $\nu_r \to \infty$ and $\kappa_r \to 0$, the more viscous upper layer acts as a perfect insulator. The thermal interface condition behaves as a fixed-flux condition. The asymptotic values Ra_1^c and k^c correspond to those of single-layer convection, with a stress-free fixed-temperature lower boundary and a no-slip fixed-flux lower boundary (calculated numerically): $Ra^c = 816.75$, $k^c = 2.22$. In this limit, convection cells are contained within the less viscous lower layer, whereas temperature perturbations extend across both layers, as illustrated in figure 5.8 (analogous to figure 4.4).

There exists a distinct region of parameter space, characterised by large ν_r and small κ_r, or vice versa, that gives rise to a critical mode in which the fluid motion and the temperature perturbation are spatially segregated between the two layers. Figure 5.9 presents an example of such a mode for $\nu_r = 5 \times 10^4$ and $\kappa_r = 0.01$. For sufficiently large ν_r, convection cells are confined to the less viscous layer, while the more viscous layer behaves effectively as a solid slab (see figure 5.3). Analogously, for sufficiently large κ_r, the temperature perturbation is localised within the layer of lower thermal diffusivity (see figure 5.5). As a result, the combination of large ν_r and small κ_r leads to a configuration in which fluid motion and temperature perturbations are confined to different layers. This mode does not survive in the asymptotic limit $\nu_r \to \infty$ and $\kappa_r \to 0$. As ν_r is increased, k^c undergoes a sharp increase beyond a certain threshold (see figure 5.6), and the critical mode progressively approaches its $\nu_r \to \infty$ limiting form. In this limit, the system becomes equivalent to a single fluid layer bounded by a solid slab of finite thermal conductivity and finite thickness, and the critical mode coincides with the classical convective mode for that configuration, as shown in figure 5.8.

5.3.2 The non-equal layer depth configuration

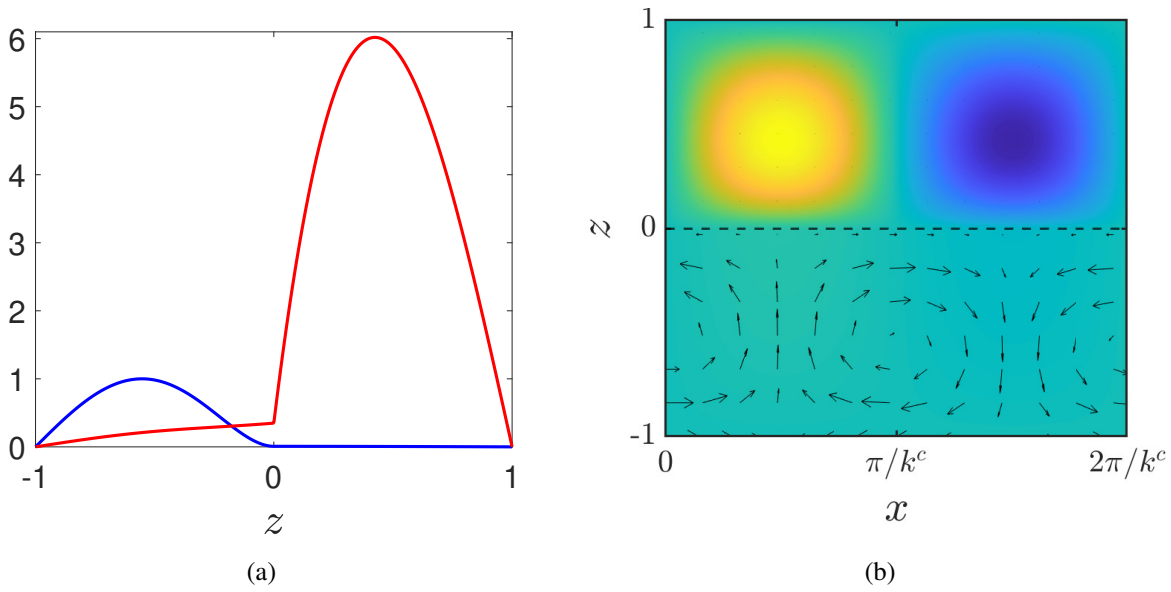
We now examine unequal layer depths, $\delta \neq 1$. Due to the system's symmetry, it is sufficient to consider the regime with $\delta < 1$, where the upper layer is always thinner than the lower one. The asymptotic behaviour with respect to ν_r and κ_r discussed in §5.3.1 remains valid when the layer depths are unequal.

Figure 5.10 shows how the critical Rayleigh numbers, Ra_1^c and Ra_2^c, and the critical wavenumber k^c vary with the viscosity ratio ν_r for several values of the depth ratio δ, with $\kappa_r = 1$. We first focus on the configuration in which the upper thin layer is more viscous, i.e., $\nu_r > 1$. For unequal layer depths, the variations of Ra_1^c, Ra_2^c, and k^c are qualitatively analogous to those obtained for equal



(a) (b)

Figure 5.8: Same as figure 5.3 for $\kappa_r = 0.01$ and $\nu_r = 10^8$ with $\delta = 1$, corresponding to $k^c = 2.22$ and $Ra_1^c = 819.15$.



(a) (b)

Figure 5.9: Same as figure 5.3 for $\kappa_r = 0.01$ and $\nu_r = 5 \times 10^4$ with $\delta = 1$, corresponding to $k^c = 1.26$ and $Ra_1^c = 688.80$.

layer depths, $\delta = 1$. When $\nu_r = 1$, the convective cell spans the entire domain, with k^c and Ra_1^c given by expression (5.55). As ν_r increases from one, k^c initially decreases, reaches a minimum, and then increases toward an asymptotic value associated with the regime in which the upper layer acts as a solid slab. As δ decreases, this increase in k^c becomes more gradual and occurs at smaller values of ν_r. The asymptotic values of Ra_1^c and k^c as $\nu_r \to \infty$ increase with decreasing δ, consistent with the findings of Chapter 4, where a detailed physical interpretation is provided (see figure 4.5). Furthermore, as $\delta \to 0$, the critical mode approaches that of single-layer convection with fixed-temperature boundaries, where one boundary is no-slip, and the other is stress-free, with Ra_1^c and k^c given by (5.67).

We now examine the case in which the thick lower layer has a higher viscosity, i.e., $\nu_r < 1$. The asymptotic behaviour as $\nu_r \to 0$ corresponds to a regime in which the lower layer acts as a solid slab. The transition to this limiting behaviour occurs at progressively smaller values of ν_r as δ decreases. Furthermore, for unequal layer depths, this transition manifests as a discontinuity in the wavenumber. Figure 5.11 shows the marginal stability curve at the point of discontinuity with $\delta = 0.5$, revealing two distinct minima and indicating two separate unstable, equally favoured modes. At the minimum with the lower wavenumber, the convective cell fills the entire domain, as shown in figure 5.12(a, b). Conversely, at the minimum with the higher wavenumber, fluid motion is confined to the less viscous layer, as shown in figure 5.12(c, d). The wavelength associated with this mode is much shorter than that of the minimum at the lower wavenumber: $2\pi/k_h^c = 1.355$ compared with $2\pi/k_l^c = 7.39$, where $k_h^c = 4.648$ corresponds to the higher wavenumber and $k_l^c = 0.847$ to the lower. The two coexisting unstable modes result from a competition between the layers, with the critical mode determined by the more favourable instability mechanism. This selection depends on whether the system preferentially develops thin, short cells confined to the lower viscosity layer or broader cells that extend into the more viscous layer.

Figure 5.13 shows the dependence of the critical Rayleigh numbers, Ra_1^c and Ra_2^c, and the critical wavenumber, k^c, on the thermal diffusivity ratio κ_r for different depth ratios δ, with $\nu_r = 1$. While the preceding results contained in this section were obtained by Wilczynski (2019) and Wilczynski and Hughes (2019), these results are novel and are not reported in either study. First, consider the case where the upper thin layer is more thermally diffusive, i.e., $\kappa_r > 1$. For unequal layer depths, the variations of Ra_1^c, Ra_2^c, and k^c are qualitatively analogous to those obtained for equal layer depths, $\delta = 1$. As κ_r increases from one, k^c and Ra_1^c rise monotonically towards their asymptotic values, while Ra_2^c decreases indefinitely with κ_r^{-2}. The asymptotic limit corresponds to the regime in which the adverse temperature gradient vanishes in the upper layer. The transition to the asymptotic regime occurs at lower κ_r values as δ decreases. As $\kappa_r \to \infty$, the asymptotic values of Ra_1^c and k^c increase with decreasing δ, tending towards the critical values observed for single-layer Rayleigh–Bénard convection with stress-free, fixed-temperature boundary conditions:

$$k^c = 2.22, \qquad Ra^c = 657.51. \tag{5.68}$$

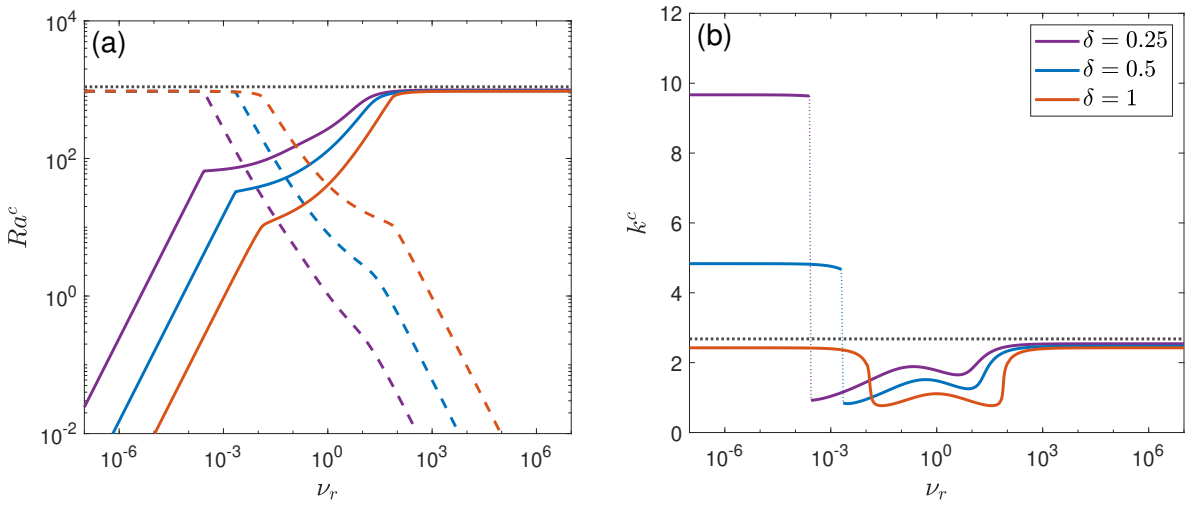


Figure 5.10: Variation of the critical (a) Rayleigh numbers, Ra_1^c (solid) and Ra_2^c (dashed), and (b) wavenumber k^c as functions of the viscosity ratio ν_r for several values of the depth ratio δ, with $\kappa_r = 1$. The dotted black line shows the critical values for single-layer convection with fixed-temperature boundaries (one no-slip, one stress-free) and a domain height of one: $Ra^c = 1100.65$ and $k^c = 2.68$.

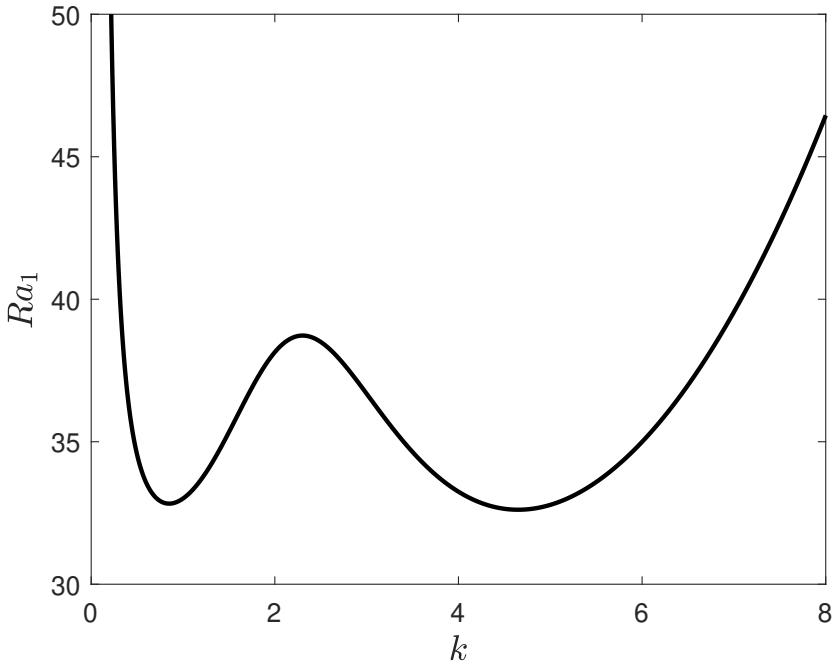


Figure 5.11: Marginal stability curve for $\nu_r = 2.217 \times 10^{-3}$ and $\delta = 0.5$, with $\kappa_r = 1$. The minima, $Ra_1^c = 32.7$, are at $k_l^c = 0.847$ and $k_h^c = 4.648$.

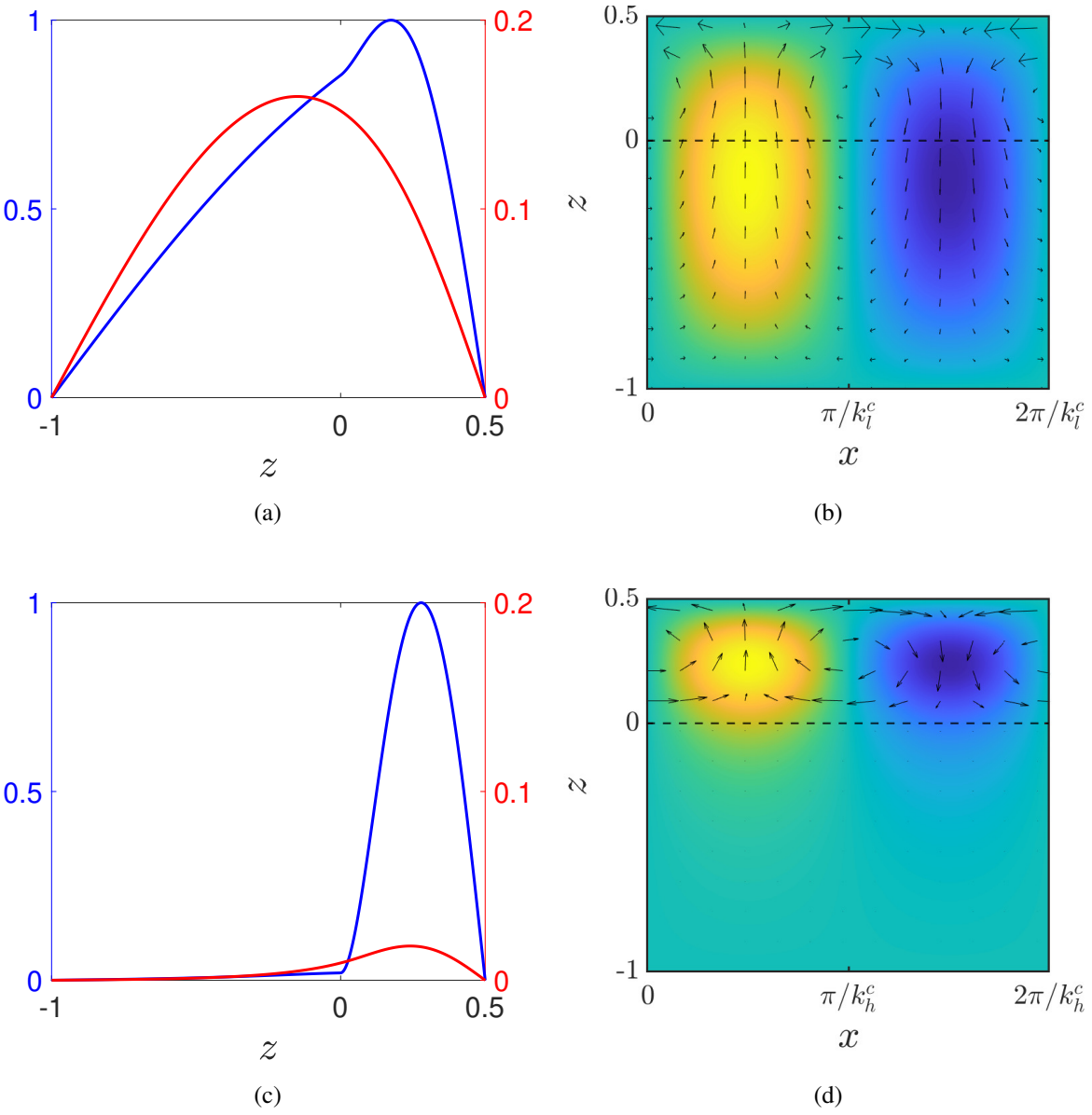


Figure 5.12: Same as figure 5.3 for $\nu_r = 2.217 \times 10^{-3}$ and $\delta = 0.5$ with $\kappa_r = 1$ corresponding to the minimum, $Ra_1^c = 32.7$, with $k_l^c = 0.847$ (top) and $k_h^c = 4.648$ (bottom) of the marginal stability curve in figure 5.11.

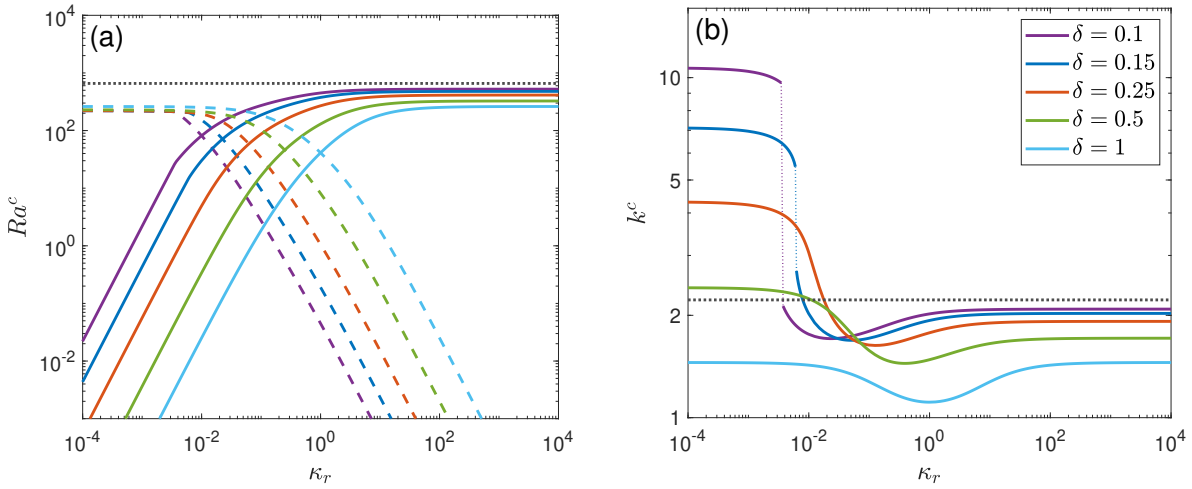


Figure 5.13: Variation of the critical (a) Rayleigh numbers, Ra_1^c (solid) and Ra_2^c (dashed), and (b) wavenumber k^c as functions of the thermal diffusivity ratio κ_r for different values of the depth ratio δ, with $\nu_r = 1$. The dotted black line shows the critical values for single-layer convection with stress-free fixed-temperature boundaries and a domain height of one: $Ra^c = 657.51$ and $k^c = 2.22$.

Now consider a less thermally diffusive thin upper layer, $\kappa_r < 1$. As $\kappa_r \to 0$, the adverse temperature gradient in the lower layer vanishes. This asymptotic regime is reached at smaller κ_r as δ decreases. For sufficiently unequal layer depths, the transition becomes a discontinuity in the wavenumber. At this discontinuity, the marginal stability curve resembles the curve for $\nu_r = 2.217 \times 10^{-3}$, $\kappa_r = 1$, and $\delta = 0.5$ in figure 5.11, with two distinct minima indicating two equally preferred unstable modes. For $\delta = 0.1$, a discontinuity occurs at $\kappa_r = 3.5 \times 10^{-3}$ for $Ra_1^c = 26.8$. At the lower-wavenumber minimum, fluid motion spans the whole domain, while temperature differences are confined to the upper layer, as shown in figure 5.14(a, b). At the higher-wavenumber minimum, motion is strongest near the interface and weaker in the lower layer, with temperature differences still confined to the upper layer but twice as large as at the lower wavenumber, as shown in figure 5.14(c, d). The wavelength of this mode is much shorter: $2\pi/k_h^c = 0.65$ versus $2\pi/k_l^c = 2.86$, where $k_h^c = 9.65$ and $k_l^c = 2.2$. Similarly to the discontinuities that arise when varying both the viscosity ratio and the depth ratio simultaneously, the two coexisting unstable modes arise from a competition between the layers, with the critical mode selected by the more efficient instability mechanism. When κ_r is small, β_r is large, implying that the adverse temperature gradient in the lower layer is weak. As κ_r initially decreases from one, the system continues to exhibit convection spanning both layers on a relatively large length scale. However, once κ_r becomes sufficiently small, a discontinuity occurs because β_r is then too large. The lower layer no longer sustains a sufficiently strong temperature gradient to drive instability. Consequently, the system abruptly transitions to a regime in which convection is confined to the upper layer, operating on a smaller length scale where a strong adverse temperature gradient is present.

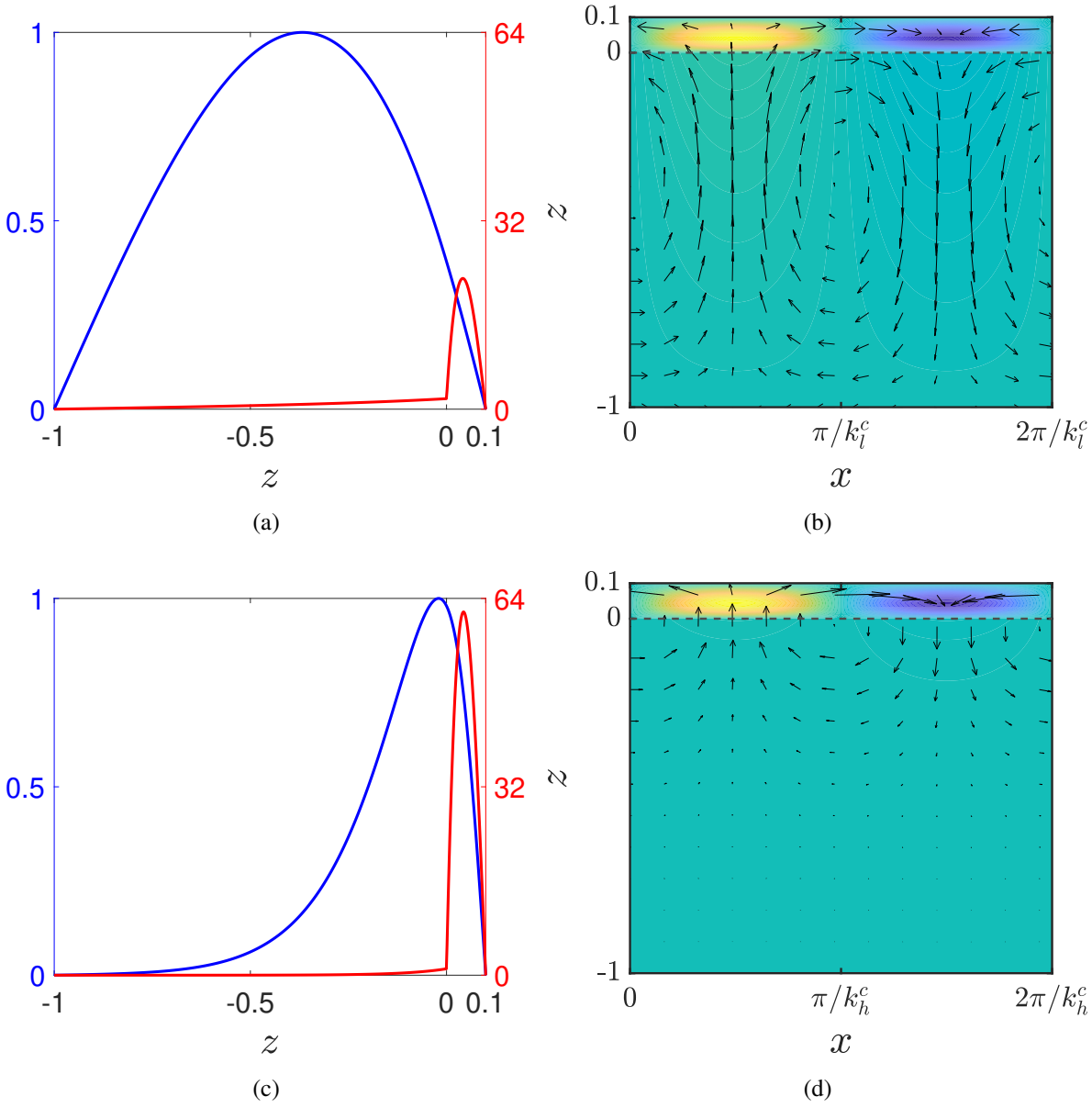


Figure 5.14: Same as figure 5.3 for $\kappa_r = 3.5 \times 10^{-3}$ and $\delta = 0.1$ with $\nu_r = 1$ corresponding to the minimum, $Ra_1^c = 26.8$, with $k_l^c = 2.2$ (top) and $k_h^c = 9.65$ (bottom) of the marginal stability curve with two equally preferred modes.

5.4 Onset of rotating steady convection

In this section, we extend the results of §5.3 to incorporate rotational effects, while continuing to focus on the onset of steady instabilities. We therefore revisit the problem governed by equations (5.36)–(5.41) and boundary conditions (5.42)–(5.44), with the growth rate set to zero, $s = 0$. As a result, the Prandtl number again does not influence the analysis. We begin by examining how variations in the thermal diffusivity ratio, for both equal and unequal layer depths, affect the onset of steady instabilities in §5.4.1. We then investigate how changes in the viscosity ratio for equal layer depths influence the onset of instability in §5.4.2.

5.4.1 Variation in the thermal diffusivity ratio

5.4.1.1 The equal layer depth configuration

We start by examining a scenario with two fluid layers of equal depth $\delta = 1$ and equal viscosity $\nu_r = 1$, and investigate the effect of varying the thermal diffusivity ratio κ_r (and consequently the temperature gradient ratio $\beta_r = \kappa_r^{-1}$) and the rotational strength Ta_1. Figure 5.15 shows the dependence of the critical Rayleigh numbers, Ra_1^c and Ra_2^c, and the critical wavenumber, k^c, on κ_r for different Taylor numbers Ta_1. The critical values are scaled via the asymptotic relations (5.56), valid for a single layer, as $Ta_1 \to \infty$: $Ra_1^c Ta_1^{-2/3}$, $Ra_2^c Ta_1^{-2/3}$, and $k^c Ta_1^{-1/6}$. The reflectional symmetry of Ra_1^c, Ra_2^c, and k^c about $\kappa_r = 1$ plotted on a log scale — as identified for $Ta_1 = 0$ in §5.3 — persists for all values of Ta_1 considered. When $\delta = \nu_r = 1$, an increase in rotational strength does not break the reflectional symmetry, because the Taylor number is independent of the thermal diffusivity and therefore, from (5.45), $Ta_1 = Ta_2$. Consequently, we restrict our analysis to $\kappa_r \geq 1$ without loss of generality. When $\kappa_r = 1$, corresponding to rotating single-layer convection, the convective cells occupy the entire vertical extent of the domain, with k^c and Ra_1^c given in (5.56), valid in the rapidly rotating limit. On increasing κ_r from one, Ra_1^c and k^c follow the same behaviour as in the non-rotating case, increasing monotonically towards asymptotic values, while Ra_2^c decreases indefinitely with κ_r^{-2} (from (5.45)). There is a slight shift towards smaller convection cells, and the less thermally diffusive layer with larger temperature gradients becomes the dominant driver of the instability.

As $\kappa_r \to \infty$, the rescaled critical mode with $Ta_1 \neq 0$ behaves qualitatively similarly to the non-rotating case ($Ta_1 = 0$) in §5.3. The fixed-temperature boundary condition rapidly penetrates through the thermally diffusive upper layer, confining temperature perturbations to the lower layer while fluid motion persists in the diffusive upper layer. Figure 5.16 ($\kappa_r = 10^4$, $Ta_1 = 10^{14}$) and figure 5.5 ($\kappa_r = 10^4$, $Ta_1 = 0$) show that the eigenfunctions are qualitatively similar, though the preferred horizontal wavelengths differ greatly: $2\pi/k^c(Ta_1 = 10^{14}) = 0.027$ and $2\pi/k^c(Ta_1 = 0) = 4.33$. Furthermore, for sufficiently large Taylor number, a thermal boundary layer of thickness $Ta_1^{-1/6}$ devel-

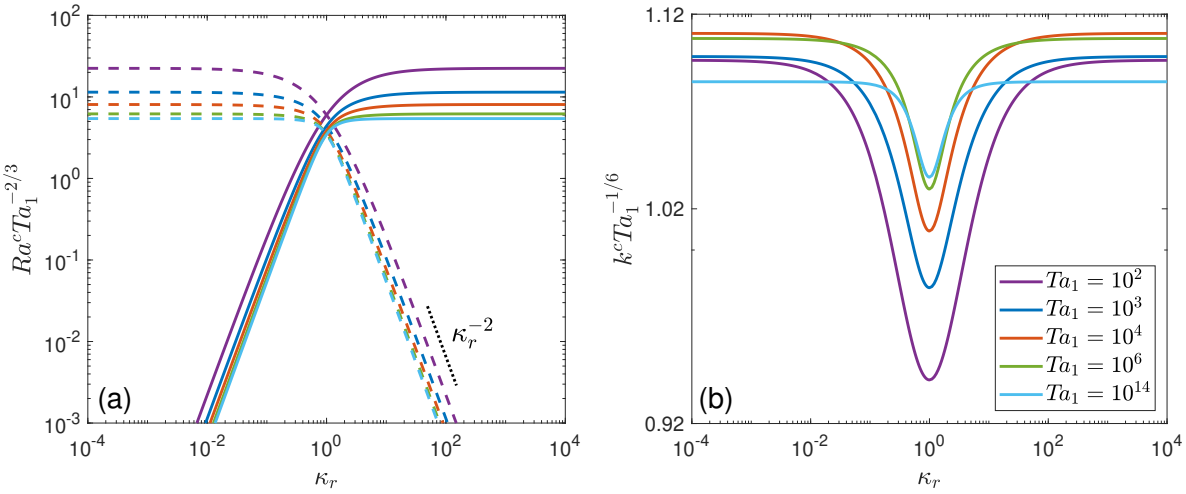
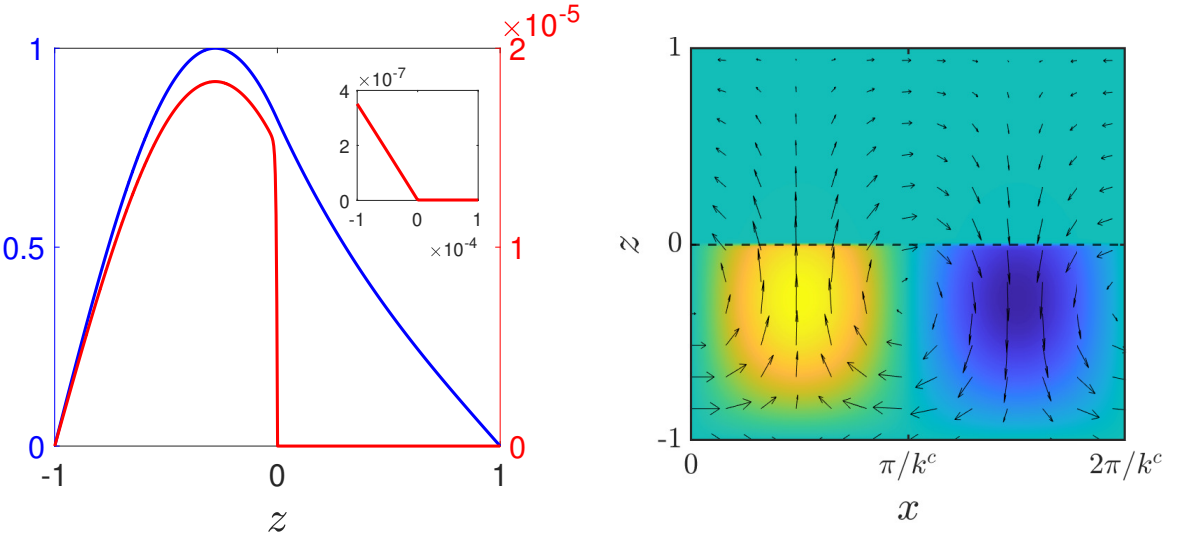


Figure 5.15: Variation of the scaled critical (a) Rayleigh numbers, Ra_1^c (solid) and Ra_2^c (dashed), and (b) wavenumber k^c as functions of the thermal diffusivity ratio κ_r, with $\delta = \nu_r = 1$, for different values of the Taylor number Ta_1.



(a) (b)

Figure 5.16: Same as figure 5.3 for $\kappa_r = 10^4$ and $Ta_1 = 10^{14}$ with $\delta = \nu_r = 1$, corresponding to $k^c = 233.59$ and $Ra_1^c = 1.17 \times 10^{10}$.

ops in the layer of lower thermal diffusivity near the interface to satisfy the interface conditions (5.44), specifically $\theta_1 = \theta_2$ and $\mathcal{D}\theta_1 = \kappa_r \mathcal{D}\theta_2$. At large κ_r, the temperature is confined to the lower layer, so the boundary layer arises at large Taylor numbers for the reasons given in Chapter 3. Under rapid rotation, a balance between Coriolis, buoyancy, and viscous terms yields a very small preferred horizontal scale, so the bulk solution is nearly independent of boundary and interface conditions.

The value of κ_r at which the system enters its $\kappa_r \to \infty$ asymptotic regime decreases with increasing Ta_1. Figure 5.17(a-c) for $Ta_1 = 10^{14}$ demonstrates that, as κ_r increases, the temperature profile develops a sharp change at the interface. In contrast, figure 5.17(d-f) for $Ta_1 = 0$ shows that the temperature perturbation exhibits only weak sensitivity to variations in κ_r when compared with the strongly rotating case $Ta_1 = 10^{14}$. In the non-rotating case, the transition to the limiting regime $\kappa_r \to \infty$ occurs gradually and extends over several orders of magnitude in κ_r. For large Ta_1, however, this transition is confined to a single order of magnitude in κ_r. Consequently, for large Ta_1 the interface enforces a fixed-temperature condition much more rapidly as κ_r increases from one, leading to a faster adjustment of the temperature profile. This behaviour is a direct consequence of strong rotation favouring very small horizontal length scales. In the limit $\kappa_r \to \infty$, θ_2 must tend to zero in order for equation (5.39) to remain balanced. In the rapidly rotating limit, the critical horizontal wavenumber scales as $k^c \sim Ta_1^{1/6}$ and is therefore large, implying that θ_2 must approach zero at substantially smaller values of κ_r. This accounts for the abrupt change in the temperature profile observed in figure 5.17.

Figure 5.18 presents the dependence of the scaled critical Rayleigh number $Ra_1^c Ta_1^{-2/3}$ and the corresponding critical wavenumber $k^c Ta_1^{-1/6}$ on Ta_1 for $\kappa_r = 1$ and $\kappa_r = 10^4$. Figure 5.15 indicates that $\kappa_r = 10^4$ is sufficiently large to be regarded as effectively representing the $\kappa_r \to \infty$ limit. For $\kappa_r = 10^4$ and $Ta_1 \to \infty$, both scaled quantities, $Ra_1^c Ta_1^{-2/3}$ and $k^c Ta_1^{-1/6}$, approach distinct asymptotic values. These asymptotic values differ from those obtained for RRBC, as well as from those predicted by any of the simplified models considered in this thesis. To characterise this asymptotic regime more systematically, the problem could be reformulated and simplified by considering an analogous configuration to the one discussed in Chapter 4. Although this analysis is beyond the scope of the present work, one plausible approach would be to examine the onset of rotating convection in a system comprising a fluid layer bounded below by a plate and above by an ideally thermally insulating layer. In such a configuration, temperature perturbations would be confined strictly to the lower fluid layer. The velocity field could extend throughout both layers, with the lower layer driven by convection and the upper layer driven solely by mechanical forcing at the interface. Investigation of this reduced system may provide insight into the dynamical behaviour emerging in the limit $\kappa_r \to \infty$.

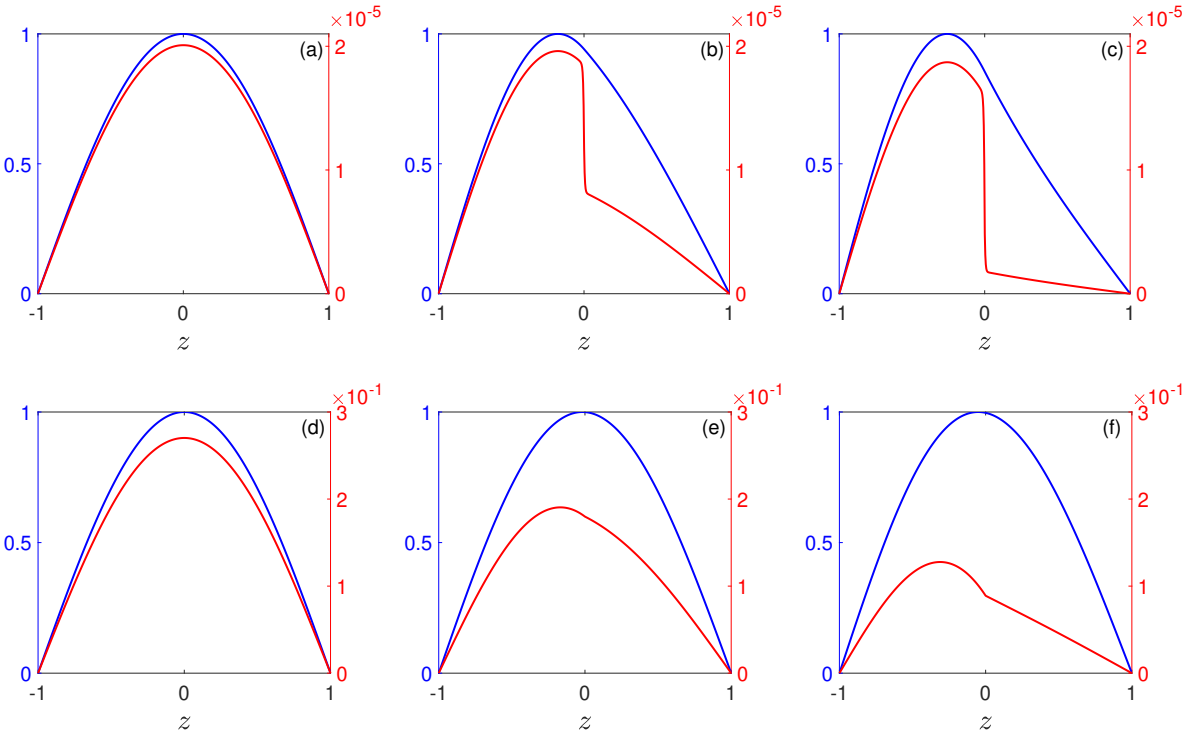


Figure 5.17: Critical mode eigenfunctions of vertical velocity w (blue) and temperature perturbation θ (red) for $\delta = \nu_r = 1$. The top row corresponds to $Ta_1 = 10^{14}$ and the bottom row to $Ta_1 = 0$. Left column: $\kappa_r = 1$, with (a) $k^c = 223.12$, $Ra_1^c = 7.44 \times 10^9$, and (d) $k^c = 1.11$, $Ra_1^c = 41.09$. Middle column: $\kappa_r = 1.5$, with (b) $k^c = 225.80$, $Ra_1^c = 9.79 \times 10^9$, and (e) $k^c = 1.12$, $Ra_1^c = 60.18$. Right column: $\kappa_r = 3$, with (c) $k^c = 231.18$, $Ra_1^c = 1.12 \times 10^{10}$, and (f) $k^c = 1.15$, $Ra_1^c = 103.08$.

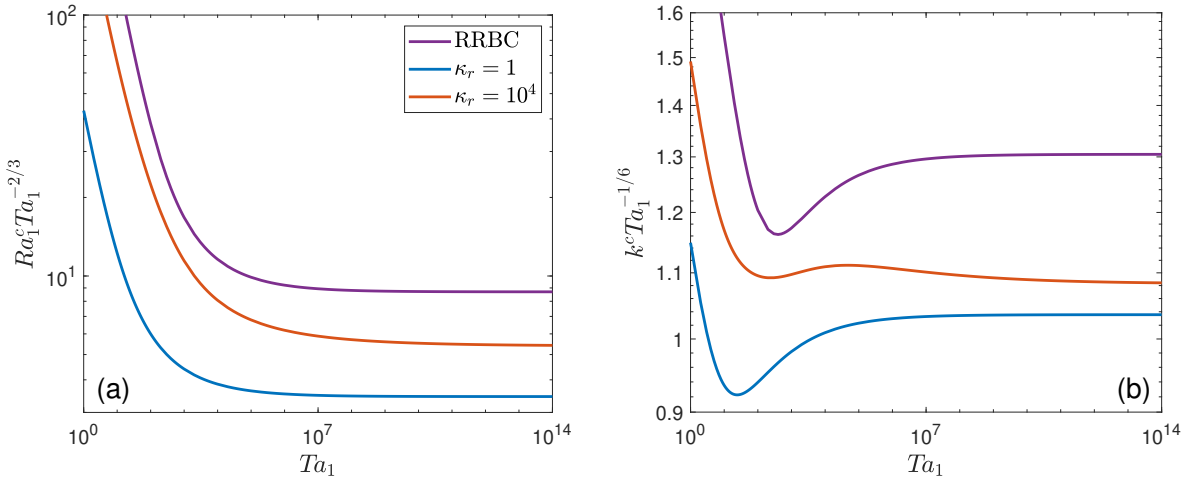


Figure 5.18: Variation of the scaled critical (a) Rayleigh number Ra_1^c, and (b) wavenumber k^c as functions of the Taylor number Ta_1, with $\delta = \nu_r = 1$, for $\kappa_r = 1$ (RRBC with domain height two) (blue) and $\kappa_r = 10^4$ (orange), and for rotating Rayleigh–Bénard convection bounded by stress-free fixed-temperature conditions with domain height one (magenta).

5.4.1.2 The non-equal layer depth configuration

We now analyse the configuration in which the two layers have unequal depths, i.e., $\delta \neq 1$. Given the system's symmetry, it suffices to consider the regime with $\delta < 1$, in which the upper layer is always thinner than the lower layer. Figure 5.19 shows the dependence of the critical Rayleigh numbers, Ra_1^c and Ra_2^c, and the critical wavenumber k^c on the thermal diffusivity ratio κ_r for several values of the depth ratio δ, with $Ta_1 = 10^{14}$ and $\nu_r = 1$. Since $\delta < 1$ and from (5.46) $Ta_2 = \delta^4 Ta_1$, the effective rotation is always weaker in the thin upper layer. The behaviour of Ra_1^c, Ra_2^c, and k^c at $Ta_1 = 10^{14}$ is qualitatively analogous to that of the non-rotating configuration discussed in § 5.3.2 (see figure 5.13). In particular, the asymptotic behaviour with respect to κ_r identified in the non-rotating case persists in the presence of rotation.

We first consider the regime in which the thinner upper layer is more thermally diffusive, i.e., $\kappa_r > 1$. In figure 5.19, as κ_r increases above one, both k^c and Ra_1^c slightly increase monotonically towards their respective asymptotic limits, whereas Ra_2^c decreases with κ_r^{-2}. Similarly to the non-rotating system, the minimum in k^c (and thus the onset of the subsequent increase towards the asymptotic regime) is attained at smaller values of κ_r as δ decreases. In contrast to the non-rotating case, however, this minimum becomes progressively less pronounced as δ is reduced. Moreover, as Ta_1 increases, the value of κ_r at which the system effectively attains its $\kappa_r \to \infty$ asymptotic regime becomes smaller, and the critical modes undergo a sudden, pronounced change in the temperature profile, analogous to the behaviour seen for the equal layer depth configuration in figure 5.17 at large Taylor numbers. In the limit $\kappa_r \to \infty$, the asymptotic values of Ra_1^c and k^c increase as δ decreases, approaching the critical values for single-layer rotating Rayleigh–Bénard convection with stress-free, fixed-temperature boundaries, given by expression (5.56) (with $\delta = 0$), which are valid in the rapidly rotating limit.

We now examine the configuration in which the thin upper layer is less thermally diffusive, i.e. $\kappa_r < 1$. In close analogy with the non-rotating system, the minimum of k^c and its subsequent increase towards an asymptotic limiting value occur at progressively smaller values of κ_r as δ decreases. This shift is accompanied by a decrease of Ra_1^c proportional to κ_r^{-2}, and, from (5.45), $Ra_2^c = \delta^4 Ra_1^c/\kappa_r^2$ tends towards its asymptotic limit. The corresponding critical Rayleigh number in the upper layer approaches asymptotic values that are several orders of magnitude smaller as δ is reduced. Since Ta_2 scales with δ^4, it follows that, at fixed κ_r, $Ra_2^c \sim Ta_2^{2/3} = \delta^{8/3} Ta_1^{2/3}$. Consequently, Ra_2^c decreases as δ decreases.

The increase of k^c towards its asymptotic limit manifests as a discontinuity for sufficiently unequal layer depths. At this discontinuity, the marginal stability curve has two distinct local minima, signalling the coexistence of two distinct yet equally preferred unstable modes. The qualitative behaviour of the critical modes at this point is analogous to that observed in the non-rotating case. For

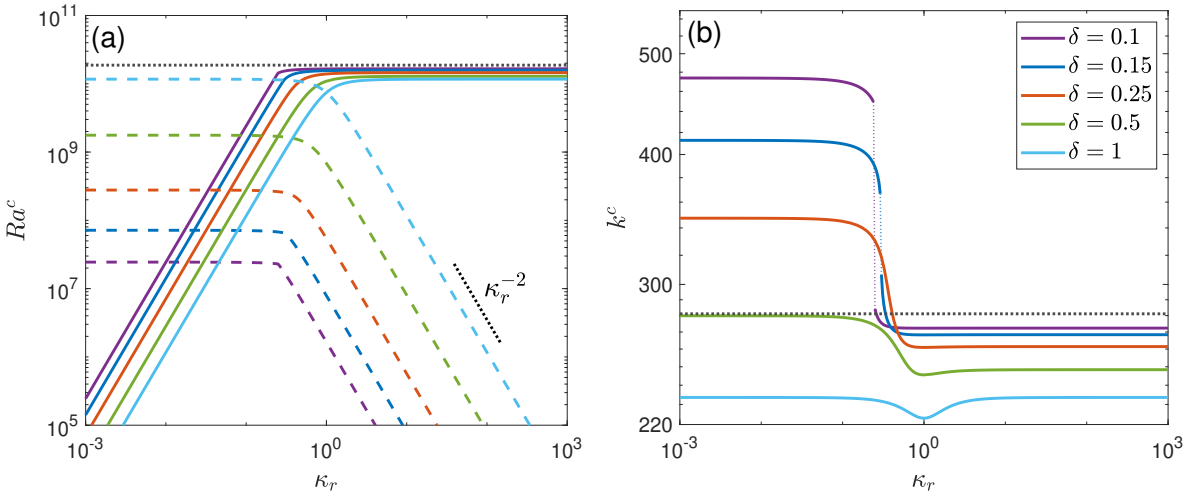


Figure 5.19: Variation of the critical (a) Rayleigh numbers, Ra_1^c (solid) and Ra_2^c (dashed), and (b) wavenumber k^c as functions of the thermal diffusivity ratio κ_r for different values of the depth ratio δ, with $\nu_r = 1$ and $Ta_1 = 10^{14}$. The dotted black line shows the critical values for single-layer convection with stress-free fixed-temperature boundaries and a domain height of one: $Ra^c = 1.87 \times 10^{10}$ and $k^c = 281.1$.

$\delta = 0.1$ and $Ta_1 = 10^{14}$ ($Ta_2 = 10^{10}$), a discontinuity occurs at $\kappa_r = 0.25$ for $Ra_1^c = 1.44 \times 10^{10}$. At the minimum associated with the lower wavenumber, the fluid motion extends throughout the entire depth of the system, while the largest temperature variations are concentrated in the upper layer, as shown in figure 5.20(a, b). In contrast to the non-rotating system, the temperature field exhibits a maximum within both layers. At the minimum corresponding to the higher wavenumber, the fluid motion is strongest near the interface and is comparatively weaker in the lower layer, with the temperature perturbations remaining confined to the upper layer, as illustrated in figure 5.20(c, d). The associated wavelength of this mode is considerably shorter: $2\pi/k_h^c = 0.022$ compared with $2\pi/k_l^c = 0.014$, where $k_h^c = 446.1$ denotes the higher wavenumber and $k_l^c = 284.2$ the lower. The two coexisting unstable modes arise from a competition between the layers. For small values of κ_r, the corresponding values of β_r become large, indicating that the adverse temperature gradient in the lower layer is weak. As κ_r is decreased slightly from one, the system continues to support convective motions that span both layers and are characterised by a large horizontal length scale. Once κ_r is reduced below a critical threshold, however, a discontinuous transition occurs because β_r becomes sufficiently large that the lower layer can no longer maintain an adverse temperature gradient strong enough to sustain instability. Consequently, the system undergoes an abrupt transition to a regime in which convection is confined to the upper layer and occurs on a smaller horizontal length scale, where a strong adverse temperature gradient is present.

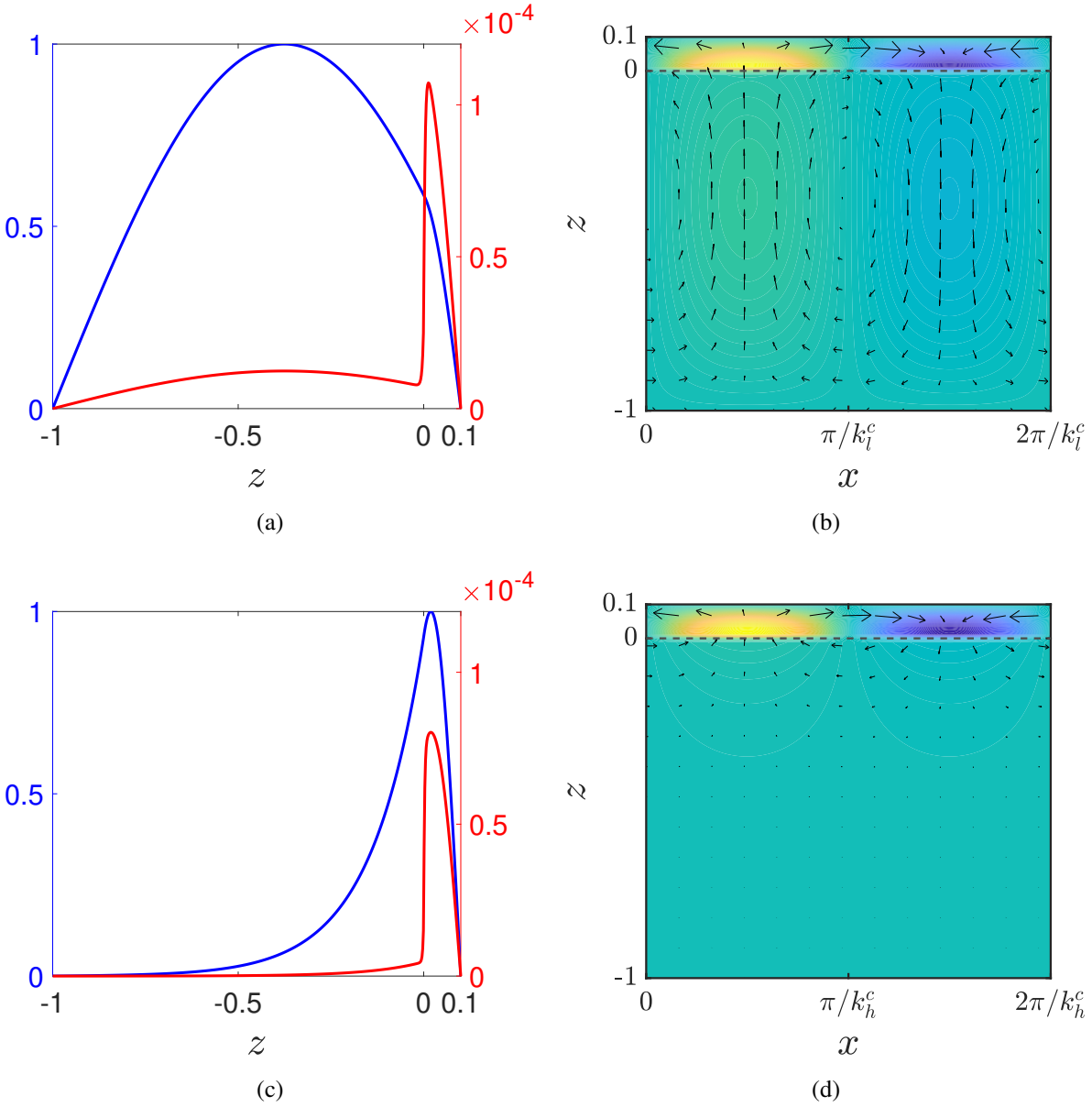


Figure 5.20: Same as figure 5.3 for $\kappa_r = 0.25$, $\delta = 0.1$, and $Ta_1 = 10^{14}$ with $\nu_r = 1$ corresponding to the minimum, $Ra_1^c = 1.44 \times 10^{10}$, with $k_l^c = 284.2$ (top) and $k_h^c = 446.1$ (bottom) of the marginal stability curve with two equally preferred modes.

5.4.2 Variation in the viscosity ratio

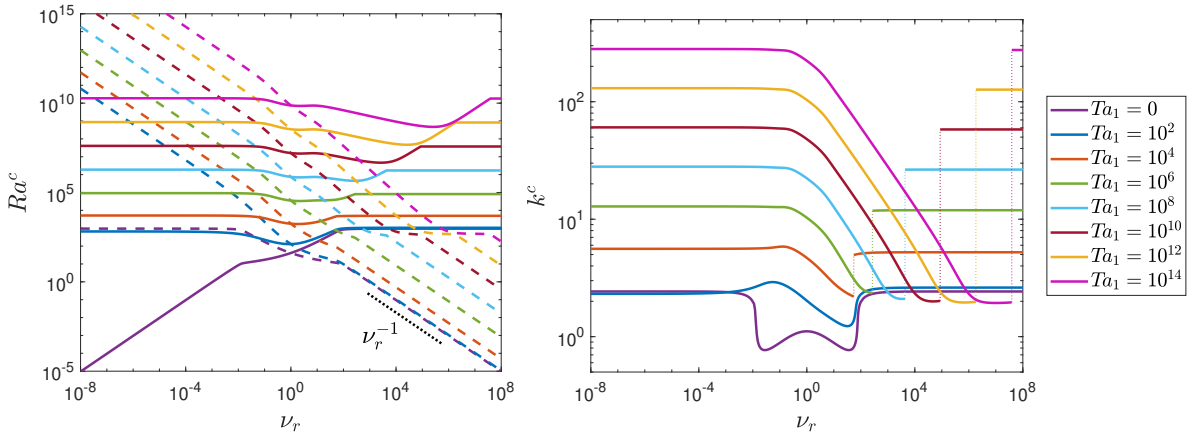
We now consider the case of two layers with equal depth $\delta = 1$ and equal thermal diffusivity $\kappa_r = 1$, and examine the effect of varying the viscosity ratio ν_r and rotation strength Ta_1. Varying ν_r affects both the effective Rayleigh number Ra_2 and Taylor number Ta_2. The reflectional symmetry of Ra_1^c, Ra_2^c, and k^c about $\nu_r = 1$ plotted on a log scale — as identified for $Ta_1 = 0$ in §5.3 — is expected to be disrupted when rotation is introduced into the system. The reflectional symmetry follows from the inherent symmetry of the system (see §5.2.3). However, since the Taylor number depends on viscosity, it follows from (5.46) that

$$Ta_2 = \frac{Ta_1}{\nu_r^2}. \tag{5.69}$$

Thus, for a fixed Ta_1, Ta_2 scales with ν_r^{-2}. The reflectional symmetry about $\nu_r = 1$ can therefore be preserved only if Ta_1 is scaled by ν_r^2 when $\nu_r < 1$, or $\nu_r > 1$.

Figure 5.21 illustrates how the critical Rayleigh numbers, Ra_1^c and Ra_2^c, along with the critical wavenumber, k^c, vary as a function of ν_r for different Taylor numbers Ta_1. The disruption of the reflectional symmetry can be seen in figure 5.21. We first examine the case where the upper layer is more viscous, i.e., $\nu_r > 1$. The interpretation of the asymptotic behaviour of Ra_1^c, Ra_2^c, and k^c in the $\nu_r \to \infty$ limit described in §5.3 also applies when rotation is added to the system. Specifically, the asymptotic behaviour in the $\nu_r \to \infty$ limit corresponds to the regime in which the interface condition behaves as a no-slip condition, and the upper layer acts as a solid slab with fluid motion confined to the less viscous lower layer. Furthermore, for a fixed Ta_1 and large ν_r, it follows from (5.69) that the resulting effective Taylor number in the upper layer is very small, e.g., if $Ta_1 = 10^{10}$ and $\nu_r = 10^8$, then $Ta_2 = 10^{-6}$. As a result, in this limit, the problem can be modelled by the system in Chapter 4. A comparison of the critical Rayleigh number Ra_1^c and wavenumber k^c as functions of the Taylor number demonstrates good agreement over the range considered between the two-fluid-layer system with $\nu_r = 10^8$ and the single-fluid-layer system bounded above by a solid slab studied in Chapter 4, as shown in figure 5.22. Furthermore, as discussed in Chapter 4, as $Ta_1 \to \infty$, the boundary slab system, and hence the two-fluid-layer system with $\nu_r = 10^8$, converges to the critical values associated with RRBC under stress-free, fixed-temperature conditions and a domain height of one.

In the absence of rotation, the transition to the $\nu_r \to \infty$ limiting behaviour is characterised by a sharp increase in k^c (see figure 5.2(b)). When rotation is sufficiently strong, the marginal stability curve develops two distinct minima, corresponding to two equally favoured unstable modes. As a result, the transition to asymptotic behaviour becomes a discontinuity. When $Ta_1 = 10^8$, the discontinuity occurs at $\nu_r = 4327$, giving $Ta_2 = 5.3$ from (5.69). The upper layer is effectively non-rotating compared to the lower layer. Since rotation inhibits convection, fluid motion localises in the layer with the smaller effective Taylor number, which, in this case, is the more viscous upper layer. The minimum at the lower wavenumber corresponds to fluid motion being restricted to the more viscous upper



(a) (b)

Figure 5.21: Variation of the critical (a) Rayleigh number within each layer: Ra_1^c (solid) and Ra_2^c (dashed), and (b) wavenumber k^c as a function of the viscosity ratio ν_r, with $\delta = \kappa_r = 1$, for different Taylor numbers Ta_1.

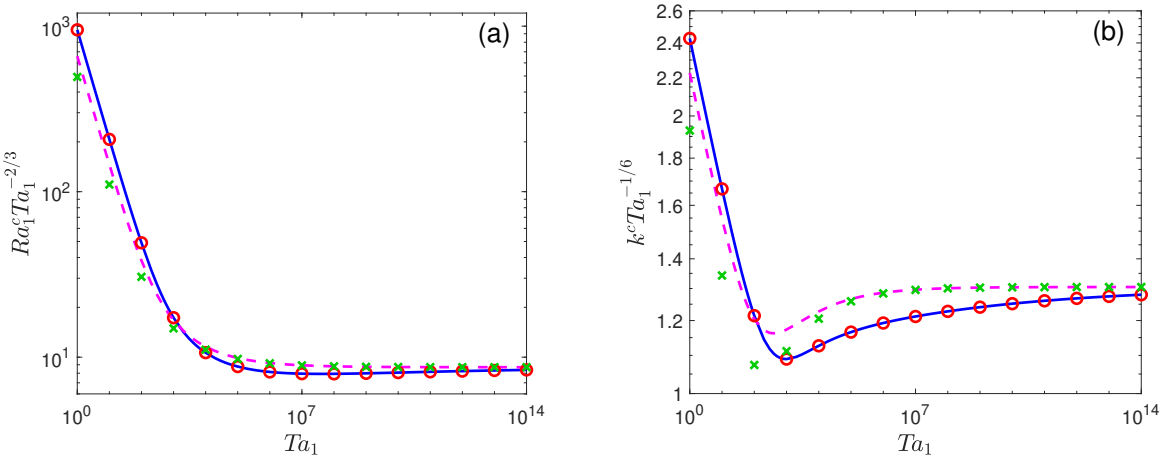


Figure 5.22: Variation of the scaled critical (a) Rayleigh number Ra_1^c, and (b) wavenumber k^c as functions of the Taylor number Ta_1 of rotating two-layer convection with $\delta = \kappa_r = 1$, $\nu_r = 10^8$ (red circles) and $\nu_r = 10^{-8}$ (green crosses), rotating Rayleigh–Bénard convection bounded by a slab of fixed conductivity (solid blue), and rotating Rayleigh–Bénard convection bounded by stress-free fixed-temperature conditions with domain height one (dashed magenta).

layer, as shown in figure 5.23(a, b). At the minimum with the higher wavenumber, fluid motion and temperature perturbations are restricted to the less viscous, strongly rotating lower layer, as shown in figure 5.23(c, d). Note that the wavelength associated with this mode is much shorter: $2\pi/k_h^c = 0.24$ compared with $2\pi/k_l^c = 2.99$, where $k_h^c = 26.4$ is the higher wavenumber and $k_l^c = 2.1$ the lower. These two coexisting unstable modes arise from a competition between the layers, with the critical mode determined by whichever layer provides the more favourable conditions. When the viscosity ratio is sufficiently small ($1 < \nu_r < 4327$ for $Ta_1 = 10^8$), strong effective rotation in the lower layer and weak effective rotation in the upper layer make the upper layer more unstable, even though it is more viscous. As viscosity in the upper layer increases, a critical point is reached at which the upper layer becomes so viscous that the weak effective rotation is no longer sufficient to maintain it as the preferred layer of instability, and a discontinuity occurs. The preferred mode shifts to the less viscous lower layer. This transition occurs at a critical ν_r that increases with Ta_1, scaling as $\nu_r \sim Ta_1^{2/3}$ (determined empirically).

Figure 5.24 shows the dependence of the critical Rayleigh number Ra_1^c and the corresponding wavenumber k^c on Ta_1 for different viscosity ratios with $\nu_r \geq 1$. The critical values are scaled via the asymptotic relations (5.56), valid as $Ta_1 \to \infty$. When first increasing Ta_1 from one, for sufficiently large ν_r, Ra_1^c and k^c approach the values associated with the $\nu_r \to \infty$ regime. On increasing Ta_1 further, a critical point is reached (for sufficiently large ν_r) at which the effective rotation in the lower layer becomes too strong for it to remain the preferred layer of instability; the preferred mode shifts into the more viscous, effectively non-rotating upper layer. Convection remains confined to the upper layer for fixed ν_r as $Ta_1 \to \infty$. It is noteworthy that for sufficiently small $\nu_r < 47$, no discontinuity in k^c occurs. Although the marginal stability curve exhibits two minima, the one associated with instability in the lower layer never becomes critical. This implies the existence of a critical value of approximately $\nu_r = 47$ above which a discontinuous jump in the preferred critical mode occurs. As $Ta_1 \to \infty$, convection remains confined to the higher viscosity, weaker effective rotation upper layer for fixed ν_r. At $Ta_1 = 10^{14}$, the critical Rayleigh numbers and wavenumber scale with the viscosity ratio, in the range $10^2 < \nu_r < 10^4$, as Ra_1^c, $k^c \sim \nu_r^{-1/3}$ and $Ra_2^c \sim \nu_r^{-4/3}$ (determined empirically). We expect this scaling to hold at higher Taylor numbers over a wider range of the viscosity ratio.

Returning to figure 5.21, we now consider the case where the lower layer is more viscous, i.e., $\nu_r < 1$. As $\nu_r \to 0$, k^c and Ra_1^c tends toward asymptotic values, while Ra_2^c increases indefinitely with ν_r^{-1}. In this limit, the lower layer becomes more viscous, while the upper layer has a larger effective Taylor number. For instance, when $\nu_r = 10^{-4}$ and $Ta_1 = 10^{14}$, (5.69) gives $Ta_2 = 10^{22}$. Although the lower layer is highly viscous, strong rotation in the upper layer inhibits convection so strongly that the instability instead favours convection in the viscous lower layer, as shown in figure 5.25. Unlike in the $\nu_r \to \infty$ limit, this regime cannot be modelled by the single-fluid-layer system bounded above by a solid slab described in Chapter 4 (see figure 5.22). At the interface, the velocity profile has a thin

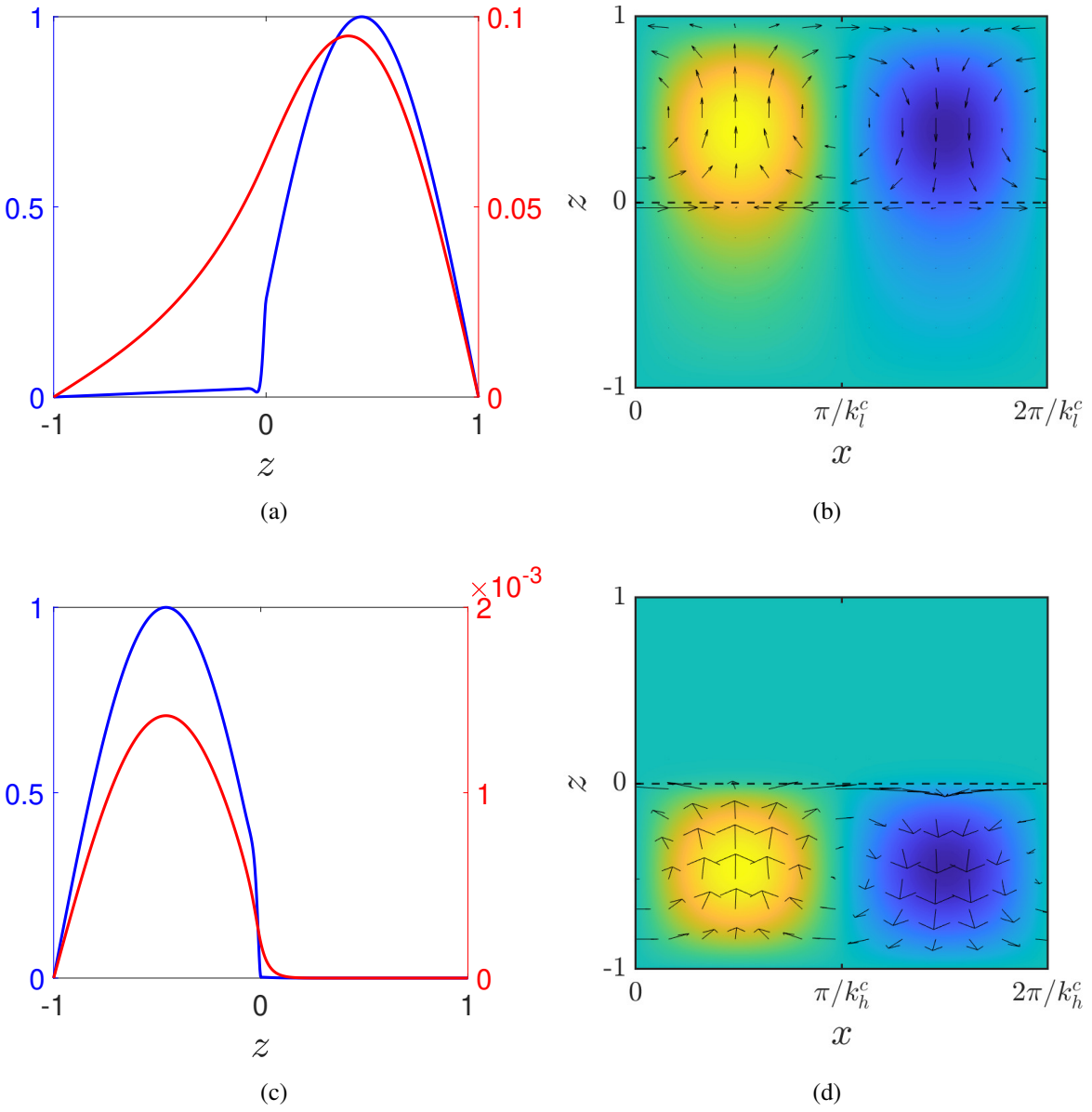
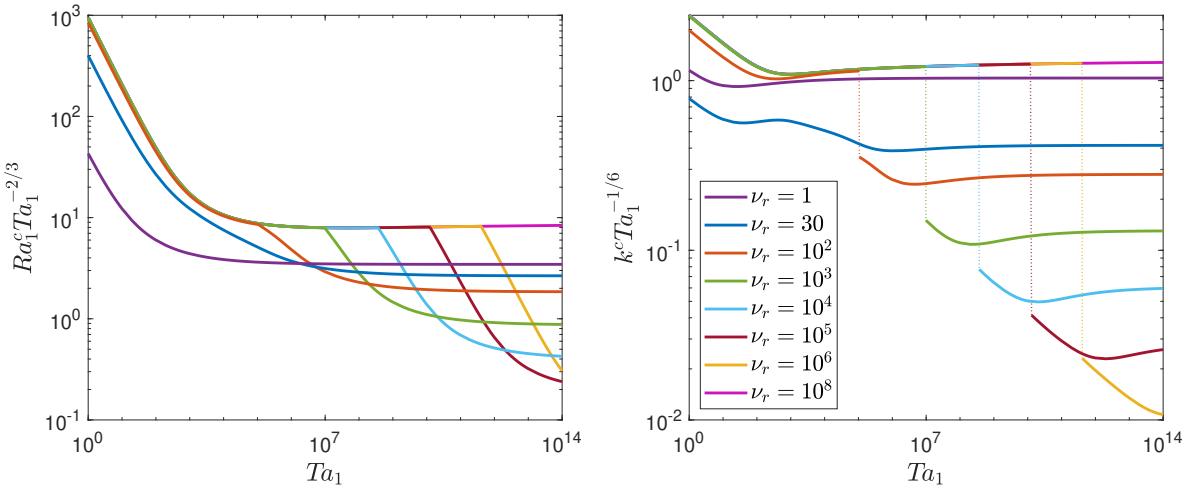
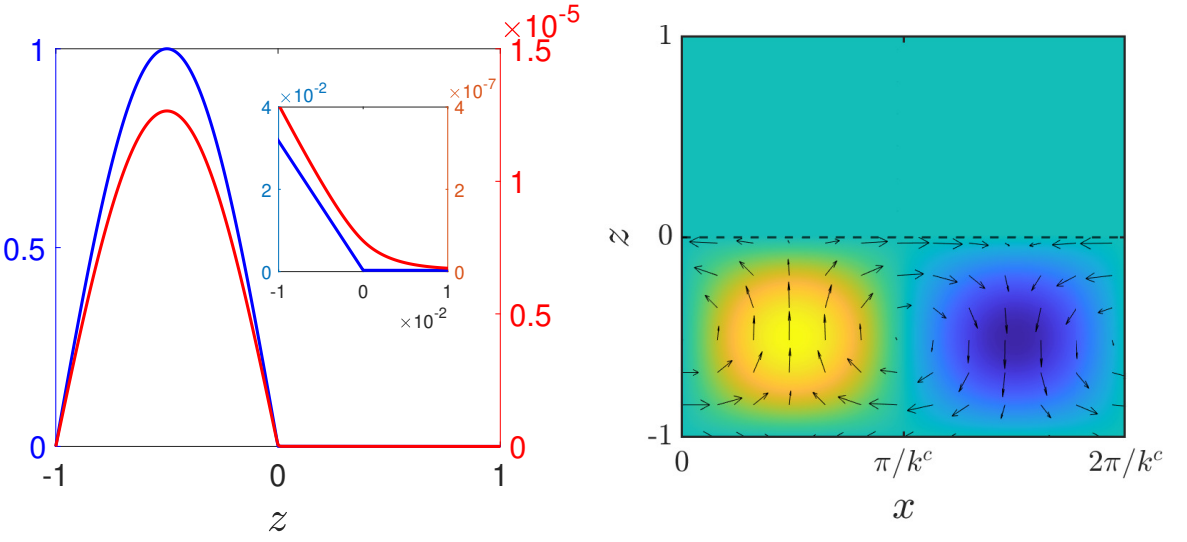


Figure 5.23: Same as figure 5.3 for $\nu_r = 4327$ and $Ta_1 = 10^8$ with $\kappa_r = \delta = 1$ corresponding to the minimum, $Ra_1^c = 1.71 \times 10^6$, with $k_l^c = 2.1$ (top) and $k_h^c = 26.4$ (bottom) of the marginal stability curve with two equally preferred modes.



(a) (b)

Figure 5.24: Variation of the (steady) scaled critical (a) Rayleigh number Ra_1^c, and (b) wavenumber k^c as functions of the Taylor number Ta_1, with $\delta = \kappa_r = 1$, for different values of the viscosity ratio $\nu_r \geq 1$.



(a) (b)

Figure 5.25: Same as figure 5.3 for $\nu_r = 10^{-4}$ and $Ta_1 = 10^{14}$ with $\delta = \kappa_r = 1$, corresponding to $k^c = 281.09$ and $Ra_1^c = 1.87 \times 10^{10}$.

boundary layer, which cannot be seen on the scale shown in figure 5.25. Fluid motion is confined to the viscous layer — something that would be impossible in the system of Chapter 4.

For a sufficiently large Ta_1, the critical mode in the two limiting cases $\nu_r \to 0$ and $\nu_r \to \infty$, results in convection being confined to the lower layer, although for fundamentally different physical reasons. In the limit $\nu_r \to \infty$, it is the high viscosity of the upper layer that confines convection to the lower layer. In contrast, in the limit $\nu_r \to 0$, although the lower layer is highly viscous, the strong rotation in the upper layer inhibits convection so effectively that the instability instead develops in the viscous lower layer.

A subsequent step would be to examine how changes in both the viscosity ratio and the depth ratio influence the onset of steady instabilities. Nonetheless, because multiple modes can become unstable simultaneously when the viscosity ratio is varied with equal layer depths, as shown in figure 5.21, and because several unstable modes may also occur for unequal layer depths as in the non-rotating system in §5.3.2, this problem is considerably more intricate and is therefore deferred to future work.

5.5 Onset of rotating oscillatory convection

In this section, we consider the case of overstable systems in which convection manifests as an oscillatory instability. The marginal state is then characterised by a complex growth rate with a zero real part and a non-zero imaginary part. Therefore, we set $s = i\omega$, where $\omega \in \mathbb{R}$ denotes the oscillation frequency, in equations (5.36)–(5.41) and boundary conditions (5.42)–(5.44). In this case, the Prandtl number strongly influences the onset of oscillatory behaviour. Throughout this section, we restrict our attention to configurations with equal layer depths, setting $\delta = 1$. We first analyse how simultaneous variations in the thermal diffusivity ratio, Prandtl number and Taylor number influence the onset of oscillatory instabilities in §5.5.1. In particular, we focus on the role of the transitional Prandtl number, Pr_1^t, which defines the threshold below which oscillatory modes are preferred. We subsequently explore how simultaneous changes in the viscosity ratio, Prandtl number and Taylor number affect the onset of instability in §5.5.2. Throughout, quantities associated with steady instabilities are denoted by a subscript s, while those corresponding to oscillatory instabilities are denoted by a subscript o.

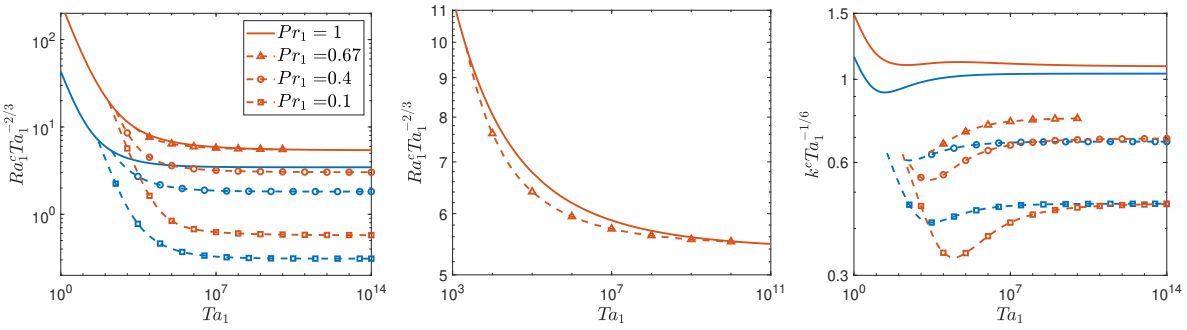
Equations (5.36)–(5.41), subject to boundary conditions (5.42) and (5.44) are solved using MATLAB's boundary value solver `BVP5C`. The same type of code allows the domain to be divided into multiple regions while simultaneously handling complex-valued solutions. In the steady system, there is a single free parameter, Ra_1, whereas in the oscillatory system, two parameters, Ra_1 and ω, must be determined. This issue is addressed by decomposing the solutions and boundary conditions into their real and imaginary components, thereby providing sufficient boundary conditions to determine both free parameters.

5.5.1 Variation in the thermal diffusivity ratio

We start by examining a scenario with two fluid layers of equal viscosity, $\nu_r = 1$. Figure 5.26 shows the asymptotically scaled critical Rayleigh number, $Ra_1^c Ta_1^{-2/3}$, and wavenumber, $k^c Ta_1^{-1/6}$, as functions of the Taylor number, Ta_1, evaluated at $\kappa_r = 1$ (single-layer) and $\kappa_r = 10^3$, for the onset of steady convection, and oscillatory convection ($Pr_1 = 0.1,\ 0.4,\ 0.67$), only when oscillatory modes are favoured at the specified Ta_1. As with the steady system, it follows from (5.46) that $Ta_1 = Ta_2$. Furthermore, it follows from (5.47) that for a fixed Pr_1, Pr_2 scales with κ_r^{-1}. Thus, when $\kappa_r = 10^3$, the Prandtl number in the upper layer is three orders of magnitude smaller than the Prandtl number in the lower layer.

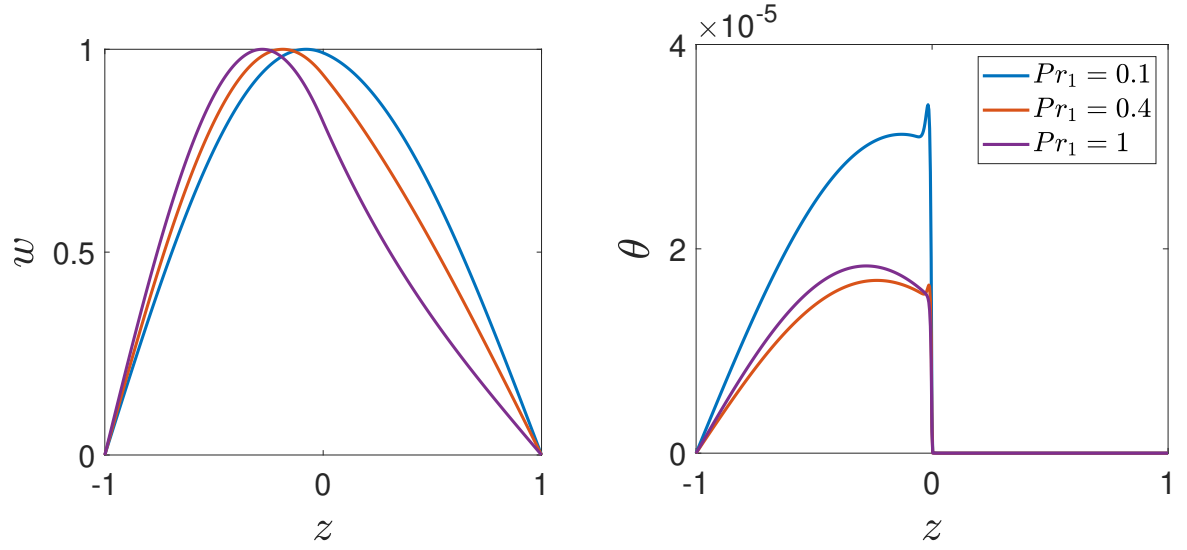
Similarly to the steady system, in the simultaneous limits $\kappa_r \to \infty$ and $Ta_1 \to \infty$, the scaled critical values $Ra_{1o}^c Ta_1^{-2/3}$ and $k_o^c Ta_1^{-1/6}$ at a fixed Prandtl number (with $Pr_1 \lesssim 0.66$) tend towards asymptotic values. These correspond to a mode in which temperature perturbations are confined to the less thermally diffusive lower layer. Fluid motion persists across both layers, with the lower layer driven by convection and the upper layer driven solely by mechanical forcing at the interface. Figure 5.27 presents profiles of the vertical velocity and temperature for the steady ($Pr_1 = 1$) and oscillatory ($Pr_1 = 0.1,\ 0.4$) critical modes at $\kappa_r = 10^3$ and $Ta_1 = 10^{14}$. For sufficiently large Ta_1, a thermal boundary layer develops within the layer of lower thermal diffusivity near the interface in order to satisfy the thermal interface conditions in (5.44), specifically $\theta_1 = \theta_2$ and $\mathcal{D}\theta_1 = \kappa_r \mathcal{D}\theta_2$. Within this boundary layer, the temperature profile of the oscillatory modes exhibits a maximum with sharper gradients as Pr_1 decreases. Moreover, the maximum of the velocity profile shifts closer to the midpoint of the domain $z = 0$ as Pr_1 decreases.

For a fixed Taylor number, there exists a transitional Prandtl number, Pr_1^t, that indicates the threshold below which oscillatory modes are preferred. Specifically, when $Pr_1 > Pr_1^t$, steady modes are preferred, whereas for $Pr_1 < Pr_1^t$, oscillatory modes are favoured. At a fixed Ta_1, the value of Pr_1 at which the oscillatory and steady branches of Ra_1^c intersect defines the transitional Prandtl number. The relationship between the Taylor number and the transitional Prandtl number can be explicitly expressed for the single-layer RRBC system with stress-free, fixed-temperature boundaries, as given by Kloosterziel and Carnevale (2003) and Hughes et al. (2022) (see equation (2.99) and figure 2.3). In this single-layer scenario, Pr_1^t increases monotonically with the Taylor number, approaching an asymptotic critical value $Pr_1^c = 0.67659$ as $Ta_1 \to \infty$. Thus, in figure 5.26(a), for $Pr_1 < Pr_1^c$, the oscillatory and steady branches of Ra_1^c intersect exactly once. However, when there is a significant thermal diffusivity contrast between the layers and Pr_1 is sufficiently large, the oscillatory and steady branches of Ra_1^c intersect twice, as shown in figure 5.26(b) for $\kappa_r = 10^3$ and $Pr_1 = 0.67$. In this case, the transitional Prandtl numbers are equal at two distinct Taylor numbers.



(a) (b) (c)

Figure 5.26: Asymptotically scaled critical (a) Rayleigh number $Ra_1^c Ta_1^{-2/3}$, (b) Rayleigh number in the range $Ra_1^c Ta_1^{-2/3} = 5$ to $Ra_1^c Ta_1^{-2/3} = 11$, and (c) wavenumber $k^c Ta_1^{-1/6}$ as functions of the Taylor number Ta_1 for $\kappa_r = 1$ (blue) and $\kappa_r = 10^3$ (orange), with $\nu_r = \delta = 1$, for the onset of steady ($Pr_1 = 1$) and oscillatory ($Pr_1 = 0.1,\ 0.4,\ 0.67$) convection.



(a) (b)

Figure 5.27: Profiles of the (a) vertical velocity w and (b) temperature perturbation θ of the critical modes for $\kappa_r = 10^3$ and $Ta_1 = 10^{14}$ with $\delta = \nu_r = 1$ for steady ($Pr_1 = 1$) and oscillatory ($Pr_1 = 0.1,\ 0.4$) modes. The eigenfunctions are normalised such that $\max(w) = 1$. The corresponding critical wavenumbers and critical Rayleigh numbers are: (1) $Pr_1 = 1$: $k_s^c = 233.6$, $Ra_{1s}^c = 1.17 \times 10^{10}$; (2) $Pr_1 = 0.1$: $k_o^c = 100.1$, $Ra_{1o}^c = 1.24 \times 10^9$; (3) $Pr_1 = 0.4$: $k_o^c = 149.7$, $Ra_{1o}^c = 6.53 \times 10^9$.

The transitional Prandtl number can be evaluated using a numerical iterative method, which yields the value of Pr_1 at which the critical Rayleigh numbers corresponding to the steady and oscillatory branches are equal. Figure 5.28 presents the transitional Prandtl number, Pr_1^t, as a function of the Taylor number, Ta_1, for $\nu_r = 1$ and several values of κ_r. For $\kappa_r = 1$, the system behaves effectively as a single-layer configuration, thus Pr_1^t can be obtained from equation (2.99) with the domain height set to two. In this case, $Pr_1^c = 0.67659$ independently of the domain height, implying that oscillatory modes are preferred for $Pr_1 < Pr_1^c$ in the asymptotic regime $Ta_1 \gg 1$, whereas for $Pr_1 > Pr_1^c$, instabilities will always manifest as stationary convection. As $Pr_1 \to 0$, the Taylor number approaches an asymptotic critical value Ta_1^c that indicates the threshold below which steady modes are preferred for all Prandtl numbers. By equation (2.99), the critical Taylor number in the RRBC system decreases with increasing domain height; for a domain height of two, one obtains $Ta_1^c = 34.04$.

For $1 \leq \kappa_r \lesssim 1.5$, Pr_1^t increases for all values of Ta_1 considered, and the corresponding curves retain strictly monotonic behaviour. For $\kappa_r \gtrsim 1.5$, however, the dependence of Pr_1^t on Ta_1 becomes non-monotonic as the curve develops a distinct maximum before decreasing towards a distinct asymptotic value as $Ta_1 \to \infty$. As a consequence, for values of Pr_1^t that lie between this asymptotic value and the maximum, there exist two distinct Taylor numbers that yield the same transitional Prandtl number. This feature is corroborated by figure 5.26, in which the oscillatory and steady branches of the critical Rayleigh number intersect twice. Moreover, the existence of a maximum necessarily implies the presence of an optimal Taylor number at which Pr_1^t is maximised. From figure 5.28, it is observed that this optimal Taylor number lies between $10^3 < Ta_1 < 10^6$. Furthermore, there exists an optimal thermal diffusivity ratio at which Pr_1^t is maximised and from figure 5.28, it is observed that this optimal thermal diffusivity ratio occurs at $\kappa_r \approx 3$. Hence, oscillatory modes are favoured at the highest Prandtl number for a particular, optimal Taylor number and thermal diffusivity ratio.

In the limit $Ta_1 \to \infty$, the transitional Prandtl number Pr_1^t attains distinct asymptotic values depending on the value of κ_r. As κ_r increases from one, the asymptotic value of Pr_1^t initially increases, reaching a maximum (occurring at $\kappa_r \approx 1.5$, as seen in figure 5.28), and subsequently decreases. In the limit $\kappa_r \to \infty$, the asymptotic value of Pr_1^t approaches the value corresponding to the regime in which the temperature perturbation is confined to the lower layer, as illustrated in figure 5.27 for $\kappa_r = 10^3$, $Ta_1 = 10^{14}$, and $Pr_1^t = 0.665$. Figure 5.28 further demonstrates that, in the limit $\kappa_r \to \infty$, this asymptotic value of Pr_1^t is slightly smaller than that of the corresponding single-layer system.

Figure 5.29 illustrates how the critical wavenumber k_o^c, transitional Prandtl number Pr_1^t, and critical frequency ω^c vary as functions of the thermal diffusivity ratio κ_r, at various values of Ta_1. Firstly, it is important to note that, by definition, the critical Rayleigh number of the oscillatory mode with $Pr_1 \equiv Pr_1^t$ equals that of the corresponding steady mode, shown in figure 5.15(a). As in the steady system discussed in §5.4.1.1 and the non-rotating system in §5.3.1, the quantities k_o^c, Pr_1^t, and Pr_2^t display a reflection symmetry about $\kappa_r = 1$ when plotted on a log scale. The critical frequency

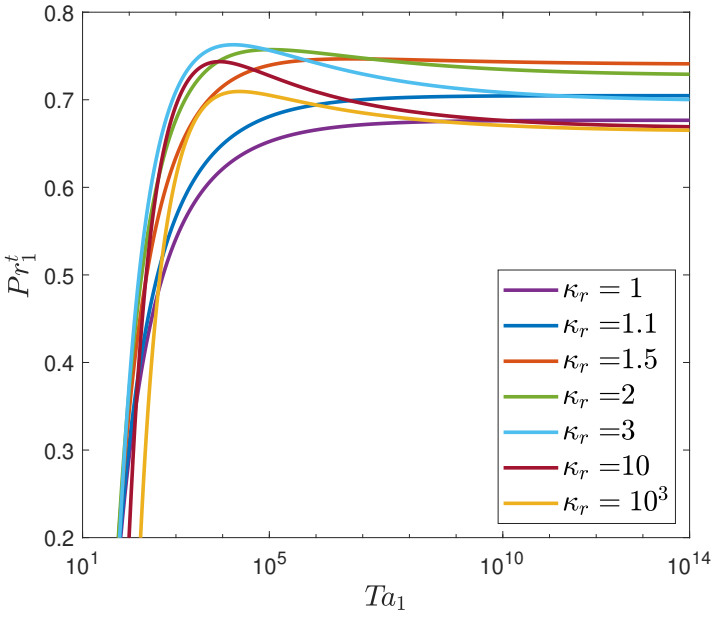


Figure 5.28: The transitional Prandtl number Pr_1^t as a function of the Taylor number Ta_1 with $\delta = \nu_r = 1$, for different κ_r values.

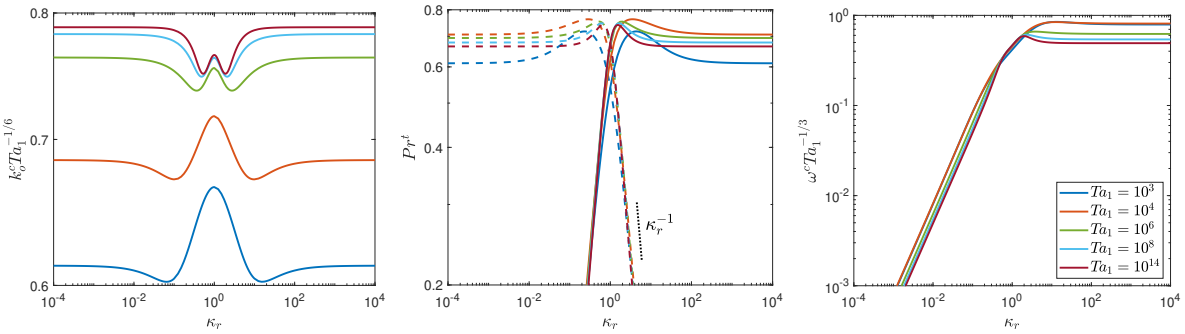
ω^c does not exhibit any symmetry around $\kappa_r = 1$, however. These properties stem from an inherent symmetry of the governing system, detailed in §5.2.3, under the interchange

$$(Ta_1, Ra_1, Pr_1, k, \omega, \kappa_r) \qquad \text{and} \qquad \left(Ta_2, Ra_2, Pr_2, k, \omega\kappa_r, \frac{1}{\kappa_r}\right),$$

with $\delta = \nu_r = 1$. Since the frequency depends explicitly on κ_r, it does not possess the same reflection symmetry.

For a fixed and sufficiently large Ta_1, increasing κ_r from one initially leads to a decrease in k_o^c, signalling a preference for larger convection cells. After reaching a minimum, k_o^c subsequently increases, indicating a transition towards smaller cells, then approaches an asymptotic value. This behaviour is accompanied by an increase in Ra_{1o}^c towards an asymptotic limit, while Pr_1^t rises to a maximum before decreasing to its asymptotic value, consistent with figure 5.28. Meanwhile, both Ra_{2o}^c and Pr_2^t decrease monotonically with κ_r^{-2} and κ_r^{-1}, respectively.

As in the steady system, the value of κ_r at which the system enters the $\kappa_r \to \infty$ asymptotic regime decreases with increasing Ta_1. In contrast to the steady system, where k_s^c in the limit $\kappa_r \to \infty$ exceeds its corresponding value at $\kappa_r = 1$ (the single-layer case) for all Ta_1, the asymptotic value of k_o^c only gradually surpasses its $\kappa_r = 1$ value as Ta_1 increases. This implies that, for moderate Ta_1, oscillatory modes in the $\kappa_r \to \infty$ limit favour larger wavelengths than in the single-layer configuration, whereas for sufficiently large Ta_1 they instead favour smaller wavelengths.



(a) (b) (c)

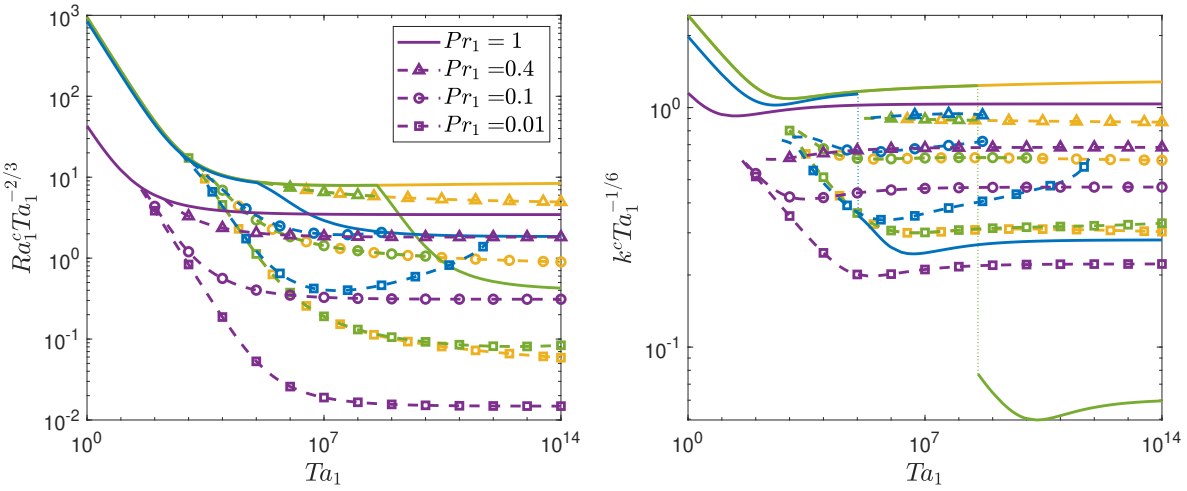
Figure 5.29: The (a) asymptotically scaled critical wavenumber $k_o^c Ta_1^{-1/6}$, (b) transitional Prandtl numbers, Pr_1^t (solid) and Pr_2^t (dashed), and (c) asymptotically scaled critical frequency $\omega^c Ta_1^{-1/3}$ at the onset of oscillatory instabilities as functions of thermal diffusivity κ_r, with $\delta = \nu_r = 1$, for a range of Taylor numbers Ta_1. Panels (a) and (c) show results for the corresponding Pr_1^t values in (b).

5.5.2 Variation in the viscosity ratio

We now examine a configuration comprising two fluid layers with identical thermal diffusivities, $\kappa_r = 1$, and investigate the influence of variations in the viscosity ratio, $\nu_r \geq 1$. Owing to the multiple modes that can be simultaneously unstable in both the steady and oscillatory systems, this problem is substantially more complex than the one in §5.5.1.

Figure 5.30 presents the asymptotically scaled critical Rayleigh number, $Ra_1^c Ta_1^{-2/3}$, and critical wavenumber, $k^c Ta_1^{-1/6}$, as functions of the Taylor number, Ta_1. These quantities are evaluated for $\nu_r = 1$ (corresponding to a single-layer configuration), $\nu_r = 10^2$, $\nu_r = 10^4$, and $\nu_r = 10^8$, for both the onset of steady convection and oscillatory convection (for $Pr_1 = 0.01,\ 0.1,\ 0.4$), where only parameter regimes in which oscillatory modes are preferred at the given Ta_1 are shown. As in the steady case, the Taylor number associated with the upper layer, Ta_2, is given by (5.69) and scales as ν_r^{-2}. Consequently, in the limit $\nu_r \to \infty$, we have $Ta_2 \to 0$, implying that the upper layer becomes effectively non-rotating. In addition, from (5.47) it follows that $Pr_2 = \nu_r Pr_1$.

In the limit $\nu_r \to \infty$ and for rapid rotation ($Ta_1 \to \infty$), the scaled oscillatory critical Rayleigh number and wavenumber at fixed Prandtl number approach asymptotic values. These correspond to a mode in which the upper layer behaves as a non-rotating slab, similarly to the steady system. When $\nu_r \to \infty$, convection is confined to the lower layer, and the problem reduces to the system analysed in Chapter 4. Within the large viscosity ratio limit, as $Ta_1 \to \infty$, temperature perturbations are likewise confined to the lower layer. From Chapter 3, the influence of boundary conditions becomes negligible at large Taylor numbers, and the flow is governed mainly by bulk dynamics. Thus, when both ν_r, $Ta_1 \to \infty$, the critical mode tends to that of single-layer rotating convection with stress-free, fixed-temperature boundaries with Rayleigh number and wavenumber given by (5.58) and (5.57).



(a) (b)

Figure 5.30: Asymptotically scaled critical (a) Rayleigh number $Ra_1^c Ta_1^{-2/3}$, and (b) wavenumber $k^c Ta_1^{-1/6}$ as functions of the Taylor number Ta_1 for $\nu_r = 1$ (purple), $\nu_r = 10^2$ (blue), $\nu_r = 10^4$ (green), and $\nu_r = 10^8$ (yellow), with $\kappa_r = \delta = 1$, for the onset of steady ($Pr_1 = 1$) and oscillatory ($Pr_1 = 0.01,\ 0.1,\ 0.4$) convection.

Figure 5.31 shows vertical velocity and temperature profiles for the steady and oscillatory critical modes ($Pr_1^t = 0.62$, $Pr_1 = 0.4,\ 0.1$) at $\nu_r = 10^8$, $Ta_1 = 10^{14}$, and $\kappa_r = 1$. For sufficiently large Ta_1, the vertical velocity w forms a boundary layer in the lower-viscosity layer near the interface to satisfy the mechanical conditions in (5.44). As Pr_1 decreases, this boundary layer exhibits less sharp gradients and the velocity maximum moves toward $z = -0.5$, the midpoint of the lower layer. The temperature perturbation θ develops a thermal boundary layer near the interface in both layers to satisfy $\theta_1 = \theta_2$ and $\mathcal{D}\theta_1 = \kappa_r \mathcal{D}\theta_2$ in (5.44). Within the thermal boundary layer, the oscillatory temperature profile reaches a minimum at increasingly lower θ as Pr_1 decreases.

In contrast to the steady system, for sufficiently large values of ν_r within the parameter regime considered here, and for fixed Pr_1, no discontinuity is observed in the oscillatory system. We shall demonstrate below that, for smaller values of ν_r, a discontinuity does arise when Pr_1 is varied.

In close analogy with the case involving variations of the thermal diffusivity contrast discussed in §5.5.1, the oscillatory and steady branches of Ra_1^c intersect for two values of Ta_1. This behaviour is evident in figure 5.30 for $\nu_r = 10^2$ and $\nu_r = 10^4$. Owing to the discontinuity in the steady system, the structure of this double intersection, and consequently the behaviour of the transitional Prandtl number, differs qualitatively from the case with a thermal diffusivity contrast, for which there exists a maximum and an associated critical Prandtl number delimiting the range over which the oscillatory and steady branches intersect twice. In the present context, the Ra_1^c branches intersect twice even at low Prandtl numbers, for example, when $\nu_r = 10^2$ and $Pr_1 = 0.01$.

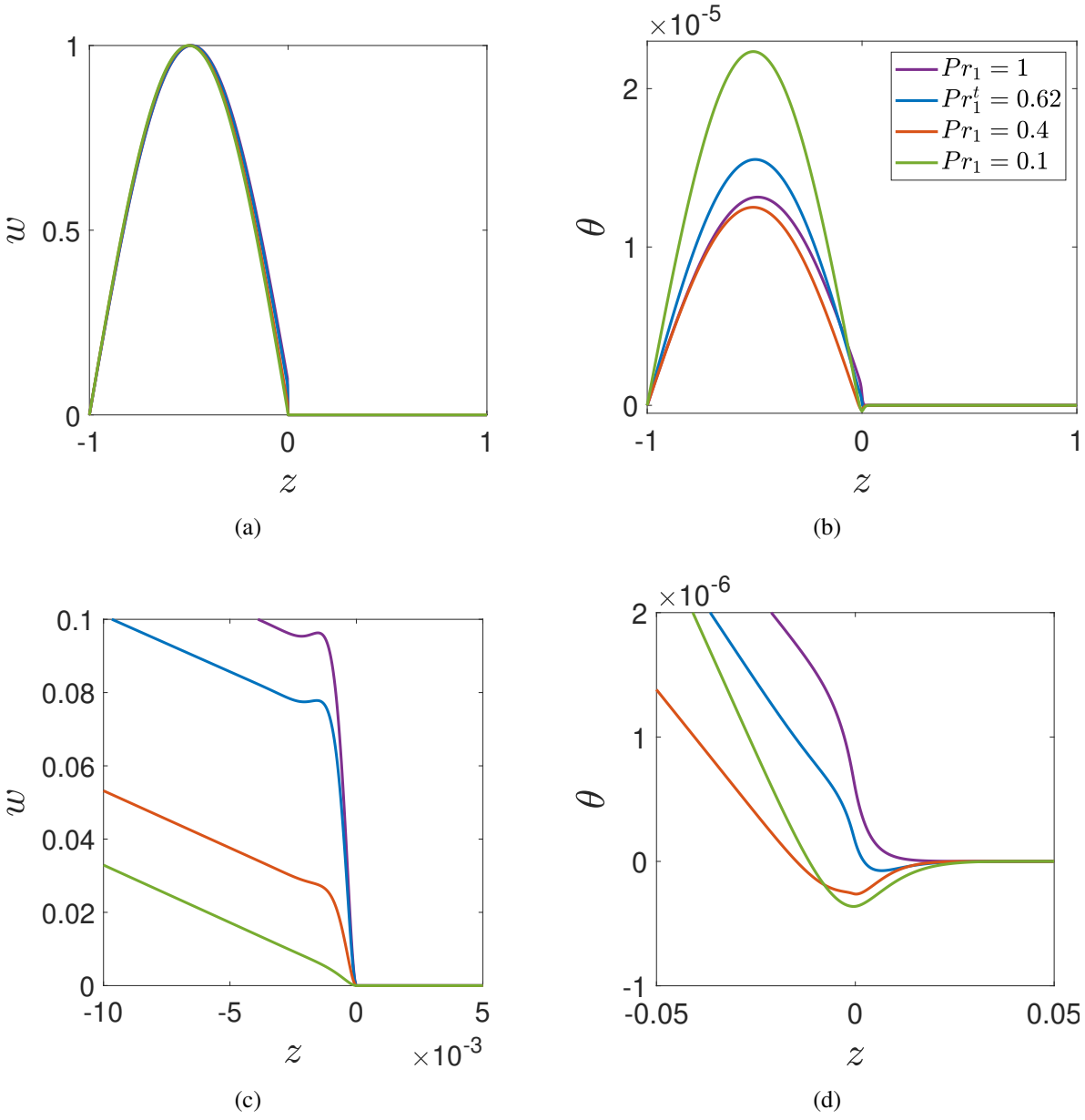


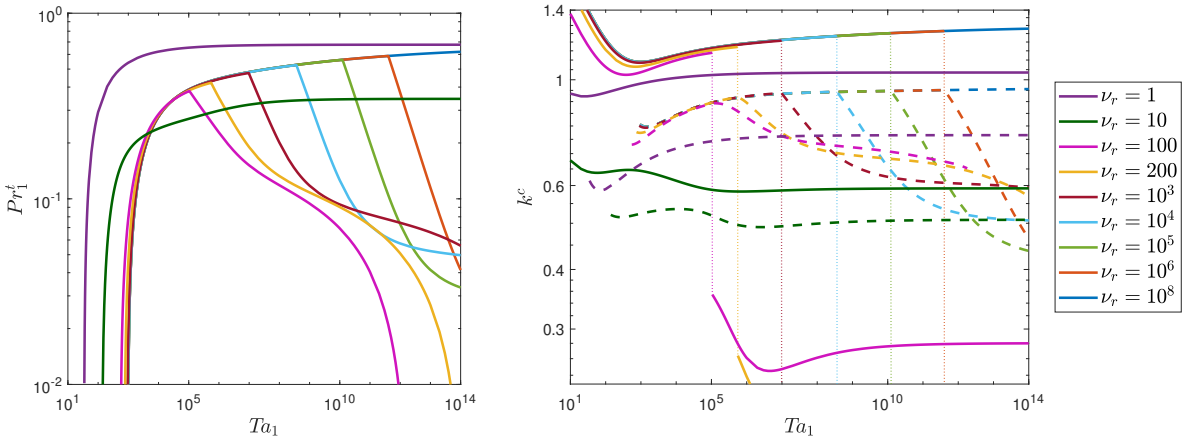
Figure 5.31: Profiles of the vertical velocity w (left) and temperature perturbation θ (right) of the critical modes for $\nu_r = 10^8$ and $Ta_1 = 10^{14}$ with $\delta = \kappa_r = 1$ for steady ($Pr_1 = 1$) and oscillatory ($Pr_1 = 0.1$, 0.4, and $Pr_1^t = 0.62$) modes. The eigenfunctions are normalised such that $\max(w) = 1$. The top row shows the entire domain, while the bottom row shows the solutions near the interface. The corresponding critical wavenumbers and critical Rayleigh numbers are: (1) $Pr_1 = 1$: $k_s^c = 275.8$, $Ra_{1s}^c = 1.80 \times 10^{10}$; (2) $Pr_1 = 0.1$: $k_o^c = 129.8$, $Ra_{1o}^c = 1.93 \times 10^9$; (3) $Pr_1 = 0.4$: $k_o^c = 187.3$, $Ra_{1o}^c = 1.07 \times 10^{10}$; (4) $Pr_1^t = 0.62$: $k_o^c = 206$, $Ra_{1o}^c = 1.80 \times 10^{10}$.

Figure 5.32 presents the transitional Prandtl number Pr_1^t and the critical wavenumber k^c as functions of the Taylor number Ta_1 for $\kappa_r = 1$ and various values of ν_r. Firstly, it is important to note that, by definition, the critical Rayleigh number of the oscillatory mode with $Pr_1 \equiv Pr_1^t$ equals that of the corresponding steady mode, shown in figure 5.24(a). For $\nu_r = 1$, the configuration is equivalent to a single-layer system and the transitional Prandtl number can be obtained from equation (2.99), with $Pr_1^c = 0.67659$ as $Ta_1 \to \infty$ and $Ta_1^c = 34.04$ as $Pr_1 \to 0$. In the limit $\nu_r \to \infty$, the critical modes approach those of the system analysed in Chapter 4, in which convection is restricted to the lower layer and bounded above by a solid slab. For the range of Taylor numbers considered here, the solutions computed with $\nu_r = 10^8$ lie within this asymptotic regime and are therefore directly comparable to the results of the boundary slab system (see figure 4.17). In this regime, as $Ta_1 \to \infty$, the temperature perturbation likewise becomes confined to the less viscous, lower layer, asymptotically recovering the single-layer RRBC system with stress-free, fixed-temperature boundaries, for the reasons detailed in §4.4. Accordingly, in this limit $Pr_1^t \to Pr_1^c = 0.67659$ as $Ta_1 \to \infty$.

Within the Taylor number range of figure 5.32, the dependence of Pr_1^t on Ta_1 at sufficiently large viscosity ratio is more complex than for $\nu_r = 1$. For moderately large viscosity ratios, $\nu_r \gtrsim 100$, and small Ta_1, the solutions behave similarly to the single-layer boundary slab problem of Chapter 4. Upon increasing Ta_1, a critical value is reached at which, in the steady regime, the effective rotation in the lower layer becomes strong enough that it no longer favours instability onset. The dominant mode then shifts to the more viscous, effectively non-rotating upper layer and, for that fixed ν_r, remains there as $Ta_1 \to \infty$. This shift appears as a discontinuity in the critical steady wavenumber k_s^c, with the critical mode switching from higher to lower wavenumber as Ta_1 increases, and is accompanied by an abrupt drop in the critical steady Rayleigh number Ra_{1s}^c. Accordingly, when Ta_1 exceeds this critical value, Ra_{1o}^c also falls sharply, and both Pr_1^t and k_o^c decrease markedly. With further increases in Ta_1, Pr_1^t continues to fall. The $\nu_r = 100$ and $\nu_r = 200$ results in figure 5.32(a) indicate, on the scale shown, that Pr_1^t decreases without bound. This suggests that, for each fixed ν_r, there is a critical Taylor number above which only steady modes are preferred at onset. Figure 5.32(a) further indicates that this qualitative behaviour of Pr_1^t persists for larger ν_r, though confirmation would require extending the analysis to higher Taylor numbers.

Analogously to the single-layer configuration, the two-layer system exhibits a maximum in Pr_1^t, above which steady modes are preferred for all values of Ta_1. In the single-layer case, this maximum occurs in the limit $Ta_1 \to \infty$. In contrast, for sufficiently large ν_r in the two-layer configuration, the maximum value of Pr_1^t occurs at the finite Taylor number at which the discontinuity in the steady critical wavenumber is observed.

The results presented in figure 5.32 (and, indeed, all results reported in this thesis) are validated by computing marginal stability curves over sufficiently large wavenumber intervals. This procedure ensures that the critical mode identified corresponds to the global minimum of the marginal curve and



(a) (b)

Figure 5.32: Variation of the (a) transitional Prandtl number Pr_1^t and (b) critical wavenumber k_s^c (solid) and k_o^c with $Pr_1 \equiv Pr_1^t$ (dashed) as functions of the Taylor number Ta_1, with $\delta = \kappa_r = 1$, for different viscosity ratios ν_r.

is therefore the correct solution. In the steady case, this verification is relatively straightforward: one may simply iterate over a wide range of k to obtain marginal stability curves, as in figure 5.11. In contrast, the oscillatory case is substantially more involved. For fixed Pr_1, the oscillatory branch of the marginal stability curve typically bifurcates from the steady branch and may intersect it at multiple wavenumbers. Furthermore, in certain parameter regimes—discussed in detail below—there exists an interval of k for which no oscillatory solutions are obtained. Consequently, a simple sweep over a wide range of k is insufficient to ensure that all local minima have been identified. Nevertheless, a straightforward check can be employed to validate the results. One may compute the complex growth rate $s = \sigma + i\omega$ over a wide range of k at fixed Ra_{1o}^c and Pr_1^t. If $\sigma \leq 0$ for all k in this range, then the previously determined mode is confirmed to be associated with the global minimum of the marginal stability curve. In this case, multiple local minima may exist; however, they are not of interest because they are not global minima.

One final point concerning figure 5.32 is that the results in the interval $10 < \nu_r < 100$, which are not displayed, are difficult to determine because k_o^c is discontinuous in this range. Figure 5.33 illustrates the dependence of the critical wavenumber k^c, the transitional Prandtl number Pr^t, and the critical frequency ω^c on the viscosity ratio ν_r, for $Ta_1 = 10^3$, $Ta_1 = 10^4$, and $Ta_1 = 10^5$. The critical oscillatory Rayleigh number Ra_{1o}^c is identical to the corresponding steady critical Rayleigh number shown in figure 5.21(a). Figure 5.33 clearly shows discontinuities in k_o^c and ω^c. In contrast, Ra_{1o}^c and Pr_1^t vary continuously across the transition. The continuity of Pr_1^t is not evident from figure 5.33(c), however, but would become clearer with additional solutions computed within the vicinity of ν_r at which the discontinuity occurs.

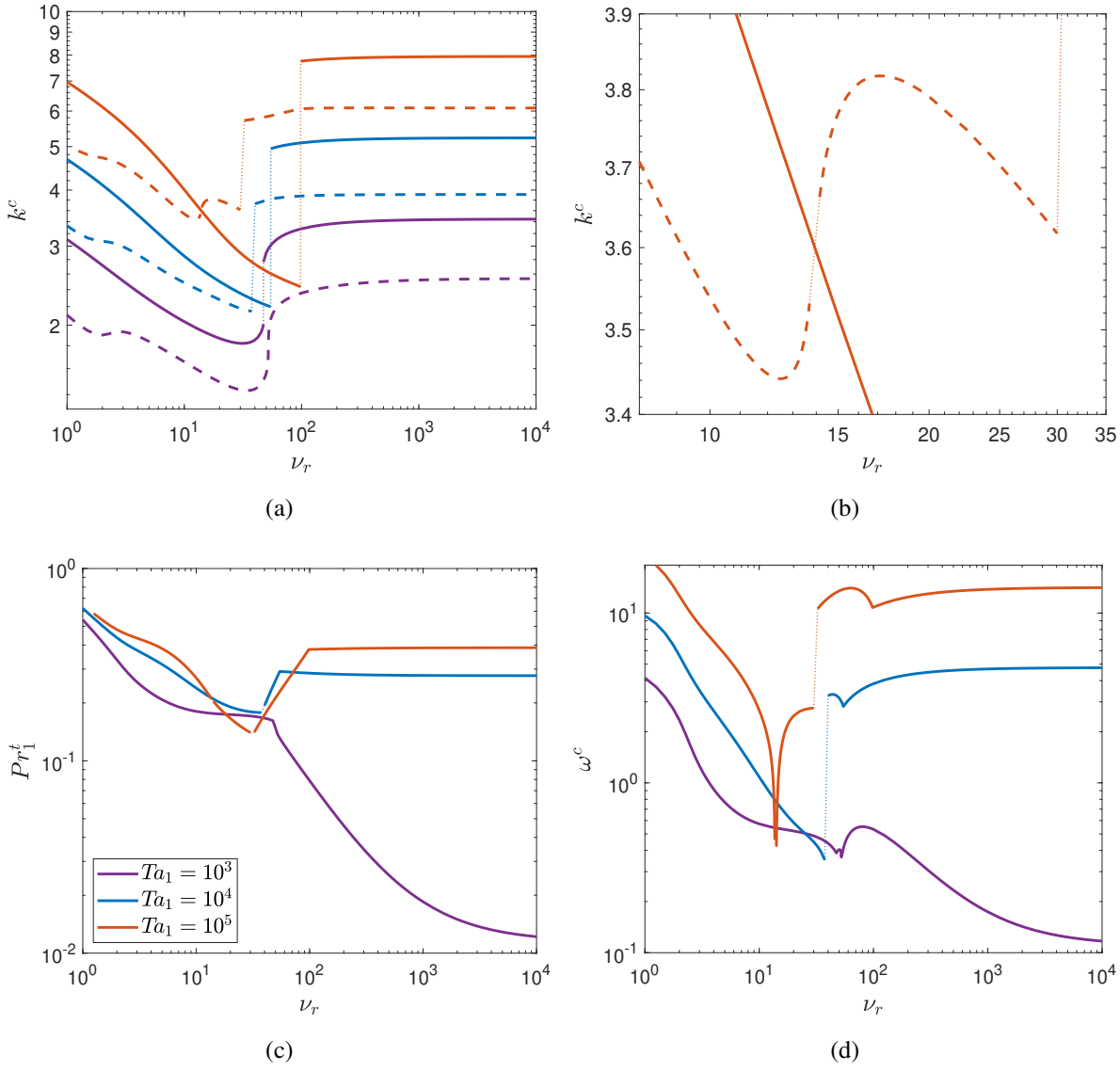


Figure 5.33: Variation of the (a) critical wavenumber k_s^c (solid) and k_o^c (dashed), (b) critical wavenumber for the interval $8 \leq \nu_r \leq 35$ with $Ta_1 = 10^5$, (c) transitional Prandtl number, Pr_1^t, and (d) critical frequency ω^c, for the onset of oscillatory instabilities as functions of the viscosity ratio ν_r, with $\delta = \kappa_r = 1$, for $Ta_1 = 10^3$, 10^4, 10^5.

For $Ta_1 = 10^3$, as ν_r is increased from one, k_o^c initially decreases to a local minimum, then increases slightly, and subsequently decreases again to attain a global minimum. Beyond this point, k_o^c exhibits a sharp but continuous increase towards its asymptotic value, while remaining smaller than k_s^c for all $\nu_r \geq 1$. At the discontinuity in k_s^c, which occurs at $\nu_r = 47.3$, three distinct modes—two steady and one oscillatory—become simultaneously critical and therefore equally preferred. This is manifested in the presence of multiple minima on the marginal stability curve, as shown in figure 5.34. For ν_r exceeding this discontinuity, Ra_{1o}^c, with $Pr_1 \equiv Pr_1^t$, must remain equal to the steady Rayleigh number associated with the global minimum, which now corresponds to the higher wavenumber steady mode. This constraint induces an abrupt change in the corresponding values of Pr_1^t and ω^c.

For $Ta_1 = 10^4$, as ν_r increases from one, k_o^c first decreases, then at $\nu_r = 37.5$ undergoes a discontinuity to the $\nu_r \to \infty$ asymptotic regime. This jump coincides with a discontinuity in ω^c and a sharp change in Pr_1^t, which switches from decreasing to increasing with ν_r. At $\nu_r = 37.5$, three instability modes are critical: one steady and two oscillatory, producing multiple minima in the marginal stability curve, as shown in figure 5.35(a). Here, the oscillatory branch with $Pr_1^t = 0.178$ intersects the steady branch three times, splitting it into two disjoint wavenumber intervals, each containing a critical oscillatory mode. The steady critical mode (s_1) and the lower wavenumber oscillatory critical mode (o_1) span the full depth of the domain, whereas the higher wavenumber oscillatory mode (o_2) is largely confined to the less viscous lower layer, signalling the onset of the transition towards the $\nu_r \to \infty$ limiting regime, as shown in figure 5.36. As ν_r is increased beyond $\nu_r = 37.5$, o_1 vanishes, and o_2 remains between s_1 and s_2. At $\nu_r = 54.5$, the steady branch has two equally preferred critical modes, giving three minima in the marginal stability curve—two steady and one oscillatory, as shown in figure 5.35(b). In this range, s_1 still spans the full depth (similarly to figure 5.36(c, d)), while o_2 and s_2 remain confined to the lower, less viscous layer (similarly to figure 5.36(e, f)). For $\nu_r > 54.5$, s_1 disappears, and the system tends to the $\nu_r \to \infty$ limiting regime.

For $Ta_1 = 10^5$ and $\nu_r > 1$, k_o^c exhibits a discontinuity at two distinct values of ν_r, as seen in figure 5.33(b). The first discontinuity occurs near $\nu_r = 14$; the oscillatory branch splits into two disjoint wavenumber intervals, each containing a local minimum and thus a critical mode. Three instability modes coexist with similar wavenumbers and eigenfunctions: one steady and two oscillatory. The globally critical mode shifts from the lower (o_1) to the higher (o_2) oscillatory branch. Figure 5.37 shows the marginal stability curve for $\nu_r = 13.7$ and $\nu_r = 14.15$, demonstrating the discontinuity in k_o^c as ν_r increases. As all critical modes have comparable wavenumbers, it is challenging to construct a single figure that clearly displays all three modes. Velocity perturbations are mainly confined to the more viscous upper layer, while temperature perturbations span the full depth, as shown in figure 5.38 for $\nu_r = 14.15$. As noted in §5.4.2, in the steady system, at low viscosity ratios and strong rotation, convection is restricted to the upper layer because rotation suppresses motion below, whereas for sufficiently large ν_r it instead localises in the less viscous, more strongly rotating lower layer.

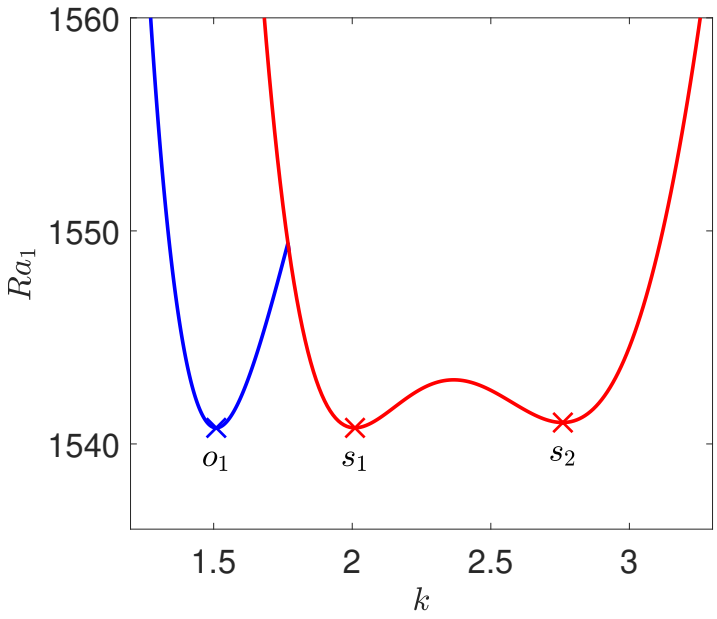
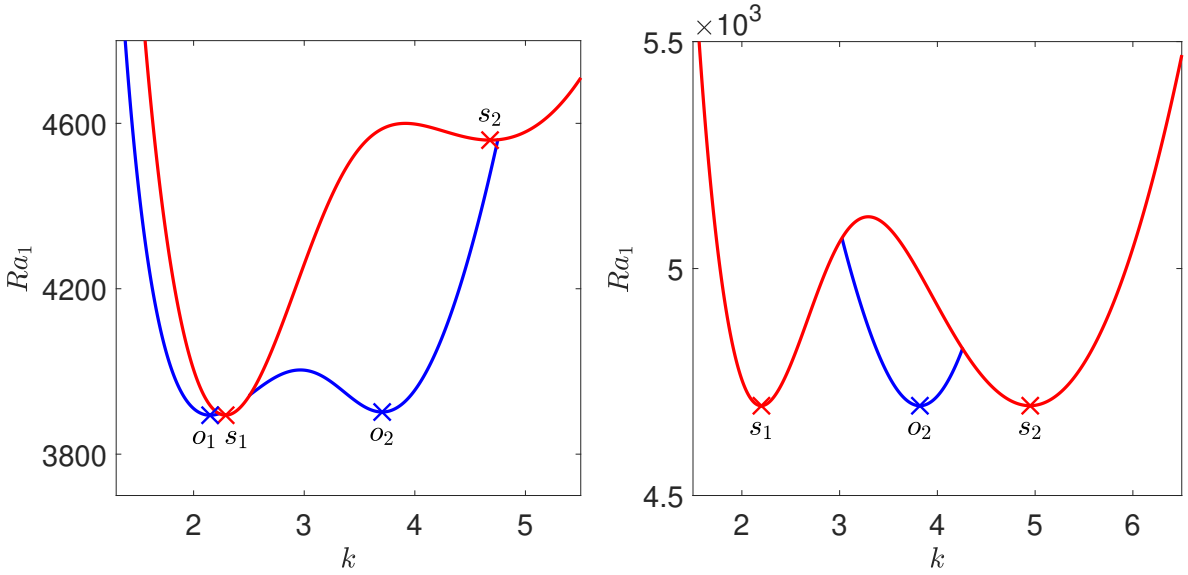


Figure 5.34: Marginal stability curve with $Ta_1 = 10^3$ and $\nu_r = 47.3$. The red branch indicates the onset of steady convection. The blue branch represent the onset of oscillatory convection with $Pr_1^t = 0.162$.



(a) (b)

Figure 5.35: Marginal stability curve with $Ta_1 = 10^4$ and (a) $\nu_r = 37.5$ with $Pr_1^t = 0.178$, and (b) $\nu_r = 54.5$ with $Pr_1^t = 0.292$. The red branch indicates the onset of steady convection. The blue branches represent the onset of oscillatory convection.

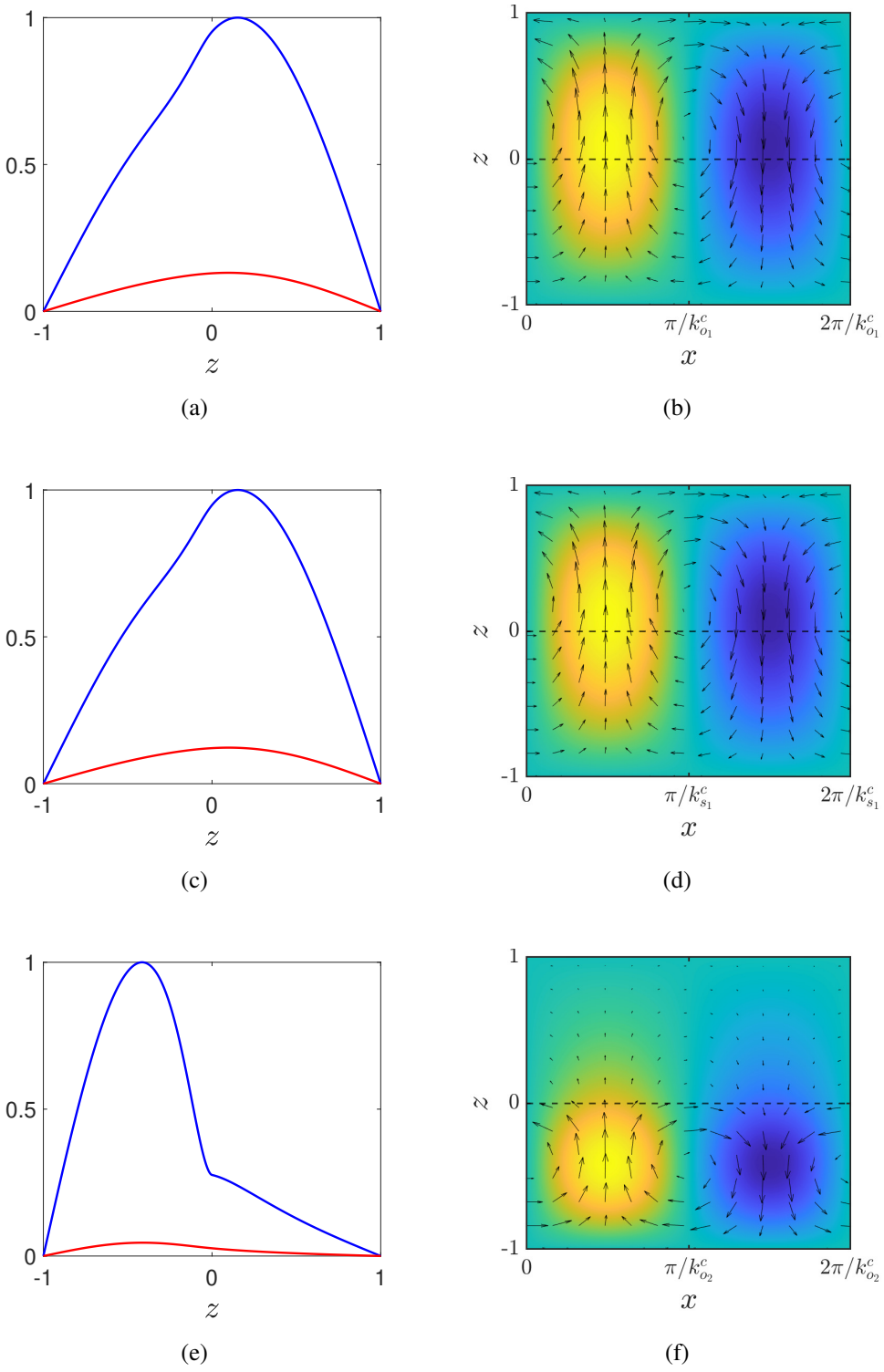
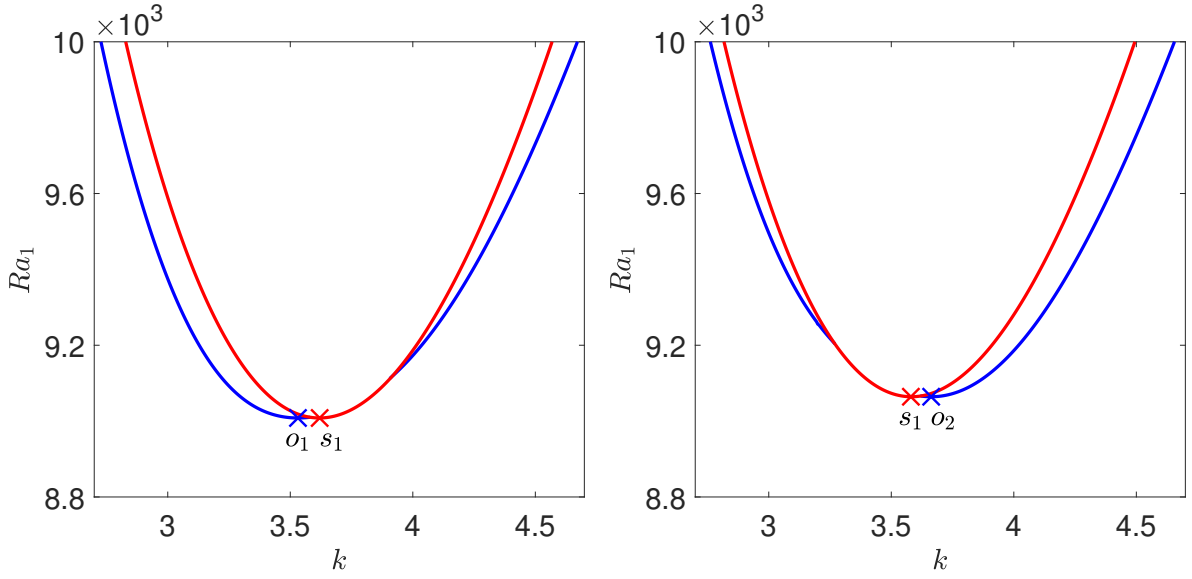
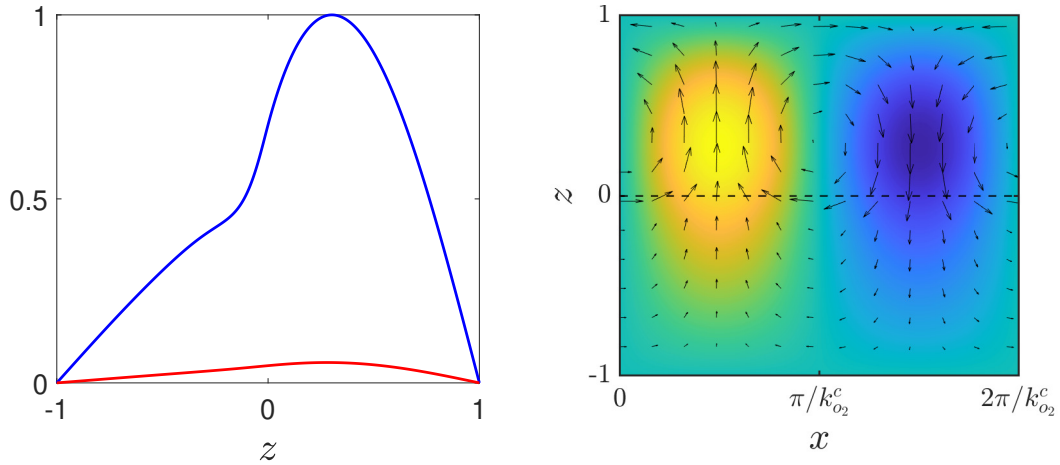


Figure 5.36: Same as figure 5.3 for $Ta_1 = 10^4$, $\nu_r = 37.5$ and $Pr_1^t = 0.178$ corresponding to the minimum, $Ra_1^c = 3894$ with $k_{o_1}^c = 2.15$ and $\omega_{o_1}^c = 0.35$ (top), $k_{s_1}^c = 2.29$ (middle) and $k_{o_2}^c = 3.70$ and $\omega_{o_2}^c = 3.12$ (bottom) of the marginal stability curve in figure 5.35(a).



(a) (b)

Figure 5.37: Marginal stability curve with $Ta_1 = 10^5$ and (a) $\nu_r = 13.7$ with $Pr_1^t = 0.210$, and (b) $\nu_r = 14.15$ with $Pr_1^t = 0.204$. The red branch indicates the onset of steady convection. The blue branches represent the onset of oscillatory convection.



(a) (b)

Figure 5.38: Same as figure 5.3 for $Ta_1 = 10^5$, $\nu_r = 14.15$ and $Pr_1^t = 0.204$ corresponding to the minimum, $Ra_1^c = 9064$, with $k_{o_2}^c = 3.66$ and $\omega_{o_2}^c = 0.42$ of the marginal stability curve in figure 5.37(b).

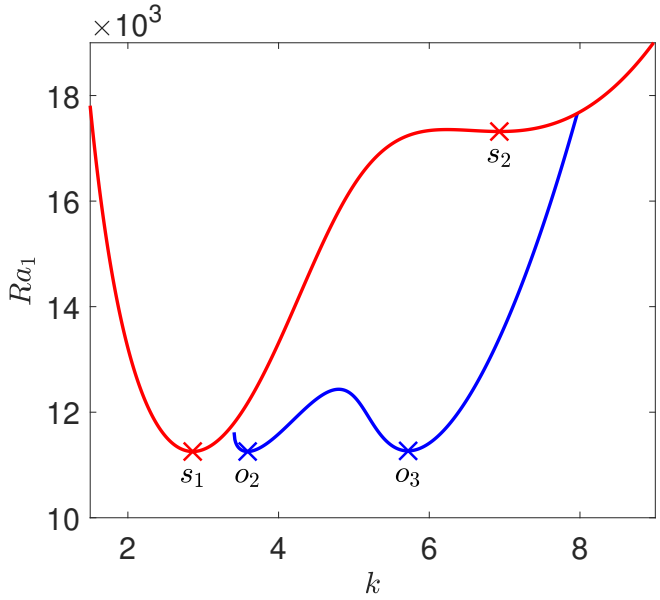


Figure 5.39: Marginal stability curve with $Ta_1 = 10^5$ and $\nu_r = 31.8$. The red branch indicates the onset of steady convection. The blue branches represent the onset of oscillatory convection with $Pr_1^t = 0.140$.

Upon increasing ν_r beyond $\nu_r = 14.15$, k_o^c increases, reaches a maximum, then decreases toward a second discontinuity at $\nu_r = 31.8$. There, the o_1 oscillatory branch loses its minimum and becomes irrelevant; both remaining minima lie on the higher wavenumber oscillatory branch (o_2 and o_3), as shown in figure 5.39. At $\nu_r = 31.8$, the three modes (one steady, two oscillatory) have qualitatively different spatial structures, as shown in figure 5.40. The steady mode s_1 remains confined to the upper layer. The o_2 mode is concentrated in the less viscous lower layer, signalling the onset of the $\nu_r \to \infty$ limiting regime. The o_2 mode exhibits intermediate behaviour, with substantial motion in both layers and temperature perturbations spanning the full depth. With further increase in ν_r, o_2 vanishes, and s_2 becomes globally critical at $\nu_r = 98.1$. The resulting marginal stability curve resembles figure 5.35(b). As ν_r increases further, s_1 also disappears, and the system approaches the $\nu_r \to \infty$ limiting regime.

The results presented in figure 5.33 are consistent with those shown in figure 5.32. From figure 5.33(c), it is apparent that, for a fixed value of ν_r in the interval $10 < \nu_r < 100$, the dependence of Pr_1^t on increasing Ta_1 exhibits progressively more intricate behaviour. In order to complete the parameter space represented in both figures, it is therefore necessary to further investigate the presence of discontinuities and multiple local minima on the marginal stability curve.

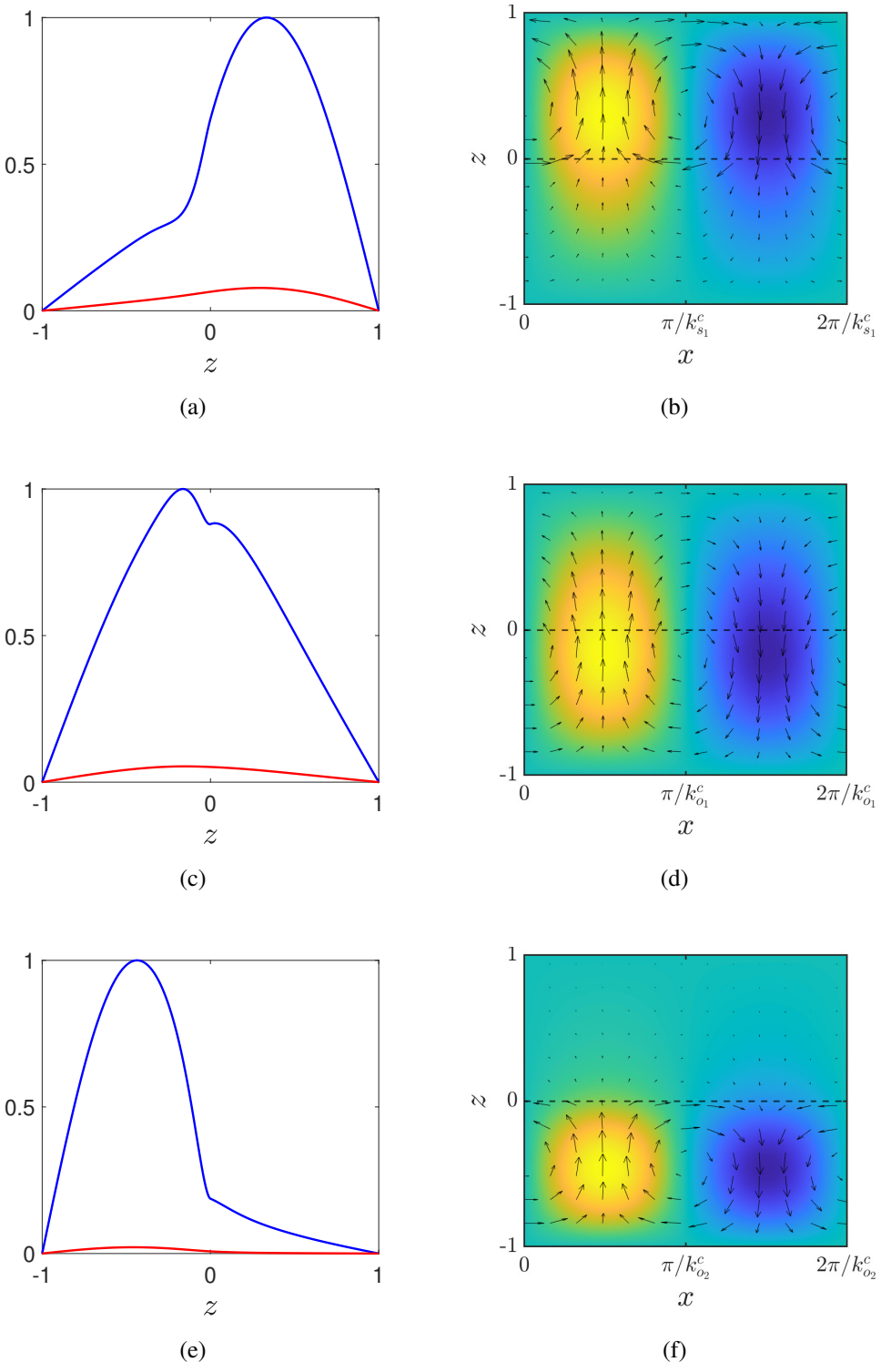


Figure 5.40: Same as figure 5.3 for $Ta_1 = 10^5$, $\nu_r = 31.8$ and $Pr_1^t = 0.140$ corresponding to the minimum, $Ra_1^c = 1.16 \times 10^4$, with $k_{s_1}^c = 2.86$ (top), $k_{o_1}^c = 3.59$ and $\omega_{o_1}^c = 2.76$ (middle) and $k_{o_2}^c = 5.72$ and $\omega_{o_2}^c = 10.43$ (bottom) of the marginal stability curve in figure 5.39.

5.6 Discussion

In this chapter, we have analysed the linear stability of a rotating two-layer convection model with uniform density. Specifically, we have examined the onset of instability as a function of the Taylor number, the Prandtl number, and the ratios of the viscosities, thermal diffusivities, and depths of the two layers.

Table 5.1 shows the asymptotic scaling of the critical Rayleigh numbers, Ra_1^c, and Ra_2^c, and wavenumber, k^c, with Ta_1 at the onset of steady rapidly rotating two-layer convection in the four limits: $\nu_r \to 0$, $\nu_r \to \infty$, $\kappa_r \to 0$, and $\kappa_r \to \infty$. The results are given for all other parameters set to one. In the limit in which the viscosity ratio tends to infinity, the critical mode corresponds to a regime in which convection is restricted to the lower, less viscous layer, while the upper layer behaves as an effectively non-rotating solid slab. Consequently, in this asymptotic limit, the problem reduces to the system considered in Chapter 4, which examines the onset of linear rotating convection in a fluid layer bounded below by a plate and above by a solid slab of finite thermal conductivity. When this limit is combined with the rapidly rotating regime, Ra_1^c and k^c asymptotically approach the corresponding values of single-layer rotating Rayleigh–Bénard convection with stress-free fixed-temperature boundaries (see figure 5.22), while Ra_2^c decreases indefinitely with $\nu_r^{-1}Ta_1^{2/3}$. In Chapter 3, we showed that, for steady instabilities in the rapidly rotating regime, the influence of the thermal boundary condition becomes negligible. Analogous conclusions have been reported regarding the influence of mechanical boundary conditions (Heard and Veronis, 1971).

In the limit in which the viscosity ratio tends to zero, the critical mode converges to a regime in which convective motions are confined to the lower, more viscous layer, since the upper layer is dominated by substantially stronger rotational effects. Despite the large viscosity in the lower layer, the strong rotation in the upper layer severely suppresses convection there, so that the instability instead favours convective motion within the viscous lower layer. Analogously to the $\nu_r \to \infty$ limit, as both ν_r, $Ta_1 \to \infty$, the quantities Ra_1^c and k^c asymptotically approach the corresponding critical values for single-layer rotating Rayleigh–Bénard convection with stress-free, fixed-temperature boundaries (see figure 5.22), while Ra_2^c increases proportionally to $\nu_r^{-1}Ta_1^{2/3}$.

In the limit in which the thermal diffusivity ratio tends to infinity, the critical mode approaches a regime in which temperature perturbations are confined to the lower, less thermally diffusive layer, whereas the fluid motion remains distributed across both layers. In the two limits simultaneously κ_r, $Ta_1 \to \infty$ the critical Rayleigh number Ra_1^c and the critical wavenumber k^c scale as $Ta_1^{2/3}$ and $Ta_1^{1/6}$, respectively (see figure 5.18), while Ra_2^c decreases indefinitely with $\kappa_r^{-2}Ta_1^{2/3}$ (determined empirically). The asymptotic values differ from those obtained for RRBC, as well as from those predicted by any of the simplified models examined in this thesis. To characterise this asymptotic regime more rigorously and determine the associated prefactors, the problem could be reformulated

	$\nu_r \to 0$	$\nu_r \to \infty$	$\kappa_r \to 0$	$\kappa_r \to \infty$
k^c	$\left(\frac{\pi^2}{2}Ta_1\right)^{1/6}$	$\left(\frac{\pi^2}{2}Ta_1\right)^{1/6}$	$Ta_1^{1/6}$	$Ta_1^{1/6}$
Ra_1^c	$3\left(\frac{\pi^2}{2}Ta_1\right)^{2/3}$	$3\left(\frac{\pi^2}{2}Ta_1\right)^{2/3}$	$\kappa_r^2 Ta_1^{2/3}$	$Ta_1^{2/3}$
Ra_2^c	$\nu_r^{-1}Ta_1^{2/3}$	$\nu_r^{-1}Ta_1^{2/3}$	$Ta_1^{2/3}$	$\kappa_r^{-2}Ta_1^{2/3}$

Table 5.1: Summary of the asymptotic scaling of the critical Rayleigh numbers and wavenumber at the onset of steady rapidly rotating two-layer convection. Results are given in the rapidly rotating limit ($Ta_1 \to \infty$), with all other parameters set to one.

and reduced by considering an analogous problem to the configuration discussed in Chapter 4. One plausible approach would be to examine the onset of rotating convection in a system comprising a fluid layer bounded below by a plate and above by an ideally thermally insulating layer. In such a configuration, temperature perturbations would be confined strictly to the lower fluid layer. The velocity field could extend throughout both layers, with the lower layer driven by convection and the upper layer driven solely by mechanical forcing at the interface. Analysis of such a reduced system may yield further insight into the dynamical behaviour emerging in the combined limits and allow determination of the prefactor associated with the scaling laws already identified. A symmetric result is obtained in the opposite limit $\kappa_r \to 0$.

Oscillatory solutions are obtained over a wide range of Taylor numbers and Prandtl numbers. The transitional Prandtl number, denoted by Pr_1^t, marks the boundary between regimes in which steady and oscillatory critical modes are preferred. Specifically, steady modes are preferred when $Pr_1 > Pr_1^t$, whereas oscillatory modes are preferred when $Pr_1 < Pr_1^t$. In RRBC, the transitional Prandtl number increases monotonically with the Taylor number and asymptotically approaches $Pr^c = 0.67659$ as $Ta \to \infty$ (see Chapter 2). In contrast, when a thermal diffusivity contrast is introduced, Pr_1^t no longer behaves monotonically: it attains a maximum at a moderate Taylor number before approaching its asymptotic regime as $Ta_1 \to \infty$, as shown in figure 5.28. This maximum implies an optimal thermal diffusivity ratio and Taylor number at which the transitional Prandtl number is maximised. Consequently, in the presence of a thermal diffusivity contrast, oscillatory modes are most strongly favoured at the largest Prandtl numbers associated with this optimal thermal diffusivity ratio and Taylor number.

The dependence of Pr_1 on the asymptotic behaviour as both κ_r, $Ta_1 \to \infty$ is too challenging to characterise using either asymptotic theory or numerical methods. However, if a fixed Prandtl number is chosen such that the preferred critical mode remains oscillatory for all Taylor numbers considered, $Pr_1 \lesssim 0.66$, then figure 5.26 suggests that the critical Rayleigh number and the critical wavenumber exhibit the same Taylor number scaling as their steady counterparts listed in Table 5.1.

In the limit of an infinitely large viscosity ratio, and for fixed values of the Taylor number and Prandtl number, the oscillatory critical Rayleigh number and wavenumber converge to asymptotic values corresponding to a regime in which convective motions are confined exclusively to the lower, less viscous layer, while the upper layer behaves as an effectively non-rotating solid slab. In this asymptotic regime, the governing problem reduces to the configuration analysed in Chapter 4. Although additional work is required to rigorously characterise the asymptotic properties of this boundary slab system, prior results by Heard and Veronis (1971), together with the analysis presented in Chapter 3, demonstrate that, for sufficiently large Taylor number, the effects of both mechanical and thermal boundary conditions become asymptotically negligible. Consequently, at fixed Prandtl number, the critical wavenumber, critical Rayleigh number, and critical frequency exhibit the same scaling as those obtained for RRBC, as given in (5.57), (5.58), and (5.59) in the rapidly rotating limit. Moreover, although this trend is not clearly visible in figure 5.32, in the limit of infinite viscosity ratio, the transitional Prandtl number is expected to approach $Pr_1^c = 0.67659$ as $Ta_1 \to \infty$. The behaviour at moderate viscosity ratio is considerably more complex, owing to the coexistence of multiple, comparably preferred steady and oscillatory critical modes, as shown, for example, in figures 5.34 and 5.35.

The analysis presented in this chapter reveals several promising directions for future research. A natural continuation of the present work is to examine the consequences of the simultaneous variation of the viscosity ratio, thermal diffusivity ratio, Taylor number, and Prandtl number. A further important next step is to explore in detail the effects of varying the coefficient of thermal expansion, and, more generally, to extend the model to allow for density variations. Another significant extension would be to incorporate an imposed magnetic field or to move beyond the Cartesian framework by introducing a spherical shell geometry. Both extensions would yield a more physically realistic representation for geophysical and astrophysical applications, albeit at the expense of substantially increased mathematical and computational complexity. Finally, beyond the linear stability analysis, it would be valuable to investigate the nonlinear evolution of the linear modes identified here to determine whether the distinct behaviours observed at the onset of instability have significant implications for the subsequent transition to, and the characteristics of, turbulent flow.

Chapter 6

Summary and Future Work

6.1 Summary

A wide range of rotating convective systems exhibit strong depth-dependent variations in their fluid properties. For example, material properties such as viscosity and thermal diffusivity change markedly with depth in the context of mantle convection (Richter and Johnson, 1974; Busse, 1981) and stellar interiors (Hurlburt et al., 1986). Similar depth-dependent variations also arise in industrial applications, for instance, in the modelling of heat and particle transport in magnetically confined fusion plasmas (Wilczynski and Hughes, 2019), and in crystal growth processes (Prakash and Koster, 1994). Of particular interest here is the emergence, stability, and morphology of large-scale polar vortices on gas giant planets, where rotating convection in a stratified fluid with depth-dependent variations in fluid properties is thought to play a central role.

French et al. (2012) showed that key properties such as viscosity, the coefficient of thermal expansion, and thermal diffusivity vary markedly along Jupiter's adiabat. Despite this, models of rotating convection that aim to reproduce the large-scale polar vortices on Jupiter and Saturn typically ignore these depth-dependent effects, instead assuming uniform viscosity and thermal diffusivity throughout the convecting layer (e.g., Gastine and Wicht, 2012; Garcia et al., 2020; Yadav and Bloxham, 2020). To address this shortcoming and refine the theoretical treatment of rotating convection with depth-dependent fluid properties, this thesis examines the onset of rotating convection in a two-layer configuration.

Chapter 1 provides an overview of rotating convection in configurations with depth-dependent fluid properties. In Chapter 2, we formulate the theoretical framework for rotating Rayleigh–Bénard convection (RRBC). Specifically, we derive the momentum, continuity, and temperature equations under the Boussinesq approximation that govern the system's dynamics, and subsequently obtain the corresponding linear, dimensionless equations describing infinitesimal perturbations about the basic

hydrostatic state. We consider a range of mechanical and thermal boundary conditions and conduct a linear stability analysis to determine the conditions for the onset of convection, with particular emphasis on distinguishing between stationary and oscillatory modes of instability.

In Chapter 3, we focus on the role of thermal boundary conditions in the system introduced in Chapter 2. Thermal boundary conditions relevant to geophysical and astrophysical contexts often lie between the extremes of fixed-flux and fixed-temperature, making an understanding of both limits crucial. For Boussinesq linear RRBC under rapid rotation, the case with impermeable, stress-free and fixed-temperature boundaries is notable because it can be solved analytically. The case with fixed-flux boundaries is more complex, as the eigenfunctions are no longer simple trigonometric functions. However, under rapid rotation, the balance between Coriolis, buoyancy and viscous terms leads to a very small preferred horizontal length scale, so the solution in the bulk of the fluid is independent of the choice of boundary conditions. Thus, different boundary conditions can be explored using perturbative methods, thereby enabling analytical progress beyond the impermeable, stress-free, and fixed-temperature case. Exploiting this property, we derive the first asymptotic solutions for the linear onset of steady, Boussinesq, RRBC under rapid rotation with impermeable, stress-free, fixed-flux boundary conditions. Our approach centres on deriving the governing equations and corresponding solutions for the departures from the fixed-temperature system. Specifically, this involves constructing a composite boundary layer structure comprising an Ekman layer of thickness $Ta^{-1/4}$ and a thermal boundary layer of thickness $Ta^{-1/6}$ to accommodate the fixed-flux boundary condition. The asymptotic corrections that capture the differences between the two systems are combined with the fixed-temperature solution to construct the corresponding solution for the fixed-flux system. This result provides insight into rotating two-layer convection, in which different asymptotic regimes converge to identical behaviour, displaying the same underlying dynamics.

The general problem of rotating two-layer convection is complex; it is instructive to first consider specific limiting cases. Thus, in Chapter 4, motivated by the need to understand the instabilities that arise in rotating two-layer convection in the limit of a large viscosity contrast, we investigate the onset of linear rotating Rayleigh–Bénard convection with a boundary slab of finite thermal conductivity (RRBC-BS). RRBC-BS is modelled as a horizontally infinite layer of Boussinesq fluid rotating about the vertical, bounded above by a solid layer, a plane below, and subject to heating from below. We enforce stress-free conditions below and a no-slip condition at the fluid-solid interface. The thermal boundary conditions consist of fixed-temperature at the bottom of the fluid and the top of the solid, and continuity of temperature and heat flux at the fluid-solid interface. We conduct a linear stability analysis as a function of the thermal conductivity contrast K_r, the layer depth ratio δ, the Taylor number Ta, and the Prandtl number Pr. For both steady and oscillatory modes, with fixed Pr and Ta, the asymptotic limits $K_r \to 0$, $K_r \to \infty$, and $\delta \to 0$ result in the thermal interface behaving as either a fixed-temperature or fixed-flux condition. Within these limits, the system behaves as RRBC

with one stress-free, fixed-temperature boundary and one no-slip boundary with either a fixed-flux or fixed-temperature condition. In the $\delta \to \infty$ limit, the thermal interface behaves as a Robin condition. In the rapidly rotating limit ($Ta \to \infty$), the critical Rayleigh number and critical wavenumber in the four asymptotic limits $K_r \to 0$, $K_r \to \infty$, $\delta \to 0$, $\delta \to \infty$ converge to the corresponding critical values of RRBC with stress-free fixed-temperature boundaries, meaning that, within these limits, the system behaves as a single-layer RRBC configuration. This result is consistent with the results of Chapter 3, where it is shown that the influence of the thermal boundary condition becomes negligible in the rapidly rotating regime. An analogous result has been determined for mechanical boundary conditions by Heard and Veronis (1971).

In Chapter 5, we address the central question of this thesis: how instability first onsets in rotating two-layer convection. The configuration consists of two superposed, horizontally extended, miscible fluid layers that are rotated about the vertical axis and uniformly heated from below. Each layer is characterised by its own set of physical parameters, thereby enabling an explicit representation of depth-dependent variations in the fluid properties. The layers are separated by a thin interface that couples their dynamics through continuity of velocity, incompressibility, vorticity, temperature, heat flux, tangential stress, and normal stress. The analysis focuses on the influence of four key dimensionless parameters: the viscosity ratio, the thermal diffusivity ratio, the Taylor number, and the Prandtl number. As the problem of rotating two-layer convection is complex, the four limits: $\nu_r \to 0$, $\nu_r \to \infty$, $\kappa_r \to 0$, and $\kappa_r \to \infty$ within the rapidly rotating regime are of particular interest.

At fixed Taylor and Prandtl numbers, for both steady and oscillatory instability modes, in the limits $\kappa_r \to 0$ and $\kappa_r \to \infty$, the temperature perturbation of the critical mode is predominantly confined to the less thermally diffusive layer, whereas the fluid flow remains distributed throughout both layers. In the additional rapidly rotating limit, the critical Rayleigh number associated with the less thermally diffusive layer and the corresponding critical wavenumber scale as $Ta_1^{2/3}$ and $Ta_1^{1/6}$, respectively. The prefactors for these asymptotic scalings remain to be determined.

At fixed Taylor and Prandtl numbers, for both steady and oscillatory modes of instability, we show that in the limit $\nu_r \to \infty$ the critical mode corresponds to a regime in which convection is confined to the lower, less viscous layer, while the upper layer behaves as an effectively non-rotating solid slab. Consequently, in this asymptotic limit, the problem reduces to the RRBC-BS system analysed in Chapter 4. When $\nu_r \to \infty$ within the rapidly rotating limit, the critical mode corresponds to the classical RRBC system with stress-free, fixed-temperature boundaries, consistent with the results of Chapters 3 and 4.

In the limit $\nu_r \to 0$, the critical mode corresponds to a regime in which convective motions are confined to the lower, more viscous layer, since the upper layer is dominated by substantially stronger rotational effects. Despite the large viscosity in the lower layer, the strong rotation in the upper layer severely suppresses convection there, so the instability instead favours convection within the viscous

lower layer. Thus, in both limiting regimes $\nu_r \to 0$ and $\nu_r \to \infty$, the critical mode is confined to the lower layer, although for fundamentally different physical reasons. Analogously to the $\nu_r \to \infty$ limit, as both $\nu_r \to 0$ and $Ta_1 \to \infty$, the critical mode corresponds to the classical RRBC system with stress-free, fixed-temperature boundaries.

The transitional Prandtl number, Pr_1^t, marks the boundary between regimes where steady and oscillatory critical modes are preferred. Thus, it is of interest to determine where this threshold lies across different parameter regimes. When a thermal diffusivity contrast is introduced, Pr_1^t attains a maximum at a moderate Taylor number before approaching its asymptotic limit as $Ta_1 \to \infty$. The presence of this maximum implies the existence of an optimal thermal diffusivity ratio and Taylor number at which the transitional Prandtl number is maximised. Consequently, in the presence of a thermal diffusivity contrast, oscillatory modes are most strongly favoured at the largest Prandtl numbers associated with this optimal thermal diffusivity ratio and Taylor number.

At moderate viscosity ratios, the stability characteristics of the oscillatory mode associated with the transitional Prandtl number become substantially more complex owing to the coexistence of multiple comparably preferred steady and oscillatory critical modes, as shown, for example, in figures 5.34 and 5.35.

6.2 Application to Jupiter

As discussed in Chapter 1, a leading hypothesis for the mechanism driving the large-scale polar vortices on Jupiter is rotating thermal convection (e.g., Chan and Mayr, 2013; Yadav and Bloxham, 2020; Garcia et al., 2020; Cai et al., 2021). In addition, it is well established that a variety of fluid properties in Jupiter's outer envelope, spanning the radial interval from approximately $0.9R_J$ to R_J (where $R_J = 6.9894 \times 10^7$ m denotes Jupiter's mean radius), vary significantly (French et al., 2012).

To better understand rotating convective systems with depth-dependent fluid properties, we have formulated and systematically analysed a rotating two-layer model. Although this configuration is simplified, it remains dynamically complex, and our approach builds on previous studies of non-rotating convection to improve understanding of rotating two-layer convection. However, to enable a meaningful comparison with a complex natural system such as Jupiter's large-scale polar vortices, it is necessary to carefully assess the simplifications inherent in the rotating two-layer framework. In particular, we neglect the presence of a magnetic field, which could significantly influence the onset and nature of flow instabilities. In addition, to reduce the number of control parameters, we assume equal density in each layer and therefore omit any density contrast. As shown in figure 1.3(a) in Chapter 1, the density varies significantly across Jupiter's outer envelope, and this variation is likely to exert a strong influence on the emergent instabilities. Furthermore, our model is restricted to the

linear onset of instability, whereas convection in gas giants is generally expected to occur in a strongly supercritical, nonlinear regime. Other simplifications to consider include boundary conditions and the use of the Boussinesq approximation. Despite these simplifications, the present model remains valuable for identifying and characterising the types of instabilities that may be relevant to, and potentially observable in, Jupiter's polar regions.

With the above caveats in mind, we can identify which type of instability is predicted from the linear theory developed in Chapter 5 by applying our model to an idealised two-layer representation of Jupiter's outer envelope. Using Tables 1 and 2 in French et al. (2012), which provide thermal and transport properties across Jupiter's radius, we obtain the necessary parameter values for each layer by averaging within each layer. The depth of the polar vortices remains unknown, but since most significant variations in the parameters required for our model occur within the outer 10% of Jupiter's radius, we place the entire box there. Table 6.1 shows the relevant parameters and the range of values they may take if our two-layer configuration is placed between $0.9R_J \lesssim r \lesssim R_J$ with the interface at different depths. We take gravity to be $g = 25\ \mathrm{m/s^2}$ and the angular velocity to be $\Omega = 1.75 \times 10^{-4}\ \mathrm{s^{-1}}$ (Gastine et al., 2014) to determine the Taylor number. Although the density ratio is not required for our rotating two-layer model, it is included in Table 6.1 to demonstrate the range of values that it may take. An important extension of the model would be to incorporate a density variation, however, this is beyond the scope of the present study.

Although all the ratio parameters listed in Table 6.1 are $\mathcal{O}(1)$, indicating that the contrasts in vertically averaged fluid properties between the two layers are relatively weak, Chapter 5 demonstrated that, at sufficiently large Taylor numbers, even modest departures of these ratios from unity can induce significant differences in the structure of the velocity and temperature profiles associated with the critical mode. In the present parameter space, the viscosity ratio is not sufficiently large to produce a pronounced alteration in the flow structure. In contrast, the value of κ_r at which the system transitions into its $\kappa_r \to \infty$ asymptotic regime decreases as Ta_1 increases (see §5.4.1.1). Consequently, the values of κ_r listed in Table 6.1 fall within the $\kappa_r \to \infty$ regime. Within this regime, temperature perturbations are confined to the less thermally diffusive lower layer, while fluid motion persists in the diffusive upper layer, driven in the lower layer by convection and in the upper layer by the mechanical forcing at the interface. When a contrast in layer depth is present, the temperature perturbation remains confined to the less thermally diffusive lower layer. For the Prandtl numbers specified in Table 6.1, the most unstable mode is stationary. In the Jovian context, this implies that fluid motions extend up to the visible surface, while heat transport is restricted to the lower portion of the convective zone. A comprehensive assessment of the influence of simultaneously varying all the parameters listed in Table 6.1 remains beyond the scope of the present work and is left for future research.

Symbol	Definition	Jupiter
δ	Depth ratio	0.1 - 1.8
ν_r	Viscosity ratio	1.24 - 1.07
κ_r	Thermal diffusivity ratio	2.55 - 3.42
α_r	Thermal expansion ratio	7.20 - 9.42
ρ_r	Density ratio	0.09 - 0.29
Pr_1	Prandtl number	0.47 - 1.04
Ta_1	Taylor number	1.16×10^{33} - 5.53×10^{31}

Table 6.1: Parameter values for the rotating two-layer configuration within the radial span $0.9R_J \lesssim r \lesssim R_J$ (where $R_J = 6.9894 \times 10^7$ m denotes Jupiter's mean radius). Tables 1 and 2 of French et al. (2012) provide values of each fluid property at specific radial locations within Jupiter. The outer region ($0.9R_J \lesssim r \lesssim R_J$) is divided into two layers, with the fluid properties averaged within each layer. The interface is placed at the largest and smallest radii within $0.9R_J < r < R_J$ reported in Tables 1 and 2 of French et al. (2012), corresponding to $z = 0.986R_J$ and $z = 0.94R_J$, and hence to $\delta = 0.1$ and $\delta = 1.8$. The resulting parameter ranges reflect the difference between configurations with a thin upper layer and those with a thick upper layer.

6.3 Future work

The analysis of the rotating two-layer model in this thesis reveals several promising avenues for future research. A natural continuation of the present work is to further characterise and understand the $\kappa_r \to \infty$ limit. One plausible approach would be to examine the onset of rotating convection in a system comprising a fluid layer bounded below by a plate and above by a thermally insulating layer. In such a configuration, temperature perturbations would be confined strictly to the lower fluid layer, whereas the velocity field could extend throughout both layers, driven in the lower layer by convection and in the upper layer by mechanical forcing at the interface. Investigation of this reduced system may provide insight into the dynamical behaviour that emerges in the limit $\kappa_r \to \infty$.

A further natural direction of the analysis is to examine how the viscosity ratio, thermal diffusivity ratio, Taylor number, and Prandtl number influence the onset of oscillatory instability modes, as discussed in §5.5. In particular, it is of interest to determine the dependence on the Prandtl number in appropriate asymptotic regimes. Moreover, the asymptotic behaviour of the transitional Prandtl number, which indicates the threshold below which oscillatory modes are preferred, warrants further

systematic investigation. Owing to the multiple modes that can be simultaneously unstable in both the steady and oscillatory systems, this problem is considerably more intricate.

Another aspect worth examining is a detailed investigation of how variations in the coefficient of thermal expansion affect the onset of both steady and oscillatory instabilities. In addition, it is essential to determine how simultaneous variations of this parameter with the viscosity ratio, thermal diffusivity ratio, depth ratio, Taylor number, and Prandtl number modify the stability characteristics we have determined here. Of particular interest are the combined values representing Jupiter's outer layer, as presented in Table 6.1. Nevertheless, one should assess whether such combined variations give rise to more distinct dynamical regimes or to multiple, equally preferred critical modes, analogous to the behaviour observed when only the viscosity ratio is varied.

To reduce the number of control parameters, we assumed equal densities across layers and therefore omitted any density contrast. An important extension in the linear limit is to include a density variation. This could be achieved in one of two ways. One could assume a distinct density for each layer. Under the assumption of equal densities, the density cancels from the governing equations when they are expressed in dimensionless form by scaling variables with the properties of the lower layer. If the densities in each layer were distinct, an additional dimensionless parameter would arise: the density ratio $\rho_r = \rho_2/\rho_1$, where ρ_1 and ρ_2 are the reference densities of the lower and upper layers. This new parameter would enter the equations and interface conditions through the viscosity ratio $\nu_r = \nu_2/\nu_1$, with $\nu_i = \mu_i/\rho_i$, where $i = 1, 2$. Another way to introduce a density variation is to use the anelastic assumption rather than the Boussinesq approximation, in which the density variation is accounted for in the reference state. However, this leads to a more complicated system of equations that is generally more difficult to solve. In fact, for a more realistic representation of gas giant planets, the fluid properties could instead be allowed to vary continuously with depth, rather than being represented by a ratio of two discrete values. Such an approach would, however, result in a considerably more complex system of equations and is therefore left to future work.

A further development of the current study involves moving beyond the Cartesian framework by adopting a spherical shell geometry. This configuration would provide a more faithful representation of global geophysical and astrophysical systems, for which spherical geometries are essential. The configuration analysed here is representative of the polar region of a spherical shell. It is well established that spherical shell geometries exhibit distinct dynamical behaviour inside and outside the tangent cylinder (e.g. Gastine and Aurnou, 2022). Extending the present analysis to a full spherical shell would thus permit more accurate modelling of natural systems, albeit at the cost of substantially increased mathematical and computational complexity.

Another significant extension would be to include an imposed magnetic field. In this context, variations in electrical conductivity are particularly important (Jones, 2014). Within Jupiter, the electrical conductivity decreases by approximately twelve orders of magnitude across the outer envelope

(French et al., 2012). Consequently, it would be of considerable interest to investigate a rotating two-layer model with a large contrast in electrical conductivity. Such a configuration could provide insight into the interaction between magnetic fields and strongly stratified conducting and convecting regions.

Our model is restricted to the linear onset of instability, whereas convection in gas giants is generally expected to occur in a strongly supercritical, nonlinear regime. Therefore, beyond the onset of linear stability, it would be valuable to investigate the development of the linear critical modes above onset and their nonlinear evolution. This would help determine whether the distinct behaviours observed at the onset of instability have significant implications for the subsequent transition to turbulence and its characteristics. Collectively, these extensions would provide a more physically realistic framework for applications in geophysics and astrophysics.

This thesis has provided new insights into the combined influence of rotation and depth-dependent fluid properties on the onset of linear instability in plane-layer thermal convection. Although challenges remain in fully characterising the dynamics in certain parameter regimes, the results presented here establish a robust theoretical and computational basis for subsequent investigations of rotating convection with depth-dependent fluid properties. The incorporation of rotational effects alongside the influence of two miscible fluid layers provides a scalable modelling framework that can be extended to relax common simplifying assumptions and approximations, such as the Boussinesq approximation. This work advances our understanding of rotating convective systems exhibiting pronounced depth-dependent variations in fluid properties.

References

Adriani, A., Bracco, A., Grassi, D., Moriconi, M., Mura, A., Orton, G., Altieri, F., Ingersoll, A., Atreya, S., Lunine, J., Migliorini, A., Noschese, R., Cicchetti, A., Sordini, R., Tosi, F., Sindoni, G., Plainaki, C., Dinelli, B., Turrini, D., Filacchione, G., Piccioni, G. and Bolton, S. (2020). Two-year observations of the Jupiter polar regions by JIRAM on board Juno, *J. Geophys. Res.: Planets* **125**(6): e2019JE006098.

Adriani, A., Mura, A., Orton, G., Hansen, C., Altieri, F., Moriconi, M. L., Rogers, J., Eichstädt, G., Momary, T., Ingersoll, A. P., Filacchione, G., Sindoni, G., Tabataba-Vakili, F., Dinelli, B. M., Fabiano, F., Bolton, S. J., Connerney, J. E., Atreya, S. K., Lunine, J. I., Tosi, F., Migliorini, A., Grassi, D., Piccioni, G., Noschese, R., Cicchetti, A., Plainaki, C., Olivieri, A., O'Neill, M. E., Turrini, D., Stefani, S., Sordini, R. and Amoroso, M. (2018). Clusters of cyclones encircling Jupiter's poles, *Nature* **555**(7695): 216–219.

Antuñano, A., del Río-Gaztelurrutia, T., Sãnchez-Lavega, A. and Hueso, R. (2015). Dynamics of Saturn's polar regions, *J. Geophys. Res.: Planets* **120**(2): 155–176.

Aurnou, J. M., Andreadis, S., Zhu, L. and Olson, P. (2003). Experiments on convection in Earth's core tangent cylinder, *Earth Planet. Sci. Lett.* **212**(1-2): 119–134.

Aurnou, J. M., Calkins, M. A., Cheng, J. S., Julien, K., King, E. M., Nieves, D., Soderlund, K. M. and Stellmach, S. (2015). Rotating convective turbulence in Earth and planetary cores, *Phys. Earth Planet. Inter.* **246**: 52–71.

Bénard, H. (1900). Etude expérimentale des courants de convection dans une nappe liquide. - régime permanent: Tourbillons cellulaires, *J. Theo. App. Phys.* **9**(1): 513–524.

Bénard, H. (1901). Les Tourbillons cellulaires dans une nappe liquide transportant de la chaleur par convection en régime permanent, *Ann. Chim. Phys.* **23**: 62–144.

Bodenschatz, E., Pesch, W. and Ahlers, G. (2000). Recent developments in Rayleigh-Bénard convection, *Annu. Rev. Fluid Mech.* **32**: 709–778.

Bolton, S. J., Adriani, A., Adumitroaie, V., Allison, M., Anderson, J., Atreya, S., Bloxham, J., Brown, S., Connerney, J. E. P., Dejong, E., Folkner, W., Gautier, D., Grassi, D., Gulkis, S., Guillot, T., Hansen, C., Hubbard, W. B., Iess, L., Ingersoll, A., Janssen, M., Jorgensen, J., Kaspi, Y., Levin, S. M., Li, C., Lunine, J., Miguel, Y., Mura, A., Orton, G., Owen, T., Ravine, M., Smith, E., Steffes, P., Stone, E., Stevenson, D., Thorne, R., Waite, J., Durante, D., Ebert, R. W., Greathouse, T. K., Hue, V., Parisi, M., Szalay, J. R. and Wilson, R. (2017). Jupiter's interior and deep atmosphere: The initial pole-to-pole passes with the Juno spacecraft, *Science* **356**(6340): 821–825.

Boubnov, B. M. and Golitsyn, G. S. (1990). Temperature and velocity field regimes of convective motions in a rotating plane fluid layer, *J. Fluid Mech.* **219**: 215–239.

Busse, F. H. (1970). Thermal instabilities in rapidly rotating systems, *J. Fluid Mech.* **44**(3): 441–460.

Busse, F. H. (1975). Patterns of convection in spherical shells, *J. Fluid Mech.* **72**(1): 67–85.

Busse, F. H. (1978). Non-linear properties of thermal convection, *Rep. Prog. Phys.* **41**(12): 1929–1968.

Busse, F. H. (1981). On the aspect ratios of two-layer mantle convection, *Phys. Earth Planet. Inter.* **24**(4): 320–324.

Cai, T., Chan, K. L. and Mayr, H. G. (2021). Deep, closely packed, long-lived cyclones on Jupiter's poles, *Planet. Sci.* **2**(2): 81.

Calkins, M. A., Hale, K., Julien, K., Nieves, D., Driggs, D. and Marti, P. (2015). The asymptotic equivalence of fixed heat flux and fixed temperature thermal boundary conditions for rapidly rotating convection, *J. Fluid Mech.* **784**: R2.

Chan, K. L. and Mayr, H. G. (2013). Numerical simulation of convectively generated vortices: Application to the Jovian planets, *Earth Planet. Sci. Lett.* **371**: 212–219.

Chandrasekhar, S. (1953). The instability of a layer of fluid heated below and subject to Coriolis forces, *Proc. R. Soc. Lond. A* **217**(1130): 306–327.

Chandrasekhar, S. (1961). *Hydrodynamic and Hydromagnetic Stability*, Clarendon Press, Oxford.

Chapman, C. J. and Proctor, M. R. (1980). Nonlinear Rayleigh-Bénard convection between poorly conducting boundaries, *J. Fluid Mech.* **101**(4): 759–782.

Cheng, J. S., Stellmach, S., Ribeiro, A., Grannan, A., King, E. M. and Aurnou, J. M. (2015). Laboratory-numerical models of rapidly rotating convection in planetary cores, *Geophys. J. Int.* **201**(1): 1–17.

Diwakar, S. V., Tiwari, S., Das, S. K. and Sundararajan, T. (2014). Stability and resonant wave interactions of confined two-layer Rayleigh–Bénard systems, *J. Fluid Mech.* **754**: 415–455.

Dowling, T. E. (1988). Rotating Rayleigh-Bénard convection with fixed flux boundaries, *Summer Study Program in Geophysical Fluid Dynamics, Woods Hole Oceanographic Institution Technical Report* pp. 223–250.

Drazin, P. G. and Reid, W. H. (2004). *Hydrodynamic Stability*, Cambridge University Press.

Favier, B., Silvers, L. J. and Proctor, M. R. (2014). Inverse cascade and symmetry breaking in rapidly rotating Boussinesq convection, *Phys. Fluids* **26**(9): 096605.

French, M., Becker, A., Lorenzen, W., Nettelmann, N., Bethkenhagen, M., Wicht, J. and Redmer, R. (2012). Ab initio simulations for material properties along the Jupiter adiabat, *Astrophys. J. Suppl. Ser.* **202**(5): 11.

Fultz, D. and Nakagawa, Y. (1955). Experiments on over-stable thermal convection in mercury, *Proc. R. Soc. Lond. A* **231**(1184): 211–225.

Fultz, D., Nakagawa, Y. and Frenzen, P. (1954). An instance in thermal convection of Eddington's "overstability", *Phys. Rev.* **94**(6): 1471–1472.

Garcia, F., Chambers, F. R. N. and Watts, A. L. (2020). Deep model simulation of polar vortices in gas giant atmospheres, *Mon. Not. R. Astron. Soc.* **499**(4): 4698–4715.

Gastine, T. and Aurnou, J. M. (2022). Latitudinal regionalization of rotating spherical shell convection, *J. Fluid Mech.* **954**: R1.

Gastine, T., Heimpel, M. and Wicht, J. (2014). Zonal flow scaling in rapidly-rotating compressible convection, *Phys. Earth Planet. Inter.* **232**: 36–50.

Gastine, T. and Wicht, J. (2012). Effects of compressibility on driving zonal flow in gas giants, *Icarus* **219**(1): 428–442.

Gilman, P. A. (1977). Nonlinear dynamics of Boussinesq convection in a deep rotating spherical shell-I, *Geophys. Astrophys. Fluid Dyn.* **8**(1): 93–135.

Godfrey, D. A. (1988). A hexagonal feature around Saturn's north pole, *Icarus* **76**(2): 335–356.

Goldstein, H. F., Knobloch, E., Mercader, I. and Net, M. (1993). Convection in a rotating cylinder. part 1: Linear theory for moderate Prandtl numbers, *J. Fluid Mech.* **248**: 583–604.

Greenspan, H. P. (1968). *The Theory of Rotating Fluids*, Cambridge University Press.

Guervilly, C., Hughes, D. W. and Jones, C. A. (2014). Large-scale vortices in rapidly rotating Rayleigh–Bénard convection, *J. Fluid Mech.* **758**: 407–435.

Guillot, T., Li, C., Bolton, S. J., Brown, S. T., Ingersoll, A. P., Janssen, M. A., Levin, S. M., Lunine, J. I., Orton, G. S. and Steffes, P. G. (2020). Storms and the depletion of ammonia in Jupiter: II. Explaining the Juno observations, *J. Geophys. Res. Planets* **125**(8): e2020JE006404.

Heard, W. B. and Veronis, G. (1971). Asymptotic treatment of the stability of a rotating layer of fluid with rigid boundaries, *Geophys. Fluid Dyn.* **2**(1): 299–316.

Heimpel, M., Gastine, T. and Wicht, J. (2016). Simulation of deep-seated zonal jets and shallow vortices in gas giant atmospheres, *Nat. Geosci.* **9**: 19–23.

Hewitt, J. M., McKenzie, D. P. and Weiss, N. O. (1980). Large aspect ratio cells in two-dimensional thermal convection, *Earth Planet. Sci. Lett.* **51**(2): 370–380.

Hughes, D. W., Proctor, M. R. E. and Eltayeb, I. A. (2022). Rapidly rotating Maxwell-Cattaneo convection, *Phys. Rev. Fluids* **7**(9): 093502.

Hurlburt, N. E., Toomre, J. and Massaguer, J. M. (1986). Nonlinear compressible convection penetrating into stable layers and producing internal gravity waves, *Astrophys. J.* **311**: 563–577.

Hurle, D. T. J., Jakeman, E. and Pike, E. R. (1967). On the solution of the Bénard problem with boundaries of finite conductivity, *Proc. R. Soc. Lond. A* **296**(1447): 469–475.

Incropera, F. P. (1988). Convection heat transfer in electronic equipment cooling, *J. Heat Transfer* **110**(4b): 1097–1111.

Jeffreys, H. (1926). The stability of plane parallel convection, *Phil. Mag.* **2**: 833–842.

Jeffreys, H. (1928). On the formation of convection-cells, *Phil. Mag.* **5**: 793–805.

Johnston, H. and Doering, C. R. (2009). Comparison of turbulent thermal convection between conditions of constant temperature and constant flux, *Phys. Rev. Lett.* **102**: 064501.

Jones, C. A. (2014). A dynamo model of Jupiter's magnetic field, *Icarus* **241**: 148–159.

Käpylä, P. J., Mantere, M. J. and Hackman, T. (2011). Starspots due to large-scale vortices in rotating turbulent convection, *Astrophys. J.* **742**(1): 34.

Kaspi, Y., Galanti, E., Hubbard, W. B., Stevenson, D. J., Bolton, S. J., Iess, L., Guillot, T., Bloxham, J., Connerney, J. E., Cao, H., Durante, D., Folkner, W. M., Helled, R., Ingersoll, A. P., Levin, S. M., Lunine, J. I., Miguel, Y., Militzer, B., Parisi, M. and Wahl, S. M. (2018). Jupiter's atmospheric jet streams extend thousands of kilometres deep, *Nature* **555**: 223–226.

Kirk, R. L. and Stevenson, D. J. (1987). Hydromagnetic constraints on deep zonal flow in the giant planets, *Astrophys. J.* **316**: 836–846.

Kloosterziel, R. C. and Carnevale, G. F. (2003). Closed-form linear stability conditions for rotating Rayleigh-Bénard convection with rigid stress-free upper and lower boundaries, *J. Fluid Mech.* **480**: 25–42.

Kraichnan, R. H. (1962). Turbulent thermal convection at arbitrary Prandtl number, *Phys. Fluids* **5**(11): 1374–1389.

Kuo, L. S. and Chen, P. H. (2009). Effects of slip boundary conditions on Rayleigh-Bénard convection, *J. of Mech.* **25**(2): 205–212.

Le Bars, M. and Davaille, A. (2002). Stability of thermal convection in two superimposed miscible viscous fluids, *J. Fluid Mech.* **471**: 339–363.

Lin, Y. and Jackson, A. (2021). Large-scale vortices and zonal flows in spherical rotating convection, *J. Fluid Mech.* **912**: A46.

Long, R. S., Mound, J. E., Davies, C. J. and Tobias, S. M. (2020). Scaling behaviour in spherical shell rotating convection with fixed-flux thermal boundary conditions, *J. Fluid Mech.* **889**: A7.

Malkus, W. V. R. (1954). The heat transport and spectrum of thermal turbulence, *Proc. R. Soc. Lond. A* **225**(1161): 196–212.

Malkus, W. V. R. and Veronis, G. (1958). Finite amplitude cellular convection, *J. Fluid Mech.* **4**(3): 225–260.

Miesch, M. S. (2005). Large-scale dynamics of the convection zone and tachocline, *Living Rev. Sol. Phys.* **2**(1): 1–139.

Mitchell, D. M., Scott, R. K., Seviour, W. J., Thomson, S. I., Waugh, D. W., Teanby, N. A. and Ball, E. R. (2021). Polar vortices in planetary atmospheres, *Rev. Geophys.* **59**(4): e2020RG000723.

Nakagawa, Y. and Frenzen, P. (1955). A theoretical and experimental study of cellular convection in rotating fluids, *Tellus* **7**(1): 2–21.

Narimousa, S. (1996). Penetrative turbulent convection into a rotating two-layer fluid, *J. Fluid Mech.* **321**: 299–313.

Nield, D. A. (1968). The Rayleigh-Jeffreys problem with boundary slab of finite conductivity, *J. Fluid Mech.* **32**(2): 393–398.

Niiler, P. P. and Bisshopp, F. E. (1965). On the influence of Coriolis force on onset of thermal convection, *J. Fluid Mech.* **22**(4): 753–761.

Paul, M. R., Chiam, K.-H., Cross, M. C., Fischer, P. F. and Greenside, H. S. (2002). Pattern formation and dynamics in Rayleigh-Bénard convection: Numerical simulations of experimentally realistic geometries, *Phys. D* **184**(1-4): 114–126.

Pellew, A. and Southwell, R. V. (1940). On maintained convective motion in a fluid heated from below, *Proc. R. Soc. Lond. A* **176**(966): 312–343.

Porco, C. C., Baker, E., Barbara, J., Beurle, K., Brahic, A., Burns, J. A., Charnoz, S., Cooper, N., Dawson, D. D., Del Genio, A. D., Denk, T., Dones, L., Dyudina, U., Evans, M. W., Giese, B., Grazier, K., Helfenstein, P., Ingersoll, A. P., Jacobson, R. A., Johnson, T. V., McEwen, A., Murray, C. D., Neukum, G., Owen, W. M., Perry, J., Roatsch, T., Spitale, J., Squyres, S., Thomas, P., Tiscareno, M., Turtle, E., Vasavada, A. R., Veverka, J., Wagner, R. and West, R. (2005). Cassini imaging science: Initial results on Saturn's atmosphere, *Science* **307**(5713): 1243–1247.

Prakash, A. and Koster, J. N. (1994). Convection in multiple layers of immiscible liquids in a shallow cavity—I. Steady natural convection, *Int. J. Multiph. Flow* **20**(2): 383–396.

Prandtl, L. (1910). A relation between heat transfer and flow resistance in fluids, *Phys. Z.* **11**: 1072–1078.

Proudman, J. (1916). On the motion of solids in a liquid possessing vorticity, *Proc. R. Soc. Lond. A-Contain. Pap. Math. Phys. Character* **92**(642): 408–424.

Rasenat, S., Busse, L. and Rehberg, I. (1989). A theoretical and experimental study of double-layer convection, *J. Fluid Mech.* **199**: 519–540.

Rayleigh, L. (1916). On convection currents in a horizontal layer of fluid when the higher temperature is on the under side, *Lond. Edinb. Dublin Philos. Mag. J. Sci.* **32**(192): 529–546.

Read, P. L., Antuñano, A., Cabanes, S., Colyer, G., del Río Gaztelurrutia, T. and Sánchez-Lavega, A. (2022). Energy exchanges in Saturn's polar regions from cassini observations: Eddy-zonal flow interactions, *J. Geophys. Res.: Planets* **127**(5): e2021JE006973.

Richter, F. M. and Johnson, C. E. (1974). Stability of a chemically layered mantle, *J. Geophys. Res.* **79**(11): 1635–1639.

Rossby, H. T. (1969). A study of Bénard convection with and without rotation, *J. Fluid Mech.* **36**(2): 309–335.

Rubio, A. M., Julien, K., Knobloch, E. and Weiss, J. B. (2014). Upscale energy transfer in three-dimensional rapidly rotating turbulent convection, *Phys. Rev. Lett.* **112**(14): 144501.

Sakuraba, A. and Roberts, P. H. (2009). Generation of a strong magnetic field using uniform heat flux at the surface of the core, *Nat. Geosci.* **2**(11): 802–805.

Schmidt, R. J. and Milverton, S. W. (1935). On the instability of a fluid when heated from below, *Proc. R. Soc. Lond. A* **152**(877): 586–594.

Shampine, L. and Kierzenka, J. (2008). A BVP solver that controls residual and error, *J. Numer. Anal. Ind. Appl. Maths* **3**(1-2): 27–41.

Sikorska, D., Brzozowska, J., Pawełkiewicz, A., Psykała, M., Błasiak, P. and Kolasiński, P. (2024). Convective heat transfer in PWR, BWR, CANDU, SMR, and MSR nuclear reactors—A review, *Energies* **17**(15): 3652.

Spiegel, E. A. and Veronis, G. (1960). On the Boussinesq approximation for a compressible fluid, *Astrophys. J.* **131**: 442–447.

Stevens, R., Lohse, D. and Verzicco, R. (2011). Prandtl and Rayleigh number dependence of heat transport in high Rayleigh number thermal convection, *J. Fluid Mech.* **688**: 31–43.

Tabataba-Vakili, F., Rogers, J. H., Eichstädt, G., Orton, G. S., Hansen, C. J., Momary, T. W., Sinclair, J. A., Giles, R. S., Caplinger, M. A. and Bolton, S. J. (2020). Long-term tracking of circumpolar cyclones on Jupiter from polar observations with JunoCam, *Icarus* **335**: 113405.

Takehiro, S. I., Ishiwatari, M., Nakajima, K. and Hayashi, Y. Y. (2002). Linear stability of thermal convection in rotating systems with fixed heat flux boundaries, *Geophys. Astrophys. Fluid Dyn.* **96**(6): 439–459.

Taylor, G. I. (1923). Experiments on the motion of solid bodies in rotating fluids, *Proc. R. Soc. Lond. A-Contain. Pap. Math. Phys. Character* **104**(725): 213–218.

Taylor, G. I. (1936). Fluid friction between rotating cylinders I—Torque measurements, *Proc. R. Soc. Lond. A-Contain. Pap. Math. Phys. Character* **157**(892): 546–564.

Vallis, G. K. (2017). *Atmospheric and Oceanic Fluid Dynamics*, Cambridge University Press.

Van Dyke, M. (1964). *Perturbation Methods in Fluid Mechanics*, Academic Press.

Vasavada, A. R., Hörst, S. M., Kennedy, M. R., Ingersoll, A. P., Porco, C. C., Genio, A. D. D. and West, R. A. (2006). Cassini imaging of Saturn: Southern hemisphere winds and vortices, *J. Geophys. Res.: Planets* **111**(E5): 1–13.

Veronis, G. (1966). Large-amplitude Bénard convection, *J. Fluid Mech.* **26**(1): 49–68.

Wilczynski, F. (2019). *Convective motions in the scrape-off layer of magnetically confined plasmas*, PhD thesis, University of Leeds.

Wilczynski, F. and Hughes, D. W. (2019). Stability of two-layer miscible convection, *Phys. Rev. Fluids* **4**(10): 103502.

Yadav, K. R., Heimpel, M. and Bloxham, J. (2020). Deep convection-driven vortex formation on Jupiter and Saturn, *Sci. Adv* **6**(46): 9298–9311.

Yadav, R. K. and Bloxham, J. (2020). Deep rotating convection generates the polar hexagon on Saturn, *Proc. Natl. Acad. Sci. U. S. A.* **117**(25): 13991–13996.

Zamora, B. (2023). A review on solar chimneys: From natural convection fundamentals to thermohydraulic best-performance proposals, *Processes* **11**(2): 386.

Zhang, K. (1994). On coupling between the Poincaré equation and the heat equation, *J. Fluid Mech.* **268**: 211–229.

Zhang, K. and Gubbins, D. (1993). Convection in a rotating spherical fluid shell with an inhomogeneous temperature boundary condition at infinite Prandtl number, *J. Fluid Mech.* **250**: 209–232.

Zhang, K. and Schubert, G. (1996). Penetrative convection and zonal flow on Jupiter, *Science* **273**(5277): 941–943.